www.GetPedia.com

theclinics.com

Clinics Home | About Clinics | Hot Topics | Special Offers | CME

Radiologic Clinics of North America

Register or Login: Password: SIGN IN Auto-Login [Reminder]

Search This Clinic for GO

Advanced Search - MEDLINE - My Recent Searches - My Saved Searches - Search Tips

CLINIC HOME
CURRENT ISSUE
PREVIOUS ISSUES
SEARCH THIS CLINIC
FORTHCOMING ISSUES
CLINIC INFORMATION
- Author Information
- Abstracting/Indexing
- Contact Information
- Media Information
- Permissions
- Buy Back Issues

RELATED SITES

More periodicals:
FIND A PERIODICAL
FIND A PORTAL
GO TO PRODUCT CATALOG

Issue

Alert me when new journal issues are available. Add TOC Alert

July 2003 (Vol. 41, Issue 4)

previous issue next issue

View Selected Abstracts

Display: without preview

CONTENTS
pages v-vii
PDF (26 KB)

FORTHCOMING ISSUES
page viii
PDF (18 KB)

Preface

Women's imaging: obstetrics and gynecology
by Levine D
page xi
Full Text | PDF (45 KB)

What's new in first trimester ultrasound
by Lazarus E
pages 663-679
Full Text | PDF (1053 KB)

Ultrasound detection of first trimester malformations: a pictorial essay
by Castro-Aragon I, Levine D
pages 681-693
Full Text | PDF (1026 KB)

Prenatal diagnosis for detection of aneuploidy: the options
by Budorick NE, O'Boyle MK
pages 695-708
Full Text | PDF (676 KB)

Complications of monochorionic twins
by Feldstein VA, Filly RA
pages 709-727
PDF (1469 KB)

Tips and tricks of fetal MR imaging
by Levine D, Stroustrup Smith A, McKenzie C
pages 729-745
Full Text | PDF (1186 KB)

MR imaging of pelvic floor relaxation
by Fielding JR
pages 747-756
Full Text | PDF (599 KB)

Imaging of female infertility
by Thurmond AS
pages 757-767
Full Text | PDF (746 KB)

☐ **Ultrasonographic evaluation of the endometrium in postmenopausal vaginal bleeding**
by Davidson KG, Dubinsky TJ
pages 769-780
Full Text | PDF (1118 KB)

☐ **Sonohysterography**
by O'Neill MJ
pages 781-797
Full Text | PDF (1463 KB)

☐ **MR imaging of the ovaries: normal appearance and benign disease**
by Togashi K
pages 799-811
Full Text | PDF (914 KB)

☐ **Osteoporosis imaging**
by Link TM, Majumdar S
pages 813-839
Full Text | PDF (1449 KB)

☐ **Current uses of ultrasound in the evaluation of the breast**
by Mehta TS
pages 841-856
Full Text | PDF (958 KB)

☐ **Index**
pages 857-862
PDF (67 KB)

View Selected Abstracts

Display: without preview

© 2004 Elsevier, Inc. | Privacy Policy | Terms & Conditions | Feedback | About Us | Help | Contact Us

CONTENTS

Preface **xi**
Deborah Levine

What's New in First Trimester Ultrasound **663**
Elizabeth Lazarus

Ultrasound performed during the first trimester confirms an intrauterine pregnancy, establishes accurate dating, and is crucial in diagnosing early pregnancy failure and ectopic pregnancy. As sonographic spatial resolution continues to improve, first trimester sonography increasingly will offer early pregnancy screening for chromosomal abnormalities and fetal structural abnormalities.

Ultrasound Detection of First Trimester Malformations: A Pictorial Essay **681**
Ilse Castro-Aragon and Deborah Levine

With improvements in ultrasound technology, it is possible to detect many fetal malformations in the first trimester. This article illustrates the types of embryonic and fetal anomalies that can be detected in the first trimester, including anencephaly, encephalocele, hydrocephalus, omphalocele, gastroschisis, megacystis, and conjoined twins. The authors also illustrate pitfalls in image interpretation of first trimester anatomy (including the normal rhombencephalon and normal gut herniation) and prospectively unrecognized cases of early omphalocele and anencephaly.

Prenatal Diagnosis for Detection of Aneuploidy: The Options **695**
Nancy E. Budorick and Mary K. O'Boyle

Prenatal diagnosis for aneuploidy consists of invasive and noninvasive testing. Second trimester biochemical screening is more accurate in determining risk for aneuploidy than maternal age alone. One or more various major abnormalities identified on a second trimester sonogram are indicative of an at-risk patient. Several minor ultrasound markers on a second trimester sonogram are sensitive and specific for aneuploidy, particularly thickened nuchal fold and a shortened humerus. Other minor abnormalities identified in the second trimester also may be associated with aneuploidy, but the method of determining exact risk based on the presence or absence of these markers is controversial. First trimester combined screening with nuchal translucency thickness and biochemical markers shows promise in early and accurate identification of the patient at risk for aneuploidy.

Complications of Monochorionic Twins **709**
Vickie A. Feldstein and Roy A. Filly

There are high risks associated with monochorionic twin gestations, partly related to the shared placenta and the presence of intertwin vascular connections. Several potential complications and syndromes are unique to monochorionic gestations. Obstetric sonography, with the use of Doppler techniques, is used to diagnose and evaluate these pregnancies. Being aware of the sonographic criteria for determining chorionicity and recognizing the features that indicate twin-twin transfusion syndrome, acardiac parabiotic twin, conjoined twins, and other complications are important for obstetric management and optimizing outcome.

Tips and Tricks of Fetal MR Imaging **729**
Deborah Levine, Annemarie Stroustrup Smith, and Charles McKenzie

MR imaging during pregnancy is being used increasingly to assess fetuses with complicated or nonspecific ultrasound diagnoses. This article illustrates common artifacts and other pitfalls in the performance of fetal MR examinations and suggestions of techniques to improve image quality. Comparisons of anatomy visualized on fetal MR imaging versus ultrasound are demonstrated.

MR Imaging of Pelvic Floor Relaxation **747**
Julia R. Fielding

MR imaging of female pelvic floor relaxation is a relatively new technique that, once mastered, is quick to perform and interpret. Rapidly acquired T2-weighted images are obtained in the sagittal plane at rest and at maximal strain. In symptomatic patients, abnormal descent of pelvic viscera on sagittal images is indicative of muscle or fascial weakness or tears. On axial images, the pelvic floor muscles can be assessed for tears and fraying. This information can be used to plan optimal surgical repair.

Imaging of Female Infertility **757**
Amy S. Thurmond

Normal reproduction requires healthy female anatomy. Cervical, uterine, tubal, ovarian, and peritoneal factors can coexist and cause female infertility. Ultrasound, hysterosalpingography, MR imaging, and fallopian tube catheterization are the radiologists' armamentarium for diagnosis. This article illustrates important findings in the infertile woman. An understanding of these entities helps in accurate and sympathetic treatment.

Ultrasonographic Evaluation of the Endometrium in Postmenopausal Vaginal Bleeding **769**
Katharine G. Davidson and Theodore J. Dubinsky

Abnormal bleeding is one of the most frequent complaints of postmenopausal women who seek gynecologic care. Ultrasound and biopsy are reasonable competing methods for evaluating the cause of the bleeding in these women. Ultrasound has better sensitivity than biopsy in depicting nonmalignant causes of bleeding, so it can establish the cause of bleeding in more patients than biopsy. Saline infusion sonohysterography is helpful in depicting endometrial pathologic conditions but can be reserved for evaluating patients in whom the transvaginal ultrasound images do not clearly depict a focal mass. Hysteroscopy is the standard for removing focal endometrial lesions, although it is too expensive to be used routinely for diagnosis of endometrial abnormalities more easily evaluated by ultrasound.

Sonohysterography **781**
Mary Jane O'Neill

Sonohysterography can distinguish focal from diffuse pathology reliably and has become a crucial imaging test in the triage of postmenopausal bleeding and in premenopausal patients with dysfunctional uterine bleeding or infertility. Polyps and submucosal fibroids are the most common focal findings at sonohysterography. In postmenopausal patients, detection and accurate localization of findings, rather than lesion characterization, are the primary goals of the procedure. Most, if not all, focal lesions in this patient population require tissue diagnosis, even when the imaging features suggest benign lesions.

MR Imaging of the Ovaries: Normal Appearance and Benign Disease **799**
Kaori Togashi

Ovaries can enlarge physiologically as a result of cyclic cyst formation. Such an enlargement and some benign conditions occasionally are mistaken as malignant disease processes. Accurate diagnoses of benign conditions as normal, along with variations, as opposed to neoplasia, inflammatory masses, and other etiologies of abnormal-appearing ovaries, including torsion, help avoid unnecessary interventions. This article reviews the MR findings of various benign conditions of adnexa that help to distinguish benign from malignant conditions.

Osteoporosis Imaging **813**
Thomas M. Link and Sharmila Majumdar

As populations age, osteoporosis becomes an increasingly important public health issue. To prevent osteoporotic fractures, patients with osteoporosis must be diagnosed at an early stage. According to the World Health Organization, osteoporosis is defined by bone mineral density measurements that are compared with measurements of a healthy, young, female population. The best established techniques to measure bone mineral density are dual energy x-ray absorptiometry of the lumbar spine and proximal femur and quantitative CT of the lumbar spine. Conventional radiographs are not suited to assess bone mass but are important in the diagnosis and differential diagnosis of osteoporotic fractures. Quantitative ultrasound and structure analysis based on high-resolution MR imaging and CT are newer techniques in the diagnosis of osteoporosis that also focus on the assessment of bone structure.

Current Uses of Ultrasound in the Evaluation of the Breast **841**
Tejas S. Mehta

Breast ultrasound is used routinely as an adjunct to mammography to help differentiate benign from malignant lesions. In patients younger than 30 years of age or patients who are pregnant, ultrasound may be the first or sole imaging modality to evaluate for breast pathology. Other less common uses of breast ultrasound include potential staging of breast cancer and evaluating breast implants. Ultrasound is useful in guiding interventional breast procedures. Although still controversial, some studies have advocated using ultrasound for screening for breast carcinoma in asymptomatic women. This article reviews the multiple current uses of ultrasound in the evaluation of the breast.

Index **857**

FORTHCOMING ISSUES

September 2003

Renal Imaging
Philip J. Kenney, MD, *Guest Editor*

November 2003

Imaging the Acute Abdomen
Emil J. Balthazar, MD, *Guest Editor*

January 2004

Arthritis Imaging
Barbara N. Weissman, MD, *Guest Editor*

RECENT ISSUES

May 2003

Multislice Helical CT of the Thorax
Phillip M. Boiselle, MD, *Guest Editor*

March 2003

Advances in Intestinal Imaging
Dean D.T. Maglinte, MD, and
Stephen E. Rubesin, MD, *Guest Editors*

January 2003

Body MR Imaging
David A. Bluemke, MD, PhD, *Guest Editor*

VISIT THESE RELATED WEB SITE

For more information about Clinics:
http://www.wbsaunders.com

RADIOLOGIC
CLINICS OF
NORTH AMERICA

Radiol Clin N Am 41 (2003) 663–679

What's new in first trimester ultrasound

Elizabeth Lazarus, MD

Department of Diagnostic Radiology, Brown Medical School, 593 Eddy Street, Providence, RI 02903, USA

With the widespread use of home pregnancy tests, women are confirming pregnancy at earlier and earlier points in gestation. The rapid technologic advances in sonography and the widespread use of endovaginal probes, has allowed imaging to keep pace, providing women with specific information regarding the status of their early pregnancies. Improved spatial resolution in ultrasonographic images has allowed earlier confirmation of normal pregnancies and earlier identification of pregnancy failures. The detection of ectopic pregnancy at younger gestational ages has led to new, less invasive treatment approaches. Recent studies indicate that the first trimester ultrasound may be effective in screening for chromosomal abnormalities and detecting structural defects. In this article, the author discusses advances in first trimester ultrasound and their effects on the interpretation of normal and abnormal studies.

Transducer technology

The transvaginal probe has helped revolutionize the assessment of early pregnancy and is believed to be the transducer of choice for evaluating all early pregnancies [1–3]. The higher frequency endovaginal probes provide near field focusing and the ability to be positioned closer to the uterus, which provides better spatial resolution and improved diagnostic accuracy. Transabdominal ultrasound provides little information regarding the fetus before the eighth week of gestation. Before this gestational age, a small hemorrhage or clump of debris can be mistaken for an embryo (Fig. 1) [4]. Endovaginal ultrasound can identify the yolk sac, fetus, and embryonic cardiac activity earlier and can confirm intrauterine pregnancies at younger gestational ages and at lower levels of human chorionic gonadotropin (hCG) [5–7].

Endovaginal probe transducer frequencies typically range from 5 to 7.5 mHz, and most of the data regarding early sac and embryo sizes are based on studies performed at these frequencies. Newer transducers with higher frequencies of 10 mHz or higher provide better spatial resolution and can identify features such as a yolk sac or double decidual reaction at even earlier points in the pregnancy [8]. These higher resolution transducers also have the potential to provide earlier diagnosis of fetal abnormalities.

Normal pregnancy

Gestational sac

The early embryo in the blastocyst stage is implanted at approximately 6 to 7 days after fertilization. The embryo becomes completely embedded in the endometrial decidua at 9.5 days after conception (24 days after last menstrual period). By the end of the second week after fertilization, the conceptus has grown to a total diameter of 2 to 3 mm and can be visualized with high-frequency endovaginal transducers. During the third week after fertilization, the exocoelomic cavity—a fluid filled cavity referred to as the "gestational sac" by sonographers—can be seen routinely when it attains a diameter of 5 mm [9].

Early attempts to describe reliable ultrasonographic finding of intrauterine pregnancy initially were developed during the age of transabdominal imaging. These signs largely have been discarded or

E-mail address: ELazarus@Lifespan.org

0033-8389/03/$ – see front matter © 2003 Elsevier Inc. All rights reserved.
doi:10.1016/S0033-8389(03)00039-3

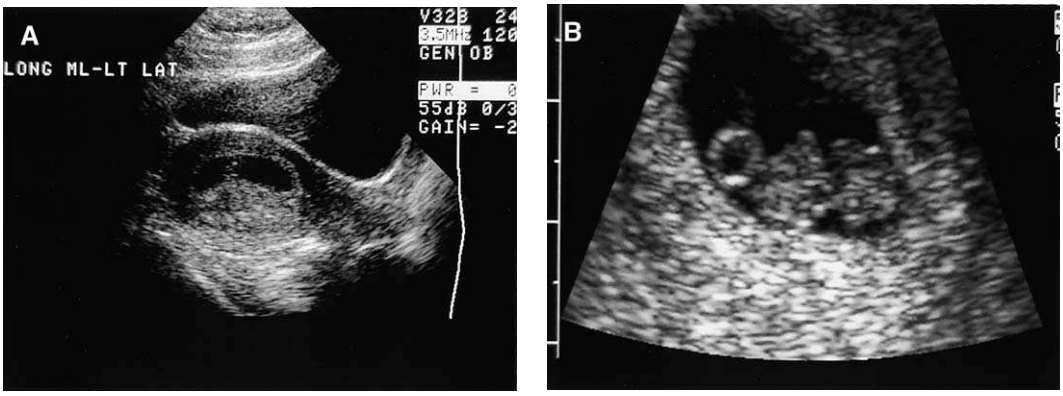

Fig. 1. (*A*) Sagittal transabdominal image of 7-week gestational sac that contains amorphous echogenic material not clearly identifiable as an embryo. (*B*) Endovaginal image obtained during the same examination clearly identifies the yolk sac and embryo within the gestational sac.

supplanted by more reliable indicators that have evolved in the age of transvaginal probes. To identify an intrauterine pregnancy before the development of a gestational sac, the concept of the ''intradecidual sign'' was first introduced by Yeh et al in 1986 [10]. This sign describes a focal anechoic area eccentrically positioned in the endometrium that does not deform the endometrium because of its small size (Fig. 2). This sign is believed to represent the conglomeration of echoes caused by the embedded blastocyst, the proliferative plasmodial trophoblasts, and the adjacent decidua. Yeh et al were able to recognize the appearance as early as 3.5 weeks' menstrual age (or 1.5 weeks after conception), the same time at which pregnancy could be verified by the bioassay method for hCG. For purposes of distinguishing between early intrauterine and ectopic pregnancy, Yeh et al reported a sensitivity rate of 92%, a specificity rate of 100%, and an overall accuracy rate of 93%.

This sign originally was described using transabdominal sonography, however, and has not been verified with transvaginal scanning. Laing et al's attempt to confirm the validity of this sign using transvaginal scanning was not as successful. Detection of the intradecidual sign resulted in relatively poor sensitivity (34%–66%) and specificity (55%–73%) rates [11]. These percentages demonstrated that the sign is unreliable and should not be used to verify a normal pregnancy in the age of transvaginal ultrasound.

The double decidual reaction reliably differentiates between a true gestational sac and an intraendometrial fluid produced from an ectopic pregnancy (pseudosac). The gestational sac first can be visualized endo-

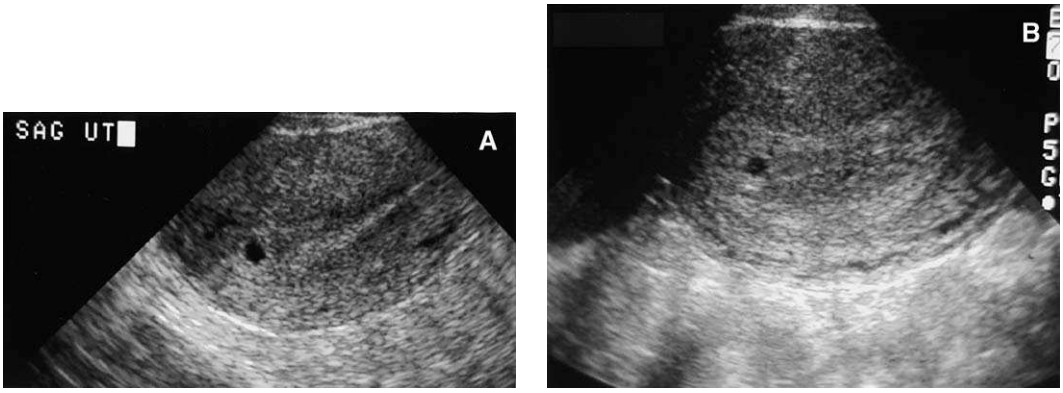

Fig. 2. (*A*) Sagittal and (*B*) transverse sonographic views of the gravid uterus demonstrate the ''intradecidual sac sign'': echogenic material surrounding a small cyst-like fluid collection located eccentrically within the endometrium.

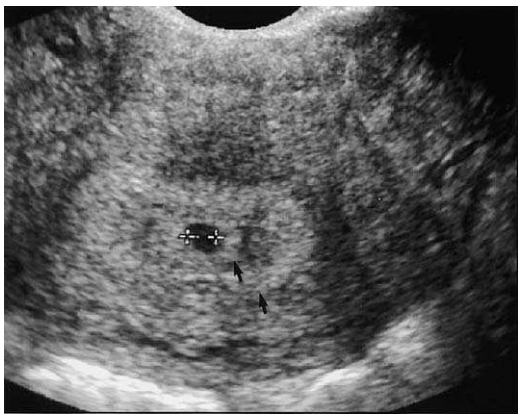

Fig. 3. Transverse endovaginal ultrasound at 5.5 weeks' menstrual age demonstrates the ''double decidual reaction'' of two concentric echogenic rings (*arrows*) around the intrauterine gestational sac implanted within the endometrium.

vaginally at 4.5 weeks' menstrual age but cannot be identified definitively as such before visualization of a yolk sac or embryo [6,12]. The double decidual reaction was described by Bradley et al in 1982 as two concentric echogenic rings surrounding the intraendometrial fluid collection that impress upon the endometrial stripe in a normal early pregnancy (Fig. 3). The inner ring represents the decidua capsularis around the chorion, and the outer ring represents the decidua parietalis, separated by a thin rim of fluid in the endometrial cavity [13]. In an ectopic pregnancy, the decidual reaction presents as only a single echogenic ring around the endometrial fluid collection.

The double decidual reaction sign of intrauterine pregnancy is present and identifiable from 2 to 9 weeks' menstrual age but also was described before the widespread use of endovaginal ultrasound. The sign was considered useful in transabdominal scanning between 4 and 6 weeks of age to establish an intrauterine pregnancy before the yolk sac can be visualized. It is universally present when the mean sac diameter (MSD) is 10 mm. Using endovaginal probes, however, a yolk sac almost always can be identified at this point, which diminishes the use of the double decidual reaction in distinguishing early intrauterine pregnancies [14].

Some researchers have explored the concept of using Doppler sonography to verify intrauterine pregnancies. Doppler ultrasound has been shown to demonstrate a high-velocity, low-impedance arterial flow adjacent to the developing trophoblast. This pattern of flow is caused by the high pressure gradient between the maternal spiral arteries and the intervillous space. Parvey et al found that this vascular flow pattern was demonstrated in only 15% of early pregnancies that did not have an identifiable embryo or yolk sac on ultrasound. They then proposed combining the Doppler signature with sonographic identification of the inner chorionic rim and demonstrated sensitivity and specificity rates of more than 90% for this combination in identifying an intrauterine pregnancy [15]. Doppler is not widely used in this setting, however, mainly because of the possible effects that the increased energy output may have on the developing fetus [11].

Yolk sac

At the end of the second week after fertilization (4 weeks' menstrual age), the primary (primitive) yolk sac begins to regress and the secondary yolk sac develops [16]. The secondary yolk sac is the first object seen sonographically in the gestational sac before the visualization of the embryo. It appears as a circular echogenic structure between 3 and 7 mm [17] and is initially detected in all patients by endovaginal ultrasound by between 37 and 40 menstrual days (Fig. 4). Transvaginal scanning can demonstrate a yolk sac with an hCG level as low as 2200 mIUnits/mL, IRP [6].

The yolk sac is a valuable feature that distinguishes normal intrauterine pregnancies. Ultrasonographically visible before the embryo, detection of a yolk sac is a reliable indicator of a true gestational sac with a positive predictive value of 100% [14]. Because it confirms an intrauterine pregnancy, the detection of a yolk sac in an endometrial fluid collec-

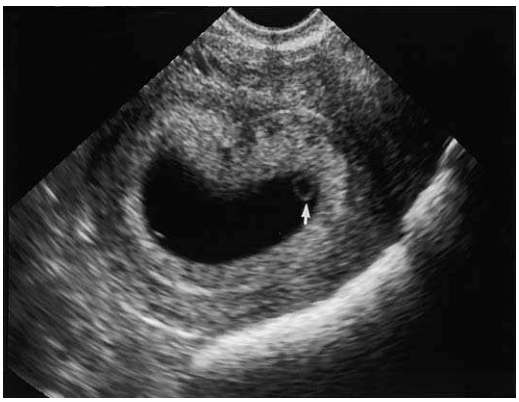

Fig. 4. Rounded echogenic structure (*arrow*) within the gestational sac represents the early yolk sac, which distinguishes this intrauterine fluid collection as a gestational sac.

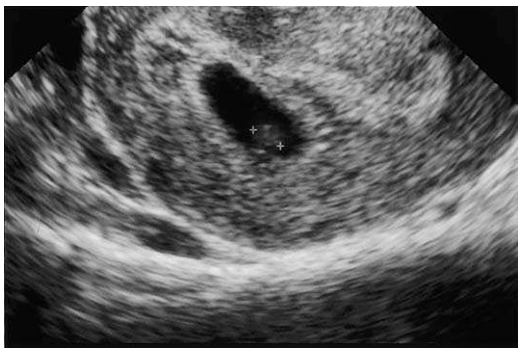

Fig. 5. Tubular echogenic structure between calipers within the gestational sac represents the early embryo identified on ultrasound as the embryonic pole.

tion in a pregnant woman usually excludes the possibility of ectopic pregnancy.

Embryonic pole

When neurulation occurs at approximately 40 menstrual days, the trilaminar embryonic disk becomes the more recognizable tubular structure usually referred to as the "fetal pole," although at this gestational age "embryonic pole" is a more appropriate term (Fig. 5). The embryonic disk lies adjacent to the secondary yolk sac, which provides a useful landmark to look for early embryonic cardiac pulsations [18].

Heartbeat

The cardiovascular system is the first embryonic system to function, and the primitive heart begins to beat at the end of the third week after fertilization (4 weeks' menstrual age) [18]. By the time the embryo is visualized on a transabdominal scan, it should demonstrate a heartbeat or be considered nonviable [19]. Endovaginal ultrasonography can detect small normal embryos before detecting their cardiac pulsations, however. In embryos smaller than 5 mm, the fetal heartbeat may not be seen by endovaginal ultrasound because cardiac activity does not begin until the end of the 5 weeks' menstrual age, when the embryo measures from 1.5 to 3 mm [19]. For embryos smaller than 5 mm that lack a visible heartbeat on endovaginal ultrasound, follow-up ultrasound is suggested to document cardiac activity.

The embryonic heart rate is earliest detectable by the human eye. Heart rate measurement should be performed via M-mode because it does not increase the power delivered to the tissue as much as does pulse Doppler. Care should be taken that maternal uterine pulsations are not mistaken for embryonic heartbeats (Fig. 6). Embryonic heart rates increase slowly between 6 and 9 weeks' menstrual age and then slowly decrease throughout the remainder of the first trimester. The mean embryonic heart rates as measured by Stefos et al were 111 ± 14 beats per minute (bpm) at 42 to 45 days' gestation, 125 ± 15 bpm at 50 to 52 days' gestation, and

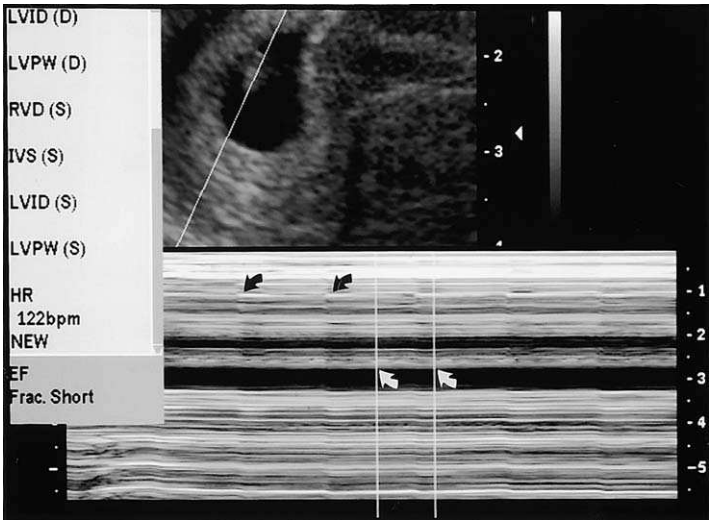

Fig. 6. M-mode ultrasound identifies and measures embryonic cardiac activity (*white arrows*) and maternal cardiac activity (*black arrows*).

157 ± 13 bpm at 53 to 56 days' gestation [20,21]. There is a low intraindividual variation in embryonic heart beats at less than 10 gestational weeks, which indicates that a single measurement of embryonic heart rate is sufficient [22]. The presence of cardiac pulsations predicts a favorable pregnancy outcome in 90% to 97% of patients [23]. Once normal cardiac activity is established, spontaneous abortion occurs in only 2% to 4% of cases [24].

Age assessment

The MSD provides the most accurate way to date an early pregnancy on ultrasound before visualization of the embryo. The MSD is a measurement of the mean gestational sac size and is obtained by adding the anteroposterior and craniocaudal diameters obtained on the sagittal view of the uterus to the transverse diameter obtained on the transverse view and dividing by three (Fig. 7) [12,25]. The sac size can be correlated with menstrual age in early pregnancy by the following formula: menstrual age in days = MSD + 30 [12]. MSD increases approximately 1 to 1.5 mm/day for the first 50 to 60 days of pregnancy. Once the embryonic pole is detected, measurement of the crown rump length of the embryo is considered the most accurate ultrasonographic way to date the pregnancy [58].

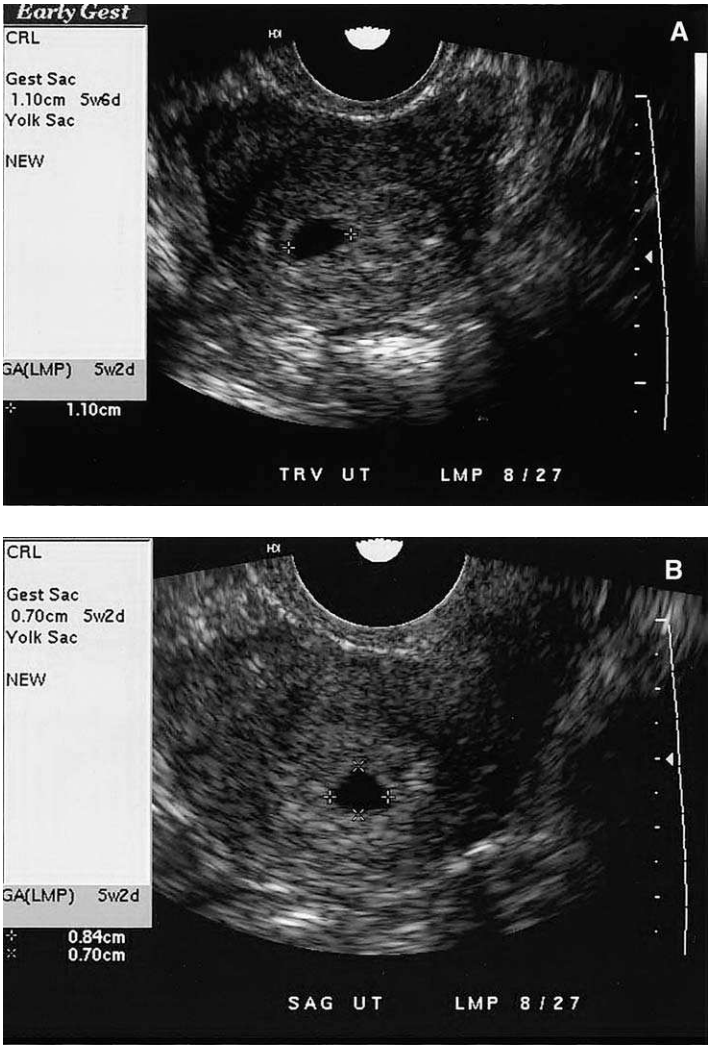

Fig. 7. Measurement of the MSD. (*A*) Single measurement indicated by calipers obtained on the transverse view of the gestational sac. (*B*) Anteroposterior and craniocaudal measurements obtained on the sagittal view of the gestational sac.

Early pregnancy failure

Studying normal healthy women, Wilcox et al demonstrated a 31% rate of early pregnancy loss [27], most of which occurs before the pregnancy is confirmed by either an ultrasound or a chemical pregnancy test. The presence of vaginal bleeding in pregnancy increases the risk of miscarriage. Vaginal bleeding occurs in approximately 25% of known first trimester pregnancies, and of these, 50% abort [23]. In these symptomatic pregnancies, ultrasound is important because it identifies which of these pregnancies may be viable and which ones will not be successful pregnancies. This determination influences patient management and significantly affects patient anxiety.

The best criteria currently available to verify a normal early intrauterine pregnancy are [1] a yolk sac within a gestational sac and [2] an embryo with cardiac activity. Without one of these signs, the possibility of early pregnancy failure must be raised. Lack of normal growth on serial ultrasound also can be used as a reliable indicator of a failed pregnancy [5]. Because follow-up mandates a delay in diagnosis, however, many attempts have been made to define ultrasonographic features that can identify the pregnancies that will fail as early as possible.

Major criteria for abnormal outcome

Nyberg et al first introduced major and minor criteria to distinguish between normal and abnormal gestational sacs in 1986 using findings on transabdominal ultrasound. Major criteria exhibited 100% predictive accuracy and 100% specificity for an abnormal pregnancy. These criteria included large sac size with a MSD of 25 mm or more with no embryo and 20 mm or more with no yolk sac, and a grossly distorted sac shape (Fig. 8) [23].

Since Nyberg introduced the concept of "discriminatory" gestational sac sizes at which a yolk sac or an embryo must be seen to be considered normal, others have reexamined the discriminatory size criteria for endovaginal ultrasound. The most widely accepted discriminatory sac sizes using endovaginal ultrasound are 8 mm MSD for visualization of the yolk sac and 16 mm MSD for visualization of the embryo [2,5]. A range of values is reported in the literature, however, with values up to 13 mm for visualizing a yolk sac and 18 mm for visualizing an embryo (Fig. 9) [5,6,28]. Some of this discrepancy can be explained by variations in patient population and ultrasound transducer frequencies from 5 to 7.5 MHz [2]. Use of a higher frequency 9-5 MHz transducer improves spatial resolution of the gestational sac and can identify sac contents at smaller MSD and earlier menstrual ages. Use of the higher frequency probe sometimes can obviate the need for follow-up sonography. Discriminatory values that rely on the use of these high-frequency transducers likely will be established in the future.

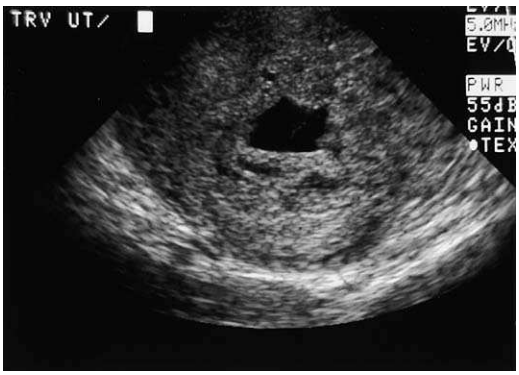

Fig. 8. Grossly distorted gestational sac with irregular margins contains no identifiable yolk sac or embryonic pole, which is consistent with an early pregnancy failure.

Other explanations for the range of discriminatory values include the rare occurrences of early monochorionic twins or early "polyhydramnios." Inexperienced sonographers also may inadvertently miss a yolk sac or embryo that can be difficult to distinguish against the wall of the gestational sac. Given the variation in published discriminatory sac sizes, in the setting of a desired pregnancy, the discriminatory size criteria should be conservative. The author recommends use of the upper limits in the literature of 13 mm for visualization of a yolk sac and 18 mm for visualization of an embryonic pole. Serial ultrasounds in conjunction with hCG levels are often valuable [28].

Minor criteria for abnormal outcome

Minor criteria for abnormal outcome, as established by Nyberg, are sonographic features that suggest an abnormal outcome but lack the specificity in isolation to diagnose early pregnancy failure. These criteria include deficient choriodecidual reaction, absent double decidual reaction, irregular contour of the gestational sac, and low position of the sac (Fig. 10) [23]. When three or more of these features are present on transabdominal ultrasound, the specificity rate for pregnancy failure approaches 100%.

Other researchers have identified additional features that portend a high likelihood of pregnancy failure, including a small sac size and slow embryonic cardiac pulsation rate. Small sac size is defined by a difference between the MSD and crown rump length of

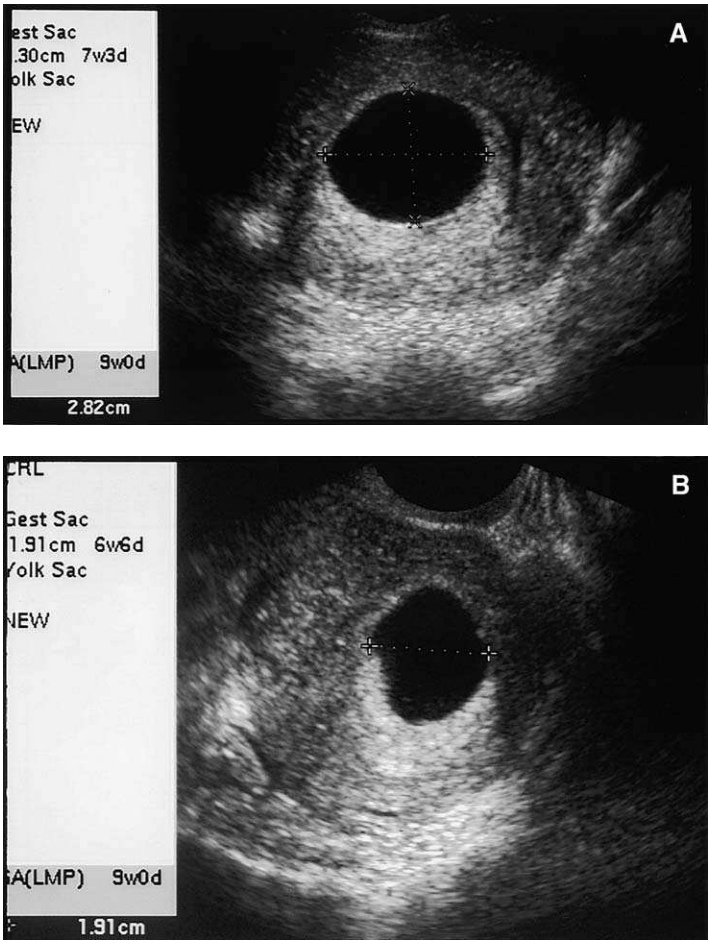

Fig. 9. (*A*) Sagittal and (*B*) transverse views of a large intrauterine gestational sac with MSD larger than 19 mm with no embryonic pole or yolk sac indentified, which is consistent with a nonviable early pregnancy.

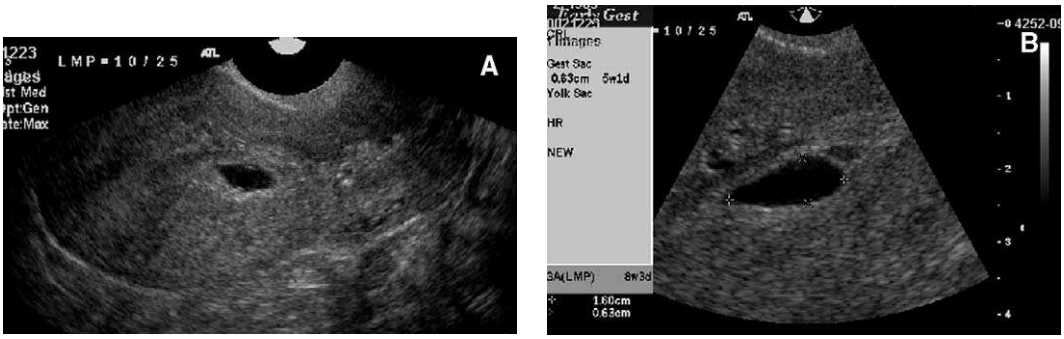

Fig. 10. (*A*) Sagittal views of the uterus with close-up view of the gestational sac (*B*) demonstrate an irregularly shaped intrauterine gestational ac that contains yolk sac positioned low within the uterus (*arrow*). This gestational sac had not grown within the past week, which is consistent with a missed abortion.

less than 5 mm measured between 5.5 and 9 menstrual weeks (Fig. 11). As indicated by Giacomello, this is not true "oligohydramnios" because the small sac size is caused by reduction of fluid outside of the amniotic membrane [29]. Bromley et al found small sacs to be predictive of miscarriage in 94% of cases [24]. In a later study by Rowling, however, at least 35% of such cases progressed to a second trimester scan or a normal delivery, which suggests this finding is not as dire as first thought. In contrast, no researcher has found that abnormally large gestational sac sizes in relation to the embryonic pole predict poor outcome. This circumstance may explain the large sacs with MSDs up to 18 mm without a yolk sac that eventually develop into normal pregnancies [28].

The embryonic heart rate increases between 6 and 9 weeks' gestation. At 6 weeks' menstrual age, the mean embryonic heart rate ranges from 90 to 133 bpm, and at 9 weeks' gestation it ranges from 144 to 170 bpm. A slow embryonic heart rate is associated with a poor outcome [30]. Specifically, rates below 100 bpm before 6.3 weeks' gestation and below 120 bpm between 6.3 and 7 weeks' gestation have been associated with a high risk of miscarriage. The lower the heart rate, the greater the chance of miscarriage. Fetuses with heart rates below 80 bpm before 6.3 weeks' gestation or below 100 bpm at 6.3 to 7 weeks' gestation have rates of loss approaching 100% [20].

Fetuses with abnormally rapid heart rates—defined as higher than 135 bpm— before 6.3 weeks' gestation or more than 155 bpm at 6.3 to 7 weeks' gestation have been shown to have a good prognosis and a high likelihood of a normal outcome [31].

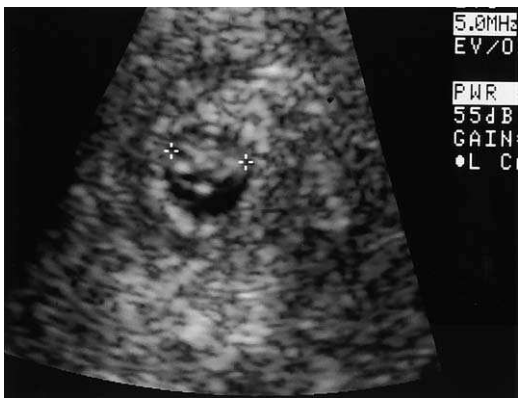

Fig. 11. Embryonic pole comprises nearly the entire volume of the gestational sac with 2 mm difference between the crown rump length and the MSD, which is consistent with a small sac size for the embryo.

Ectopic pregnancy

The estimated number of ectopic pregnancies has been increasing steadily since 1970. This increased incidence correlates with increasing prevalence of risk factors, including infection by Chlamydia and other sexually transmitted diseases, ovulation induction, tubal sterilization [32], and improved detection of ectopic pregnancies, which may have remained otherwise unrecognized and possibly resolved without intervention [33]. Ectopic pregnancy was the leading cause of pregnancy-related maternal death in the first trimester in the United States from 1990 to 1992. During that time period, ectopic pregnancy accounted for approximately 2% of all reported pregnancies and 9% of all pregnancy-related maternal deaths in the United States [32].

The "classic" clinical triad of pain, abnormal vaginal bleeding, and a palpable adnexal mass is present in less than half of patients with ectopic pregnancy. Of patients with these symptoms, most are not pregnant [34]. Because the clinical presentation is neither sensitive nor specific, diagnosis relies on a combination of clinical, biochemical, and imaging findings.

Because any woman of child-bearing range is at risk for ectopic pregnancy, establishing the location of pregnancy is recommended for any pregnant woman who presents for pelvic ultrasonography [35]. Approximately 97% of all ectopic pregnancies occur in the fallopian tubes, specifically in the ampullary region. They may occur occasionally in the cervical region, interstitial portion of the fallopian tube, abdominal cavity, or ovary [36]. Transvaginal ultrasound is clearly superior to transabdominal ultrasound in evaluating the endometrium and adnexa and provides a definitive diagnosis more often and earlier than transabdominal ultrasound. Endovaginal sonography may miss an ectopic pregnancy located high out of the field of view of the endovaginal probe or when a pelvic mass, such as a fibroid or bowel gas, is located between the vagina and the adnexal mass [37–40]. In cases in which a diagnosis of ectopic pregnancy can be made absolutely on endovaginal ultrasound, transabdominal scanning is not necessary [38]. A limited transabdominal scan is recommended in all cases of suspected ectopic pregnancy in which the endovaginal ultrasound does not provide a clear diagnosis, however. Including the transabdominal study may increase the sensitivity rate up to 5% over transvaginal studies alone (Fig. 12) [40]. In this setting, it is not necessary always to fill the bladder before the transabdominal scan [41].

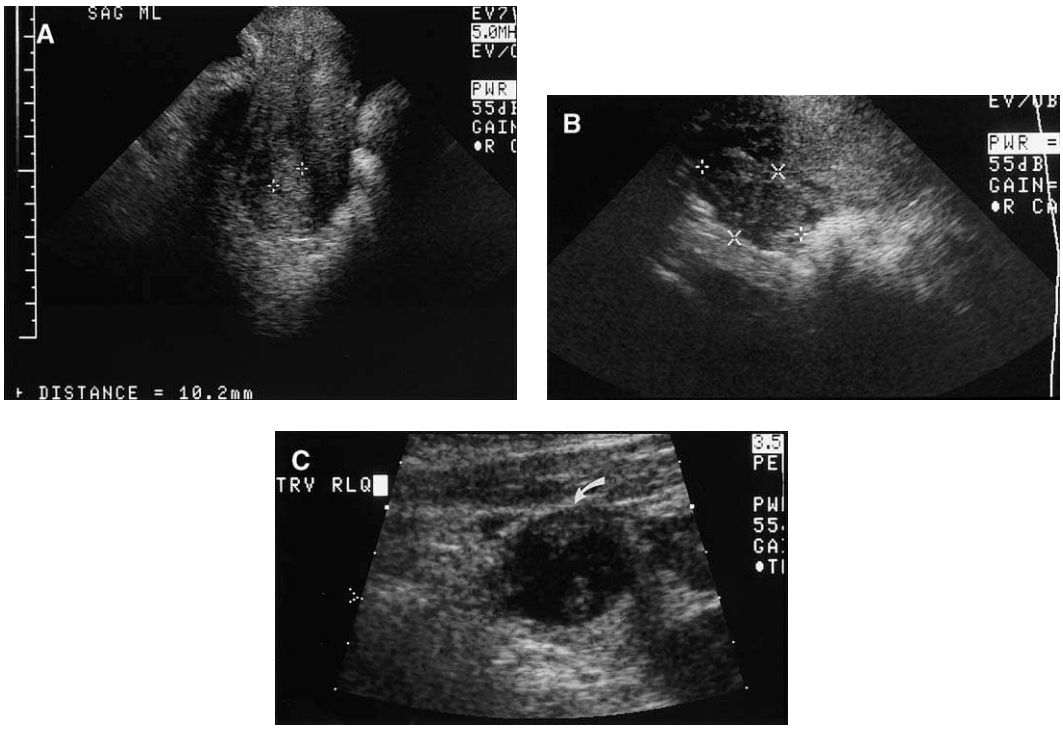

Fig. 12. (*A*) Endovaginal ultrasound shows a sagittal view of the uterus with a normal appearing endometrial stripe marked by calipers. (*B*) Normal right ovary marked by calipers. (*C*) Transabdominal ultrasound of the right lower quadrant shows a complex mass (*arrow*) high in the pelvis that contains a yolk sac and fetal embryonic pole, consistent with ectopic pregnancy.

Because the frequency of coexistent intrauterine pregnancy and ectopic pregnancy (heterotopic pregnancy) is low at between 1/4000 and 1/7000 [42,43], the diagnosis of an intrauterine pregnancy effectively excludes ectopic pregnancy in most patients [39]. Even in the presence of an intrauterine pregnancy, however, evaluation of the adnexa should be performed to screen for a possible coexistent ectopic pregnancy, especially in women who present with pelvic pain and women with a history of assisted fertilization (Fig. 13) [36].

The rate of ectopic pregnancy is higher in women who undergo assisted fertility. Mol et al found an overall incidence of ectopic pregnancy after in vitro

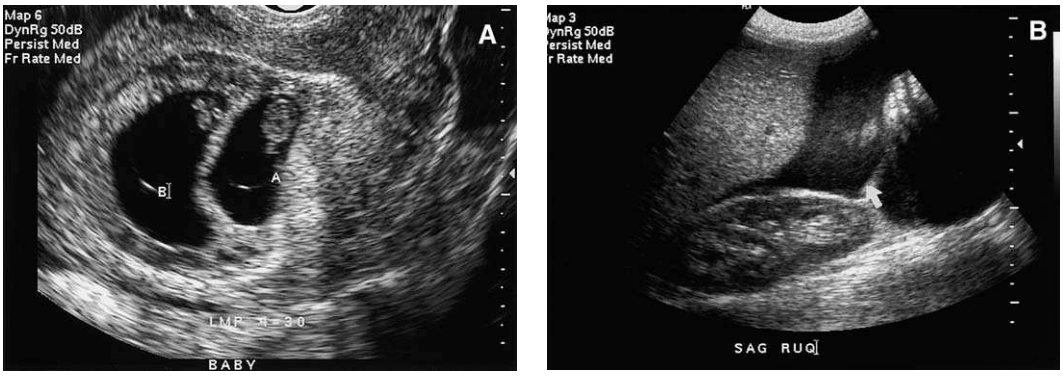

Fig. 13. Heterotopic pregnancy in a patient who had been taking Pergonal. (*A*) Intrauterine diamniotic twin pregnancy and (*B*) large amount of echogenic free fluid in Morrison's pouch (*arrow*) caused by heterotopic triplet pregnancy. The ectopic pregnancy was removed surgically, and the patient delivered twins at term. (Courtesy of Deborah Levine, MD, Boston, MA.)

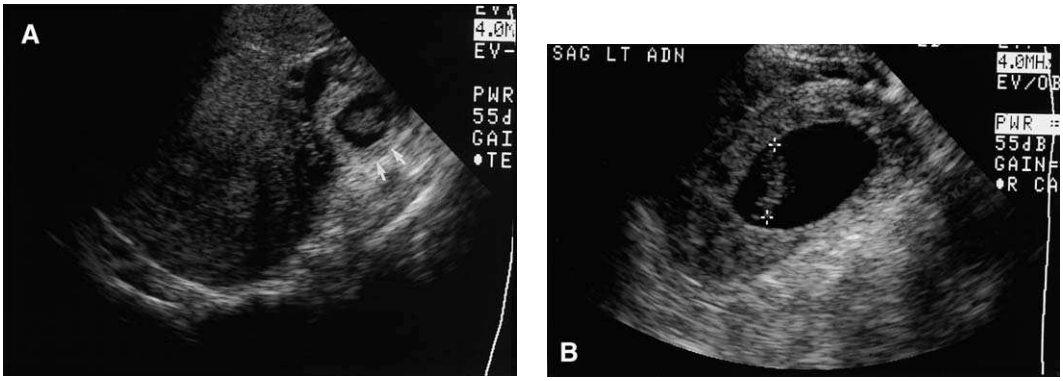

Fig. 14. Extrauterine gestational sac that contains yolk sac and embryonic pole in the adnexa, which are consistent with ectopic pregnancy. (*A*) Transverse endovaginal image shows an empty uterus and left adnexal mass (*arrows*). (*B*) Close-up view of left adnexa shows extrauterine gestational sac, which contains an embryonic pole marked by calipers and yolk sac.

fertilization and embryo transfer to be 5.1% [44]. The rate of heterotopic pregnancy has been increasing, partly because of this expanding patient population. The incidence of heterotopic pregnancy is approximately 1% of all pregnancies after in vitro fertilization [43,45]. In this population, ectopic pregnancy cannot be excluded even if an intrauterine pregnancy is detected. Because more than one embryo is typically transferred after in vitro fertilization, hCG levels are less helpful in diagnosing ectopic pregnancy, and ultrasound plays an even larger role in detection.

Sonographic diagnosis of ectopic pregnancy: specific findings

The most specific sonographic sign of ectopic pregnancy is visualization of an extrauterine gestational sac that contains a yolk sac or embryo (Fig. 14). This sign carries a specificity rate of 100% but a low sensitivity rate of 15% to 20% [37,40,46].

Nonspecific findings

Free fluid

Small amounts of free pelvic fluid can be seen in ectopic and intrauterine pregnancies. The presence of echogenic fluid, especially when found in high quantities or in association with an adnexal mass, indicates a high risk of ectopic pregnancy. Echogenic fluid correlates with hemoperitoneum at surgery (Fig. 15) [47].

The presence of a moderate to large amount of free fluid demonstrates a sensitivity rate of 28% but a high specificity rate of 96% and positive predictive value of 86% for ectopic pregnancy. The presence of echogenic free fluid increases the sensitivity rate even higher to 56% [46]. Ultrasonographic assessment of the pelvis has almost completely replaced culdocentesis for the diagnosis of hemoperitoneum. Culdocentesis is invasive, less sensitive than transvaginal ultrasonography for the detection of blood, and has a lower negative predictive value [47]. Transabdominal scanning of the paracolic gutters and Morrison's pouch may show free intraperitoneal fluid not appreciated on the transvaginal approach [38,41].

Adnexal mass

An adnexal mass is the most common ultrasonographic finding in ectopic pregnancy, found in 65% to 84% of cases [40,48–50]. The adnexal mass can demonstrate various appearances. It can appear as a sac-like ring that correlates with an intact tube that contains a gestational sac (Fig. 16). Alternatively, the mass can be solid or complex, which typically correlates with an incomplete tubal abortion or, less likely, a ruptured tube (Fig. 17) [50]. The appearance also can be subtle, recognized only by an asymmetry

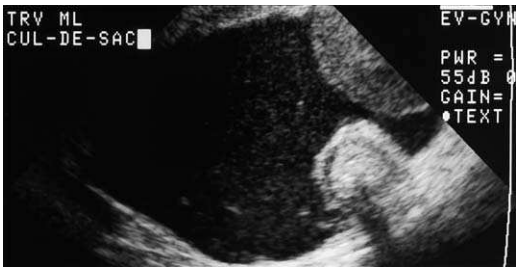

Fig. 15. Large amount of echogenic free fluid in the posterior cul de sac in surgically proven ectopic pregnancy.

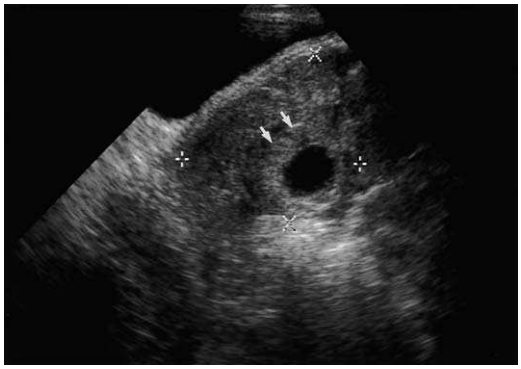

Fig. 16. Complex adnexal mass (marked by calipers) caused by ectopic pregnancy. Sac-like area within the mass (*arrows*) likely represents the fallopian tube dilated by the extrauterine gestation sac.

between the size of the ovaries of 2 cm or more [37]. The size of the adnexal mass typically correlates well with the size found at surgery with a discrepancy of less than 1 cm [50].

If the adnexal mass contains either a yolk sac or an embryo, the specificity rate for ectopic pregnancy approaches 100%. The presence of any extraovarian adnexal mass in a patient with clinically suspected ectopic pregnancy increases the likelihood of ectopic pregnancy to more than 90%, however [40,48,49]. Other entities that can cause a complex adnexal mass in this setting include an endometrioma, hemorrhagic corpus luteal cyst with or without rupture, and hydrosalpinx [39,49,51].

Endometrial appearance

Pregnancy, regardless of its location, produces a decidual reaction in the endometrium. In the setting of an ectopic pregnancy, the endometrium can have a varied appearance and may not add to the sonographic diagnosis. The most common appearance of the endometrium is normal or a generalized increased echogenicity [37].

Pseudogestational sacs are endometrial fluid collections surrounded by echogenic endometrium from a prominent decidual reaction. These sacs are present in approximately 5% to 10% of cases [36,37]. They are typically lenticular in configuration with irregular contour (Fig. 18) but can be smooth and rounded and contain debris that could be mistaken for products of conception.

The thickness of the endometrium does not help distinguish between ectopic and normal or abnormal intrauterine gestations [52]. Although Lavie et al found a sonographic three-layer endometrial pattern similar to that seen in the late proliferative phase of a normal pregnancy to have a sensitivity rate of 62.2% and a specificity rate and positive predictive value of 100% for ectopic pregnancy [53], these findings have not been reproduced by others [54]. A normal appearance of the pelvis on ultrasound with an empty uterus does not exclude ectopic pregnancy.

Serum human chorionic gonadotropin levels

Serum hCG levels play an important adjunctive role with ultrasonography in the early diagnosis of ectopic pregnancy. A negative hCG level effectively excludes the possibility of pregnancy in the setting of a woman with pelvic pain. Many institutions rely on the discriminatory hCG level, usually held at 2000 mIU/mL IRP for endovaginal scans, to help distinguish ectopic from intrauterine pregnancy [6,26,49,50]. The discriminatory level indicates the lowest hCG level at which an intrauterine gestational sac should be visualized [55]. If the hCG level is above the discriminatory level and no gestational sac

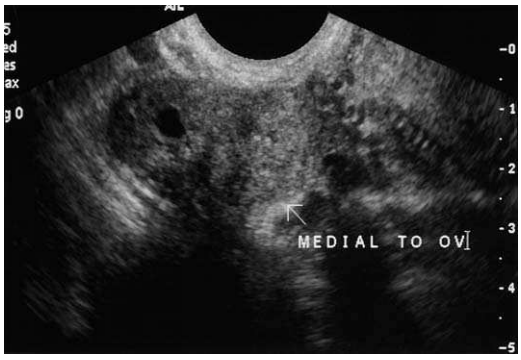

Fig. 17. Solid echogenic mass medial to right ovary represents the adnexal mass of an ectopic pregnancy.

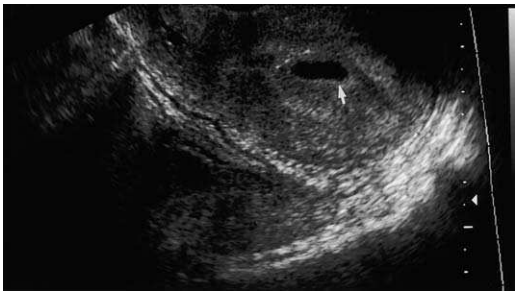

Fig. 18. Elongated cresentic intrauterine fluid collection (*arrow*) caused by a pseudo-gestational sac from an ectopic pregnancy.

is detected, the pregnancy may be abnormal, and ectopic pregnancy should be considered. Mehta et al reported that 33% of 51 patients without a definite gestational sac and with hCG levels more than 2000 mIU/mL IRP had normal intrauterine pregnancies on follow-up [26]. Strict reliance on a single discriminatory hCG value is probably unwise, and serial values can be more helpful in distinguishing among intrauterine, ectopic, and failed pregnancies. Ultrasound may provide valuable information regardless of the hCG level.

Management

Managing ectopic pregnancy in the outpatient setting has become a more viable option with earlier detection through endovaginal ultrasound and sensitive hCG assays. Outpatient management strategies include laparoscopic salpingectomy or salpingostomy, methotrexate administration, and close monitoring for spontaneous resolution [32].

Spontaneous resolution of ectopic pregnancy can occur. Early sonographic diagnosis of ectopic pregnancy likely identifies some cases that would have escaped diagnosis because of spontaneous resolution without intervention. Atri reported that 24% of ectopic pregnancies sonographically diagnosed over a 19-month period resolved spontaneously [56]. Pregnancies that are more likely to resolve demonstrate findings such as a longer time interval from the last menstrual period [33], small adnexal masses of less than 3.5 cm and preferably less than 2 cm, low serum hCG levels of less than 1000 mIU/mL, rapidly decreasing hCG levels, lack of a gestational sac, and no cardiac activity detected. The more advanced and vascular the adnexal mass or hematosalpinx caused by the ectopic pregnancy, the less likely it is to resolve spontaneously [33,56]. While resolving, the adnexal mass of an ectopic pregnancy may increase in size and become more vascular on ultrasound [56]. Ultrasound is not reliable for identifying cases that are undergoing spontaneous resolution. The diagnosis is based on continuing clinical stability of the patient and decreasing serial hCG levels [33].

Although spontaneous resolution of ectopic pregnancy may occur, expectant management of patients with confirmed diagnoses remains controversial. The benefit of expectant management over other conservative treatments, such as medical treatment with methotrexate or minimally invasive laparoscopic surgery, has not been established [36,57].

Since the late 1980s there has been a shift toward treating ectopic pregnancy in the outpatient setting and reaping significant medical cost savings compared with surgical treatment [32]. Administration of methotrexate has become an increasingly popular therapy for the treatment of ectopic pregnancy [32,58,59]. Pharmacologic therapy often results in decreased patient morbidity and increased preservation of reproductive capability [32]. Methotrexate, administered either intramuscularly or intratubularly [36,58], causes either resorption or tubular abortion of the conceptus. Women who demonstrate lack of free fluid outside of the pelvis on ultrasound, hemodynamic stability, and no other comorbid conditions are considered candidates for medical therapy. Most protocols limit candidates to women with an adnexal mass of less than 3 to 4 cm, lack of embryonic cardiac activity, and hCG levels of less than 5000 to 10,000 mIU/mL. Failure of treatment is most closely linked to high hCG levels and the presence of embryonic cardiac activity [58]. At follow-up of patients treated with methotrexate, ultrasound may demonstrate that the adnexal mass or affected fallopian tube has grown in size and become more vascular. Treatment success can be monitored with declining hCG levels [58,59].

Fetal abnormalities

A series of recent studies suggested that the sonographic observation of increased fetal nuchal translucency in the first trimester can be used as a screening tool for chromosomal defects. Some other fetal structural abnormalities are also identifiable in the first trimester on ultrasound. As sonographic technology improves, better spatial resolution also may enable earlier diagnosis of more structural abnormalities.

Nuchal translucency

Szabo and Gellen [60] were the first to report an association between increased nuchal translucency in the first trimester and chromosomal abnormalities. Nuchal translucency describes the subcutaneous accumulation of fluid in the back of the fetal neck, which can occur early in pregnancy. On sonography, nuchal translucency represents the maximum thickness of the subcutaneous translucency between the skin and the soft tissue overlying the cervical spine (Figs. 19, 20) [61,62]. According to the criteria published by the Fetal Medicine Foundation [63], images of nuchal translucency must include a midsagittal section, sufficient magnification of the image, differentiation between fetal skin and amnion, and placement of the calipers on the echogenic lines (on-to-on measurement) so that the maximal thickness

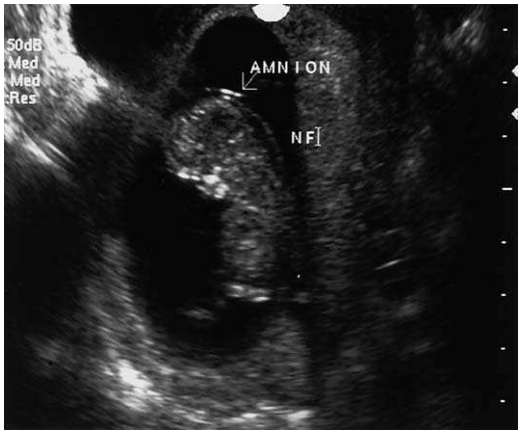

Fig. 19. Endovaginal ultrasound shows a sagittal view of the of 11-week embryo with thickened nuchal translucency shown separate from the amnion.

of the lucent area is measured. The choice of transabdominal versus transvaginal approach is left to the examiner.

Because nuchal translucency increases with gestational age, a single measurement threshold to establish a population at higher risk for aneuploidy used over the first trimester may not be valid [64,65]. Although a gestational age-dependent normal range may be most useful to minimize false-positive results, a discriminatory value equal to or more than 3 mm is most commonly used, which falls between the ninetieth and ninety-fifth percentile for crown-rump length when measured between 10 and 14 weeks' gestation [61,66].

Using a cutoff of 3 mm, approximately 1% to 5% of first trimester fetuses demonstrate nuchal translucency [61,63,67–69]. Depending on the cutoff used, the prevalence of chromosomal abnormality in fetuses with abnormal nuchal translucency ranges from 19% to 75% [66], with the risk of aneuploidy increasing with the degree of nuchal translucency. In a screening population, Thilaganathan et al found thickened nuchal translucency to have a positive predictive value of 1:31 for Down syndrome and 1:12 for all major aneuploidies. These ratios compare favorably to the positive predictive value for second trimester maternal serum biochemistry of 1:50 [70].

Because of study differences in cutoff values, study population, and technique, the precise sensitivity of screening with nuchal translucency is unclear. Data support nuchal translucency measurement as an effective noninvasive screening method for trisomy 21 and other chromosomal abnormalities in an unselected population. The combination of first trimester ultrasound evaluation with serum-free β hCG, pregnancy-associated plasma protein, and maternal age data further improve the accuracy of risk assessment. Currently two large, prospective, multicenter trials are underway to provide further data on the role of first trimester aneuploidy screening, including the First and Second Trimester Evaluation of Risk for Aneuploidy Trial in the United States and the Serum Urine and Ultrasound Screening Study in the United Kingdom [71].

A review of studies using nuchal translucency measurements to screen the general population revealed a range of Down syndrome (trisomy 21) detection rates of 29% to 91%. [72]. Variability in detection rates is caused by differences in study design, such as time allowed for the study, patient follow-up, cutoff measurement used, and differences in the maternal age in the study population and experience of the technologist [72,73]. The largest prospective trial undertaken by Snijders et al on 96,127 patients found a detection rate of Down syndrome of 72% [63].

Even in chromosomally normal fetuses with increased fetal nuchal translucency, there is an increased risk of poor prognosis because of a higher incidence of spontaneous abortion and other structural fetal abnormalities, particularly cardiac abnormalities [66,68,74,75]. The likelihood of poor pregnancy outcome also increases with larger nuchal translucency measurements ranging from 32% at 3 mm to 100% at 5 mm [66]. At least one study that examined early childhood follow-up of fetuses with increased nuchal translucency has shown that cases with a normal karyotype and no additional abnormalities on follow-up sonography have a good prognosis for normal delivery and early childhood. Typically,

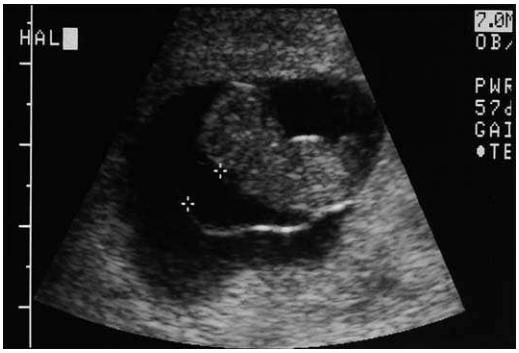

Fig. 20. Fetus at 10.5 weeks' menstrual age with markedly thickened nuchal translucency.

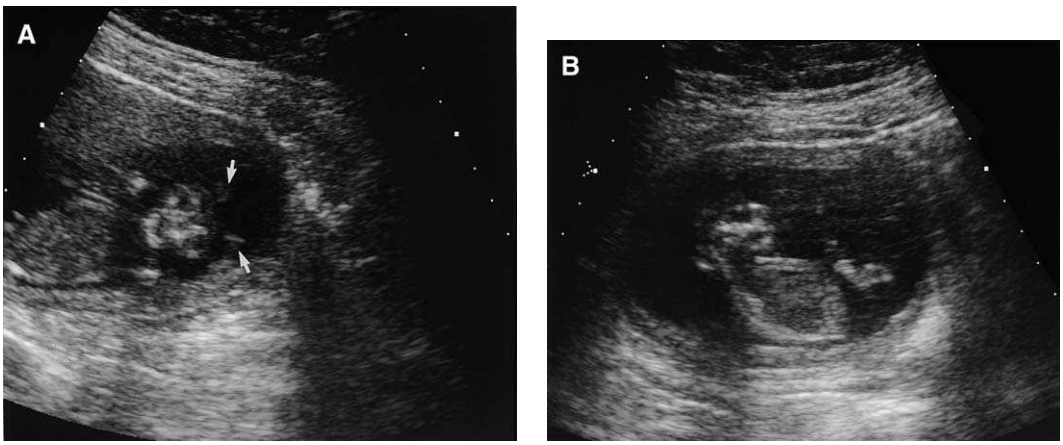

Fig. 21. (*A*) Coronal and (*B*) sagittal ultrasound of a 12-week fetus with absence of the cranium and separation of the cranial soft tissue into two masses (*arrows*), which are consistent with anencephaly.

thickened nuchal translucency does not lead to a cervical structural abnormality in the child [68].

Fetal structural abnormalities

Improvements in sonographic resolution have made it possible to detect the presence of a wide range of fetal defects in the first trimester. In some cases, the sonographic features are similar to those described on second and third trimester scans, and in other cases there are characteristic features unique to these early studies [76]. First trimester ultrasound is particularly sensitive in detecting abnormalities in the central nervous system, cervical region, and renal and gastrointestinal organs and is weak at detecting spina bifida and cardiac and limb deformities. In a screening study of an unselected low-risk population of more than 6000 pregnant women scanned between 11 and 14 weeks' gestation, the detection rate for structural abnormalities was 68% in early pregnancy. When combined with the second trimester scan, the rate increased to 85% [77].

Anencephaly, characterized by absence of the cranial vault and subsequent disruption of the cerebral cortex, was one of the first fetal abnormalities diagnosed by ultrasound. The first trimester findings are notably different from those identifiable on second trimester scans [77]. Whereas in the second trimester the diagnosis of anencephaly is made partially by the finding of prominent orbits and no brain tissue or skull above the orbits, the first trimester diagnosis relies on noting the absence of cranium because cerebral tissue (angiomatous stroma) still may be present. In anencephaly, the crown rump length usually measures less than expected by gestational age. Because mineralization of the skull occurs at approximately 10 weeks' gestation, diagnosis theoretically can be made after this point. Two studies performed in the United Kingdom demonstrated that in units in which the sonographer was instructed to look for signs of acrania, sensitivity rate for detecting anencephaly in the first trimester was 100% with no false-positive cases [78,79]. First trimester fetuses with anencephaly may demonstrate the ''Mickey Mouse Sign,'' which describes the appearance of the cerebral lobes in the coronal plane as two semicircular structures above the orbits surrounded by amniotic fluid (Fig. 21) [78].

Several of the soft signs for aneuploidy typically examined in the second trimester also can be detected in the first trimester. Whitlow et al studied soft

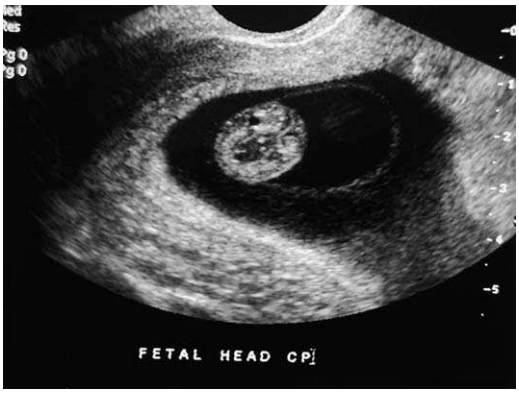

Fig. 22. Transverse image of a fetal head at 12 weeks' menstrual age demonstrates a choroid plexus cyst.

markers for aneuploidy, including pyelectasis, echogenic intracardiac focus, and choroid plexus cysts [80]. They found that choroid plexus cysts were more common in the first trimester than in the second, with a prevalence of 2.2%, and were not significantly associated with aneuploidy (Fig. 22). Echogenic cardiac foci and pyelectasis had a similar prevalence in the first and second trimesters, and their presence in the first trimester was significantly associated with aneuploidy. The presence of more than one marker was more significant as a risk for aneuploidy than the presence of one marker. Although this study confirms that such findings can be detected in the first trimester, more studies examining larger populations are needed before any firm conclusions can be made regarding the significance of their presence.

An overview of fetal structural abnormalities is given in another article in this issue of *Radiologic Clinics of North America*.

Summary

There are several advantages to ultrasound examination in early pregnancy. Ultrasound performed during the first trimester confirms an intrauterine pregnancy, establishes accurate dating, and is crucial in diagnosing early pregnancy failure and ectopic pregnancy. As sonographic spatial resolution continues to improve, first trimester sonography increasingly will offer early pregnancy screening for chromosomal abnormalities and fetal structural abnormalities.

References

[1] Economides DL. Early pregnancy screening for fetal abnormalities. Ultrasound Obstet Gynecol 1999;13:81–3.

[2] Rowling SE, Langer JE, Coleman BG, et al. Sonography during early pregnancy: dependence of threshold and discriminatory values on transvaginal transducer frequency. AJR Am J Roentgenol 1999;172:983–8.

[3] Pennell RG, Baltarowich OH, Kurtz AB, et al. Complicated first-trimester pregnancies: evaluation with endovaginal US versus transabdominal technique. Radiology 1987;165:79–83.

[4] Hill LM, Kislak S. An extensive intrauterine hematoma mimicking a nonviable early pregnancy. J Ultrasound Med 1986;5:515–6.

[5] Levi CS, Lyons EA, Lindsay DJ. Early diagnosis of nonviable pregnancy with endovaginal US. Radiology 1988;167:383–5.

[6] Bree RL, Edwards M, Bohn-Velez M, et al. Transvaginal sonography in the evaluation of normal early pregnancy: correlation with HCG level. AJR Am J Roentgenol 1989;153:75–9.

[7] Goldstein RB. Endovaginal sonography in very early pregnancy: new observations. Radiology 1990;176:7–8.

[8] Benacerraf BR, Shipp TD, Bromley B. Does the 10 MHz transvaginal transducer improve the diagnostic certainty that an intrauterine fluid collection is a true gestational sac? J Clin Ultrasound 1999;27:374–7.

[9] Laing FC, Frates MC. Ultrasound evaluation during the first trimester of pregnancy. In: Callen PW, editor. Ultrasonography in obstetrics and gynecology. 4th edition. Philadelphia: WB Saunders; 2000. p. 105–45.

[10] Yeh H-C, Goodman JD, Carr L, Rabinowitz JG. Intradecidual sign: an US criterion of early intrauterine pregnancy. Radiology 1986;161:463–7.

[11] Laing FC, Brown DL, Price JF, et al. Intradecidual sign: Is it effective in diagnosis of an early intrauterine pregnancy? Radiology 1997;204:655–60.

[12] Nyberg DA, Filly RA, Mahony GS, et al. Early gestation: correlation of HCG levels and sonographic identification. AJR Am J Roentgenol 1985;144:951–4.

[13] Bradley WG, Fiske CE, Filly RA. The double sac sign of early intrauterine pregnancy: use in exclusion of ectopic pregnancy. Radiology 1982;143:223–6.

[14] Nyberg DA, Mack LA, Harvey D, Wang K. Value of the yolk sac in evaluation of early pregnancies. J Ultrasound Med 1988;7:129–35.

[15] Parvey HR, Dubinsky TJ, Johnston DA, Maklad NF. The chorionic rim and low-impedance intrauterine arterial flow in the diagnosis of early intrauterine pregnancy: evaluation of efficacy. AJR Am J Roentgenol 1996;167:1479–85.

[16] Moore KL. Formation of the bilaminar embryo. In: Wonsiewicz M, editor. The developing embryo. 4th edition. Philadelphia: WB Saunders; 1988. p. 38–49.

[17] Mantoni M, Pedersen JF. Ultrasound visualization of the human yolk sac. J Clin Ultrasound 1979;7:459–60.

[18] Moore KL. Formation of the trilaminar embryo. In: Wonsiewicz M, editor. The developing embryo. 4th edition. Philadelphia: WB Saunders; 1988. p. 50–64.

[19] Levi CS, Lyons EA, Zheng XH, et al. Endovaginal US: demonstration of cardiac activity in embryos of less than 5.0 mm in crown-rump length. Radiology 1990;176:71–4.

[20] Doubilet PM, Benson CB, Chow JS. Long-term prognosis of pregnancies complicated by slow embryonic heart rates in the early first trimester. J Ultrasound Med 1999;18:537–41.

[21] Stefos TI, Lolis DE, Sotiriadis AJ, Ziakas GV. Embryonic heart rate in early pregnancy. J Clin Ultrasound 1998;26:33–6.

[22] Montenegro N, Ramos C, Matias A, Barros H. Variation of embryonic fetal heart rate at 6–13 weeks' gestation. Ultrasound Obstet Gynecol 1998;11:274–6.

[23] Nyberg DA, Laing FC, Filly RA. Threatened abortion: sonographic distinction of normal and abnormal gestation sacs. Radiology 1986;158:397–400.

[24] Bromley B, Harlow BL, Laboda LA, Benacerraf BR.

Small sac size in the first trimester: a predictor of poor fetal outcome. Radiology 1991;178:375–7.
[25] Filly RA, Hadlock FP. Sonographic determination of menstrual age. In: Callen PW, editor. Ultrasonography in obstetrics and gynecology. 4th edition. Philadelphia: WB Saunders; 2000. p. 146–70.
[26] Mehta TS, Levine D, Beckwith B. Treatment of ectopic pregnancy: is a human chorionic gonadotropin level of 2000 mIU/ml a reasonable threshold? Radiology 1997;205:569–73.
[27] Wilcox AJ, Weinberg CR, O'Connor JF, et al. Incidence of early loss of pregnancy. New England Journal of Pregnancy 1988;319:189–94.
[28] Rowling SE, Coleman BG, Langer JE, et al. First-trimester US parameters of failed pregnancy. Radiology 1997;203:211–7.
[29] Giacomello F. Small sac size as a predictor of poor fetal outcome [letter]. Radiology 1992;184:578.
[30] Benson CB, Doubilet PM. Slow embryonic heart rate in early first trimester: indicator of poor pregnancy outcome. Radiology 1994;192:343–4.
[31] Doubilet PM, Benson CB, Chow JS. Outcome of pregnancies with rapid embryonic heart rates in the early first trimester. AJR Am J Roentgenol 2000;175:67–9.
[32] Centers for Disease Control. Current trends ectopic pregnancy: United States, 1990–1992. MMWR Morb Mortal Wkly Rep 1995;44:46–8.
[33] Atri M, Chow C-M, Kintzen G, et al. Expectant treatment of ectopic pregnancies. AJR Am J Roentgenol 2001;176:123–7.
[34] Schartz R, DiPietro D. BHCG as a diagnostic aid for suspected ectopic pregnancy. Obstet Gynecol 1980;56: 197–203.
[35] Filly RA. Ectopic pregnancy: the role of sonography. Radiology 1987;162:661–8.
[36] Frates MC, Laing FC. Sonographic evaluation of ectopic pregnancy: an update. AJR Am J Roentgenol 1995;165:251–9.
[37] Thorsen MK, Lawson TL, Aiman EJ, et al. Diagnosis of ectopic pregnancy: endovaginal vs. transabdominal sonography. AJR Am J Roentgenol 1990;155: 307–10.
[38] Zinn HL, Cohen HL, Zinn DL. Ultrasonographic diagnosis of ectopic pregnancy: importance of transabdominal imaging. J Ultrasound Med 1997;16:603–7.
[39] Dashefsky SM, Lyons EA, Levi CS, Lindsay DJ. Suspected ectopic pregnancy: endovaginal and transvesical US. Radiology 1988;169:181–4.
[40] Brown D, Doubilet P. Transvaginal sonography for diagnosing ectopic pregnancy. J Ultrasound Med 1994; 13:259–66.
[41] Hertzberg BS, Kliewer MA, Bowie JD. Sonographic evaluation for ectopic pregnancy: transabdominal scanning of patients with nondistended urinary bladders as a complement to transvaginal sonography. AJR Am J Roentgenol 1999;173:773–5.
[42] Hann LE, Bachman DM, McArdle CR. Coexistent intrauterine and ectopic pregnancy: a reevaluation. Radiology 1984;152:151–4.
[43] Rizk B, Tan SL, Morcos S, et al. Heterotopic pregnancies after in vitro fertilization and embryo transfer. Am J Obstet Gynecol 1991;164:161–4.
[44] Mol SWJ, van der Veen F, Hajenius PJ, et al. Diagnosis of ectopic pregnancy after in vitro fertilization and embryo transfer. Fertil Steril 1997;68:1027–32.
[45] Goldman GA, Fisch B, Ovadia J, Tadir Y. Heterotopic pregnancy after assisted reproductive technologies. Obstet Gynecol Surv 1992;47:217–21.
[46] Nyberg DA, Hughes MP, Mack LA, Wang KY. Extrauterine findings of ectopic pregnancy at transvaginal US: importance of echogenic fluid. Radiology 1991; 178:823–6.
[47] Chen PC, Sickler GK, Dubinsky TJ, et al. Sonographic detection of echogenic fluid and correlation with culdocentesis in the evaluation of ectopic pregnancy. AJR Am J Roentgenol 1998;170:1299–302.
[48] Nyberg DA, Mack LA, Jeffrey RB, Laing FC. Endovaginal sonographic evaluation of ectopic pregnancy: a prospective study. AJR Am J Roentgenol 1987;149: 1181–6.
[49] Fleisher AC, Pennell RG, McKee MS, et al. Ectopic pregnancy: features at transvaginal sonography. Radiology 1990;174:375–8.
[50] Cacciatore B. Can the status of tubal pregnancy be predicted with transvaginal sonography? A prospective comparison of sonographic, surgical, and serum hCG findings. Radiology 1990;177:481–4.
[51] Hertzberg BS, Kliewer MA, Bowie JD. Adnexal ring sign and hemoperitoneum caused by hemorrhagic ovarian cyst: pitfall in the sonographic diagnosis of ectopic pregnancy. AJR Am J Roentgenol 1999;173: 1301–2.
[52] Mehta TS, Levine D, McArdle CR. Lack of sensitivity of endometrial thickness in predicting the presence of an ectopic pregnancy. J Ultrasound Med 1999;18: 117–22.
[53] Lavie O, Boldes R, et al. Ultrasonographic "endometrial three-layer" pattern: a unique finding in ectopic pregnancy. J Clin Ultrasound 1996;24:179–83.
[54] Wachsberg R, Karimi S. Sonographic endometrial three-layer pattern in symptomatic first trimester pregnancy: not diagnostic of ectopic pregnancy. J Clin Ultrasound 1998;26:199–201.
[55] Laing FC, Brown DL. Human chorionic gonadotropin levels in the evaluation of ectopic pregnancy [letter]. Radiology 1998;208:271.
[56] Atri M, Bret PM, Tulandi T. Spontaneous resolution of ectopic pregnancy: initial appearance and evolution at transvaginal ultrasound. Radiology 1993;186:83–6.
[57] Zacur HA. Expectant management of ectopic pregnancy. Radiology 1993;186:11–2.
[58] Lipscomb GH, McCord ML, Stovall TG, et al. Predictors of success of methotrexate treatment in women with tubal ectopic pregnancies. N Engl J Med 1999;341: 1974–8.
[59] Atri M, Bret PM, Tulandi T, Senterman MK. Ectopic pregnancy: evolution after treatment with transvaginal methotrexate. Radiology 1992;185:749–53.

[60] Szabo J, Gellen J. Nuchal fluid accumulation in trisomy-21 detected by vaginosonography in the first trimester. Lancet 1990;336:1133.
[61] Hafner E, Schuchter K, Liebhart E, Phillip K. Results of routine fetal nuchal translucency measurement at weeks 10–13 in 4233 unselected pregnant women. Prenat Diagn 1998;18:29–34.
[62] Herman A, Dreazen E, Samandarov A, et al. On-to-on versus on-to-out nuchal translucency measurements. Ultrasound Obstet Gynecol 2000;15:126–30.
[63] Snijders RJM, Noble P, Sebire N, et al. UK multicentre project on assessment of risk of trisomy 21 by maternal age and fetal nuchal translucency thickness at 10–14 weeks of gestation. Lancet 1998;351:343–6.
[64] Scott F, Boogert A, Sinosich M, Anderson J. Establishment and application of a normal range for nuchal translucency across the first trimester. Prenat Diagn 1996;16:629–34.
[65] Pajkrt E, Bilardo CM, van Lith JMM, et al. Nuchal translucency measurement in normal fetuses. Obstet Gynecol 1995;86:994–7.
[66] Adekunle O, Gopee A, El-Sayed M, Thilaganathan B. Increased first trimester nuchal translucency: pregnancy and infant outcomes after routine screening for Down's syndrome in an unselected antenatal population. Br J Radiol 1999;72:457–60.
[67] Taipale P, Hiilesmaa V, Salonen R, Ylostalo P. Increased nuchal translucency as a marker for fetal chromosomal defects. N Engl J Med 1997;337:1654–8.
[68] Van Vugt JMG, Tinnemans BWS, Van Zalen-Sprock RM. Outcome and early childhood follow-up of chromosomally normal fetuses with increased nuchal translucency at 10–14 weeks' gestation. Ultrasound Obstet Gynecol 1998;11:407–9.
[69] Pajkrt E, Mol BWJ, van Lith JMM, et al. Screening for Down's syndrome by fetal nuchal translucency measurement in a high-risk population. Ultrasound Obstet Gynecol 1998;12:156–62.
[70] Thilaganathan B, Sairam S, Michailidis G, Wathen NC. First trimester nuchal translucency: effective routine screening for Down's syndrome. Br J Radiol 1999; 72:946–8.
[71] Stewart TL, Malone FD. First trimester screening for aneuploidy: nuchal translucency sonography. Semin Perinatol 1999;23:369–81.
[72] Malone FD, Berkowitz RL, Canick JA, Dalton ME. First trimester screening for aneuploidy: research or standard of care? Am J Obstet Gynecol 2000;182: 490–6.
[73] Snijders RJM, Johnson S, Sebire NJ, et al. First-trimester ultrasound screening for chromosomal defects. Ultrasound Obstet Gynecol 1996;7:216–26.
[74] Pandya PP, Brizot ML, Kuhn P, et al. First trimester fetal nuchal translucency thickness and risk for trisomies. Obstet Gynecol 1994;84:420–3.
[75] Reynders CS, Pauker SP, Benacerraf BR. First trimester isolated fetal nuchal lucency: significance and outcome. J Ultrasound Med 1997;16:101–5.
[76] Souka AP, Nicolaides KH. Diagnosis of fetal abnormalities at the 10–14-week scan. Ultrasound Obstet Gynecol 1997;10:429–42.
[77] Whitlow BJ, Chatzipapas IK, Lazanakis ML, et al. The value of sonography in early pregnancy for the detection of fetal abnormalities in an unselected population. Br J Obstet Gynaecol 1999;106:929–36.
[78] Chatzipapas IK, Whitlow BJ, Economides DL. The ''Mickey Mouse'' sign and the diagnosis of anencephaly in early pregnancy. Ultrasound Obstet Gynecol 1999;13:196–9.
[79] Johnson SP, Sebire NJ, Snijders RJM, et al. Ultrasound screening for anencephaly at 10–14 weeks of gestation. Ultrasound Obstet Gynecol 1997;9:14–6.
[80] Whitlow BJ, Lazanakis ML, Kadir RA, et al. The significance of choroid plexus cysts, echogenic heart foci, and renal pyelectasis in the first trimester. Ultrasound Obstet Gynecol 1998;12:385–90.

RADIOLOGIC
CLINICS OF
NORTH AMERICA

Radiol Clin N Am 41 (2003) 681–693

Ultrasound detection of first trimester malformations: a pictorial essay

Ilse Castro-Aragon, MD, Deborah Levine, MD*

Department of Radiology, Beth Israel Deaconess Medical Center, 330 Brookline Avenue, Boston, MA 02215, USA

Ultrasound is commonly performed in the first trimester for determining cause of bleeding or pain, establishing dates, and evaluating nuchal translucency in screening for aneuploidy. With improvements in ultrasound technology, the fine structures of the developing embryo and fetus can be visualized [1,2], which allows for early detection of embryonic and fetal structural abnormalities. A combination of transabdominal and transvaginal scanning allows for assessment of anatomy in up to 95% of fetuses at 12 to 13 weeks' gestation [3]. In a study of low-risk women, 68% of fetal structural abnormalities were detected during first trimester sonography [4]. Early detection of structural anomalies is helpful in the diagnosis of aneuploidy and in counseling patients regarding potential outcome when chromosomes are normal. This article illustrates pathologic conditions that can be detected in early pregnancy and potential pitfalls in the evaluation of the developing embryo and fetus.

Central nervous system

The sonographic appearance of the brain in the first trimester is different from its appearance later in gestation. Between 7 and 9 weeks' gestational age, the developing rhombencephalon is visible as a cystic space in the embryonic head, which should not be mistaken for an abnormality (Fig. 1). This structure contributes to the fourth ventricle, the brain stem and the cerebellum, and should not be confused with a Dandy Walker cyst or hydrocephalus. Later in gestation, the choroid plexus fills the lateral ventricle, which occupies most of the hemisphere (Fig. 2) [5].

Calvarial ossification occurs at approximately 10 weeks' gestational age, which is why anencephaly (Fig. 3) is difficult to appreciate early in the first trimester (Fig. 4). Even after 10 weeks, the absence of a calcified cranium may be overlooked because the underlying cranial tissue may appear normal [6]. In a study by Johnson et al of 55,237 fetuses at 10 to 14 weeks' gestation, 47 fetuses were diagnosed with anencephaly. In the initial portion of the study, the diagnosis was missed in 8 of 31 fetuses. After review of these cases, sonographers were given feedback regarding the first trimester appearance of anencephaly; in the second portion of the study, 16 of 16 cases were diagnosed. This demonstrates that attention to ossification of the skull aids in the early diagnosis of anencephaly. In this study, the diagnosis of anencephaly was made when there was absence of the calvarium, even if the underlying brain tissue appeared normal. When tissue is visualized above the orbits, some call this exencephaly (Figs. 5, 6). Because nearly all cases of anencephaly in the first trimester have tissue present above the orbits, it is believed that exencephaly is a precursor to anencephaly [7,8].

Encephalocele is the least common open neural tube defect, with an incidence of 1 to 4:10,000 live births. The bony calvarial defect allows herniation of the meninges alone or the brain and the meninges out of the boundaries of the skull. The most common site of occurrence is the occipital midline (Fig. 7) (75%) followed by the frontal midline (13%) and the parietal regions (12%).

* Corresponding author.
E-mail address: dlevine@caregroup.harvard.edu (D. Levine).

0033-8389/03/$ – see front matter © 2003 Elsevier Inc. All rights reserved.
doi:10.1016/S0033-8389(03)00045-9

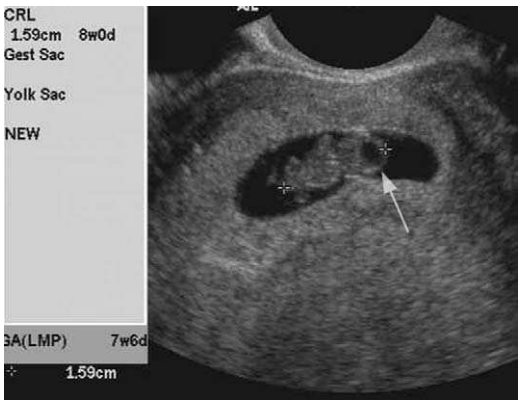

Fig. 1. Rhombencephalon (*arrow*) in coronal plane; the embryo is 8 weeks' gestational age. This is a common pitfall for imaging interpretations and should not be mistaken for an abnormal finding.

Hydrocephalus (Fig. 8) is not commonly visualized in the first trimester because the ventricles normally occupy most of the hemispheres (see Fig. 2). In severe cases, hydrocephalus can be diagnosed in the first trimester when the ventricle is enlarged, and the choroid plexus, which normally occupies the entire ventricle, is dangling and surrounded by fluid [9].

Nuchal translucency

Increased nuchal translucency is associated with aneuploidy and poor obstetric outcome. The method of measurement of the nuchal translucency for screening for aneuploidy is discussed elsewhere in this issue. When the translucency contains septations, it carries a risk greater than that of simple nuchal translucency (Fig. 9) [10,11]. Even if the nuchal translucency resolves, there is still an increased risk of poor outcome, including cardiac anomalies, congenital diaphragmatic hernia, and growth restriction [11–13]. A patient whose the fetus has been diagnosed with first trimester increased nuchal translucency should have a formal anatomic survey in the mid-second trimester and should be followed to assess adequate growth throughout pregnancy.

Generalized edema around the body of the fetus is called lymphangiectasia (Fig. 10). This condition carries a grim prognosis and is associated with impending fetal demise.

Umbilical cord

Small umbilical cord cysts can be identified in the first trimester (Fig. 11). These avascular structures appear as echolucent cysts within the cord that do not obstruct the flow from the umbilical arteries and vein. There is a range of incidence reported with these cysts, from 0.4% [14] to 3.4%. [15] This variation in reported incidence is likely caused by the amount of attention paid to the umbilical cord during scanning. Umbilical cord cysts (Fig. 12) may be located anywhere along the cord and are separate from the mass created by physiologic bowel herniation. In most cases there is resolution of the cyst on follow-up examination, but this does not completely exclude an abnormality, and a detailed second trimester survey is indicated [15–17]. In one study of pregnancies with umbilical cord cysts seen at 7 to 12 weeks' gestation, 26% were found to have fetal structural defects [15]; however, in other studies none of the cases had abnormalities on follow-up [14,17]. Whereas second trimester large, irregular cord cysts have a high

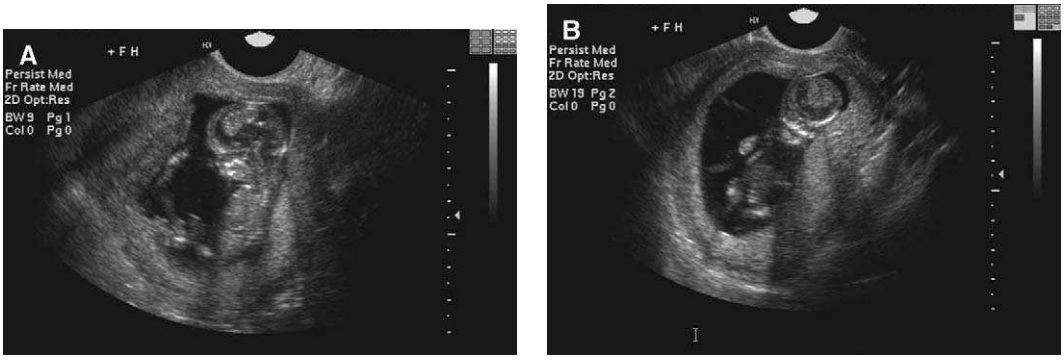

Fig. 2. Sagittal (*A*) and coronal views (*B*) of a 12-week gestational age fetus with a normal brain. Note that the choroid plexus fills the ventricle, and the ventricle fills almost the entire hemisphere.

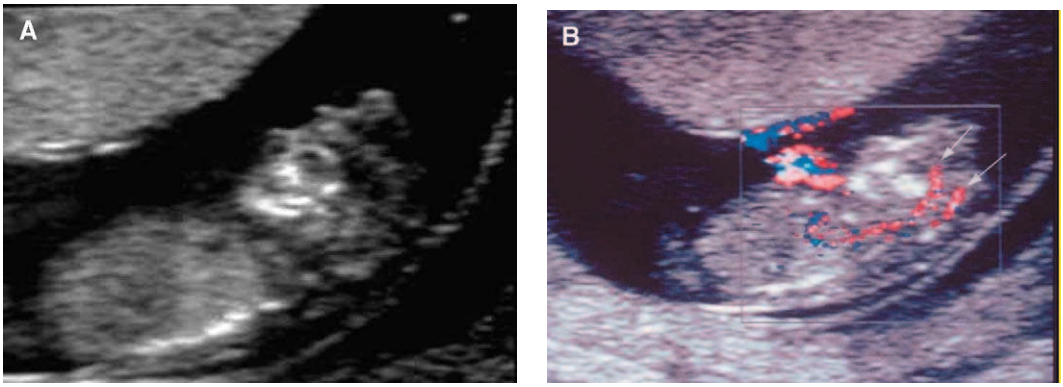

Fig. 3. Anencephaly. Sagittal Gray-scale (*A*) and color Doppler (*B*) views show lack of an ossified cranium above the orbits. The internal carotid arteries are seen to extend to the skull base and then abruptly terminate (*arrows*). (Courtesy of Dr. Peter Callen, San Francisco, CA).

association with anomalies and poor outcome, small, smooth cysts that disappear after the first trimester have a more benign course [18].

Anterior abdominal wall

Physiologic herniation of the fetal bowel into the base of the umbilical cord occurs normally between 8 and 12 weeks' gestation (Fig. 13). This midgut herniation is visualized sonographically as slightly echogenic areas in the base of the abdominal insertion of the umbilical cord. Failure of the intestinal loops to return to the abdominal cavity results in the formation of an omphalocele, which is a membrane-covered midline abdominal wall defect. When the length of the bowel herniation is more than 7 mm, an abdominal wall defect is likely, because in normal fetuses this length is 6 mm or less [19]. If the contents consist of liver or stomach and if the protrusion is covered by membrane, then an omphalocele is present (Figs. 14, 15). No herniation should be visible once the crown rump length is 45 mm or more [19,20]. Early diagnosis of omphalocele is important because it is a common feature of trisomies 18 and 13 [21,22]. In a study by Snijders, 61% of cases of omphalocele detected in the first trimester were aneuploid [22].

If the bowel loops have an irregular margin, then the defect is likely a gastroschisis (Fig. 16). Differentiation of gastroschisis from omphalocele is important because gastroschisis is not associated with aneuploidy.

When the cord insertion site appears enlarged, it is prudent to obtain a follow-up sonogram in 1 to 2 weeks. Because the bowel generally returns to the abdominal cavity in that time period, the patient can be counseled and managed appropriately.

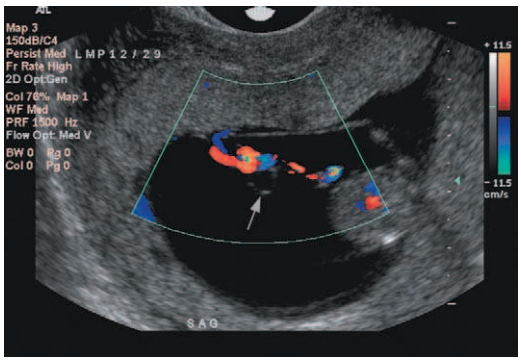

Fig. 12. Longitudinal view of umbilical cord from a scan at 11 weeks' gestation. Color Doppler image delineates a 3-mm umbilical cord cyst (*arrow*). Sonographic follow-up showed resolution of the cyst. The baby was normal at delivery.

Genitourinary tract

The fetal kidneys are echodense at 9 to 10 weeks' gestation and become slightly echolucent at 11 weeks. By 11 weeks' gestation, one third of kidneys can be visualized with transvaginal sonography, and by 13 weeks almost all kidneys can be visualized transvaginally [23]. The fetal bladder is generally visualized by 11 to 12 weeks' gestation [24]. Because excretory function occurs after 11 weeks, renal tract anomalies are unlikely to be visualized before this time. An enlarged bladder in the late first trimester

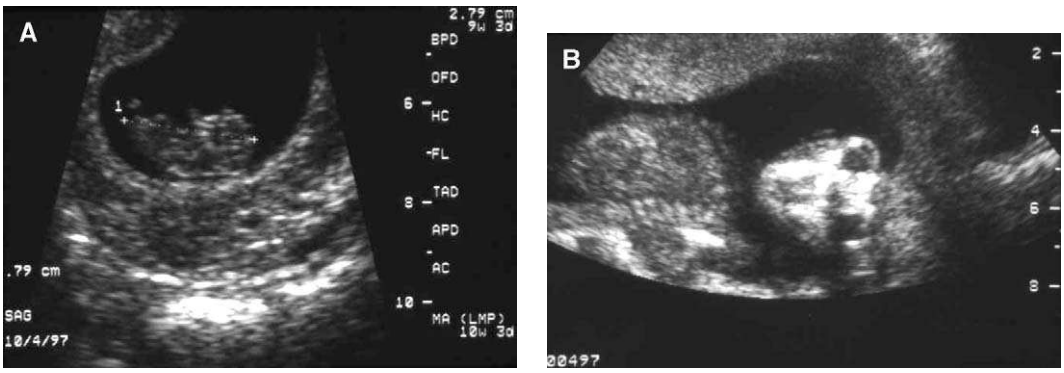

Fig. 4. (*A*) Sagittal view of embryo at 9 weeks and 3 days was interpreted as normal but with size less than dates. (*B*) Coronal view of fetus during the second trimester demonstrates absence of brain structures above the orbits, consistent with anencephaly that was missed in the initial scan.

has a differential diagnosis similar to that of an enlarged bladder later in gestation, including posterior urethral valves, urethral atresia, megacystitis/megaureter, or anorectal imperforation (Fig. 17). The prognosis of early fetal megacystitis is dismal [25]. There is a high rate of aneuploidy (25%) and a high percentage of associated malformations, especially intestinal malformations (33%) [26].

Congenital heart disease

Diagnoses of congenital heart defects have been made as early as 10 weeks' gestational age with the use of transvaginal sonography [27]. When diagnosed in the first trimester, these defects commonly are associated with abnormal fluid collections, such as ascites, pleural effusions, pericardial effusion, and lymphangiectasia [27].

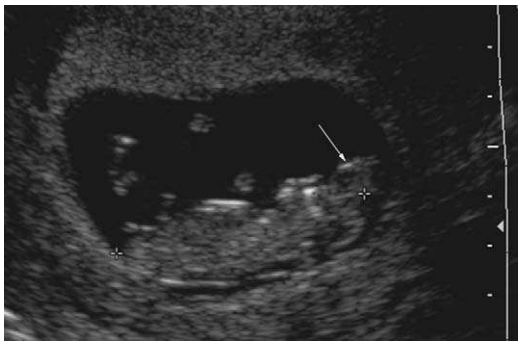

Fig. 5. Exencephaly. Sagittal view of a fetus at 12 weeks' gestation. Note the presence of angiomatous stroma (*arrow*) above the skull base. The calvarium is not visualized.

Skeletal anomalies

First trimester diagnoses of skeletal anomalies have been reported [28–31]. Specific diagnosis is facilitated when the patient has a history of a prior affected pregnancy.

Triploidy

Triploidy is the most common chromosomal anomaly in human gestation, and it occurs in 1% of all conceptions [32]. It results from three complete sets of chromosomes (total of 69 chromosomes). Most cases of triploidy end in spontaneous abortions during the first trimester, which leads to a prevalence of triploid pregnancy at 16 to 20 weeks' gestation of 0.002% [33]. Usually these fetuses have congenital abnormalities of multiple organ systems. They also can have first trimester onset of intrauterine growth restriction (Figs. 18–20) [34]. In a study of first trimester diagnosis of triploidy of 58,862 singleton fetuses at 10 to 14 weeks' gestation, there were 18 cases of triploidy. Fetal defects were observed in 8 of 18 (44.4%), including holoprosencephaly, omphalocele, and posterior fossa cyst. Increased nuchal translucency, growth restriction, and placental molar changes were present in 33%, 62%, and 67% of cases, respectively [34]. There are two different phenotypes depending on the parental origin of the extra haploid set. The cases of triploidy that result from a double paternal contribution have mild growth restriction and a thick placenta with multiple cystic spaces. The cases of triploidy with a double maternal contribution have severe asymmetric growth retardation and normal appearing placentas [34]. When an

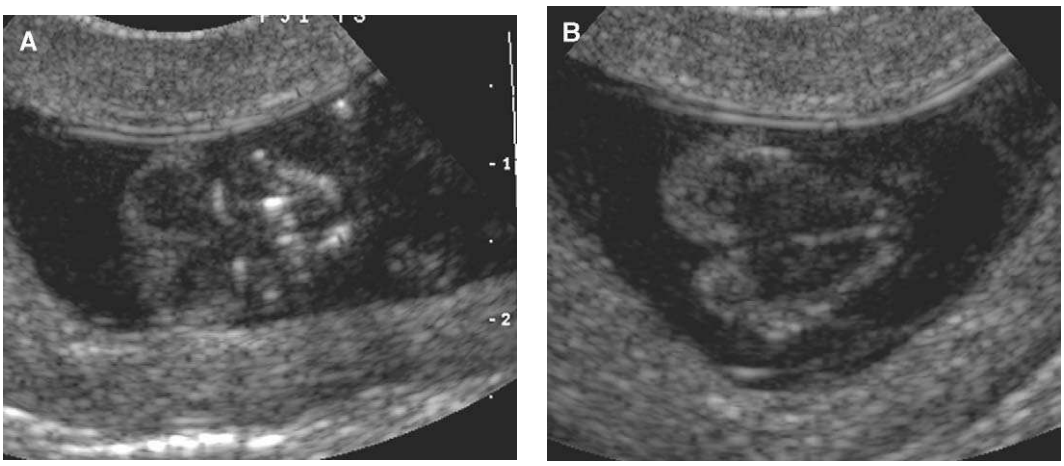

Fig. 6. Exencephaly. Coronal view of the fetus (*A*) and axial views of brain tissue (*B*) in fetus at 12 weeks and 4 days with absent calvarium. Note the appearance of malformed cerebral hemispheres as demonstrated by lack of demonstrable cerebral ventricles.

early pregnancy is scanned and the placenta appears enlarged or has cystic spaces, a follow-up scan in 1 to 2 weeks is recommended.

Triploidy is different from a classic complete hydatidiform molar pregnancy, in which there is no fetal tissue. Partial hydatidiform mole refers to the combination of a fetus with localized placental molar degeneration [35,36]. Histologically, it is characterized by focal swelling of the villous tissue, focal trophoblastic hyperplasia, and embryonic or fetal tissue. In approximately 90% of cases, partial moles are triploid and have two sets of paternal and one set of maternal chromosomes [37,38]. After dilatation and curettage, persistent gestational trophoblastic disease develops in 4% to 11% of patients with a partial mole [39].

Conjoined twins

Conjoined twins are rare, estimated to occur in 1:30,000 to 1:100,000 live births [40]. Conjoined twins are monozygotic twins that had a late and incomplete fission of the inner cell mass during the third week of gestation. The sonographic signs include inability to visualize a membrane between twins, inability to visualize a complete separation of the twins, fetal spines in unusual proximity, unusual embryonic or fetal shapes, single cardiac pulsation with two adjacent fetal poles or two cardiac pulsations in a single fused fetal pole, and more than three vessels in the umbilical cord (Fig. 21). Sonography in the first trimester can delineate the extent of organ sharing [41]. Common pitfalls for the diagnosis of

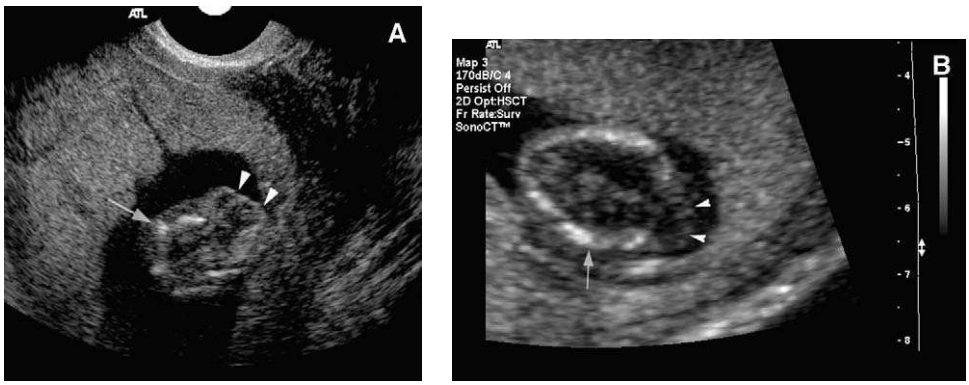

Fig. 7. Transabdominal (*A*) and transvaginal (*B*) views of the head in a 13-week gestational age fetus demonstrate herniated brain tissue consistent with a large posterior encephalocele (*arrowheads*) with a normally ossified anterior skull (*arrows*).

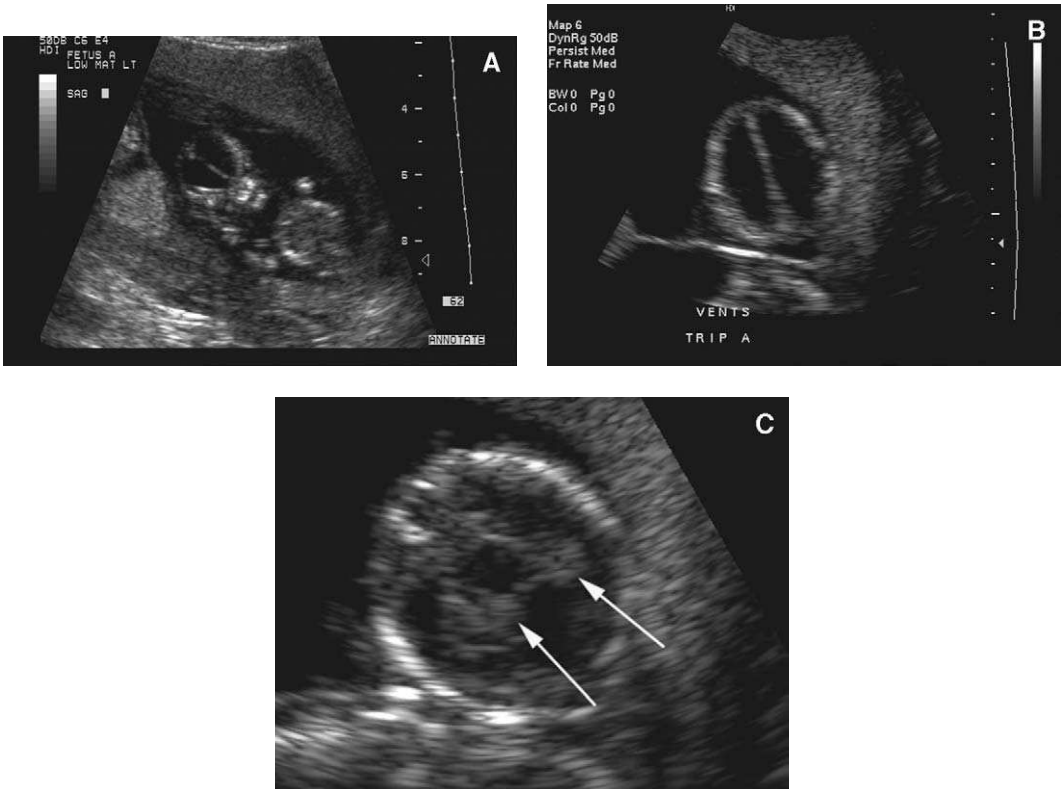

Fig. 8. Coronal (*A*) and transverse (*B*) views of the lateral ventricles and coronal view of the posterior fossa (*C*) of a 12-week gestational age fetus with dilatation of the lateral ventricles, seen as lucency in the cerebral hemispheres without choroid plexus. The third ventricle is enlarged and there is splaying of the cerebellar hemispheres (*long arrows*). Although cerebellar abnormalities are notoriously difficult to diagnose in the first trimester because the cerebellum is still developing, the constellation of findings in this case is consistent with a Dandy Walker malformation.

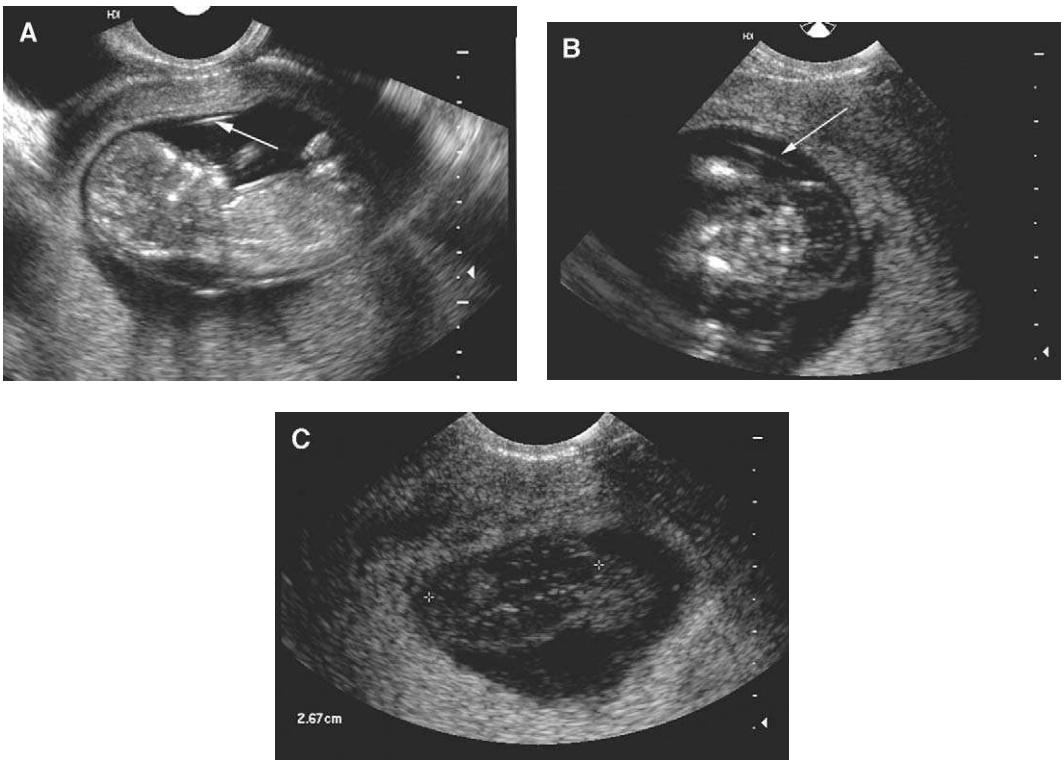

Fig. 9. Sagittal (*A*), axial (*B*), and coronal (*C*) views of a 12-week, 3-day gestation demonstrate nuchal translucency with septations. The extent of the translucency along the back of the fetus is denoted with calipers. This is clearly separate from the amnion (*arrow*). Chromosomal analysis showed trisomy 21.

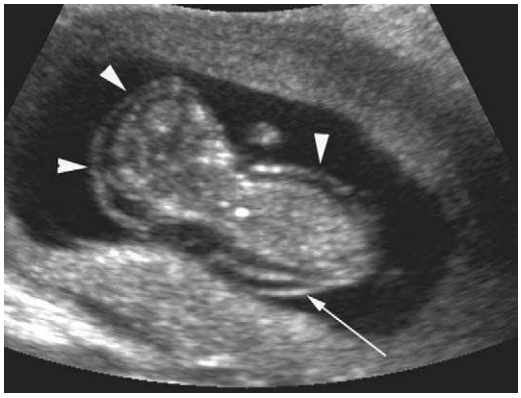

Fig. 10. Coronal view of a 12-week gestational age fetus with diffuse lymphangiectasia. Note diffuse lucency under the skin (*arrowheads*), which is clearly separate from the amnion (*arrow*). Chromosomal analysis showed trisomy 18.

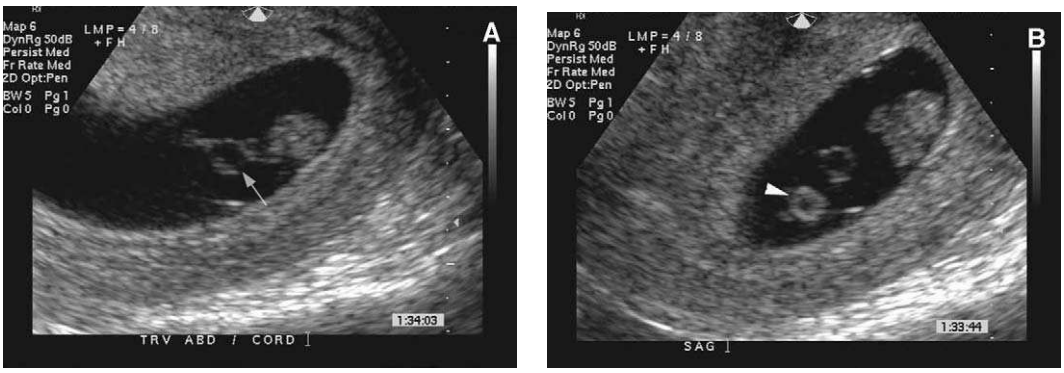

Fig. 11. (*A, B*) Transverse images of the fetal abdomen and umbilical cord at 9 weeks' gestational age demonstrate a 4-mm cyst (*arrow*) separate from the yolk sac (*arrowhead*). The cyst was not visualized 4 weeks later in a follow-up examination.

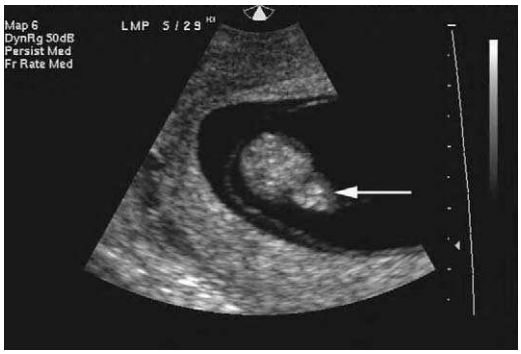

Fig. 13. Transverse view of the abdomen at 10 weeks and 2 days' gestational age demonstrates physiologic bowel herniation. Note the individual loops of bowel (*arrow*) within the base of the umbilical cord.

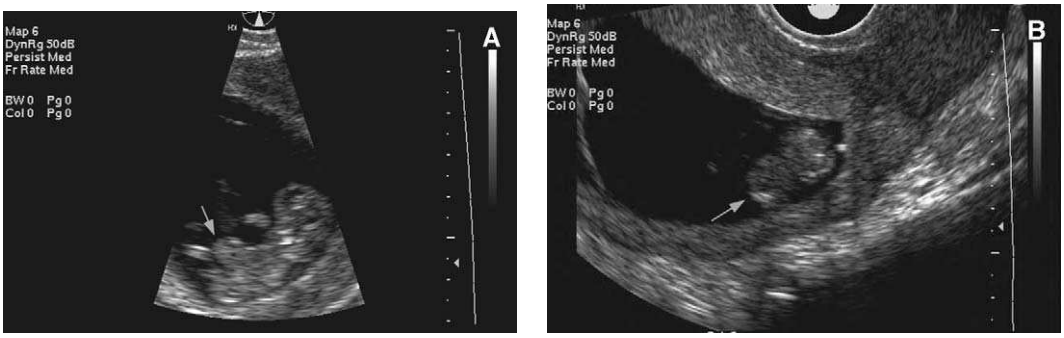

Fig. 14. Two fetuses with omphalocele and trisomy 18. Sagittal view (*A*) of 10-week gestation and transverse view (*B*) in a 12-week gestation each demonstrate an omphalocele (*arrow*).

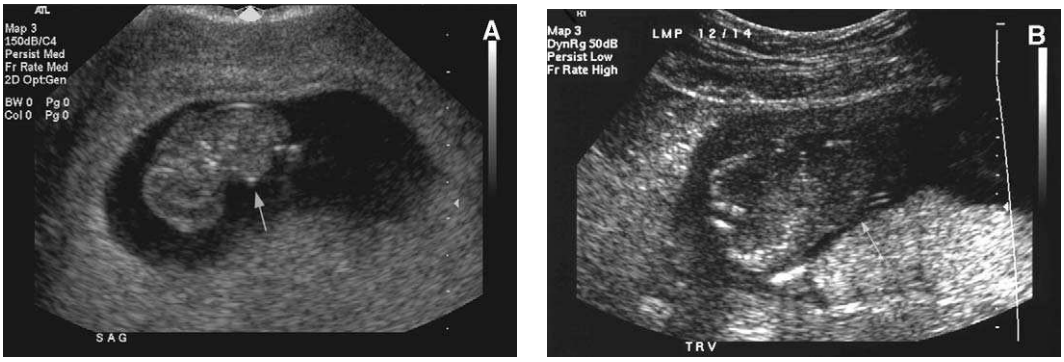

Fig. 15. (*A*) Sagittal view of an 8-week embryo with a prominent cord insertion site (*arrow*). This was not noted prospectively. (*B*) Follow-up examination at 16 weeks axial view of abdomen demonstrated an omphalocele. The chromosomal abnormality was a de novo terminal deletion of the short arm of chromosome 5 with a karyotype of 46, XY, del(5) (p15.3).

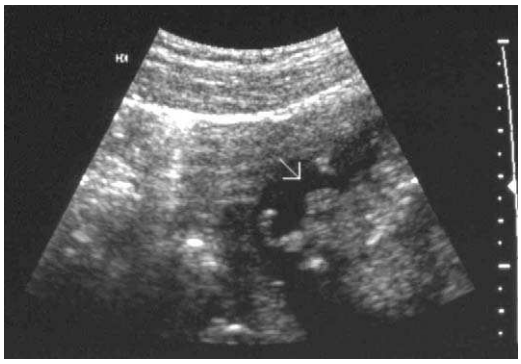

Fig. 16. Sagittal view of the fetal abdomen at 11 weeks and 5 days' gestation illustrates a prominent cord insertion site (*arrow*). Follow-up was suggested, but the fetus was not scanned again until 19 weeks' gestation, when the scan confirmed the presence of gastroschisis.

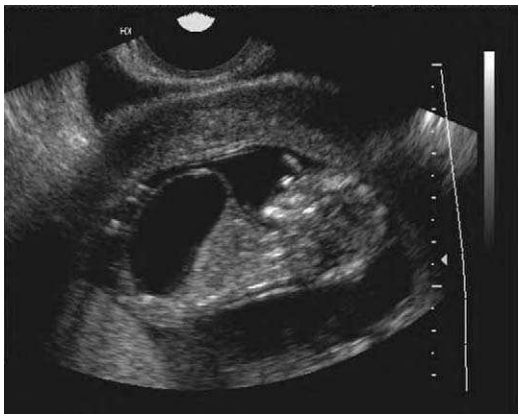

Fig. 17. Sagittal view of a 13-week gestational age fetus shows a dilated pear-shaped bladder and a normal amount of amniotic fluid. The presumed diagnosis was posterior urethral valves.

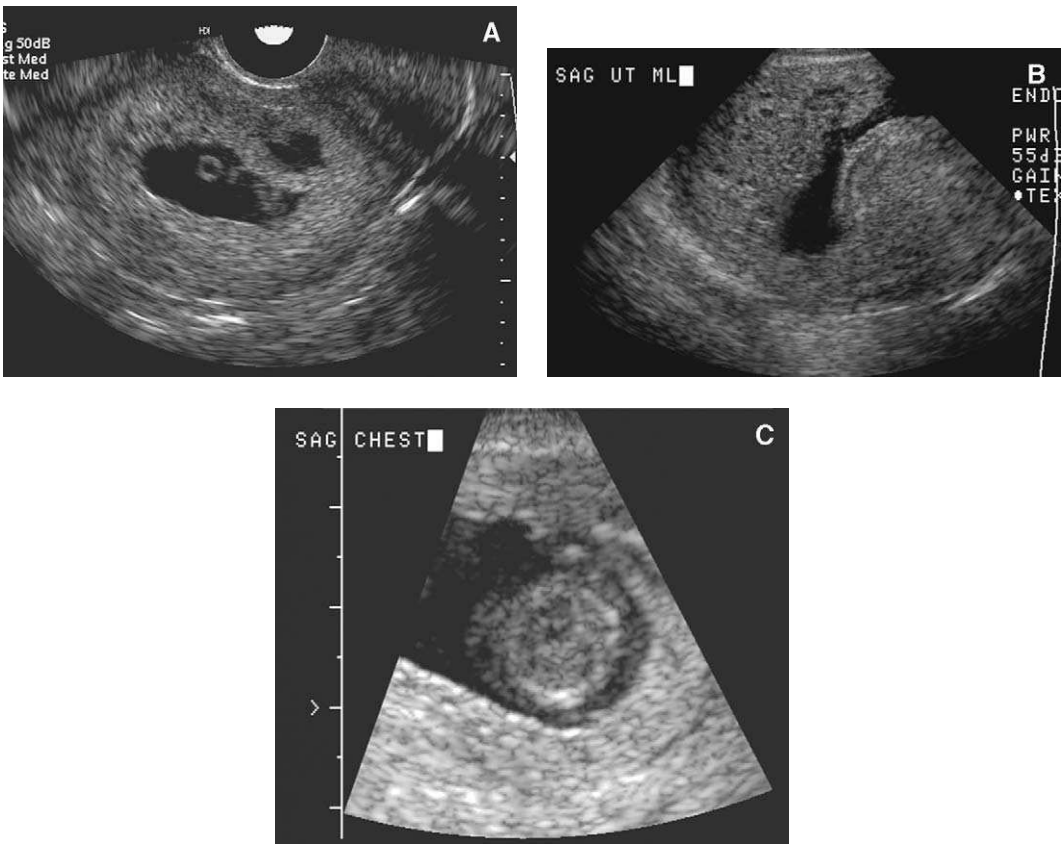

Fig. 18. Triploidy. (*A*) Sagittal view of uterus at 11 weeks' gestation by unsure dates and 8 weeks 6 days' gestation by crown rump length. The placenta is slightly heterogeneous with some cysts. (*B*) Sagittal view of the placenta 3 weeks later shows an enlarged placenta with multiple small cysts. (*C*) Axial view at levels of chest shows diffuse skin thickening consistent with lymphangiectasia. The combination of cystic placenta and abnormal fetus suggests the diagnosis of triploidy. Chromosomal analysis showed triploidy, and histology of the placenta showed partial mole.

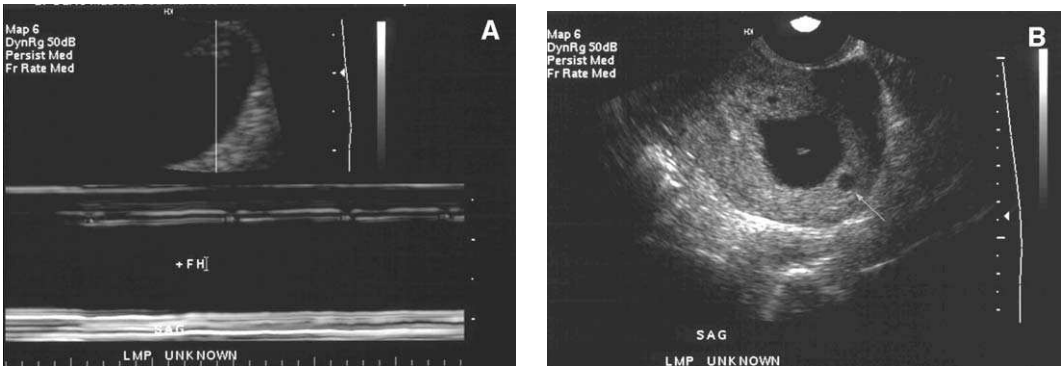

Fig. 19. Triploidy. (*A*) Transvaginal M-mode of a 7-mm embryonic pole demonstrates severe bradycardia (heart rate of 54). (*B*) There are subtle placental cystic changes (*arrow*). The patient had a miscarriage, and histologic examination demonstrated a partial mole.

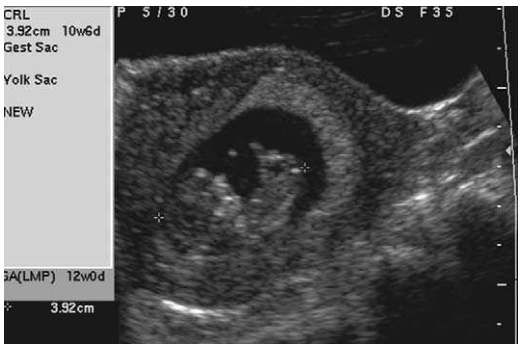

Fig. 20. Triploidy. Sagittal view of fetus at 12 weeks' gestation by dates and 10 weeks and 6 days' gestation by crown rump length. Note the small size of the fetal torso compared with the head caused by early asymmetric growth restriction.

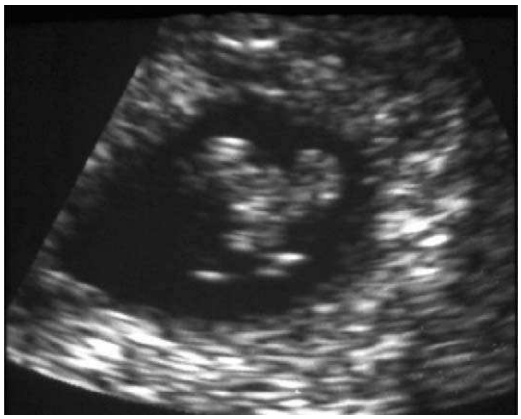

Fig. 21. Conjoined twins at 7 weeks' gestational age. Two heart beats were visualized.

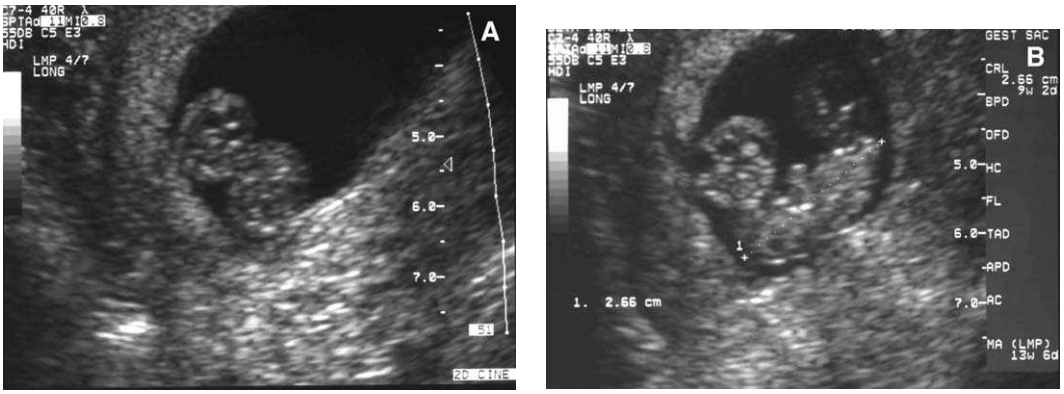

Fig. 22. (*A*) Transverse view of a monoamniotic monochorionic twin gestation at 9 weeks 2 days. The fetal abdomens are imaged together both in the transverse plane with no membrane seen between them. (*B*) Image obtained a few minutes later demonstrates a separation between the embryos, and the more posterior twin is in the longitudinal plane. The change in position and seperation of the twins exclude the possibility of conjoined twins.

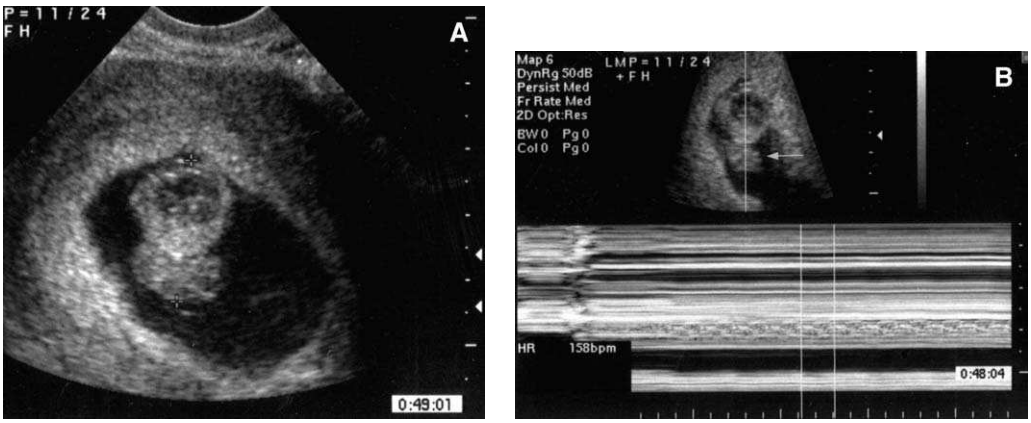

Fig. 23. Intraamniotic hematoma mimicking conjoined twins. (*A*) Transvaginal view of an embryo at 9 weeks' gestational age by last menstrual period shows an abnormal embryonic contour (*calipers*). (*B*) M-mode shows that the cardiac activity is in the posterior aspect of the tissue (*arrow*). Differential diagnosis was hematoma adjacent to the fetal pole or conjoined twins. Follow-up showed resolution of the mass. There were no abnormalities at birth.

conjoined twins include monochorionic monoamniotic twins that are in close proximity (Fig. 22) and intraamniotic hematoma adjacent to embryo (Fig. 23).

Summary

Knowledge of normal and abnormal anatomy in the first trimester aids in early detection of anomalies and the avoidance of potential pitfalls.

References

[1] Timor-Tritch IE, Farine D, Rosen MG. A close look at early embryonic development with the high-frequency transvaginal transducer. Am J Obstet Gynecol 1988; 159:676–81.
[2] Quashie C, Weiner S, Bolognese R. Efficacy of first trimester transvaginal sonography in detecting normal fetal development. Am J Perinatol 1992;9:209–13.
[3] Braithwaite JM, Armstrong MA, Economides DL. Assessment of fetal anatomy at 12–13 weeks of gestation transabdominal and transvaginal sonography. Br J Obstet Gynaecol 1996;103:82–5.
[4] Economides DL, Whitlow BJ, Braithwaite JM. Ultrasonography in the detection of fetal anomalies in early pregnancy. Br J Obstet Gynaecol 1999;106:516–23.
[5] Blaas HG, Eik-Ness SH, Kiserud T, Hellevik LR. Early development of the forebrain and midbrain: a longitudinal study from 7 to 12 weeks of gestation. Ultrasound Obstet Gynecol 1994;4:183–92.
[6] Johnson SP, Sebire NJ, Snijders RJ, Tunkel S, Nicolaides KH. Ultrasound screening for anencephaly at 10–14 weeks of gestation. Ultrasound Obstet Gynecol 1997;9:14–6.
[7] Hendricks SK, Cyr DR, Nyberg DA, Raabe R, Mack LA. Exencephaly: clinical and ultrasonic correlation to anencephaly. Obstet Gynecol 1988;72:898–901.
[8] Wilkins-Haug L, Freedman W. Progression of exencephaly to anencephaly in the human fetus: an ultrasound perspective. Prenat Diagn 1991;11:227–33.
[9] Bronshtein M, Ben-Shlomo I. Choroid plexus dysmorphism detected by transvaginal sonography: the earliest sign of fetal hydrocephalus. J Clin Ultrasound 1991; 19:547–53.
[10] Bronshtein M, Bar-Hava I, Blumenfeld I, Bejar J, Toder Z, Blumenfeld Z. The difference between septated and nonseptated nuchal cystic hygroma in the early second trimester. Obstet Gynecol 1993;81:683–7.
[11] van Vugt JM, Zalen-Sprock RM, Kostense PJ. First-trimester nuchal translucency: a risk analysis on fetal chromosome abnormality. Radiology 1996;200:537–40.
[12] Bromley B, Benacerraf BR. The resolving nuchal fold in second trimester fetuses: not necessarily reassuring. J Ultrasound Med 1995;14:253–5.
[13] Pandya PP, Brizot ML, Kuhn P, Snijders RJ, Nicolaides KH. First-trimester fetal nuchal translucency thickness and risk for trisomies. Obstet Gynecol 1994;84: 420–3.
[14] Skibo LK, Lyons EA, Levi CS. First-trimester umbilical cord cysts. Radiology 1992;182:719–22.
[15] Ross JA, Jurkovic D, Zosmer N, Janiaux E, Hacket E, Nicolaides KH. Umbilical cord cysts in early pregnancy. Obstet Gynecol 1997;89:442–5.
[16] Sepulveda W, Gutierrez J, Sanchez J, Be C, Schnapp C. Pseudocyst of the umbilical cord: prenatal sonographic appearance and clinical significance. Obstet Gynecol 1999;93:377–81.
[17] Sepulveda W, Leible S, Ulloa A, Ivankovic M, Schnapp C. Clinical significance of first trimester umbilical cord cysts. J Ultrasound Med 1999;18:95–9.
[18] Osborne NG, Bonilla-Musoles F, Raga F, Bonilla F.

Umbilical cord cysts: color Doppler and three dimensional ultrasound evaluation. Ultrasound Quarterly 2000;16:133–9.
[19] Blaas H, Eik-Nes SH, Kiserud T, Hellevik LR. Early development of the abdominal wall, stomach and heart from 7–12 weeks of gestation: a longitudinal ultrasound study. Ultrasound Obstet Gynecol 1995;6: 240–9.
[20] Bowerman RA. Sonography of fetal midgut herniation: normal size criteria and correlation with crown-rump length. J Ultrasound Med 1993;5:251–4.
[21] Sherod C, Sebire NJ, Soares W, Snijders RJ, Nicolaides KH. Prenatal diagnosis of trisomy 18 at the 10–14 week ultrasound scan. Ultrasound Obstet Gynecol 1997;10: 387–90.
[22] Snijders RJ, Sebire NJ, Souka A, Santiago C, Nicolaides KH. Fetal exomphalos and chromosomal defects: relationship to maternal age and gestation. Ultrasound Obstet Gynecol 1995;6:250–5.
[23] Bronshtein M, Yoffe N, Brandes JM, Blumenfeld Z. First and early second trimester diagnosis of fetal urinary tract anomalies using transvaginal ultrasonography. Prenat Diagn 1990;10:653–66.
[24] Hoshino T, Ihara Y, Shirane H, Ota T. Prenatal diagnosis of prune belly syndrome at 12 weeks of pregnancy: case report and review of the literature. Ultrasound Obstet Gynecol 1998;12:362–6.
[25] Abbott J, Levine D, Wapner R. Posterior urethral valves: inaccuracy of prenatal diagnosis. Fetal Diagn Ther 1998;13:179–83.
[26] Favre R, Kohler M, Gasser B, Muller F, Nisand I. Early fetal megacystitis between 11 and 15 weeks of gestation. Ultrasound Obstet Gynecol 1999;14:402–6.
[27] Achiron R, Rotstein Z, Lipitz S, Mashiach S, Hegesh J. First-trimester diagnosis of fetal congenital heart disease by transvaginal ultrasonography. Obstet Gynecol 1994;84:69–72.
[28] den Hollander NS, van der Harten HJ, Vermeij-Keers C, Niermeijer MF, Wladimiroff JW. First-trimester diagnosis of Blomstrand lethal osteochondrodysplasia. Am J Med Genet 1997;73:345–50.
[29] Meizner I, Barnhard Y. Achondrogenesis type I diagnosed by transvaginal ultrasonography at 13 weeks' gestation. Am J Obstet Gynecol 1995;173:1620–2.
[30] Soothill PW, Vuthiwong C, Rees H. Achondrogenesis type 2 diagnosed by transvaginal ultrasound at 12 weeks' gestation. Prenat Diagn 1993;13:523–8.
[31] Hobbins JC, Jones OW, Gottesfeld S, Persutte W. Transvaginal ultrasonography and transabdominal embryoscopy in the first-trimester diagnosis of Smith-Lemli-Opitz syndrome, type II. Am J Obstet Gynecol 1994;171:546–9.
[32] Doshi N, Surti U, Szulman AE. Morphologic anomalies in triploid liveborn fetuses. Hum Reprod 1983;14: 716–23.
[33] Ferguson-Smith MA, Yates JR. Maternal age specific rates for chromosome aberrations and factors influencing them: report of a collaborative European study on 52,965 amniocentesis. Prenat Diagn 1984;4:5–44.
[34] Jauniaux E, Brown R, Snijders RJ, Noble P, Nicolaides KH. Early prenatal diagnosis of triploidy. Am J Obstet Gynecol 1997;176:550–4.
[35] Szulman AE, Surti U. The syndromes of hydatidiform mole: I. Cytogenetic and morphologic correlations. Am J Obstet Gynecol 1978;131:665–71.
[36] Szulman AE, Surti U. The syndromes of hydatidiform mole: II. Morphologic evolution of the complete and partial mole. Am J Obstet Gynecol 1978;132:20–7.
[37] Jacobs PA, Szulman AE, Funkhouser J, Matsuura JS, Wilson CC. Human triploidy: relationship between parental origin of the additional haploid complement and development of partial hydatidiform mole. Ann Hum Genet 1982;46:223–31.
[38] McFadden DE, Kwong LC, Yam IY. Parental origin of triploidy in human fetuses: evidence for genomic imprinting. Hum Genet 1993;92:465–9.
[39] Berkowitz RS, Goldstein DP. Chorionic tumors. N Engl J Med 1996;335:1740–8.
[40] Edmonds LD, Layde PM. Conjoined twins in the United States, 1970–1977. Teratology 1982;25:301–8.
[41] Lam YH, Sin SY, Lam C, Lee CP, Tang MH, Tse HY. Prenatal sonographic diagnosis of conjoined twins in the first trimester: two case reports. Ultrasound Obstet Gynecol 1998;11:289–91.

RADIOLOGIC
CLINICS OF
NORTH AMERICA

Radiol Clin N Am 41 (2003) 695–708

Prenatal diagnosis for detection of aneuploidy: the options

Nancy E. Budorick, MD[a,*], Mary K. O'Boyle, MD[b]

[a]*Department of Radiology, Columbia University, Columbia Presbyterian Medical Center, Milstein Hospital Building 4-156, 177 Fort Washington Avenue, New York, NY 10032, USA*
[b]*Department of Radiology, University of California, San Diego, Medical Center, 200 West Arbor Drive, San Diego, CA 92103-8759, USA*

Remarkable strides have been made in the past several decades in the area of prenatal diagnosis. This development largely has been driven by the evolution of DNA analysis and changes in the childbearing population. Screening tests of serum analytes and ultrasound technology also have added to the current complex algorithm that gives the lowest risk assurance of a euploid fetus. This article describes the available invasive (definitive) and noninvasive (screening) testing that is available to diagnose aneuploidy, with special emphasis on the role of ultrasound.

Background

Autosomal trisomy is a result of meiotic nondisjunction, which increases with maternal age, such that at 35 years of age the inherent midtrimester risk of trisomy 21, Down syndrome (DS), at 1/270, is similar to the generally quoted rate of pregnancy complication from amniocentesis at 1/200 [1,2]. Therefore, at age 35 and older, genetic amniocentesis has traditionally been offered routinely, since the risk of pregnancy complication from amniocentesis is similar to the risk of carrying a fetus with autosomal trisomy. Historically, most children with trisomy 21 have been born to women younger than 35 years of age [3] because younger women have constituted most of the child-bearing population, and only a minority of trisomy 21 fetuses have been born to women aged 35 and older (12.9%) [4]. Current birth records in the United States indicate that there is a change in the child-bearing population, however, with more women bearing children at advanced maternal age ($\geq$35 years at time of delivery), such that use of maternal age detects approximately 50% of Down syndrome cases [5].

Besides women aged 35 years or older at time of delivery, patients at risk for fetal aneuploidy include women with previous pregnancy complicated by autosomal trisomy, a fetus with one major structural defect or two or more minor structural defects identified at sonography, prior fetus with sex chromosome aneuploidy, parents with a known chromosomal translocation, parents who carry known chromosome inversions, and parents with aneuploidy themselves [6].

Invasive testing: definitive detection/exclusion of aneuploidy

Amniocentesis is a procedure usually offered between 15 and 20 weeks' gestation in which amniotic fluid is removed under direct ultrasound guidance for culture and cytogenetic analysis. The risk of pregnancy complication associated with amniocentesis is generally quoted as 1:200 (0.5%) [1,2]. Complications include amnionitis, [7] rhesus isoimmunization, [8,9], which can be prevented with prophylactic administration of anti-D immunoglobulin to Rh-negative women, amniotic fluid leak or vaginal blood loss [10,11],

* Corresponding author. Ultrasound – Department of Radiology, Milstein Hospital Building 4-156, Columbia Presbyterian Medical Center, 177 Fort Washington Avenue, New York, NY 10032.
E-mail address: nb202@columbia.edu (N.E. Budorick).

0033-8389/03/$ – see front matter © 2003 Elsevier Inc. All rights reserved.
doi:10.1016/S0033-8389(03)00044-7

cramping and lower abdominal discomfort for up to 8 hours [12], and pregnancy loss [1,2]. Cytogenetic results are available between 10 and 14 days after the procedure, and the diagnostic accuracy is more than 99% [13].

Early amniocentesis is offered between 11 and 13 weeks' gestation for patients who desire earlier evaluation of karyotype [14–17]. The complication rate is higher than with traditional amniocentesis, however. The risk of pregnancy loss is 2.5% compared with 0.5% to 0.7% with traditional amniocentesis [17]. Risk of talipes may be up to 1.4% over that with traditional amniocentesis at 0.1% (background) [17]. Membrane rupture is more likely with early amniocentesis, and there are significantly more culture failures than with traditional amniocentesis [17]. Because of these factors, early amniocentesis is rarely performed.

In chorionic villus sampling, a sample of chorionic villi is removed from the placenta through a plastic catheter via transabdominal or transcervical approach using ultrasound guidance. This procedure is performed between 10 and 12 weeks' gestation, so results are available earlier in pregnancy than in routine amniocentesis. The transcervical route is the most commonly used approach. The transcervical route can be used for either anterior or posterior placentas, but there are several contraindications, including the absolute contraindication of an active cervical infection and several relative contraindications, such as vaginal infection, vaginal bleeding or spotting, extreme anteversion or retroversion of the uterus, and large patient habitus that prohibits access to the uterus or adequate visualization of intrauterine structures at sonography [18,19]. The transabdominal approach is used when the placenta is anterior or fundal and not easily sampled by the transcervical route. The risk of pregnancy loss at 1.1% to 1.3% is 0.6% to 0.8% higher than with traditional amniocentesis [13,20–24]. Oromandibular-limb hypogenesis is more common among chorionic villus sampling–exposed infants, especially when performed before 7 weeks' gestation and less so after 9 weeks' gestation [24–26].

Cordocentesis, or percutaneous umbilical blood sampling, is puncture of the umbilical vein under direct ultrasound guidance for karyotype analysis of the fetal blood cells. This technique has the advantage of available results within 24 to 48 hours, but the rate of pregnancy loss is relatively high, reported at less than 2% [2,27]. This technique is used for various nongenetic situations (eg, blood transfusion, fetal blood evaluation). Regarding genetic uses, percutaneous umbilical blood sampling is used for rare situations in which a karyotype is urgently needed to assist pregnancy management.

Noninvasive testing for aneuploidy

Maternal serum screening in the second trimester

Serum biochemical screening in the second trimester yields a higher case detection rate for aneuploidy than maternal age screening alone. Maternal blood is drawn between 15 and 20 weeks' gestation for serum analyte evaluation. The results from 16 to 18 weeks' gestation are the most accurate. Pregnancies complicated by fetal Down syndrome have maternal serum alpha-fetoprotein levels that are low (0.7 multiples of the median [MoM] or less) [28–30]. Human chorionic gonadotropin (hCG) levels are elevated (2.04 MoM or more) in fetal Down syndrome [31–34]. A third serum analyte that is altered in fetal Down syndrome is unconjugated estriol, which is also found at lower levels (0.79 MoM or less) in affected pregnancies [31–34].

The relative risk of aneuploidy derived from maternal serum screening of these analytes is factored with race and diabetic status to modify the maternal age-related risk of aneuploidy [34–36]. At a 5% or more screen-positive rate, these three analytes identify 60% of trisomy 21 in women younger than 35 years of age. In women older than 35 years of age, it detects 75% or more of all trisomy 21 cases and can detect other aneuploid fetuses, because the screen-positive rate increases with maternal age [37].

Screen-positive cutoffs are chosen using either the midtrimester Down syndrome risk of a 35-year-old woman as the screen positive cutoff (1:250) or a cutoff that results in an acceptable balance of high detection rate and low screen-positive rate (1:190 or 1:200) [6]. These screening protocols may face future revision, because they are based on calculations of risk as determined by the maternal age-related risk of Down syndrome calculated in the 1980s. Because current rates of birth to women older than 35 years of age have increased since the 1980s, the screening premise may be obsolete [6].

Multiple-marker screening also can detect 60% to 75% of trisomy 18 fetuses. The profile is low levels of all three analytes [38–41]. Other aneuploidies are not detected with great frequency using biochemical screening; however, those missed are usually lethal, such as trisomy 13, or are sex chromosome abnormalities that are not associated with severe mental retardation or other severe physical or developmental limitations [6]. A new and promising serum analyte

Box 1. Second trimester ultrasound findings in trisomy 21

Major structural abnormalities

- Cardiac defects
- Cystic hygroma
- Duodenal atresia
- Generalized hydrops

Minor ultrasound markers

- Clinodactyly
- Echogenic intracardiac focus
- Frontal lobe shortening
- Hyperechoic bowel
- Mild ventriculomegaly
- Nasal bone ossification abnormality
- Nuchal thickening $\geq$6 mm
- Pelvic angle widening
- Pyelectasis $\geq$4 mm
- Sandal gap foot deformity

recently introduced is dimeric inhibin A [42–44]. Inhibin A is generally elevated in pregnancies affected by Down syndrome and is abnormally low in pregnancies affected by trisomy 18. The four-analyte combination gives 67% to 76% detection of Down syndrome in women younger than age 35 [44,45].

Second trimester ultrasound evaluation

It is irrefutable that structural anomalies are associated with aneuploidy. Using this information to determine or recalculate risk of an aneuploid fetus is an issue of controversy, however. The type and degree of abnormality (major abnormality or minor abnormality), the a priori risk of carrying an aneuploid fetus based on serum screening results, maternal age, or any other risks traditionally have been taken into consideration when determining risk of fetal aneuploidy. The precise manner in which these factors are weighted and used is complex, somewhat varied, and controversial.

Major ultrasound structural abnormalities

Most major organ or structural abnormalities, whether single or multiple, indicate risk for fetal aneuploidy [46,47]. Certain abnormalities are more common in particular types of aneuploidies, and a specific diagnosis may be suggested based on the sonographic abnormality identified. Boxes 1–5 list structural abnormalities associated with the more commonly occurring aneuploidies.

Regardless of the age-based or serum biochemical-based risk, a fetus with one or more of the major structural abnormalities listed in Boxes 1–5 is at high risk for aneuploidy. The benefit of undergoing invasive prenatal testing is generally considered worth the risk of serious complication of the procedure.

Trisomy 21 is the most common of the autosomal trisomies, with a reported incidence of 1 in 660 newborns [48]. Approximately one third of affected fetuses have a major structural abnormality on second trimester ultrasound, including cardiac anomalies (ventriculoseptal defects and common atrioventricular canals), ventriculomegaly, cerebellar hypoplasia, duodenal atresia (Fig. 1), hydrops, and omphalocele (Fig. 2) [49–53] (see Box 1).

Trisomy 18 (Edward syndrome) is the second most common autosomal trisomy at 3 per 1000 live

Box 2. Second trimester ultrasound findings in trisomy 18

Major abnormalities

- Agenesis of the corpus callosum
- Arthrogrypotic hands/wrists
- Cardiac defects
- Cerebellar dysgenesis
- Clubbed feet
- Cleft lip and palate
- Cystic hygroma
- Diaphragmatic hernia
- Intrauterine growth restriction
- Microcephaly
- Micrognathia
- Neural tube defects
- Ocular abnormalities
- Omphalocele
- Polyhydramnios
- Radial ray abnormalities
- Rocker bottom feet

Minor markers

- Brachycephaly/strawberry-shaped skull
- Choroid plexus cysts
- Limb shortening
- Single uterine artery

Box 3. Second trimester ultrasound findings in trisomy 13

Major abnormalities

- Cardiac defects
- Central nervous system abnormalities
- Cystic hygroma
- Facial abnormalities, including cleft lip and palate
- Echogenic kidneys (polycystic)
- Intrauterine growth restriction
- Holoprosencephaly
- Microcephaly
- Neural tube defects
- Ocular abnormalities
- Omphalocele
- Polydactyly
- Rocker bottom feet

Minor markers

- Echogenic intracardiac focus
- Mild ventriculomegaly
- Pyelectasis
- Single umbilical artery

births. It is more common in female live births by a ratio of 3:1, with a multiplicity of associated structural and sonographic abnormalities [48] (see Box 2). Fetuses affected with trisomy 18 frequently die during pregnancy or undergo miscarriage. Fetuses carried to term usually die during the first year of life, with occasional survivors beyond 1 year being profoundly mentally retarded [48].

Nyberg [54] and Benacerraf [55] have demonstrated that fetal trisomy 18 largely can be detected sonographically; 80% to 83% of cases have a major malformation, and most eventually develop intrauterine growth restriction. The typical arthrogrypotic hand of trisomy 18 yields disordered ossification centers of the hand and fingers (Fig. 3). Cardiac defects, clubfoot (Fig. 4), small omphalocele, and cleft lip (Fig. 5) and palate are also major malformations frequently seen in trisomy 18 (see Box 2).

Trisomy 13 (Pateau syndrome) has an incidence of 1 in 5000 births and has a high infant mortality rate, with most babies surviving less than 1 month and few long-term survivors [48]. Major sonographic abnormalities are seen in 91% of affected fetuses [56]. The characteristic features of midline facial abnormalities with holoprosencephaly (Fig. 6) are typical sonographic findings. Polydactyly and polycystic kidneys may mimic Meckel-Gruber syndrome. Cardiac anomalies and rocker bottom feet also may be seen (see Box 3).

Turner syndrome refers to XO karyotype that results from absence of one sex chromosome. Turner syndrome occurs in 1 in 200 live-born girls, but it is estimated that most XO conceptuses result in first trimester miscarriage. Fetuses that survive to the second trimester often have large, septated, cystic hygromas [57] (Fig. 7), which variably involve the entire fetus, with third-spacing in the pleural space, the peritoneum, and other potential spaces [58–60]. Cardiac anomalies are common [48].

Triploidy syndrome results from a complete extra set of chromosomes, which occurs in 2% of conceptuses. In 70% of cases, the extra complement of chromosomes is paternally derived, caused either by double fertilization of an egg or fertilization with a diploid sperm. Few are the result of fertilization of a

Box 4. Second trimester ultrasound findings in Turner syndrome (XO)

Major abnormalities

- Cardiac defects
- Cystic hygroma
- Hydrops
- Renal anomalies
- Shortened femur

Box 5. Second trimester ultrasound findings in triploidy

Major abnormalities

Fetus

- Cardiac defects
- Central nervous system anomalies
- Club feet
- Cystic hygroma
- Facial abnormalities, including hypertelorism
- Intrauterine growth restriction
- Micrognathia

Placenta

- Hydatidiform placental changes

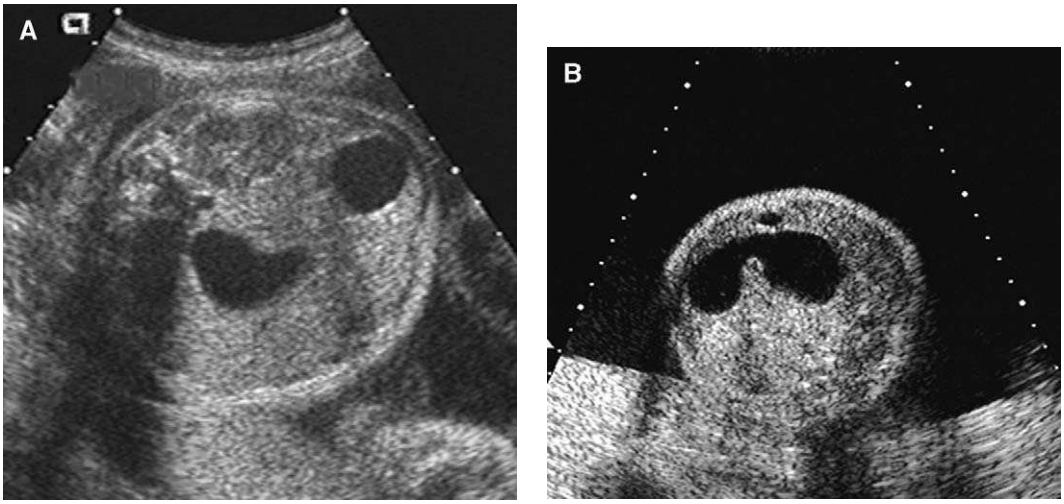

Fig. 1. "Double bubble" appearance in the upper abdomen in a 22-week gestation. (*A*) The stomach and proximal duodenum are fluid filled and dilated. (*B*) The two fluid-filled structures are seen to join, eliminating other diagnostic possibilities. There is polyhydramnios from the upper tract gastrointestinal obstruction. This is characteristic of duodenal atresia, which may be seen in trisomy 21.

diploid egg. The most common complement is XXY and most of the rest are XXX. Miscarriage is common and accounts for 20% of abnormal spontaneous abortuses. Toxemia may accompany a triploid pregnancy [48]. Triploid fetuses typically have multiple major malformations (up to 93% of cases) [61,62] and may have early-onset asymmetric intrauterine growth restriction, so the head may be disproportionately large compared with the body if detected in the second trimester [62]. When the extra chromosome complement is maternally derived, the placenta is relatively small and there is severe intrauterine growth restriction. When the extra chromosome complement is paternally derived, the placenta is large and contains hydropic villi [63].

Minor ultrasound markers

Minor ultrasound abnormalities or minor ultrasound markers are abnormalities that are of limited consequence in and of themselves but may indicate risk of underlying karyotype abnormality. For the most part, this category of abnormality is useful in detection of Down syndrome and includes thickened second trimester nuchal fold (Fig. 8), shortened humerus, shortened femur, pyelectasis of 4 mm or more (Fig. 9), echogenic intracardiac focus (Fig. 10), hyperechoic bowel (Fig. 11), and mild ventriculomegaly (Fig. 12) (see Boxes 1–3). Choroid plexus cysts (Fig. 13) are another minor ultrasound marker, but they are markers for trisomy 18 and not for Down syndrome [64]. An ultrasound performed for detection of abnormalities that may alter a patient's a priori risk of aneuploidy is called the genetic sonogram.

Use of minor ultrasound markers has changed from previously described scoring systems [65–69] to patient-specific risk adjustment schemata. Nyberg developed a method of risk assignment that is based on the specific ultrasound findings combined with the a priori age-related risk of aneuploidy. This system is called the Age Adjusted Ultrasound Risk Assessment (AAURA) for Down syndrome [70,71]. In the AAURA system, the ultrasound markers are not considered equally but are weighted by the likelihood

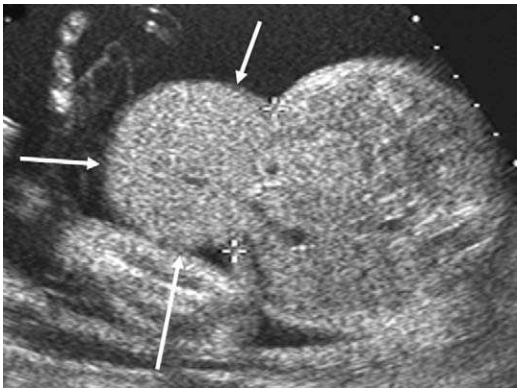

Fig. 2. Omphalocele (*arrows*) in a 21-week gestation. The anterior abdominal wall defect is between the electronic calipers.

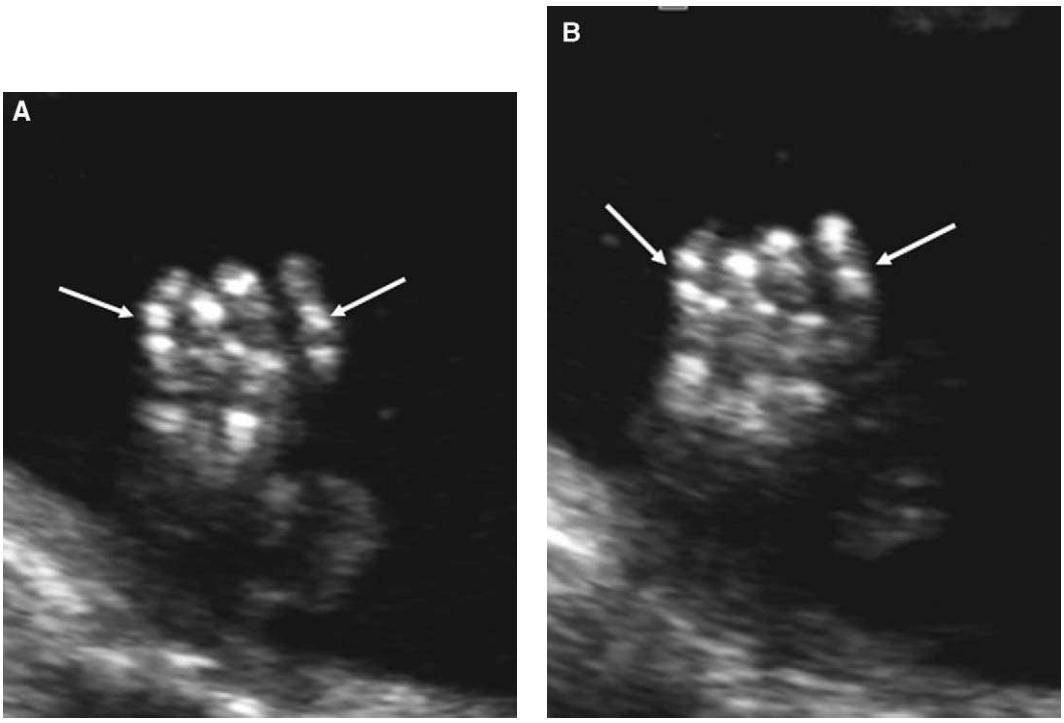

Fig. 3. Arthrogryposis of the hands in a 19-week gestation. Two images, one slightly more volar (*A*) and one slightly more dorsal (*B*), of the same hand demonstrate disarrayed ossification centers of the phalanges (*between arrows*). This appearance is characteristic of fixed clenching and overlapping of the fingers that may be seen with trisomy 18.

ratios (of associated aneuploidy) of the individual sonographic findings. Using AAURA and a threshold of 1:200, 74% of fetuses with Down syndrome were identified overall: 61.5% of those from women younger than 35 years (4% false-positive rate), 67.2% of those from women aged 35 to 39 years (12.5% false-positive rate), and 100% of those from women aged 40 years or older (false-positive rate = 0).

Bromley [72] recently published a modification of the sonographic scoring index system initially pub-

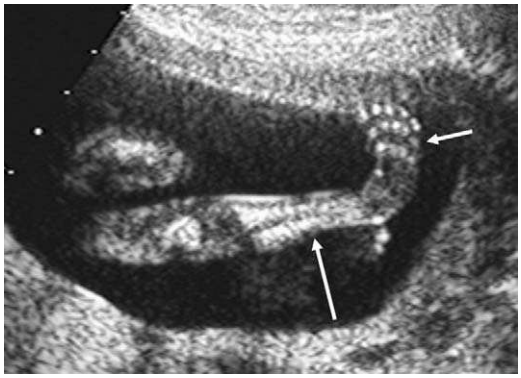

Fig. 4. Clubfoot in a 20-week gestation, in which there is an abnormal relationship between the forefoot (*short arrow*) and lower leg bones (*long arrow*), which remains fixed during fetal movement. This abnormality may be seen in any of the trisomy syndromes.

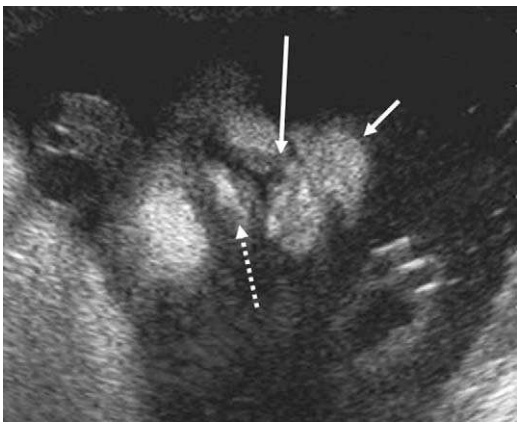

Fig. 5. Cleft upper lip (*long arrow*) in a 30-week gestation. Nose (*short arrow*). Intact lower lip (*dashed arrow*). This abnormality may be seen in several of the trisomy syndromes.

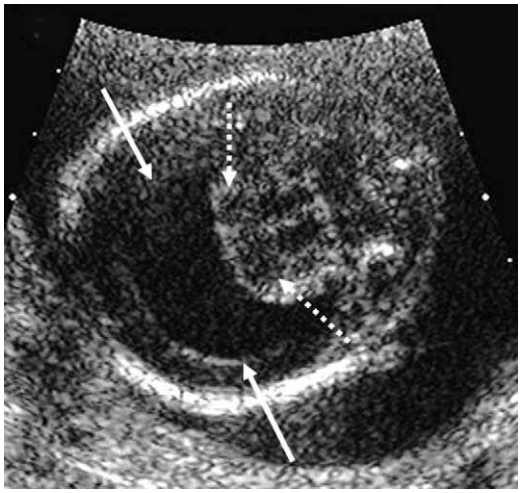

Fig. 6. Alobar holoprosencephaly in a 21-week gestation. There is a monoventricle (*arrows*) with fused thalami (*dashed arrows*).

lished by Benacerraf [65–69]. In an evaluation of 10 years worth of data, likelihood ratios of the different sonographic markers were derived. Each patient's risk adjustment is achieved through Bayes Theorem: a priori risk multiplied by the likelihood ratio yields the revised risk, and amniocentesis is offered when the revised risk is 1:270 or more. Likelihood ratios for most of the markers were calculated as isolated findings and as part of a multiple marker scheme [72]. The greatest sensitivity rate for detection of Down syndrome using this method was 80.5% (12.4% false-positive rate), and the absence of any markers decreased the risk of Down syndrome by 80% [72]. Thickened nuchal fold, short humerus, a major structural abnormality, and any combination of two minor ultrasound markers carried the most significant risks for aneuploidy [72]. Other less formalized scoring systems have demonstrated similar associations with aneuploidy [73–76].

Several articles have described a risk reduction in women at risk for fetal aneuploidy if the sonogram is normal, first suggested by Nyberg [77]. In the at-risk patient population described by Sohl et al [76], the a priori risk of aneuploidy was 1:26 and the a priori Down syndrome risk was 1:50. A normal sonogram reduced these risks to 1:67 and 1:120, respectively [73]. Similar findings were demonstrated by Vergagni [78], Bahado-Singh [79], Vintzileos [76], and Bromley [72].

Various reviews have resulted in controversy regarding the use of ultrasound to assess and modify risk for aneuploidy. Published likelihood ratios are not entirely consistent, and practitioners are left with a dilemma as to which likelihood ratios to use. The use of an isolated minor ultrasound marker in the risk adjustment of a previously low-risk patient also may

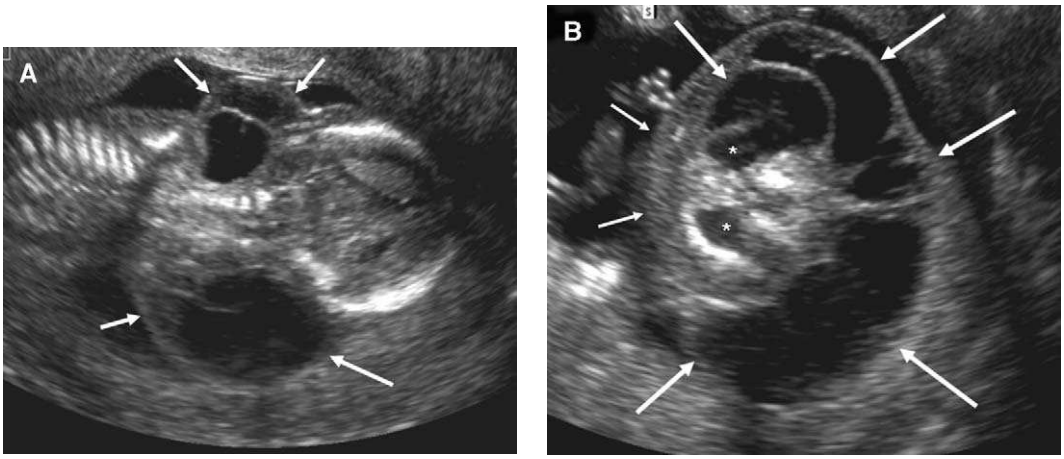

Fig. 7. Large, septated cystic hygroma in a Turner syndrome (XO) fetus in an 18-week gestation. (*A*) Longitudinal image demonstrates bulging, septated cystic hygroma in the neck region (*arrows*). (*B*) Axial image demonstrates the nearly circumferential nature of this cystic hygroma (*large arrows*), with only sparing of the anterior chest skin (*small arrows*). Bilateral pleural effusions are identified in the apical thoracic spaces bilaterally (*). (*C*) There also is ascites, surrounding suspended bowel loops (*arrow*) and liver (*dashed arrow*).

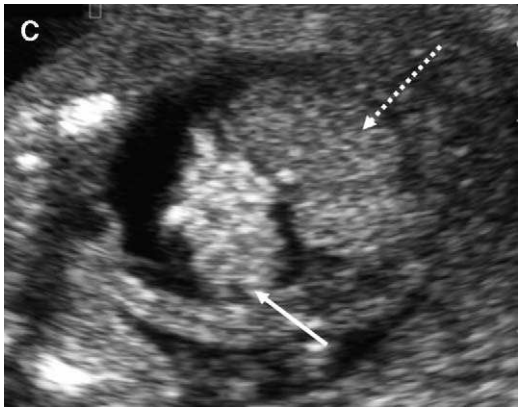

Fig. 7 (*continued*).

result in a significant number of patients with false-positive results who consequently undergo substantial anxiety [80] and potential fetal loss if invasive testing is elected [81].

The conclusions reached by Smith-Bindman in a recent metaanalysis of published ultrasound literature regarding this subject surprised the ultrasound community by putting forth a serious challenge to current practices of risk modification based on ultrasound findings [81]. In this comprehensive review, 56 articles that described 1930 fetuses with Down syndrome and 130,365 unaffected fetuses were analyzed. Sensitivities for detection of Down syndrome of the minor ultrasound markers were grossly inconsistent across the different studies included in the metaanalysis. The differences in accuracy were not caused by threshold differences among the studies, year of study, study design (case control versus prospective study), risk of the patients, or setting of the study. The most important variable that explained the extreme variation of all the markers was whether the minor ultrasound findings were isolated or non-isolated, and most of the reported accuracy of minor ultrasound markers in the various studies was the result of the associated abnormalities in fetuses with non-isolated findings. The conclusions from this metaanalysis, however, are limited regarding the global use of ultrasound to modify risk assessment for aneuploidy, because the analysis only addressed minor ultrasound markers seen in isolation. Minor ultrasound markers seen in isolation were found not to be helpful in either confirming or excluding Down syndrome, with the exception of a thickened nuchal fold, which was associated with a 17-fold increased risk of Down syndrome [81].

Although the study raised much controversy in the ultrasound community, the conclusions regarding isolated sonographic markers are not a complete surprise. The management of an otherwise low-risk patient with an isolated ultrasound marker has long been and remains controversial. Risk modification for aneuploidy with the use of multiple ultrasound markers and the use of ultrasound markers in conjunction with major fetal structural abnormalities, biochemical screening, and maternal age are prudent [82]. A fundamental issue that is still in question is the assumption that maternal biochemical and sonographic markers are independent variables of aneuploidy risk assessment [82]. This assumption never has been proven, however [81], and only if these are independent screening variables can one be used accurately to change the risk based on the other [81].

The presence of a choroid plexus cyst (see Fig. 13) raises the risk for trisomy 18 but not Down syndrome [64]. The incidence of choroid plexus cyst in the general population is 1.4%, and the incidence of choroid plexus cyst in fetuses with Down syndrome is also 1.4% [64]. Choroid plexus cysts are seen in at least 25% to 30% of trisomy 18 fetuses [54,55]. Some authors report association of cyst size (> 1 cm) [83] and bilaterality [84] with a higher risk of trisomy 18, whereas other authors report no higher association with either cyst size or bilaterality [55,85]. Management of a previously low-risk patient with an isolated choroid plexus cyst is somewhat controversial. It is generally agreed that if an isolated choroid plexus cyst is identified at sonography, however, correlation with biochemical markers, maternal age,

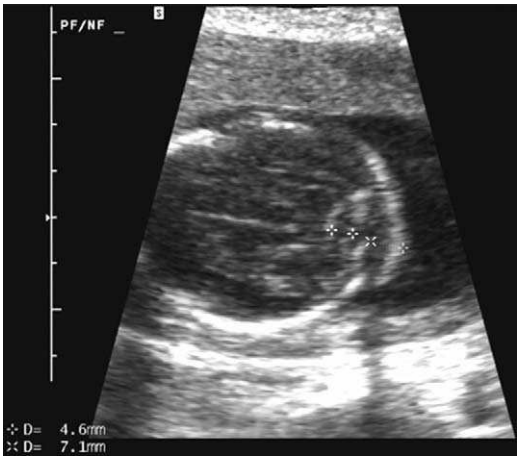

Fig. 8. Nuchal fold thickening at 19 weeks' gestation. Axial image through the posterior fossa and neck demonstrates a normal cisterna magna measurement (*electronic caliper "+"*) at 4.6 mm and an abnormally thickened nuchal fold at 7.1 mm (*electronic caliber "x"*).

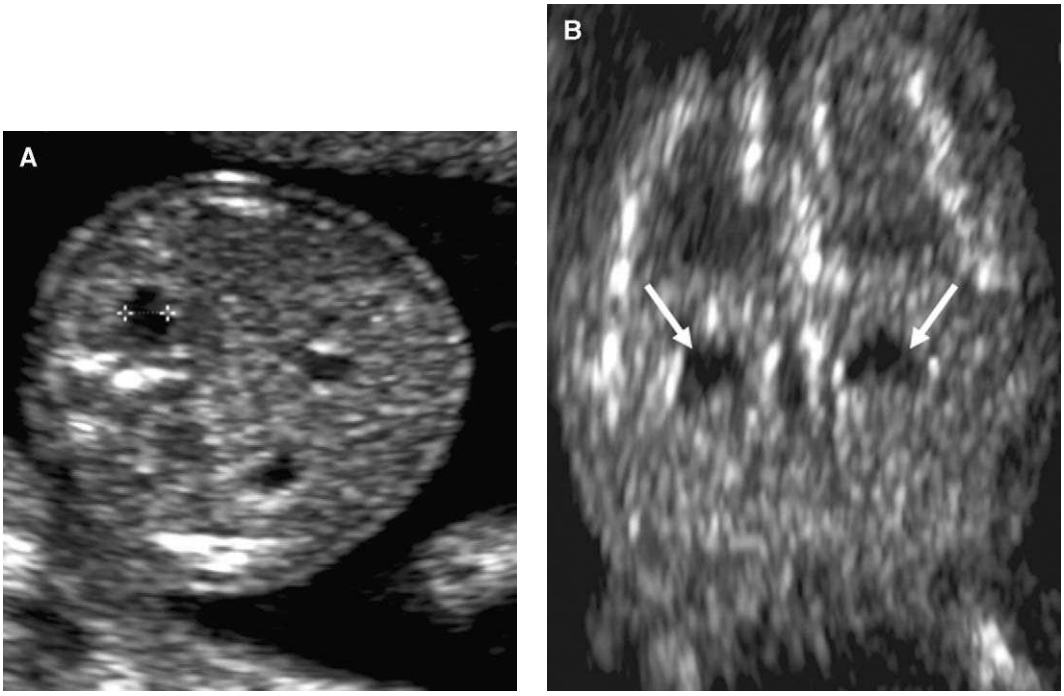

Fig. 9. Pyelectasis at 16 weeks' gestation. (*A*) In the axial image through the fetal kidneys, the anterior-to-posterior dimension is measured (*electronic "+"*) and was more than 4 mm bilaterally. (*B*) In the coronal image, the configuration is that of a dilated renal pelvis without caliectasis (*arrows*).

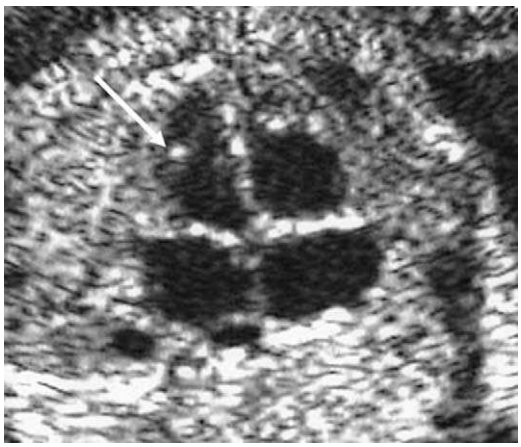

Fig. 10. Echogenic intracardiac focus at 22 weeks' gestation. There is a focal bright spot in the left cardiac ventricle (*arrow*) on the four-chamber view of the heart.

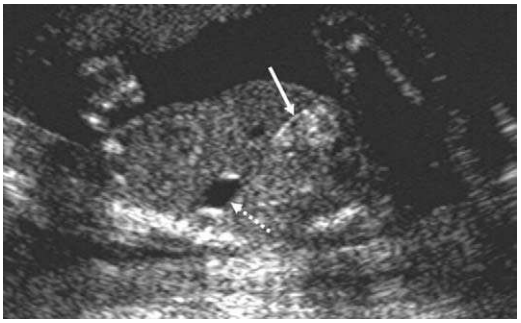

Fig. 11. Sagittal view of the fetal abdomen at 17 weeks' gestation demonstrates a focally hyperechoic area (*arrow*) in the expected location of the fetal bowel. (Dashed arrow = stomach.)

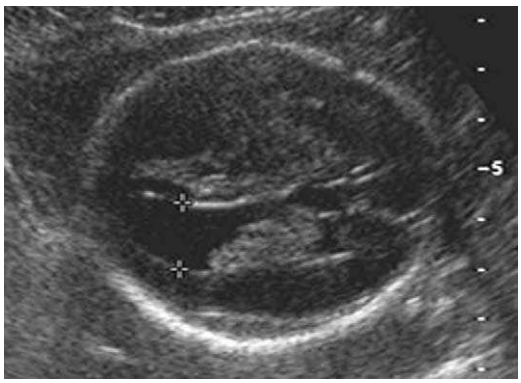

Fig. 12. Mild ventriculomegaly at 21 weeks' gestation. The ventricular atrium (*electronic calipers "+"*) measured 13 mm.

and other sonographic abnormalities is necessary to determine whether invasive testing should be offered [64,86,87].

First trimester screening

Maternal serum screening in the first trimester

Much work has been done on serum analyte testing in the first trimester for Down syndrome, but the results are controversial. The best analytes from 11 to 14 weeks are free beta-hCG and pregnancy-associated plasma protein A (PAPP-A) [88,89]. Affected Down syndrome pregnancies have a median-free beta-hCG of 1.79 MoM and a median PAPP-A of 0.43 MoM. The combination of maternal serum analyte results and maternal age gives a detection rate of 63% for Down syndrome (5.5% false-positive rate) [90], which is comparable to second trimester serum screening. The problem with these analytes is that free beta-hCG may not be higher in Down syndrome fetuses compared with euploid fetuses until 12 weeks' gestation, and PAPP-A loses its discrimination value after 13 weeks' gestation [91].

First trimester ultrasound evaluation

Nuchal translucency refers to the normal clear area in the fetal neck seen in early pregnancy that lies between the skin and the soft tissues overlying the cervical spine. Nuchal translucency should be measured with the fetus in a neutral position and in the sagittal plane. With magnification, the fetus should occupy at least three quarters of the image. Care should be taken to distinguish fetal skin from the amnion. The proper nuchal translucency measurement is the maximum thickness between the inner skin echo and the most posterior echo of the neck soft tissues (Fig. 14). Nuchal translucency is generally only used between 11 and 14 weeks' gestation. Ultrasound measurement of nuchal translucency has been shown to distinguish normal from abnormal gestations [92–94]. The combined use of nuchal translucency measurement and maternal age identifies 27% to 89% of Down syndrome pregnancies with a screen positive rate of 2.8% to 9.3% [91]. Nuchal translucency increases with gestational age [95]. Use of multiples of the median data (for gestational age) can help provide patient-specific risk when a nuchal translucency measurement is obtained.

A newer and promising phenomenon recently described by Cicero in the 11- to 14-week period is absent nasal bone ossification, which in preliminary

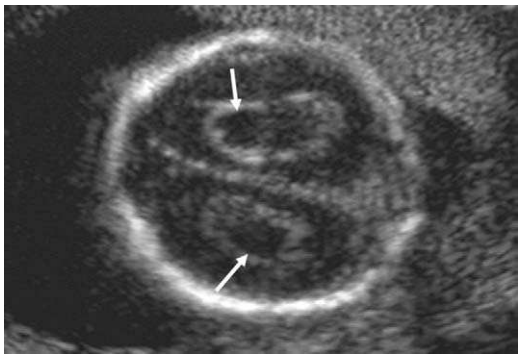

Fig. 13. Multiple, confluent choroid plexus cysts in a 16-week fetus with trisomy 18.

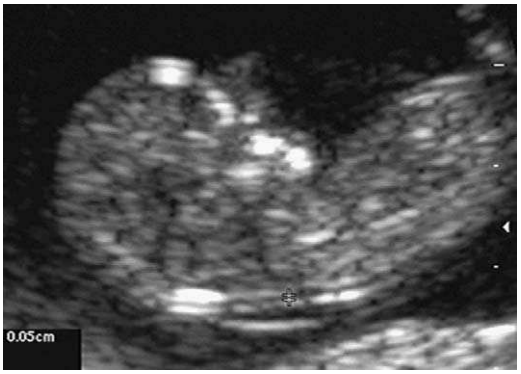

Fig. 14. First trimester gestation with nuchal fold measurement (*electronic calipers "+"*).

studies seems to have high specificity for Down syndrome [96].

Combined first trimester screening approach

The National Institutes of Health has funded a prospective, multicenter trial to evaluate first trimester screening that combines nuchal translucency measurements with biochemical markers and maternal age a priori risk, called the First and Second Trimester Evaluation of Risk trial. In this study, first trimester nuchal translucency measurement, PAPP-A and free beta-hCG levels, and maternal age are factored to determine risk for Down syndrome. In the second trimester, the same patients are reevaluated as a control. The second trimester evaluation consists of screening with the four serum analytes (free beta-hCG, alpha-fetoprotein, unconjugated estriol, and dimeric inhibin A) and maternal age to calculate risk of trisomy 21, trisomy 18, and neural tube defect. The results of this and other similar trials will determine how first trimester screening compares with second trimester screening and how first trimester screening is ultimately implemented in this country.

Summary

The value of all noninvasive prenatal tests must be viewed with the perspective of the consequences of invasive testing. Regarding second trimester noninvasive testing, biochemical screening is more accurate in establishing risk than maternal age alone. One or more major ultrasound abnormalities, nuchal thickening, or a shortened humerus should raise concern for Down syndrome regardless of the patient's a priori risk based on age or biochemical markers. Isolated minor ultrasound markers should not be used in calculating risk in low-risk patients regarding Down syndrome unless the biochemical profile already places the patient at risk or in a borderline risk zone. If the ultrasound finding is hyperechoic bowel, problems other than aneuploidy may be the cause, including cystic fibrosis, infection, or hemorrhage, and these problems must be considered if hyperechoic bowel is an isolated finding. Improved risk adjustment seems to be applicable to a priori high-risk patients with completely normal sonograms. Genetic sonograms with specific risk adjustment schemata may be used to adjust a priori risk (either maternal age or biochemical screening results) at centers in which this has proven to be accurate, but whether this is statistically sound remains to be determined. The goal of second trimester ultrasound screening is to identify at-risk fetuses better and offer invasive testing to a more select group of patients. As the value of first trimester screening becomes more evident and practical, and if the risk of chorionic villus sampling becomes an acceptable norm, the patient population that reaches the second trimester of pregnancy will be select. Therefore, we can anticipate that second trimester screening and invasive testing may be needed only in a minority of cases, and the practice standards of prenatal testing and sonography (including minor ultrasound markers) will change entirely.

References

[1] Hook EB, Cross PK, Schreinemachers DM. Chromosomal abnormality rates at amniocentesis and in live-born infants. JAMA 1983;249:2034–8.
[2] Gardner RJM, Sutherland GR. Prenatal diagnostic procedures. Oxford Monographs on Medical Genetics 1996;29:336–44.
[3] Shah YG, Eckl CJ, Stinson SK, Woods Jr JR. Biparietal diameter/femur length ratio, cephalic index, and femur length measurements: not reliable screening techniques for Down syndrome. Obstet Gynecol 1990; 75:186–8.
[4] Ventura SJ, Martin JA, Curtin SC, Mathews TJ, Park MM. Births: final data for 1998. Natl Vital Stat Rep 1998;48:1–100.
[5] Egan JFX, Benn P, Borgida AF, et al. Efficacy of screening for fetal Down syndrome in the United States from 1974 to 1997. Obstet Gynecol 2000;96:979–85.
[6] Prenatal Diagnosis of Fetal Chromosomal Abnormalities. ACOG Practice Bulletin 2001;27:1–12.
[7] Turnbull AC, MacKenzie IZ. Second-trimester amniocentesis and termination of pregnancy. Br Med Bull 1983;39:315–21.
[8] Golbus MS, Loughman WD, Ferrazi E. Prenatal genetic diagnosis in 3000 amniocenteses. N Engl J Med 1979;300:157–63.
[9] Hill LM, Platt LD, Kellogg B. Rh-sensitization after genetic amniocentesis. Obstet Gynecol 1980;56: 459–61.
[10] Amniocentesis Registry NICHD. Midtrimester amniocentesis for prenatal diagnosis: safety and accuracy. JAMA 1976;236:1471–80.
[11] Simpson JL, Socol ML, Aladjem S. Normal fetal growth despite persistent amniotic fluid leakage after genetic amniocentesis. Prenat Diagn 1981;1:277–9.
[12] Bianchi DW, Crombleholme TM, D'Alton ME. Prenatal diagnostic procedures. In: Fetology: diagnosis and management of the fetal patient. New York: McGraw-Hill; 2000. p. 11–33.
[13] Jackson LG, Zachary JM, Fowler SE, Desnick RJ, Golbus MS, Ledbetter DH. A randomized comparison

of transcervical and transabdominal chorionic-villus sampling. N Engl J Med 1992;327:594–8.
[14] Nicolaides K, Brizot ML, Patel F, Snijders R. Comparison of chorionic villus sampling and amniocentesis for fetal karyotyping at 10–13 weeks' gestation. Lancet 1994;344:435–9.
[15] Johnson JM, Wilson RD, Winsor EJ, Singer J, Dansereau J, Kalousek DK. The early amniocentesis study: a randomized clinical trial of early amniocentesis versus midtrimester amniocentesis. Fetal Diagn Ther 1996; 11:85–93.
[16] Sundberg K, Bang J, Smidt-Jensen S, Brocks V, Lundsteen C, Parner J. Randomised study of risk of fetal loss related to early amniocentesis versus chorionic villus sampling. Lancet 1997;350:697–703.
[17] Canadian Early and Mid-Trimester Amniocentesis Trial (CEMAT). Randomized trial to assess safety and fetal outcome of early and mid-trimester amniocentesis. Lancet 1998;351:242–7.
[18] Brambati B, Oldrini A, Ferrazi E, Lanzani A. Chorionic villus sampling: an analysis of the obstetric experience of 1,000 cases. Prenat Diagn 1987;7:157–69.
[19] Brambati B, Lanzani A, Oldrini A. Transabdominal chorionic villus sampling: clinical experience of 1159 cases. Prenat Diagn 1988;8:609–17.
[20] Canadian Collaborative CVS-Amniocentesis Clinical Trial Group. Multicentre randomised clinical trial of chorion villus sampling and amniocentesis: first report. Lancet 1989;1:1–6.
[21] Rhoads GG, Jackson LG, Schlesselman SE, de la Cruz FF, Desnick RJ, Golbus MS. The safety and efficacy of chorionic villus sampling for early prenatal diagnosis of cytogenetic abnormalities. N Engl J Med 1989;320: 609–17.
[22] Ledbetter DH, Martin AO, Verlinsky Y, Pergament E, Jackson L, Yang-Feng T. Cytogenetic results of chorionic villus sampling: high success rate and diagnostic accuracy in the United States collaborative study. Am J Obstet Gynecol 1990;162:495–501.
[23] MRC Working Party on the Evaluation of Chorion Villus Sampling. Medical Research Council European trial of chorion villus sampling. Lancet 1991;337:1491–9.
[24] Kuliev A, Jackson L, Froster U, Brambuti B, Simpson JL, Verlinsky Y. Chorionic villus sampling safety: report of World Health Organization/EURO meeting in association with the Seventh International Conference on Early Prenatal Diagnosis of Genetic Diseases. Tel-Aviv, Israel, May 21, 1994. Am J Obstet Gynecol 1996;174:807–11.
[25] Holmes LG. Report of National Institute of Child Health and Human Development workshop on chorionic villus sampling and limb and other defects. October 20, 1992. Teratology 1993;48:7–13.
[26] Botto LD, Olney RS. Chorionic villus sampling and transverse digital deficiencies: evidence for anatomic and gestational-age specificity of the digital deficiencies in two studies. Am J Med Genet 1996; 62:173–8.
[27] Ghidini A, Sepulveda W, Lockwood CJ, Romero R. Complications of fetal blood sampling. Am J Obstet Gynecol 1993;168:1339–44.
[28] Cuckle HS, Wald NJ, Lindenbaum RH. Maternal serum alpha-fetoprotein measurement: a screening test for Down syndrome. Lancet 1984;1:926–9.
[29] Cuckle HS, Wald NJ, Thompson SG. Estimating a woman's risk of having a pregnancy associated with Down's syndrome using her age and serum alpha-fetoprotein level. Br J Obstet Gynaecol 1987;94:387–402.
[30] New England Regional Genetics Group Prenatal Collaborative Study of Down Syndrome Screening. Combining maternal serum alpha-fetoprotein measurements and age to screen for Down syndrome in pregnant women under age 35. Am J Obstet Gynecol 1989;160:575–81.
[31] Bogart MH, Pandian MR, Jones OW. Abnormal maternal serum chorionic gonadotropin levels in pregnancies with fetal chromosome abnormalities. Prenat Diagn 1987;7:623–30.
[32] Wald NJ, Cuckle HS, Densem JW, Nanchahal K, Canick JA, Haddow JE. Maternal serum unconjugated oestriol as an antenatal screening test for Down's syndrome. Br J Obstet Gynaecol 1988;95: 334–41.
[33] Wald NJ, Cuckle HS, Densem JW, Nanchahal K, Royston P, Chard T. Maternal serum screening for Down's syndrome in early pregnancy. BMJ 1988; 297:883–7.
[34] Haddow JE, Palomaki GE, Knight GJ, Williams J, Pulkkinen A, Canick JA. Prenatal screening for Down's syndrome with use of maternal serum markers. N Engl J Med 1992;327:588–93.
[35] Cheng EY, Luthy DA, Zebelman AM, Williams MA, Lieppman RE, Hickok DE. A prospective evaluation of a second-trimester screening test for fetal Down syndrome using maternal serum alpha-fetoprotein, hCG, and unconjugated estriol. Obstet Gynecol 1993;81: 72–7.
[36] Wenstrom KD, Williamson RA, Grant SS, Hudson JD, Getchell JP. Evaluation of multiple-marker screening for Down syndrome in a statewide population. Am J Obstet Gynecol 1993;169:793–7.
[37] Haddow JE, Palomaki GE, Knight GJ, Cunningham GC, Lustig LS, Boyd PA. Reducing the need for amniocentesis in women 35 years of age or older with serum markers for screening. N Engl J Med 1994;330: 1114–8.
[38] Canick JA, Palomaki GE, Osathanondh R. Prenatal screening for trisomy 18 in the second trimester. Prenat Diagn 1990;10:546–8.
[39] Greenberg F, Schmidt D, Darnule AT, Weyland BR, Rose E, Alpert E. Maternal serum alpha-fetoprotein, beta-human chorionic gonadotropin, and unconjugated estriol levels in midtrimester trisomy 18 pregnancies. Am J Obstet Gynecol 1992;166:1388–92.
[40] Palomaki GE, Haddow JE, Knight GJ, et al. Risk-based prenatal screening for trisomy 18 using alpha-fetoprotein, unconjugated oestriol and human chorionic gonadotropin. Prenat Diagn 1995;15:713–23.

[41] Yankowitz J, Fulton A, Williamson R, Grant SS, Budelier WT. Prospective evaluation of prenatal maternal serum screening for trisomy 18. Am J Obstet Gynecol 1998;178:446–50.
[42] Aitken DA, Wallace EM, Crossley JA, et al. Dimeric inhibin A as a marker for Down's syndrome in early pregnancy. N Engl J Med 1996;334:1231–6.
[43] Wenstrom KD, Chu DC, Owen J, Boots L. Maternal serum alpha-fetoprotein and dimeric inhibin A detect aneuploidies other than Down syndrome. Am J Obstet Gynecol 1998;179:966–70.
[44] Wenstrom KD, Owen J, Chu DC, Boots L. Prospective evaluation of free beta-subunit of human chorionic gonadotropin and dimeric inhibin A for aneuploidy detection. Am J Obstet Gynecol 1999;181:887–92.
[45] Wald NJ, Densem JW, George L, Muttukrishna S, Knight PG. Prenatal screening for Down's syndrome using inhibin-A as a serum marker. Prenat Diagn 1996;16:143–53.
[46] Williamson RA, Weiner CP, Patil S, Benda J, Varner MW, Abu-Yousef MM. Abnormal pregnancy sonogram: selective indications for fetal karyotype. Obstet Gynecol 1987;69:15–20.
[47] Wladimiroff JW, Sachs ES, Reuss A, Stewart PA, Pijpers L, Niermeijer MF. Prenatal diagnosis of chromosome abnormalities in the presence of fetal structural defects. Am J Med Genet 1988;29:289–91.
[48] Jones KL. Smith's recognizable patterns of human malformation. 5th edition. Philadelphia: WB Saunders; 1997.
[49] Balcar I, Grant DC, Miller WA, Bieber FA. Antenatal detection of Down syndrome by sonography. AJR Am J Roentgenol 1984;143:29–30.
[50] Nyberg DA, Resta RG, Luthy DA, Hickok DE, Mahony BS, Hirsch JH. Prenatal sonographic findings of Down syndrome: review of 94 cases. Obstet Gynecol 1990;76:370–7.
[51] Paladini D, Calabro R, Palmieri S, D'Andrea T. Prenatal diagnosis of congenital heart disease and fetal karyotyping. Obstet Gynecol 1993;81:679–82.
[52] DeVore GR, Alfi O. The use of color Doppler ultrasound to identify fetuses at increase risk for trisomy 21: an alternative for high-risk patients who decline genetic amniocentesis. Obstet Gynecol 1995;85:378–86.
[53] Rotmensch S, Liberati M, Bronshtein M, et al. Prenatal sonographic findings in 187 fetuses with Down syndrome. Prenat Diagn 1997;17:1001–9.
[54] Nyberg DA, Kramer D, Resta RG, et al. Prenatal sonographic findings in trisomy 18: review of 47 cases. J Ultrasound Med 1993;2:103–13.
[55] Benacerraf BR, Harlow B, Frigoletto FD. Are choroid plexus cysts an indication for second-trimester amniocentesis? Am J Obstet Gynecol 1990;162:1001–6.
[56] Lehman CD, Nyberg DA, Winter III TC, Kapur RP, Resta RG, Luthy DA. Trisomy 13 syndrome: prenatal US findings in a review of 33 cases. Radiology 1995; 194:217–22.
[57] Rabinow M, Spisso K, Buschi AJ, Brenbridge AN. Turner syndrome: sonography showing fetal hydrops simulating hydramnios. AJR AM J Roentgenol 1980; 135:846–8.
[58] Chervenak FA, Isaacson G, Blakermore KJ, et al. Fetal cystic hygroma: cause and natural history. N Engl J Med 1983;309:822–5.
[59] Garden AS, Benzie RJ, Miskin M, Gardner HA. Fetal cystic hygroma colli: antenatal diagnosis, significance and management. Am J Obstet Gynecol 1986;154: 221–5.
[60] Linden MG, Bender BG, Robinson A. Intrauterine diagnosis of sex chromosome aneuploidy. Obstet Gynecol 1996;87:468–75.
[61] Lockwood C, Scioscia A, Stiller R, Hobbins J. Sonographic features of the triploid fetus. Am J Obstet Gynecol 1987;156:285–7.
[62] Jauniaux E, Brown R, Rodeck C, Nicolaides KH. Prenatal diagnosis of triploidy during the second trimester of pregnancy. Obstet Gynecol 1996;88:983–9.
[63] Rubenstein JB, Swayne LC, Dise CA, Gersen SL, Schwartz JR, Risk A. Placental changes in fetal triploidy syndrome. J Ultrasound Med 1986;5:545–50.
[64] Bromley B, Lieberman E, Benacerraf BR. Choroid plexus cysts: not associated with Down syndrome. Ultrasound Obstet Gynecol 1996;8:232–5.
[65] Benacerraf BR, Neuberg D, Bromley B, Frigoletto Jr F. Sonographic scoring index for prenatal detection of chromosomal abnormalities. J Ultrasound Med 1992; 11:449–58.
[66] Benacerraf BR, Nadel AS, Bromley B. Identification of second-trimester fetuses with autosomal trisomy by use of a sonographic scoring index. Radiology 1994; 193:135–40.
[67] Bromley B, Lieberman E, Benacerraf BR. The incorporation of maternal age into the sonographic scoring index for the detection at 14–20 weeks of fetuses with Down's syndrome. Ultrasound Obstet Gynecol 1997; 10:321–4.
[68] Bromley B, Shipp T, Benacerraf BR. Genetic sonogram scoring index: accuracy and clinical utility. J Ultrasound Med 1999;13:523–8.
[69] Bromley B, Shipp T, Benacerraf BR. Genetic sonogram scoring index: accuracy and clinical utility [erratum]. J Ultrasound Med 1999;18:594.
[70] Nyberg DA, Luthy DA, Resta RG, Nyberg BC, Williams MA. Age-adjusted ultrasound risk assessment for fetal Down's syndrome during the second trimester: description of the method and analysis of 142 cases. Ultrasound Obstet Gynecol 1998;12:8–14.
[71] Nyberg DA, Souter VL, El-Bastawissi A, Young S, Luthhardt F, Luthy DA. Isolated sonographic markers for detection of fetal Down syndrome in the second trimester of pregnancy. J Ultrasound Med 2001;20: 1053–63.
[72] Bromley B, Lieberman E, Shipp TD, Benacerraf BR. The genetic sonogram: a method of risk assessment for Down syndrome in the second trimester. J Ultrasound Med 2002;21:1087–96.
[73] Sohl BD, Scioscia AL, Budorick NE, Moore TR. Utility of minor ultrasonographic markers in the prediction

of abnormal fetal karyotype at a prenatal diagnostic center. Am J Obstet Gynecol 1999;18:898–903.
[74] Vintzileos AM, Egan JFX. Adjusting the risk for trisomy 21 on the basis of second-trimester ultrasonography. Am J Obstet Gynecol 1995;172:837–44.
[75] Vintzileos AM, Campbell WA, Guzman ER, Smulian DA, McLean DA, Anath CV. Second-trimester ultrasound markers for detection of trisomy 21: which markers are best? Obstet Gynecol 1997;89:941–4.
[76] Vintzileos AM, Guzman ER, Smulian JC, Day-Salvatore DL, Knuppel RA. Indication-specific accuracy of second-trimester genetic ultrasonography for the detection of trisomy 21. Am J Obstet Gynecol 1999; 181:1045–8.
[77] Nyberg DA, Luthy DA, Cheng EY, Sheley RC, Resta RG, Williams MA. Role of prenatal ultrasonography in women with positive screen for Down syndrome on the basis of maternal serum markers. Am J Obstet Gynecol 1995;173:1030–5.
[78] Vergani P, Locatelli A, Piccoli MG, et al. Best second trimester sonographic markers for the detection of trisomy 21. J Ultrasound Med 1999;18:469–73.
[79] Bahado-Singh RO, Deren O, Oz U, et al. An alternative for women initially declining genetic amniocentesis: individual Down syndrome odds on the basis of maternal age and multiple ultrasonographic markers. Am J Obstet Gynecol 1998;179:514–9.
[80] Filly RA. Obstetric sonography: the best way to terrify a pregnant woman. J Ultrasound Med 2002;19:1–5.
[81] Smith-Bindman R, Hosmer W, Feldstein VA, Deeks JJ, Goldberg JD. Second-trimester ultrasound to detect fetuses with Down syndrome: a meta-analysis. JAMA 2001;285:1044–55.
[82] Nyberg DA, Souter VL. Sonographic markers of fetal trisomies: second trimester. J Ultrasound Med 2001;20: 655–74.
[83] Twining P, Succolo J, Clewes J, Swallow J. Fetal choroid plexus cysts: a prospective study and review of the literature. Br J Radiol 1991;64:98–102.
[84] Hertzberg BS, Kay HH, Bowie JD. Fetal choroid plexus lesions: relationship of antenatal sonographic appearance to clinical outcome. J Ultrasound Med 1989;8:77–82.
[85] Gupta JK, Cave M, Lilford RJ, et al. Clinical significance of fetal choroid plexus cysts. Lancet 1995;346: 724–9.
[86] Gratton RJ, Hogge WA, Aston CE. Choroid plexus cysts and trisomy 18: risk modification based on maternal age and multiple-marker screening. Am J Obstet Gynecol 1996;175:1493–7.
[87] Reinsch RC. Choroid plexus cysts: association with trisomy. Prospective review of 16,059 patients. Am J Obstet Gynecol 1997;176:1381–3.
[88] Wald NJ, George L, Smith D, Densem JW, Peterson K. Serum screening for Down's syndrome between 8 and 14 weeks of pregnancy. International Prenatal Screening Research Group. Br J Obstet Gynaecol 1996;103: 407–12.
[89] Haddow JE, Palomaki GE, Knight GJ, Williams J, Miller WA, Johnson A. Screening of maternal serum for fetal Down's syndrome in the first trimester. N Engl J Med 1998;338:955–61.
[90] Canick JA, Kellner LH, Saller JD, Palomaki GE, Walker RP, Osathanondh R. Second-trimester levels of maternal urinary gonadotropin peptide in Down syndrome pregnancy. Prenat Diagn 1998;15:739–44.
[91] Wald NJ, Kennard A, Hackshaw A, McGuire A. Antenatal screening for Down's syndrome. Health Technol Assess 1998;2:1–112.
[92] Snijders RJM, Noble P, Sebire N, Souka A, Nicolaides KH. UK multicentre project on assessment of risk of trisomy 21 by maternal age and fetal nuchal-translucency thickness at 10–14 weeks of gestation. Lancet 1998;352:343–6.
[93] Pajkrt E, Bilardo CM, Van Lith JM, Mol BW, Bleker OP. Nuchal translucency measurement in normal fetuses. Obstet Gynecol 1995;86:994–7.
[94] Pajkrt E, Van Lith JM, Mol BW, Bleker OP, Bilardo CM. Screening for Down's syndrome by fetal nuchal translucency measurement in a general obstetric population. Ultrasound Obstet Gynecol 1998;12: 163–9.
[95] Pandya PP, Brizot ML, Kuhn P, Snijders RJM, Nicolaides KH. First-trimester fetal nuchal translucency thickness and risk for trisomies. Obstet Gynecol 2002;84:420–3.
[96] Cicero S, Curcio P, Papageorghiou A, Sonek J, Nicolaides K. Absence of nasal bone in fetuses with trisomy 21 at 11–14 weeks of gestation: an observational study. Lancet 2001;358:1665–7.

RADIOLOGIC
CLINICS OF
NORTH AMERICA

Radiol Clin N Am 41 (2003) 709–727

Complications of monochorionic twins

Vickie A. Feldstein, MD*, Roy A. Filly, MD

Department of Radiology and of Obstetrics, Gynecology and Reproductive Sciences, University of California, San Francisco, Medical Center, Box 0628, 505 Parnassus Avenue, Room L-374, San Francisco, CA 94143-0628, USA

Morbidity and mortality are significantly increased in twin gestations compared with singleton pregnancies [1]. Among twin pregnancies, the relative risk of complications depends on whether each fetus is attached to its own placenta (dichorionic [DC]) or must share a placenta (monochorionic [MC]). The relative increase in risk of MC compared with DC twin pregnancies is of a magnitude similar to that of twin compared with singleton pregnancies. MC twins have a higher prevalence of growth retardation and death compared with DC twins, and several unique and threatening syndromes occur only in MC gestations [2]. The high risks of MC twin gestations are largely related to the vascular anatomy of the shared placenta and the presence of intertwin vascular connections. These anastomoses are implicated in twin-twin transfusion syndrome (TTTS) and co-twin sequelae after intrauterine demise of one twin. Only MC twins can be monoamniotic. If the fetuses share a placenta and an amniotic cavity, they face a high risk of mortality [3,4].

The identification of a MC twin pregnancy has important obstetric implications, some of which influence pregnancy management and limit certain treatment options. The sonographic examination of all twin pregnancies should include a specific effort to determine chorionicity and amnionicity [5]. Before considering the sonographic features useful in the prediction of chorionicity and amnionicity, it is helpful to review the embryology of placentation in twin pregnancies.

* Corresponding author.
E-mail address: Vickie.Feldstein@radiology.ucsf.edu (V.A. Feldstein).

Embryology of twin placentation

Twin pregnancies result either from fertilization of two ova (dizygotic) or from fertilization of a single ovum with subsequent cleavage (monozygotic). Dizygotic twins are more common (70%) than monozygotic twins (30%). All dizygotic twins have DC placentation, and all DC twins are diamniotic. Monozygotic twins may be either DC (25%) or MC (75%) depending on the embryologic stage at which cleavage occurs [6].

Unfortunately, two discrete placentas cannot always be identified, even on gross pathologic inspection after the birth of DC twins. Occasionally, two developing placental masses abut and fuse; therefore, a single placental mass is identified.

For monozygotic twins, the stage at which cleavage occurs determines the chorionicity and amnionicity of the pregnancy. Dichorionicity occurs in approximately 25% of monozygotic twins. For monozygotic twins to be DC, division must occur before the fourth day after fertilization. If division occurs between the fourth and eighth days after fertilization (the blastocyst has formed, but the amnion is not yet developed), then MC diamniotic twins result. This occurs in approximately 75% of MZ twin pregnancies.

Rarely, cleavage occurs after the eighth day after fertilization—after the chorion and the amnion already have formed—and the twins share not only a placenta but also a single amniotic cavity (monoamniotic). If division occurs after formation of the amnion, the structure that cleaves is the embryonic disc. If division of the embryonic disc is incomplete, various degrees of twin conjoining result.

Knowledge of the embryologic sequence is important in understanding the imaging manifestations

0033-8389/03/$ – see front matter © 2003 Elsevier Inc. All rights reserved.
doi:10.1016/S0033-8389(03)00046-0

of twin placentation, amnion formation, and some of the unique syndromes seen in twins. Because all dizygotic twins result from the implantation of two blastocysts, all such twins must be DC. Only monozygotic twins can have MC placentation. Because placental formation precedes amnion formation, all DC twins are also diamniotic. Conversely, all monoamniotic twins must be MC, and all conjoined twins also must be monoamniotic and MC. No other embryologic possibilities can occur.

Judging chorionicity and amnionicity by sonography

Dizygotic twins are the more common twin type, and all have DC placentation [1]. 25% of monozygotic twins also are DC. Approximately half of DC placentas are fused along their border, and it may not be possible to identify two discrete placental masses. The sensitivity of sonographic visualization of two placentas in detecting dichorionicity is low; however, when two placentas are seen, dichorionicity can be predicted reliably (Table 1) (Fig. 1) [7].

Similarly, if a membrane is identified separating the twins, diamnionicity can be predicted. In 90% of diamniotic pregnancies, a separating membrane can be identified sonographically [8]. The visualization of a membrane permits accurate prediction of diamnionicity, but the inability to identify a membrane that separates the fetuses of a twin pregnancy is insufficient evidence to diagnose a monoamniotic twin pregnancy.

If a single placental mass is identified sonographically, it is uncertain whether the placenta is DC (fused) or MC. The next and simplest step to take in this circumstance is to determine fetal gender (see Table 1). If one can show convincingly that one of the twins is male and the other is female, then dizygocity is confirmed and dichorionicity and diamnionicity may be inferred with certainty (Fig. 2). Unfortunately, if a single placental mass is seen and the twins are of the same gender, zygosity remains uncertain and chorionicity cannot be predicted.

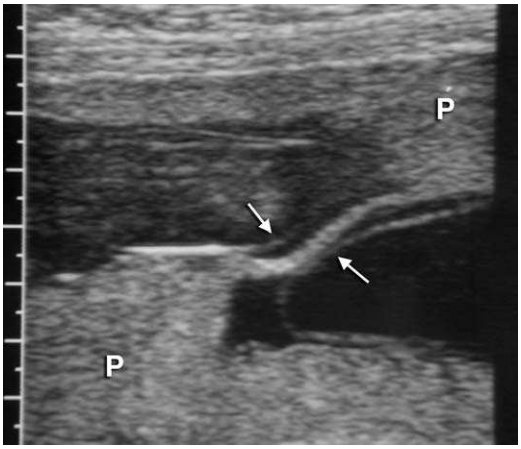

Fig. 1. Dichorionic twin pregnancy. Placental tissue (P) is seen anterior and posterior. The amniotic and chorionic layers have not yet fused; thus, the layers of the dichorionic diamniotic intertwin membrane are visible (*arrows*).

The membrane that separates the twins consists of two layers of amnion in a MC diamniotic twin pregnancy, whereas two layers of amnion plus two layers of chorion separate the twins in a fused, DC

Table 1
Sonographic prediction of chorionicity and amnionicity

	Sonographic findings		Clinical/pathologic findings	
Placental masses	Membrane	Twin genders	Chorionicity amnionicity	Zygosity
2	Yes	Differ	DC/DA	DZ
2	Yes	Same	DC/DA	Either
1	Yes	Differ	DC*/DA	DZ
1	Yes	Same	DC*/DA	Either
			MC/DA	
	Thick[a]		DC*/DA	Either
	Thin[a]		MC/DA	MZ
1	Not seen	Same	Uncertain	Either
	(Stuck twin[b])		MC/DA	MZ
	(Entangled cord)		MC/MA	MZ

Abbreviations: DC, dichorionic placentation (nonfused); DA, diamniotic; DZ, dizygotic; DC*, dichorionic placentation (fused); MC, monochorionic placentation; MA, monoamniotic; MZ, monozygotic.

[a] For membrane thickness, probability of correct prediction is highest early in pregnancy.

[b] Membrane present, although it may not be seen.

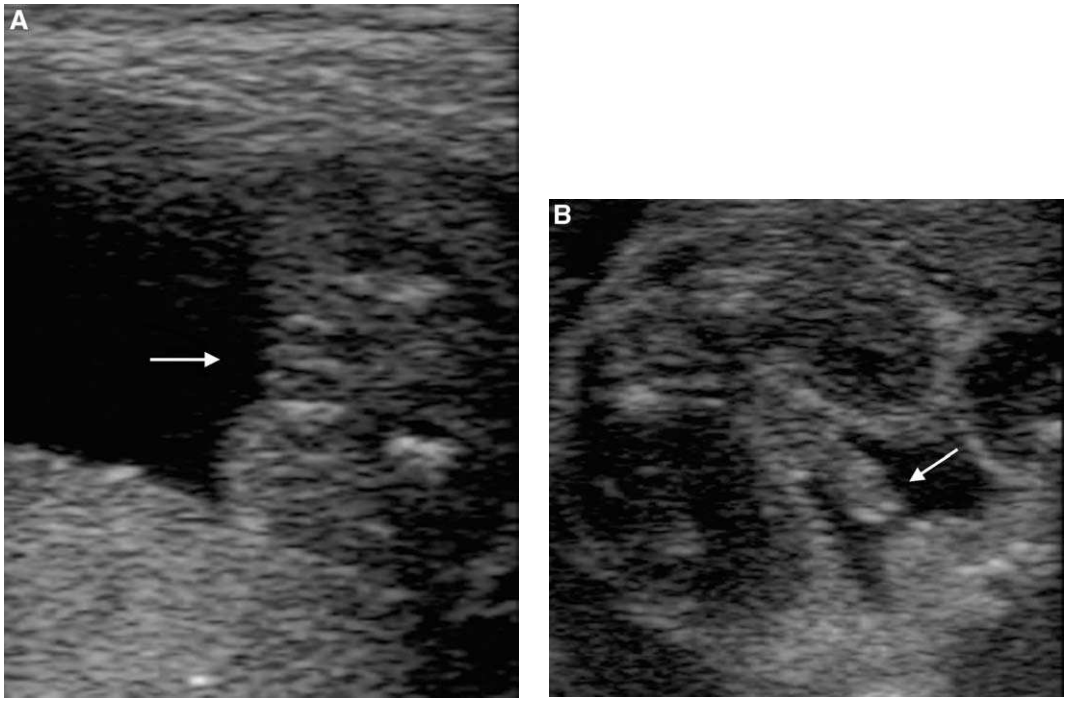

Fig. 2. (*A*) This twin is female. (*B*) This twin is male. This is a dizygotic—and necessarily dichorionic—diamniotic twin pregnancy.

diamniotic twin pregnancy. Because of the additional layers, the DC membrane is thicker than the MC membrane. It is theoretically and practically possible to determine chorionicity on the basis of the thickness of the visualized membrane (Fig. 3) [7,8]. One of the weaknesses of the membrane thickness approach is the lack of a strict definition regarding what constitutes a thick versus a thin membrane. With increasing gestational age, membranes also become progressively thinner in appearance. Judgment of

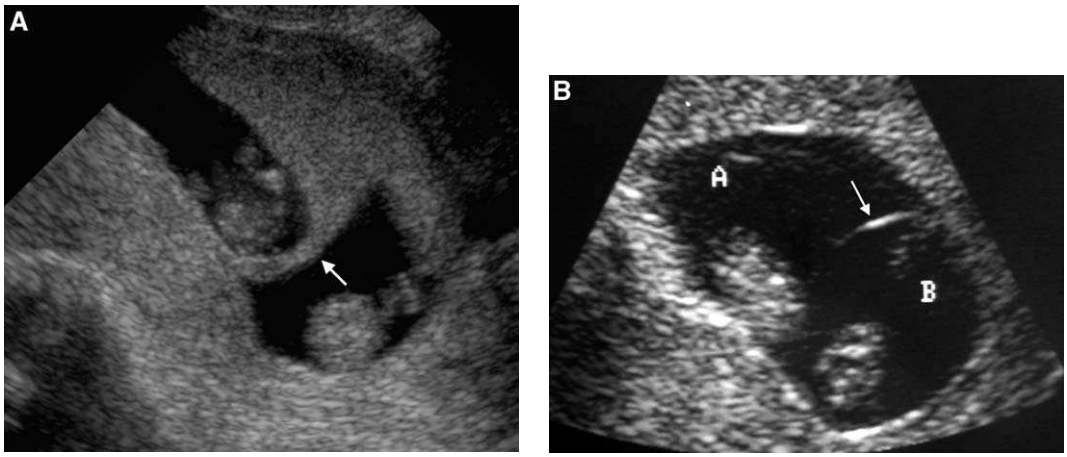

Fig. 3. First trimester obstetric sonograms with comparison of membrane thickness. (*A*) In this case, a thick membrane (*arrow*) is seen, which indicates dichorionic—and therefore diamniotic—gestation. (*B*) In comparison, a thin intertwin membrane (*arrow*) is seen in this monochorionic diamniotic pregnancy. This thin membrane represents two opposing layers of amnion.

membrane thickness is always more accurate early in pregnancy.

Although in some cases of MC diamniotic pregnancy a membrane may not be visualized because it is thin and wispy, in others it is not visualized because of its close apposition to the fetus in one amniotic sac. This is caused by an abnormal volume of amniotic fluid within the sac. This important phenomenon is discussed in greater detail later.

The membrane that separates a DC placenta contains fused chorionic leaves. Because chorion is contained in the membrane, it is possible for chorionic villi to grow into the junction of the membrane with the fused placental masses. This phenomenon creates a distinctive appearance of the membrane base, which Finberg has dubbed the "twin peak" sign (Fig. 4) [9]. Like other membrane-related signs of fused DC placentation, this sonographic feature, when present, is most useful early in pregnancy.

Recently, the accuracy of antenatal prediction of chorionicity in twin pregnancies was reported [10]. Antenatal chorionicity was determined using the number of placental masses, the presence or absence of a twin peak sign, and fetal gender. Chorionicity was correctly determined in 95% of cases (91% of the MC and 96% of the DC pregnancies). If chorionicity was assessed before 14 weeks' gestation, the correct diagnosis was made in all except one case. Determination of chorionicity and amnionicity is important, is most reliable when done early in pregnancy, and should be addressed in the initial sonographic examination of all twin pregnancies.

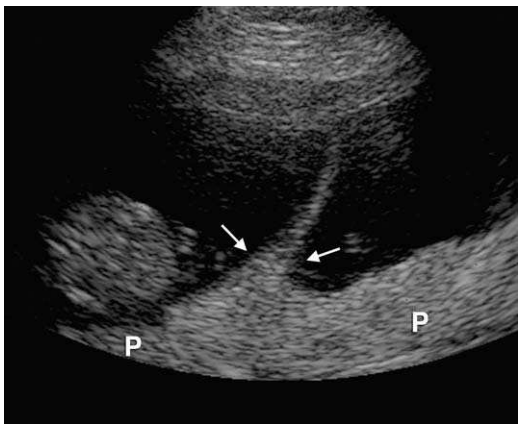

Fig. 4. Fused placental masses (P) in a posterior monochorionic diamniotic twin pregnancy. Triangular wedge of chorionic tissue is shown protruding into the base of the intertwin membrane (*arrows*), referred to as the "twin peak" sign.

Monochorionic twin syndromes

Determining that twins are MC is important because of the extraordinary unique risk inherent in such pregnancies. When twins are MC, the probability is high (85%–100%) that the fetuses share vascular anastomoses at the placental level [3,11,12]. The high risks of MC twin gestations are largely related to the vascular anatomy of the shared placenta and the presence of intertwin vascular connections. These anastomoses are implicated in several syndromes, which can complicate MC pregnancies and are discussed in detail later.

Placental vascular anatomy

Almost all MC placentas demonstrate intertwin vascular connections on postpartum placental injection studies (Fig. 5) [11–13]. Three types of intertwin vascular connections can occur. Arterio-arterial (A-A) anastomoses are frequent, direct, end-to-end connections on the placental surface. They do not communicate with the placental parenchyma. A-A anastomoses are present in 75% of MC placentas, and there is seldom more that one such connection per placenta. Detection of A-A anastomoses by means of Doppler ultrasound (US) findings has been reported [14]. A-A anastomoses are confirmed by means of characteristic bidirectional pulsatile spectral Doppler waveforms (Fig. 6). The demonstration of an A-A anastomosis indicates, with certainty, monochorionicity. Veno-venous anastomoses that are seen in approximately 5% of MC placentas, and have not been detected by US, also are direct end-to-end connections coursing on the fetal surface of the placenta.

Arteriovenous (AV) anastomoses are a common form of intertwin vascular connection and are implicated as a causative mechanism in the development of TTTS. AV anastomoses occur deep within the placental parenchyma and do not manifest abnormal pathognomonic spectral Doppler waveforms. However, based on observations made at post-partum placental injection studies, the characteristic anatomic configuration of AV anastomoses has been delineated. Normally, in singleton and twin gestations, an artery and a vein are paired and are found along the fetal surface of the placenta, emanating from and returning to the fetal cord insertion site. An AV anastomosis is referred to as a deep connection for it is within the placental parenchyma, and not via a direct superficial connection on the surface of the placenta, that blood passes from an arterial branch of one twin, across the capillary bed of the cotyledon, into a draining venous branch of the other twin. Placental injection studies

have shown that the feeding arterial and draining venous components of an AV anastomosis approach each other along the placental surface "unpaired." They abut "nose to nose" on the surface where they dive through a common foramen to supply blood to and drain blood from a single shared cotyledon (Fig. 7). They are distinguished from a normal artery/vein pair not by unusual blood flow patterns or spectral Doppler waveforms, but by their distinctive anatomic configuration [15,16] (Fig. 8).

Unequal placental sharing

Detailed US examination of twin pregnancies should include biometric assessment and determination of estimated fetal weight (EFW). It is helpful to calculate the percent discordance [(larger EFW - smaller EFW)/larger EFW × 100] between MC twins. Discordance is often caused by unequal parenchymal sharing of the placenta, with one twin having a marginal/velamentous cord insertion and a small parenchymal share, while the larger twin has a more central cord insertion [17] (Fig. 9). The smaller twin may be growth restricted and develop oligohydramnios, but this condition should not be diagnosed as TTTS. US assessment of placental sharing may be gleaned by demonstrating the cord insertion sites into the placenta (Fig. 10). Discordant twins, without evidence of TTTS, warrant close surveillance, but rarely is therapeutic intervention indicated.

Twin-twin transfusion syndrome

Twin-twin transfusion syndrome results from intrauterine vascular shunting between the circulations of twins who share a placenta, and it is the most common complication of MC twinning, occurring in approximately 10% to 20% of MC twin pregnancies [2,12,13,18]. Via intertwin vascular connections, blood is transfused from the donor, who becomes growth restricted and develops oligohydramnios, to the recipient, who develops circulatory overload and responds with polyuria, which results in polyhydramnios. The sonographic demonstration of oligohydramnios/polyhydramnios in a MC twin pair is indicative of TTTS (Fig. 11) [19]. Often, but not always, there is also discordance in fetal size between the smaller donor and larger recipient twin. The difference in fetal size is often, at least in part, a reflection of unequal placental sharing. The donor twin often has a velamentous, marginal, or eccentric cord insertion site, and the recipient has a more central one [20]. It is important to remember that normal amniotic fluid volume in one sac and abnormal (increased or decreased) amniotic fluid volume in the co-twin sac can be the result of many causes, but is not a manifestation of TTTS. Concomitant oligohydramnios and polyhydramnios in a MC twin pair are the requisite sonographic findings for the diagnosis of TTTS (Fig. 12).

It is critically important to be as certain as possible that twins are MC before the diagnosis of TTTS is suggested. If sonographic findings confirm dichorionicity because of different genders of the twins, the ability to identify two placental masses, early confirmation of two gestational sacs, the "twin peak" sign, or a thick membrane, then a diagnosis of TTTS should not be made, regardless of other features that may suggest it.

In addition to monochorionicity, other sonographic findings must be present before TTTS can be diagnosed [18,19]. There is a discrepancy in volume status and urine production between the twins; the recipient often has a distended bladder and the donor has a small or—in some cases—not visible urinary bladder, despite the presence of kidneys. As a result, there is a visible disparity in the amount of amniotic fluid surrounding each twin. This condition is often accompanied by significant disparity in the size of the twins. Most often, one twin (the recipient) is normal sized or nearly so and the other (the donor) is small and commonly satisfies the established criteria for intrauterine growth retardation. Alternatively, the predicted weight of the smaller twin may not be less than the tenth percentile for gestational age but may be discordantly small compared with the larger twin.

With TTTS, the disparity in the volume of amniotic fluid can progress to extremes, in which one twin is in a markedly polyhydramniotic sac and the other is in a virtually anhydramniotic sac. The appearance of this extreme disparity has come to be known as the "stuck twin" sign [21,22]. The "stuck twin" phenomenon originally was described within the context of proving diamnionicity when no membrane was sonographically visible. One fetus of a twin pair moved freely within a normal or increased amount of amniotic fluid, but the other fetus resided in a position adjacent to the lateral or anterior uterine wall (Fig. 13). Changes in position of the pregnant woman failed to show an appropriate gravitational response by the "stuck twin," which indicated that the fetus was held in place by an unapparent membrane. Once convinced that the fetus is being held in place by a membrane, searching the margins of the fetus often discloses the membrane (Fig. 14). Since its original description, it has been noted that the "stuck twin" phenomenon occurs most commonly with TTTS.

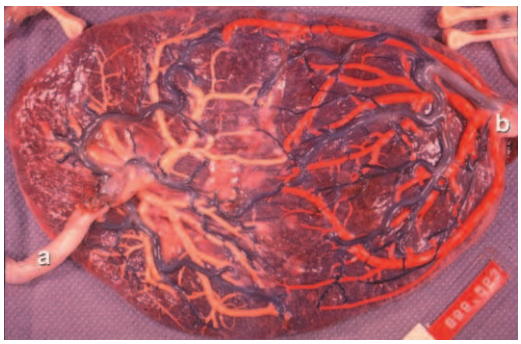

Fig. 5. Postpartum placental injection specimen from a monochorionic pregnancy. The vessels within the umbilical cord of each twin (a, b) are cannulated and injected with dye. This specimen shows multiple vascular connections between the twins' circulations.

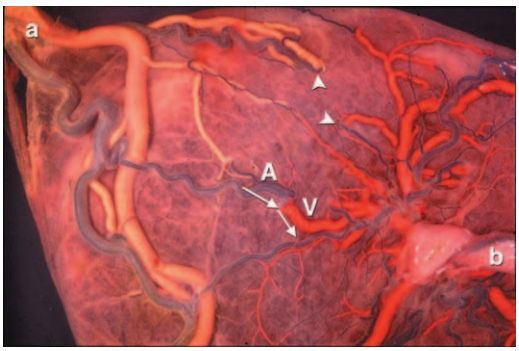

Fig. 7. This monochorionic twin placental vascular injection study shows an arteriovenous anastomosis with blood flow in the direction of the arrows, from donor (A) to recipient (b). The arterial (A) and venous (V) limbs of this anastomosis have a characteristic configuration. Also shown are normal arterial/venous pairs for each twin (*arrowheads*).

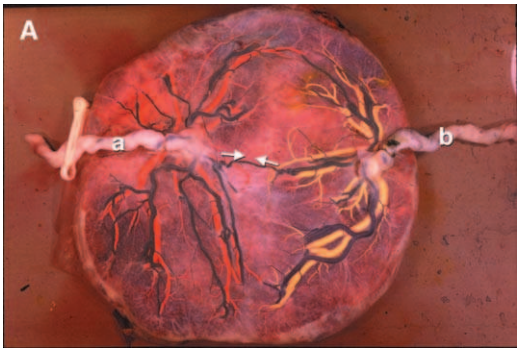

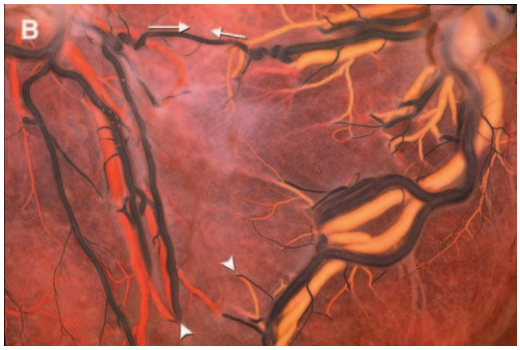

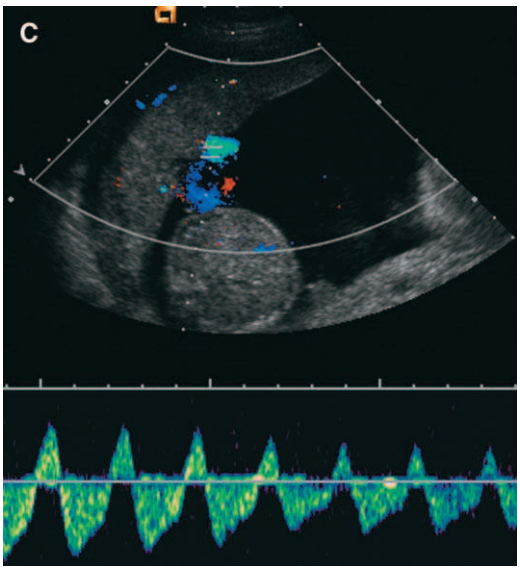

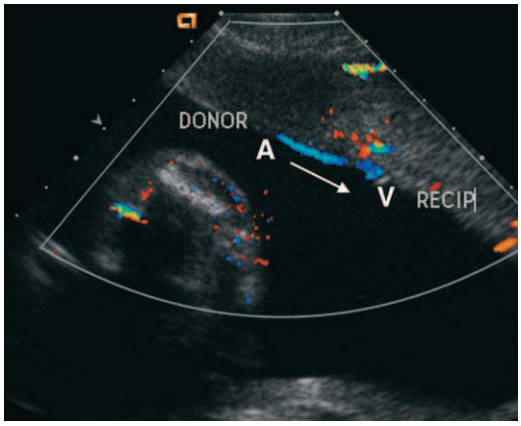

Fig. 8. Color Doppler sonogram of an arteriovenous anastomosis with flow in the direction of the arrows. There is pulsatile flow in the afferent arterial limb (A) from the donor and continuous monophasic flow in the efferent venous limb (V) toward the recipient.

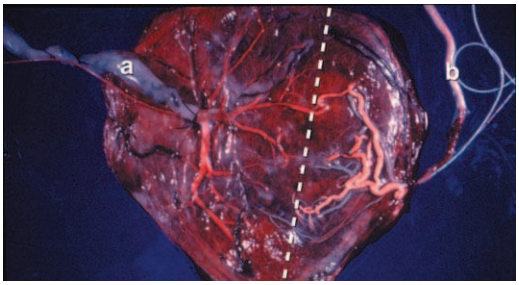

Fig. 9. Unequal placental sharing. Twin A (a) has a large cord that is centrally inserted into the shared monochorionic placenta. Twin B (b) has a small cord with a velamentous insertion and small placental share. The dotted line delineates the placental equator, which roughly defines the placental territory perfused by each twin. Intertwin vascular connections occur at this level and cross this plane.

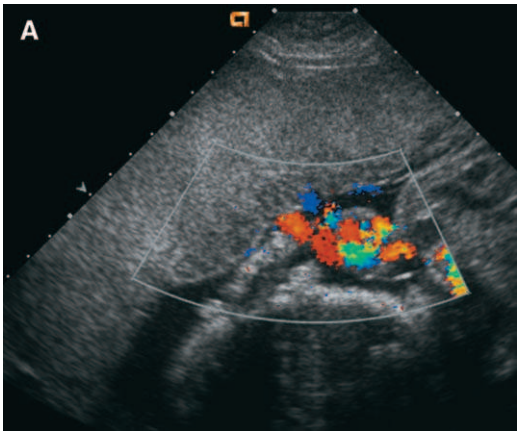

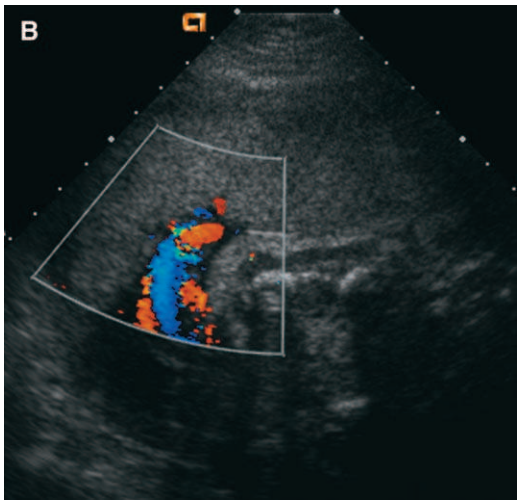

Fig. 10. Color Doppler sonograms show cord insertion sites into the shared anterior monochorionic placenta. (*A*) Central cord insertion site for this twin. (*B*) Eccentric, almost marginal cord insertion site at the lateral aspect of the placenta for this twin.

Fig. 6. (*A*) Overview and (*B*) close-up photograph of an injection study of a monochorionic placenta. The umbilical cord of each twin (a, b) was injected. Their vascular connections include a superficial arterio-arterial anastomosis on the placental surface, with flow in the direction shown (*arrows*). Also shown are examples of normal arterial/venous pairs for each twin (*arrowheads*). (*C*) Spectral Doppler waveform of an arterio-arterial anastomosis with characteristic bidirectional pulsatile flow.

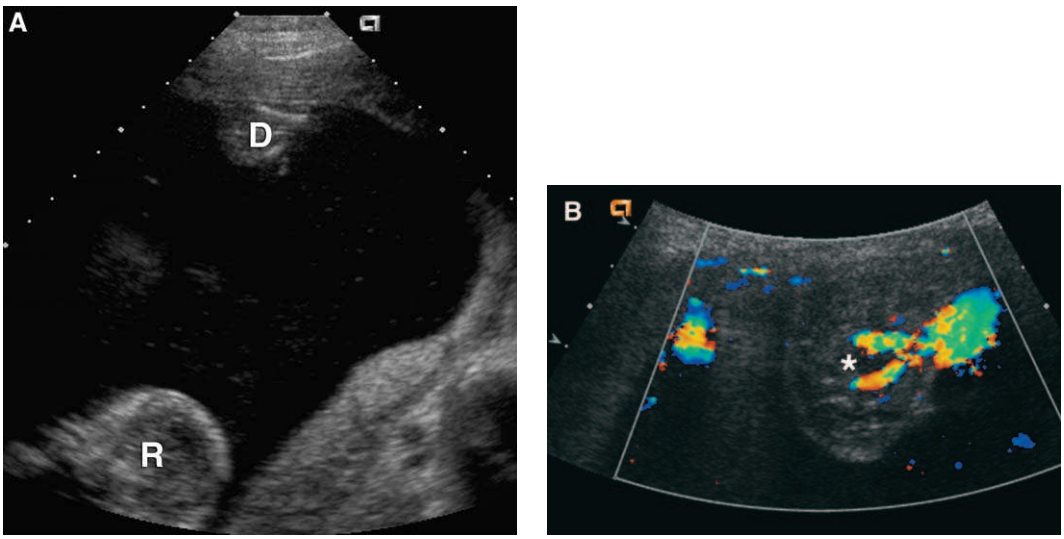

Fig. 13. (*A*) Severe twin-twin transfusion syndrome. There is marked polyhydramnios of the recipient twin (R) and marked oligohydramnios of the donor twin (D), which appears "stuck" adjacent to the anterior uterine wall. (*B*) Color Doppler sonogram through the pelvis of the stuck twin shows flow in the umbilical arteries, flanking an empty urinary bladder (*).

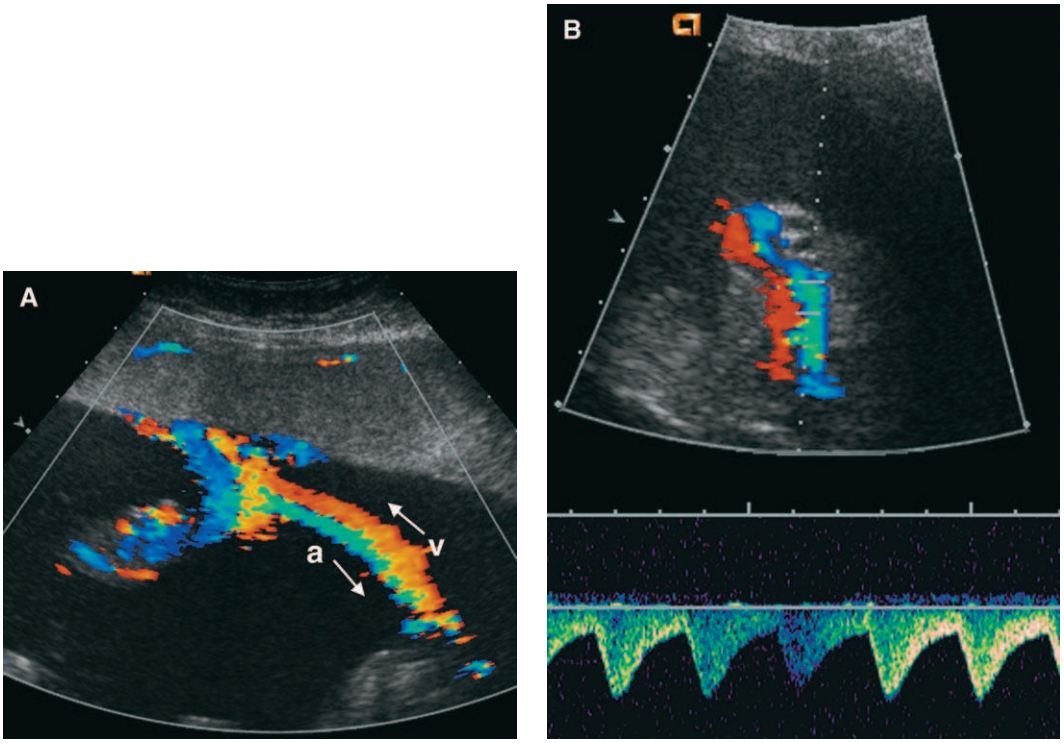

Fig. 17. Twin reversed arterial perfusion sequence. (*A*) Color Doppler sonogram shows close proximity of the two umbilical cord insertion sites at the shared anterior placenta. Flow direction (*arrow*) within the umbilical artery (a) of the acardiac twin is reversed. (*B*) Reversed umbilical arterial blood flow, away from the placenta and toward the abdomen, is shown on spectral Doppler interrogation of the acardiac twin.

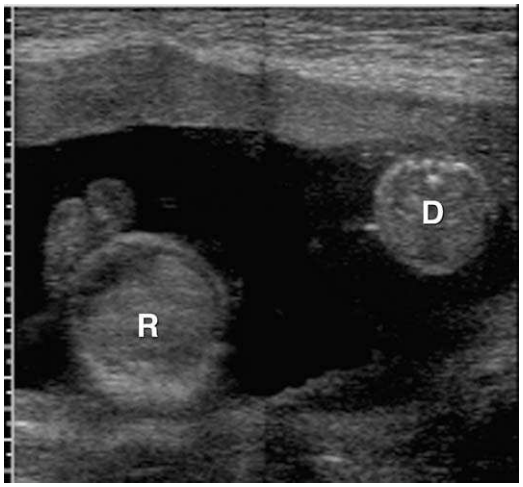

Fig. 11. Twin-twin transfusion syndrome. There is oligohydramnios of the donor (D), which is "stuck" in the nondependent portion of the uterus, and polyhydramnios of the recipient (R) in this monochorionic twin pair.

Wide variation in the manifestations of TTTS, including the gestational age at presentation, acuity of onset, and severity, has been observed, probably reflecting the particular vascular anatomy, which is unique in each case. Researchers have theorized that the occurrence, range in manifestations, and course of TTTS in MC twin gestations relates to the particular intertwin vascular connections within the shared placenta. Several studies have revealed that the angioarchitecture of the MC placenta is related to and responsible for the development of TTTS, the response to treatment, and the outcome [23–28].

Twin-twin transfusion syndrome results from net transfusion across an AV connection, from donor to recipient, in the MC placenta [11,13]. Most MC placentas demonstrate complicated anatomy with multiple bidirectional connections, including A-A anastomoses that prevent net transfusion. If transfusion via an AV anastomosis is not compensated by other vascular connections, which allow for return of blood from recipient to donor, TTTS develops. The median number of anastomoses in placentas from pregnancies with TTTS is significantly less than in placentas without TTTS. The anastomoses in the TTTS group are significantly more likely to be of AV than superficial (A-A or veno-venous) type [25]. The absence of an A-A anastomosis is associated with a greater risk of developing TTTS, and the presence of an A-A anastomosis is protective [23,25–28]. TTTS was diagnosed in 58% of pregnancies in which no A-A anastomoses were detected, compared with 5% in which an A-A anastomosis was found [23]. In the rare instances in which TTTS develops despite the presence of an A-A anastomosis, better outcomes have been reported [25–28]. This information about placental vascular anatomy can be used to understand the variability of pregnancies complicated by TTTS and may help explain the difference in response to therapy.

Twin-twin transfusion syndrome is a progressive disorder with reported fetal mortality rate of more than 90% if not treated. Without treatment, the recipient twin may decompensate and develop hydrops (Fig. 15). TTTS is associated with a high risk of miscarriage, perinatal death, and subsequent morbidity that involves multiple organ systems in survivors [29]. Donor and recipient twins are at risk. Morbidity among survivors may include cardiac, renal, and serious neurologic impairment, especially if there is in utero death of the co-twin [30]. Clinical management of pregnancies complicated by TTTS is one of the most difficult problems in obstetric practice, and there is ongoing controversy regarding this issue. Because of the high morbidity and mortality rates for this complicated condition, various aggressive and unusual therapies have been tried. The options for obstetric management include pregnancy termination, amnioreduction, septostomy, selective fetal termination and, most recently, laser coagulation of placental vessels.

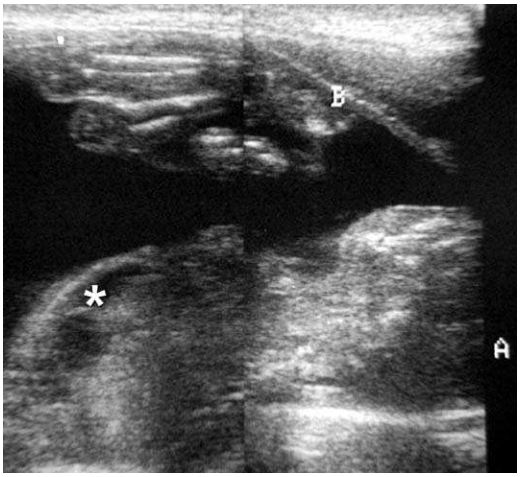

Fig. 12. Twin-twin transfusion syndrome shown on a dual-array sonogram. The donor twin (B) is located anteriorly within an oligohydramniotic sac, and the recipient twin (A) is dependent within a polyhydramniotic sac. The recipient is hydropic, with ascites (*).

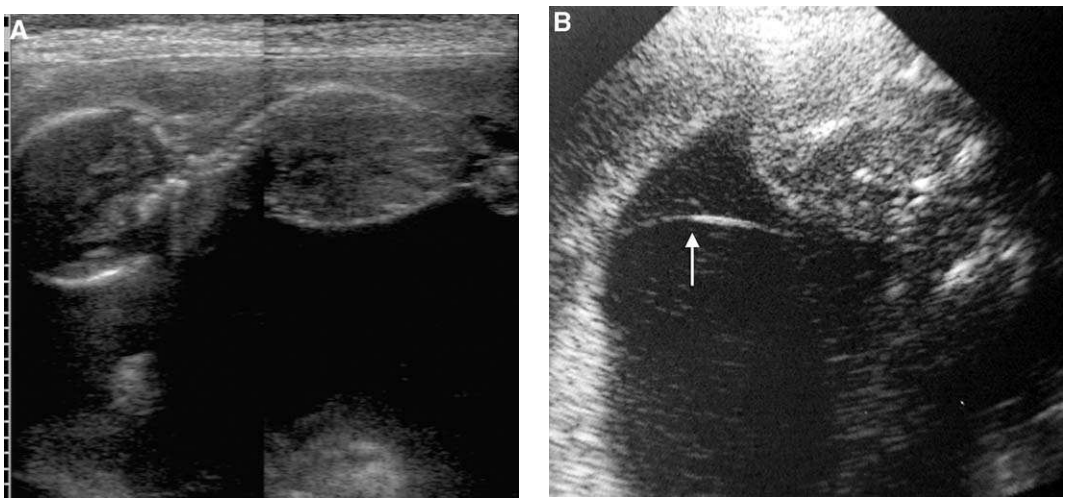

Fig. 14. (*A*) The donor twin in this case of twin-twin transfusion syndrome is "stuck" within an anhydramniotic sac, closely adherent to the anterior uterine wall. (*B*) Careful sonographic evaluation along the margins of the stuck donor twin reveals a thin intertwin membrane (*arrow*) in this monochorionic diamniotic gestation.

Some cases of TTTS respond to serial, large-volume amniocenteses of the polyhydramniotic sac, and an overall survival rate of 50% to 60% has been reported with this technique [31–34]. The mechanism by which large-volume amnioreduction works is not well understood. Some cases have demonstrated dramatic response after amnioreduction, with demonstration of increased urine production and filling of the donor bladder on short-interval (approximately 24-hour) follow-up US (Fig. 16). The presence of improved fluid volume within the donor sac with continued empty donor bladder may be seen as a result of intentional or inadvertent septostomy. The presence of a well-visualized donor bladder can be considered a manifestation of "response" to amnioreduction, however. Such response has been reported to be associated with an improved outcome for both twins [35]. In one series, the reaccumulation of urine in the bladder of the "stuck" twin after amniocentesis was a predictive prognostic marker of survival in both twins, with sensitivity and specificity rates of 100% [36]. Researchers have suggested that this response results from the presence of compensatory connections which allow for blood to return from recipient to donor, in addition to at least one causative AV anastomosis. The returning flow may be improved as a result of the amnioreduction procedure. In some cases, however, no such response is seen, and alternate therapy could be considered for these twins.

Laser photocoagulation of the placental vascular anastomoses has been advocated by several authors as

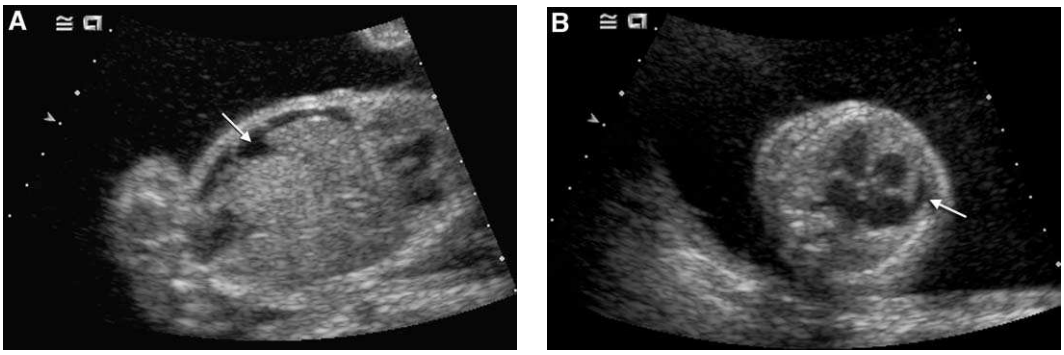

Fig. 15. Twin-twin transfusion syndrome with hydrops of the recipient twin. (*A*) Coronal sonogram through the abdomen reveals ascites (*arrow*). (*B*) Transverse image through the chest shows an enlarged heart with a small pericardial effusion (*arrow*).

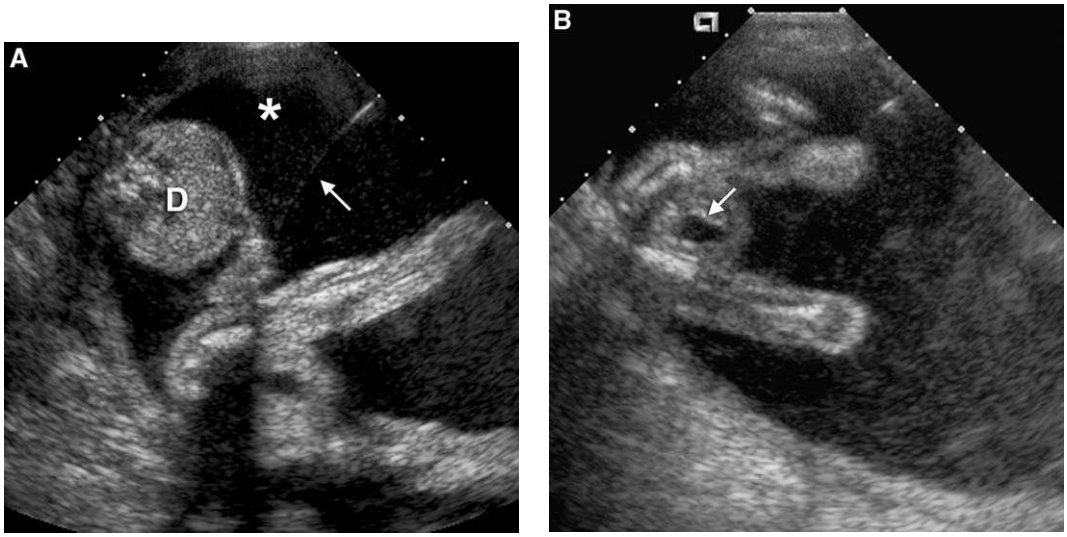

Fig. 16. (*A*) After large volume amnioreduction for twin-twin transfusion syndrome, fluid (*) is seen within the amniotic sac of the donor twin (D). The thin intertwin membrane is visible (*arrow*). (*B*) Urine is seen within the donor bladder (*arrow*). Before the procedure, the donor twin had appeared ''stuck'' with an empty bladder.

a more direct, definitive therapy that targets the causative mechanism [37–42]. Some investigators elect to coagulate all vessels seen crossing the interfetal septum, whereas others aim to coagulate only the intertwin communicating vessels by distinguishing them at fetoscopy from appropriate arteriovenous pairs connected to only one twin [41,42].

There are ongoing trials and recent reports of outcomes from TTTS treated with amnioreduction compared with laser. In one series, the overall fetal survival rate was not significantly different between cases treated with fetoscopic laser coagulation compared with serial amniocenteses (61%, 89/146, verses 51%, 44/86; $P = 0.239$) [43]. Some reports of therapy for TTTS do not distinguish severity, or they use amnioreduction or laser photocoagulation exclusively. It is possible that neither therapy is optimal for all cases. These therapies perhaps should be viewed not as alternative or rival methods of treatment. Rather, it is postulated that the treatment algorithm should rely on careful sonographic assessment and observation of response to treatment in sequence. Large-volume amnioreduction can be used as a therapeutic maneuver and as a diagnostic one. If response is observed by US (if increase in size of donor bladder is observed 24 hours after amnioreduction), the pregnancy could be observed carefully with US surveillance. If there is no response to amnioreduction, it is postulated that compensatory returning vascular connections are absent or inadequate. For such pregnancies, selective laser photocoagulation of intertwin vascular connections with fetoscopic guidance may be of greatest need and benefit.

Significant potential complications of TTTS are fetal demise and brain pathology of survivors. Assessment also can include MR imaging of the fetal brain before and after intervention for TTTS. In utero MR imaging to assess for the presence of sonographically occult parenchymal brain injury also is particularly helpful if there has been demise of one of a MC twin pair. This application is discussed further in the following section on twin embolization syndrome. Because of the high mortality and frequently rapid onset of severe TTTS, a high index of suspicion is needed whenever a MC twin pair is identified. Even an apparent minor degree of fluid imbalance between the amniotic sacs is an indication for careful short-term sonographic follow-up.

Twin embolization syndrome

A rare complication of MC pregnancy follows the in utero demise of one twin [44–47]. Benirschke [3] noted a case of hydranencephaly, splenic infarction, and bilateral renal cortical necrosis in a surviving monozygotic twin in which the co-twin had died in utero. He theorized that the infarcted organs in the surviving twin resulted from transfusion of thromboplastin-rich blood from the dead twin to the live co-twin through the vascular anastomoses in the shared placenta. Researchers also have theorized that clot or detritus from the dead twin embolizes into the

circulation of the surviving twin. Alternatively, the cessation of cardiac activity and the loss of vascular tone in the dead co-twin may result in a large amount of blood volume entering the dead twin from the surviving twin. This extra volume may result in exsanguination or profound hypotension.

More recently, researchers have postulated that rather than actual embolization, the injury suffered by the surviving fetus after the in utero death of one of a MC twin pair results from a sudden change in placental vascular territory perfused by the still beating heart. The impact of co-twin demise and the likelihood of resultant injury to the survivor is likely related to the degree of placental sharing, the number and type of intertwin vascular connections, and the timing of demise. Bajoria et al studied the outcome for the surviving twin after intrauterine co-twin death [30]. For MC twins without TTTS, perinatal mortality was higher in the group with superficial A-A or veno-venous channels than the group with only multiple bidirectional AV anastomoses. In the MC twin pregnancies complicated by TTTS, however, perinatal outcome for the surviving twin depended on whether the recipient or the donor twin died first. Outcomes, including the presence of intracranial abnormalities at birth, were significantly worse if the recipient twin died first.

The damage to the surviving fetus is related, at least in part, to its gestational age at the time of death of the co-twin. Demise of the co-twin early in pregnancy results in atresia and tissue loss; demise later in pregnancy results in tissue infarction, probably as a result of hypoperfusion from hypotension and bradycardia. Rapidly proliferating organs, such as the growing brain, kidneys, and gut, seem to be particularly susceptible [48]. Brain lesions noted with this syndrome include hydranencephaly, porencephaly, cystic encephalomalacia, and ex vacuo hydrocephalus.

The prevalence of twin embolization syndrome in the setting of antepartum demise of one of a MC twin pair is not firmly established. When this syndrome occurs, however, the prognosis is grim. MR imaging has the potential to enhance the ability to identify brain abnormalities that may not be detectable by means of obstetric sonography [49–52]. Because MR imaging has a higher intrinsic sensitivity than US to tissue contrast, fetal MR imaging offers the potential to visualize subtle brain abnormalities.

This technology is of particular use in the evaluation of MC diamniotic twins. There is a high risk of neurologic handicap in survivors of TTTS and other complications of MC placentation, including twin embolization syndrome. The timing and cause of the brain injury suffered by MC twins with co-twin demise is not well known or understood. MRI can help assess for the presence of brain injury that resulted from in utero events, which may be occult by US.

It is likely that immediate injury is triggered by co-twin demise and that severe, irreversible damage has occurred by the time the imaging abnormalities are apparent. Outcomes are probably not improved by triggering immediate preterm delivery of the surviving fetus. Monitoring of MC pregnancies with a dead twin may enable recognition of characteristic structural defects in the survivor, however. Recognition of this syndrome is especially important for providing accurate counseling for parents about prognostic implications and anticipated poor outcome.

Acardiac parabiotic twin

Acardiac parabiotic twins can be seen only in MC pregnancies [53–55]. Although some acardiac twins have an anomalous heart, fundamentally what is seen is a fetus in utero who, without the aid of a functioning cardiac pump within its own torso, continues to grow progressively, albeit abnormally, during gestation. The co-twin, termed the ‘‘pump twin,’’ is providing the blood supply to its anomalous sibling.

Among the vascular communications, at the least an A-A and veno-venous communication must be present to complete the circuit. These large vascular communications are often seen along the placental surface that courses between the cord insertion sites, which are usually close in position. This circulatory connection allows for blood to bypass the placenta and perfuse the acardiac twin with ‘‘used’’ blood from the pump twin. Perfusion of the acardiac fetus depends entirely on the blood supplied by the pump through the vascular anastomoses at the placental level.

In the acardiac fetus, the direction of blood flow in the umbilical cord is reversed [54]. In the umbilical vein, flow is away from the fetus. Flow is toward the fetus and away from the placenta in the umbilical artery (Fig. 17). This occurs because the blood entering the body of the anomalous fetus is being pumped by the co-twin into the umbilical artery of the acardiac twin. This phenomenon has led to an alternative name for this rare, anomalous situation, the so-called twin reversed arterial perfusion sequence.

The acardiac parabiotic twin may share the same amniotic cavity with the co-twin, which places the pregnancy at additional risk of cord knotting, although these pregnancies are usually MC, diamniotic. A disparity usually exists in the distribution of fluid between the twins; the anomalous twin is in the sac that contains less amniotic fluid (usually oligohydramniotic). The anomalous twin sac may be anhy-

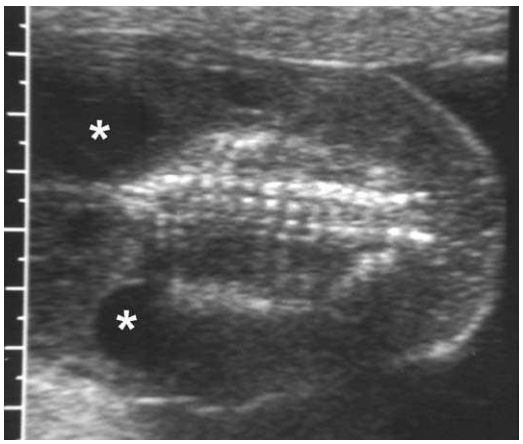

Fig. 18. Coronal sonogram of an acardiac parabiotic twin. There is no head. There is diffuse integumentary edema and cystic hygromas (*). No heart is present within the thorax.

dramniotic, with the acardiac twin apparently ''stuck'' to the uterine wall.

Acardiac fetuses have a relatively characteristic appearance (Fig. 18). Usually the fetus has no head, which leads to one of several synonyms for this entity, acardia acephaly. Anencephaly or severe microcephaly may be present, however. These fetuses tend to have diffuse integumentary edema, and nearly all have cystic hygromas. The upper extremities are either rudimentary or completely absent. The lower extremities are better formed, and the femur, which often appears normal in configuration, can be measured and growth is evident when serial examinations are done.

Usually, the thoracic region of the fetus is characterized by the absence of any visible cardiac pulsation. Doppler flow signals can be obtained in the umbilical cord, although the direction of flow is reversed. Diagnosis of twin reversed arterial perfusion requires recognition that an absent heart beat may mean an absent heart, not a heart that is not beating. On targeted Doppler US interrogation, reversed arterial flow direction, from the placenta up the cord toward the abdominal wall of the acardiac fetus, can be shown and is definitive.

Identification of this syndrome has important clinical implications. The anomalous fetus has no potential for survival. Unfortunately, there is substantial risk to the morphologically normal pump twin who is providing the blood supply to the anomalous fetus. The presence of an acardiac twin burdens the cardiac load of the pump twin. Hemodynamically, the fetus must circulate blood for its own body and for the body of the co-twin. Because it has the only beating heart, it is perfusing the entire placental territory. The mortality rate for the normal co-twin has been estimated at 50% [53]. The possible perinatal sequelae of acardiac twin gestations include cardiac failure of the pump twin, polyhydramnios, hydrops, preterm delivery, and in utero demise [55].

If the pump twin can be delivered successfully after a point of achieving viability, normal development can be anticipated. The likelihood that the normal fetus will die seems to be partly related to the size of the anomalous co-twin; the larger the anomalous co-twin, the more likely the pump twin will not survive. Sonographic factors cannot always reliably predict which pregnancies are at highest risk and are candidates for intervention before pump twin decompensation or demise. There is another concern about the possible risks faced by the pump twin. It is theorized that the pump twin is likely compromised by receiving into its circulation ''twice used'' blood, which bypasses placental cotyledons going to and returning from the acardiac twin.

The pump twin is at risk for high-output cardiac failure and may develop hydrops. In such cases, depending in part on gestational age, termination of the acardiac twin may be required in an effort to salvage the pump twin. The pump twin already perfuses the entire placental parenchyma, and there is no danger of sudden alteration in placental perfusion when the cord of the acardiac twin is selectively occluded. The treatment goal for this condition is to obliterate blood flow to the acardiac, nonviable fetus and protect the morphologically normal pump twin without threatening its viability. In the past, extraction of an acardiac parabiotic fetus was attempted, although this was not often successful and is no longer performed. More recently, several other techniques have been investigated with variable success.

A new minimally invasive percutaneous technique for selective reduction of the acardiac twin using radiofrequency ablation has been described and has been shown to be safe and effective [56]. Using real-time US guidance, the radiofrequency ablation device is inserted percutaneously into the mid-abdomen of the acardiac fetus at the level of the umbilical artery and vein and deployed (Fig. 19). Radiofrequency ablation is a high-energy technique that is known to be an efficacious modality for various clinical applications, most notably in treating malignant hepatic neoplasms. As the radiofrequency ablation device is deployed into tissue, energy is disbursed to the tines, which causes a coagulative effect. In this setting, the device avoids injury to the potentially viable pump twin by directing energy, only to the tissue of the acardiac twin in contact with the tines. Often, the acardiac twin is stuck within an oligohydramniotic

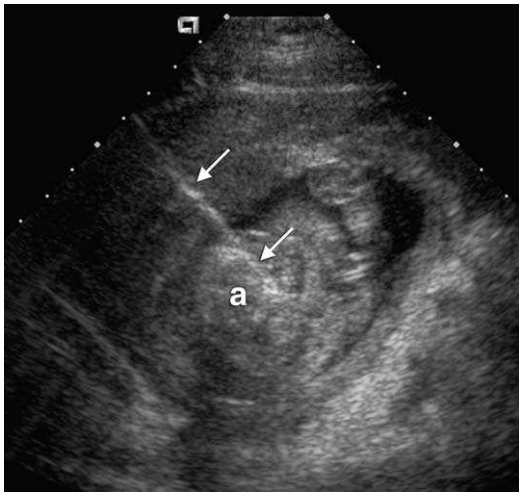

Fig. 19. Transabdominal intraoperative ultrasound image reveals the radiofrequency ablation device (*arrows*) deployed within the abdomen of the acardiac fetus (a).

sac of a diamniotic gestation and is located away from the potentially viable pump twin.

In twin pregnancies complicated by twin reversed arterial perfusion sequence, the beating heart of the pump twin already provides all of the circulation to and from the shared placenta and the acardiac twin. Obliteration of blood flow to the acardiac twin by radiofrequency ablation does not alter the placental circulation provided by the pump twin. Radiofrequency ablation with US guidance and other forms of selective, minimally invasive, percutaneous termination recently described seems to protect the pump twin effectively and improve outcome.

Twin reversed arterial perfusion sequence in acardiac MC twin gestations is a rare anomaly that compromises the viability of the morphologically normal, pump twin. At the least, careful monitoring of this highly anomalous situation is warranted to assess the normal co-twin for growth, development of hydrops fetalis, or other evidence of decompensation.

Discordant anomalies

Monozygotic twins are usually discordant for lethal major congenital anomalies. Although rare, a major structural abnormality may be detected in one of a MC twin pair, and the co-twin is usually spared. It is incorrect to assume that discordant malformed twins are dizygotic and therefore DC. A wide range of discordant abnormalities have been seen in MC twin pairs, including anencephaly and other neural tube defects, diffuse lymphangiectasia, and diaphragmatic hernia (Fig. 20) [11]. If the malformed twin is likely to die in utero or cause difficulties during pregnancy or delivery, selective fetal termination is considered.

If selective termination is considered, firm determination of the chorionicity of the gestation is essential to define fully the risks to the surviving twin. DC twins are not at risk, whereas MC twins are at risk for injury suffered at the time of co-twin

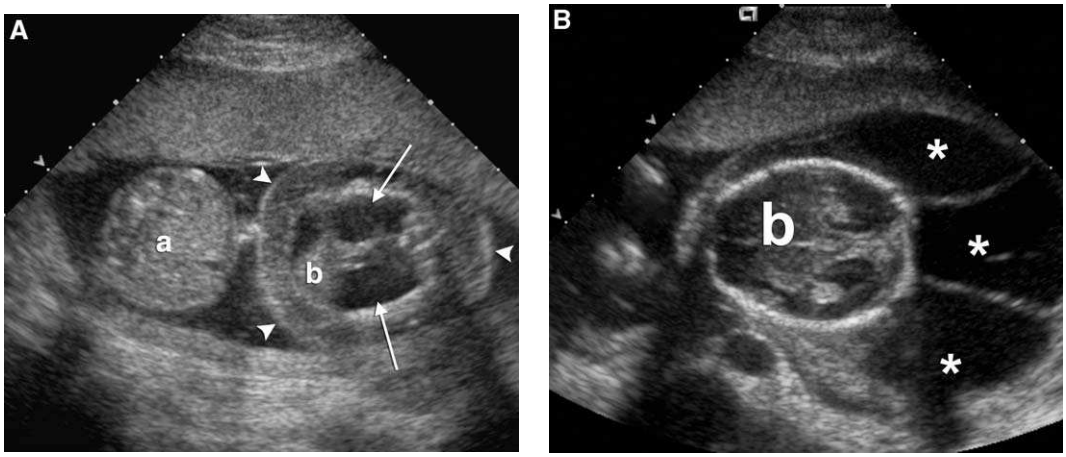

Fig. 20. Monochorionic twin pregnancy discordant for major anomaly. (*A*) Transverse sonogram through the abdomen of the normal twin (a) and the thorax of the affected twin (b). This is not a case of twin-twin transfusion syndrome or acardiac, parabiotic twin. Amniotic fluid volume was normal for each twin, and twin B was shown to have a beating heart with normal flow direction in its umbilical artery. Twin B has diffuse lymphangiectasia with integumentary edema (*arrowheads*) and bilateral pleural effusions (*arrows*). (*B*) On another image of twin B, multiple large cystic hygromas (*) are shown.

demise. In MC twin pregnancies with two living fetuses, each with a beating heart, both provide blood flow to and drain blood from a portion of the shared placenta. In almost all MC twin pregnancies, vascular communications at the placental level also connect the circulations of the twins [13]. When selective feticide is performed in the management of discordant lethal anomalies that affect one of a MC pair or in other situations, including TTTS, twin embolization syndrome should be considered as an additional risk to the surviving twin. Isolated ligation or occlusion of the cord of the anomalous fetus is risky. In some instances, depending on the degree of placental sharing and the type of interfetal vascular connections, attempts should be made first to separate the two circulations (eg, by means of selective laser occlusion at fetoscopy) before cord occlusion [57,58].

Conjoined twins

Conjoined twins are a rare malformation of monoamniotic twins; the estimated incidence is 1:50,000 to 1:100,000 births [59]. As with all pathologic events associated with monozygosity, conjoined twinning occurs sporadically. Conjoined twins develop from incomplete division of the embryonic disc. Division of the embryonic disc more than 13 days after fertilization is usually incomplete and results in fusion of the twins [6]. Most of these twins are born premature, and the mortality rate is high.

Prenatal diagnosis of conjoined twins and characterization of the severity of the malformations is desirable for optimal obstetric management [60]. Severe forms of conjoined twins diagnosed early can be offered termination via vaginal delivery. In late pregnancy, severity of conjoining influences predictions of viability and decisions regarding mode of delivery. Cesarean section is reserved for potentially viable and separable fetuses to minimize fetal morbidity and mortality and for conjoined twin configurations that obstruct labor.

The site and extent of twin fusion are highly variable. Classification systems for conjoined twins are based on the fused anatomic region. The name of the region usually is followed by the suffix *-pagus*, Greek for "fastened." For example, craniopagus is head-to-head fusion; thoracopagus is chest-to-chest fusion; omphalopagus is abdomen-to-abdomen fusion. These fusions are usually anterior-anterior and may involve more than one body region. The most common types of conjunction are thoracopagus, omphalopagus, and thoraco-omphalopagus twins. Side-to-side fusions usually begin at the head or buttock end and tend to be extensive. It is customary to name these large lateral fusions, which incorporate multiple regions, on the basis of the anatomic part that remains separate. For example, dicephalus means two heads with fusion of the thorax and abdomen (Fig. 21).

Prenatal sonographic diagnosis of conjoined twins may be straightforward: joining of fetal parts may be obvious; however, a careful approach is necessary to avoid misdiagnosis. The diagnosis should be considered only when a single placental site is seen and no separating amniotic membrane is demonstrated (no DC or diamniotic twin gestation can be conjoined). Significant sonographic findings include inability to detect separate fetal skin contours, appearance of both fetal heads persistently at the same level, no change

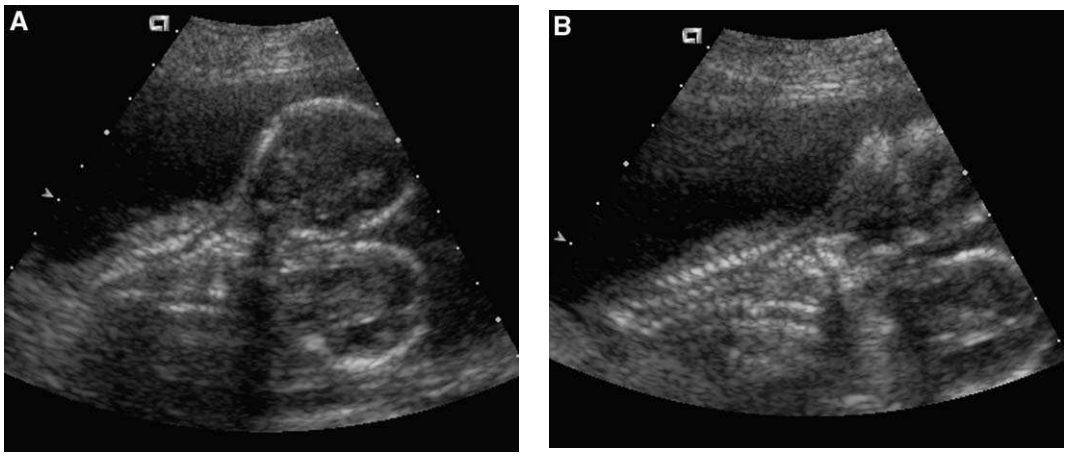

Fig. 21. (*A*, *B*) Conjoined twins: dicephalus. There is fusion of the thorax and abdomen, with separate calvaria and partially duplicated spines.

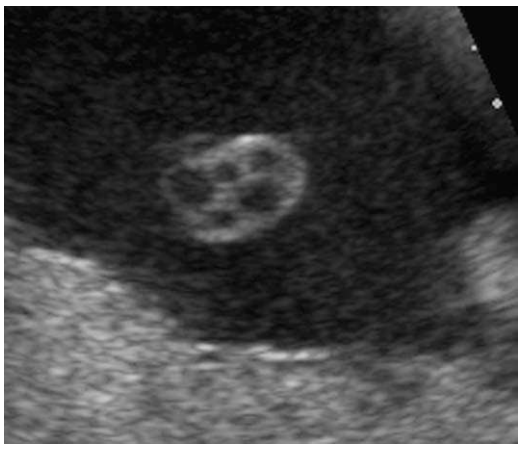

Fig. 22. A single five-vessel cord is identified in a case of conjoined twins.

in the relative position of the fetuses, bibreech position, and, less commonly, bicephalic presentation, backward flexion of the cervical spine, and a single umbilical cord with more than three vessels (Fig. 22). Other findings include shared heart, liver, brain, or other fetal organs [61].

Prenatal diagnosis of conjoined twins allows planned obstetric management, including decisions on approach for delivery and minimization of maternal and fetal morbidity and mortality. Precise delineation of the conjoining is important in determining the likelihood of postnatal viability, separability, and mode of delivery. The identification of a shared heart, in particular, carries a poor prognosis with essentially no hope for successful postnatal separation. Prenatally, sonography is the most definitive method for diagnosis and characterization of conjoining, thereby predicting chances for postnatal survival.

Monoamniotic twins

Sonographic identification of nonconjoined monoamniotic twin pregnancies is important prognostically and can affect obstetric management. MC monoamniotic twin pregnancies have the highest mortality rate of otherwise uncomplicated twin pregnancies [4]. This rate is related to a high frequency of complications present in all twin pregnancies (particularly preterm delivery) and complications that are unique to these gestations.

The lack of a membrane separating the twin fetuses in monoamniotic pregnancies distinguishes these pregnancies from all other twin pregnancies and potentially permits prenatal sonographic diagnosis. Studies have shown, however, that lack of sonographic visualization of a membrane does not, on its own, predict monoamnionicity [7,10].

Lack of a separating membrane between the fetuses allows the two umbilical cords to contact each other and become tangled. Because several loops of apparently intertwined umbilical cord may be either the entangled cords of two twins or only the redundant cord of a single twin folded on itself, it is essential to trace both fetal cords to the entangled mass before suggesting the diagnosis of monoamnionicity [62].

A complication that accounts for most of the increased mortality in monoamniotic twins is true knotting of the cords (Fig. 23) [63]. A true knot may cut off circulation and result in sudden fetal death, and it undoubtedly accounts for the high fetal loss rate observed in this group. This appearance is the basis for the diagnosis of monoamnionicity and is the only reliable feature for diagnosing this problem sonographically. If the cords of the twins are entangled, it can be inferred accurately that no membrane separates the fetuses. Intertwining of twin extremities is not reliable because the extremities can deform a separating membrane.

An important adjunct to the diagnosis of monoamniotic twins is the use of CT amniography. If within hours after a single US-guided intraamniotic injection of radiocontrast agent, it is swallowed and the contrast is seen in the intestinal tract of both fetuses, monoamnionicity is confirmed [64]. When monoamniotic nonconjoined twins are suspected but the sonographic findings are indeterminate, CT amniography is indicated.

The potential for umbilical cord entanglement does not exist in all monoamniotic twin pregnancies. All

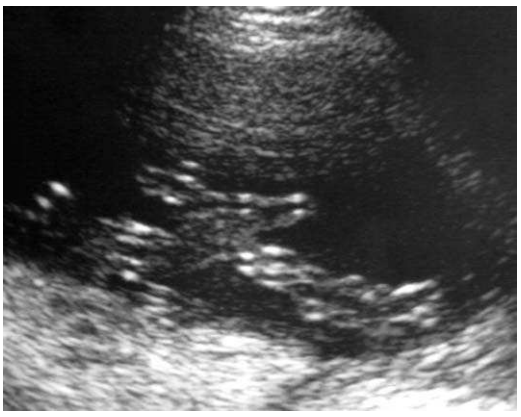

Fig. 23. Monoamniotic twin gestation with entangled umbilical cords shown by ultrasound.

conjoined twins are monoamniotic; however, such twins must move in unison. They cannot entangle their cords to form true cord knots in the same way that nonconjoined monoamniotic twins can. In many conjoined twins the umbilical cords are fused. The high mortality rate noted in conjoined twinning is unrelated to cord accidents caused by knotting.

It is unlikely that any form of monitoring is useful in predicting an acute cord accident that can result in the sudden demise of both fetuses in a nonconjoined monoamniotic pair. An unusual cord complication also may occur at the time of vaginal delivery of monoamniotic twins. The cord of the second twin unknowingly may be divided at the time of delivery of the first twin, if it is wrapped around the neck of the first twin. Accurate diagnosis of monoamnionicity before delivery could prevent such a mishap.

Foreknowledge that a twin pregnancy is monoamniotic is important and allows informed obstetric planning. Prenatal recognition of monoamnionicity dictates cesarean delivery, usually performed preterm.

Summary

Sonography has made a dramatic impact on the obstetric management of complicated twin pregnancies. This is based in part on the ability to use prenatal US to diagnose syndromes and complications of MC twinning. All twin pregnancies are at high risk for perinatal morbidity and mortality compared with singleton gestations, but when one of the described complications is recognized, the difficulties in management are compounded dramatically. Despite the relative rarity of some of the entities described, it is vitally important to be familiar with these problems and their sonographic evaluation and diagnosis.

Acknowledgment

The authors would like to thank Dr. Geoffrey A. Machin, fetal/placental pathologist, for his contributions to the preparation of the manuscript and for the figures that show placental injection studies.

References

[1] Chitkara U, Berkowitz RL. Multiple gestations. In: Gabbe SG, Niebyl JR, Simpson JL, editors. Obstetrics. 3rd edition. New York: Churchill-Livingstone; 1996. p. 821–62.

[2] Sebire N, Snijders R, Hughes K, Sepulveda W, Nicolaides KH. The hidden mortality of monochorionic twin pregnancies. Br J Obstet Gynaecol 1997; 104:1203–7.

[3] Benirschke K. Twin placenta in perinatal mortality. N Y J Med 1961;61:1499–508.

[4] Bernirschke K, Kim CK. Multiple pregnancy. N Engl J Med 1973;288:1276–329.

[5] Bajoria R, Kingdom J. The case for routine determination of chorionicity and zygosity in multiple pregnancy. Prenat Diagn 1997;17:1207–25.

[6] Moore KL. The developing human: clinically oriented embryology. 4th edition. Philadelphia: WB Saunders; 1988.

[7] Mahony BS, Filly RA, Callen PW. Amnionicity and chorionicity in twin pregnancies: prediction using ultrasound. Radiology 1985;155:205–9.

[8] Townsend RR, Simpson GF, Filly RA. Membrane thickness in ultrasound prediction of chorionicity of twin gestations. J Ultrasound Med 1988;7:327–32.

[9] Finberg HJ. The ''twin peak'' sign: reliable evidence of dichorionic twinning. J Ultrasound Med 1992;11: 571–7.

[10] Stenhouse E, Hardwick C, Maharaj S, Webb J, Kelly T, Mackenzie FM. Chorionicity determination in twin pregnancies: how accurate are we? Ultrasound Obstet Gynecol 2002;19:350–2.

[11] Machin GA, Keith LG. An atlas of multiple pregnancy: biology and pathology. New York: Parthenon Publishing Group; 1999.

[12] Robertson EG, Neer KJ. Placenta injection studies in twin gestation. Am J Obstet Gynecol 1983;147:170–4.

[13] Machin G, Still K, Lalani T. Correlation of placental vascular anatomy and clinical outcomes in 69 monochorionic twin pregnancies. Am J Med Genet 1996; 61:229–36.

[14] Taylor MJ, Denbow ML, Tanawattanacharoen S, Gannon C, Cox PM, Fisk NM. Doppler detection of arterio-arterial anastomoses in monochorionic twins: feasibility and clinical application. Hum Reprod 2000; 15:1632–6.

[15] Machin GA, Feldstein VA, van Gemert MJ, Keith LG, Hecher K. Doppler sonographic demonstration of arterio-venous anastomosis in monochorionic twin gestation. Ultrasound Obstet Gynecol 2000;16:214–7.

[16] Taylor MJ, Farquharson D, Cox PM, Fisk NM. Identification of arterio-venous anastomoses in vivo in monochorionic twin pregnancies: preliminary report. Ultrasound Obstet Gynecol 2000;16:218–22.

[17] Hanley ML, Ananth CV, Shen-Schwarz S, Smulian JC, Lai YL, Vintzileos AM. Placental cord insertion and birth weight discordancy in twin gestations. Obstet Gynecol 2002;99:477–82.

[18] Rausen AR, Seki M, Strauss L. Twin transfusion syndrome. J Pediatr 1965;66:613–28.

[19] Brown DL, Benson CB, Driscoll SG, Doubilet PM. Twin-twin transfusion syndrome: sonographic findings. Radiology 1989;170:61–3.

[20] Bajoria R. Vascular anatomy of monochorionic placen-

ta in relation to discordant growth and amniotic fluid volume. Hum Reprod 1998;13:2933–40.
[21] Patten RM, Mack LA, Harvey D, Cyr DR, Pretorius DH. Disparity of amniotic fluid volume and fetal size: problem of stuck twin. Ultrasound studies. Radiology 1989;172:153–7.
[22] Mahony BS, Petty CN, Nyberg DA, Luthy DA, Hickok DE, Hirsch JH. The "stuck twin" phenomenon: ultrasonographic findings, pregnancy outcome, and management with serial amniocenteses. Am J Obstet Gynecol 1990;163:1513–22.
[23] Denbow M, Cox P, Talbert D, Fisk N. Colour Doppler energy insonation of placental vasculature in monochorionic twins: absent arterio-arterial anastomoses in association with twin-twin transfusion syndrome. Br J Obstet Gynaecol 1998;105:760–5.
[24] van Gemert MJ, Umur A, Tijssen JG, Ross MG. Twin-twin transfusion syndrome: etiology, severity and rational management. Curr Opin Obstet Gynecol 2001; 13:193–206.
[25] Bajoria R, Wigglesworth J, Fisk N. Angioarchitecture of monochorionic placentas in relation to the twin-twin transfusion syndrome. Am J Obstet Gynecol 1995;172: 856–63.
[26] Taylor MJ, Denbow ML, Duncan KR, Overton TG, Fisk NM. Antenatal factors at diagnosis that predict outcome in twin-twin transfusion syndrome. Am J Obstet Gynecol 2000;183:1023–8.
[27] Denbow ML, Cox P, Taylor M, Hammal DM, Fisk NM. Placental angioarchitecture in monochorionic twin pregnancies: relationship to fetal growth, fetofetal transfusion syndrome, and pregnancy outcome. Am J Obstet Gynecol 2000;182:417–26.
[28] Umur A, van Gemert MU, Nikkels PG, Ross MG. Monochorionic twins and twin-twin transfusion syndrome: the protective role of arterio-arterial anastomoses. Placenta 2002;23:201–9.
[29] Van Heteren CF, Nijhuis JG, Semmekrot BA, Mulders LGM, Van den Berg PP. Risk for surviving twin after fetal death of co-twin in twin-twin transfusion syndrome. Obstet Gynecol 1998;92:215–9.
[30] Bajoria R, Wee LY, Anwar S, Ward S. Outcome of twin pregnancies complicated by single intrauterine death in relation to vascular anatomy of the monochorionic placenta. Hum Reprod 1999;14:2124–30.
[31] Elliott JP, Urig MA, Clewell WH. Aggressive therapeutic amniocentesis for treatment of twin-twin transfusion syndrome. Obstet Gynecol 1991;77:537–40.
[32] Trespidi L, Boschetto C, Caravelli E, Villa L, Kustermann A, Nicolini U. Serial amniocenteses in the management of twin-twin transfusion syndrome: when is it valuable? Fetal Diagn Ther 1997;12: 15–20.
[33] Dennis LG, Winkler CL. Twin-to-twin transfusion syndrome: aggressive therapeutic amniocentesis. Am J Obstet Gynecol 1997;177:342–9.
[34] Mari G. Amnioreduction in twin-twin transfusion syndrome: a multicenter registry, evaluation of 579 procedures. Am J Obstet Gynecol 1998;178:S28.
[35] Bajoria R. Chorionic plate vascular anatomy determines the efficacy of amnioreduction therapy for twin-twin transfusion syndrome. Hum Reprod 1998; 13:1709–13.
[36] Kilby MD, Howe DT, McHugo JM, Whittle MJ. Bladder visualization as a prognostic sign in oligohydramnios polyhydramnios sequence in twin pregnancies treated using therapeutic amniocentesis. Br J Obstet Gynaecol 1997;104:939–42.
[37] De Lia JE, Kuhlmann RS, Harstad T, Cruikshank DP. Fetoscopic laser ablation of placental vessels in severe previable twin-twin transfusion syndrome. Am J Obstet Gynecol 1995;172:1202–11.
[38] Quintero RA, Morales WJ, Mendoza G, Allen M, Kalter CS, Giannina G, et al. Selective photocoagulation of placental vessels in twin-twin transfusion syndrome: evolution of a surgical technique. Obstet Gynecol Surv 1998;53:S97–103.
[39] Ville Y, Hecher K, Gagnon A, Sebire N, Hyett J, Nicolaides K. Endoscopic laser coagulation in the management of severe twin-to-twin transfusion syndrome. Br J Obstet Gynaecol 1998;105:446–53.
[40] Hecher K, Diehl W, Zikulnig L, Vetter M, Hackeloer BJ. Endoscopic laser coagulation of placental anastomoses in 200 pregnancies with severe mid-trimester twin-to-twin transfusion syndrome. Eur J Obstet Gynecol Reprod Biol 2000;92:135–9.
[41] Quintero RA, Comas C, Bornick PW, Allen MH, Kruger M. Selective versus non-selective laser photocoagulation of placental vessels in twin-twin transfusion syndrome. Ultrasound Obstet Gynecol 2000; 16:230–6.
[42] Feldstein VA, Machin GA, Albanese CT, Sandberg P, Farrell JA, Farmer DL, et al. Twin-twin transfusion syndrome: the "SELECT" procedure. Fetal Diagn Ther 2000;15:257–61.
[43] Hecher K, Plath H, Bregenzer T, Hansmann M, Hackelöer BJ. Endoscopic laser surgery versus serial amniocenteses in the treatment of severe twin-twin transfusion syndrome. Am J Obstet Gynecol 1999;180: 717–24.
[44] Petersen IR, Nyholm HC. Multiple pregnancies with single intrauterine demise. Acta Obstet Gynecol Scand 1999;78:202–6.
[45] Langer B, Boudier E, Gasser B, et al. Antenatal diagnosis of brain damage in the survivor after the second trimester death of a monochorionic monoamniotic cotwin: case report and literature review. Fetal Diagn Ther 1997;12:286–91.
[46] Anderson RL, Golbus MS, Curry CR, Callen PW, Hastrup WH. Central nervous system damage and other anomalies in surviving fetus following second trimester antenatal death of co-twin. Prenatal Diagn 1990;10:513–8.
[47] Bejar R, Vigliocco G, Gramajo H, et al. Antenatal origin of neurologic damage in newborn infants: II. Multiple gestations. Am J Obstet Gynecol 1990;162: 1230–6.
[48] Patten RM, Mack LA, Nyberg DA, Filly RA. Twin

embolization syndrome: prenatal sonographic detection and significance. Radiology 1989;173:685–9.
[49] Levine D, Barnes PD, Madsen JR, Abbott J, Mehta T, Edelman RR. Central nervous system abnormalities assessed with prenatal magnetic resonance imaging. Obstet Gynecol 1999;94:1011–9.
[50] Levine D, Barnes PD, Madsen JR, et al. Fetal CNS anomalies: MR imaging augments sonographic diagnosis. Radiology 1997;204:635–42.
[51] Angtuaco TL, Shah SR, Mattison DR, Quirk JG. MR imaging in high-risk obstetric patients: a valuable complement to US. Radiographics 1992;12: 91–109.
[52] Simon EM, Goldstein RB, Coakley FV, Filly RA, Broderick KC, Musci TJ, et al. Fast MR imaging of fetal CNS anomalies in utero. Am J Neuroradiol 2000;21: 1688–98.
[53] Van Allen MI, Smith DW, Shepart JH. Twin reversed arterial perfusion (TRAP) sequence: a study of 14 twin pregnancies with acardius. Semin Perinatol 1983;7: 285–93.
[54] Benson CB, Bieber FR, Genest DF, Doubilet PM. Doppler demonstration of reversed umbilical blood flow in an acardiac twin. J Clin Ultrasound 1989;17: 291–5.
[55] Moore TR, Gale S, Benirschke K. Perinatal outcome of forty-nine pregnancies complicated by acardiac twinning. Am J Obstet Gynecol 1990;163:907–12.
[56] Tsao KJ, Feldstein VA, Albanese CT, Sandberg PL, Lee H, Harrison MR, et al. Selective reduction of acardiac twin by radiofrequency ablation. Am J Obstet Gynecol 2002;187:635–40.
[57] Sydorak RM, Feldstein V, Machin G, Tsao K, Lee HS, Farmer DL, et al. Fetoscopic treatment for discordant twins. J Pediatr Surg 2002;37:1736–9.
[58] Quintero RA, Bornick PW, Morales WJ, Allen MH. Selective photocoagulation of communicating vessels in the treatment of monochorionic twins with selective growth retardation. Am J Obstet Gynecol 2001;185: 689–96.
[59] Edmonds LD, Layde PM. Conjoined twins in the United States 1970–1977. Teratology 1982;25:301–8.
[60] Sakala EP. Obstetric management of conjoined twins. Obstet Gynecol 1986;67:21S–5S.
[61] Maggio M, Callen NA, Hamod KA, Sanders RC. The first-trimester ultrasonographic diagnosis of conjoined twins. Am J Obstet Gynecol 1985;152:833–5.
[62] Townsend RR, Filly RA. Sonography of non conjoined monoamniotic pregnancy. J Ultrasound Med 1988;7: 665–70.
[63] Auckerman H, Berzezinski A. Monoamniotic twin pregnancy. Gynaecologic 1960;150:290.
[64] Finberg HJ, Clewell WH. Definitive prenatal diagnosis of monoamniotic twins: swallowed amniotic contrast agent detected in both twins on sonographically selected CT images. J Ultrasound Med 1991;10:513–6.

RADIOLOGIC CLINICS OF NORTH AMERICA

Radiol Clin N Am 41 (2003) 729–745

Tips and tricks of fetal MR imaging

Deborah Levine, MD[a,*], Annemarie Stroustrup Smith[b,c], Charles McKenzie, PhD[a]

[a]*Department of Radiology, Beth Israel Deaconess Medical Center, 330 Brookline Avenue, Boston, MA 02215, USA*
[b]*Harvard Medical School, Boston, MA 02215, USA*
[c]*Harvard-MIT Division of Health Science and Technology, Boston, MA 02215, USA*

MR imaging during pregnancy is being used increasingly to assess fetuses with complicated or nonspecific ultrasound (US) diagnoses [1–13]. This article illustrates common artifacts and other pitfalls in the performance of fetal MR examinations and suggests techniques to improve image quality. Comparisons of anatomy visualized on fetal MR imaging versus US are demonstrated. The cases illustrated in this article have been gleaned from more than 400 fetal MR imaging cases performed in the past 6 years at Beth Israel Deaconess Medical Center (Boston, MA).

Practical comments: how we perform fetal MR examinations

Is the study indicated?

A fetal MR examination may be ordered for an indication more appropriately answered by US. If the anatomy can be evaluated adequately on US, then the MR examination is likely not needed.

Is high-quality ultrasound available for comparison?

Quality of US varies among sites. It is helpful to have a sonogram performed by an individual experienced in detection and characterization of fetal anomalies, which lessens the perceived impact of MR imaging on patient care (Fig. 1).

Is a recent ultrasound available for comparison?

Optimally, the US is performed immediately before the MR examination (Fig. 2). Besides providing sonographic diagnoses for comparison with the MR examination, an US that precedes the MR examination is helpful in directing placement of the surface coil to the area of interest in the fetus with respect to the maternal body (Fig. 3).

What type of consent should be obtained?

All pregnant patients should be informed regarding the risks and benefits of MR imaging. The authors inform patients that no conclusive scientific evidence supports a direct relationship between exposure to MR imaging and any hazard to the developing fetus [14–21]. Because fetal cells in the first trimester of pregnancy are particularly susceptible to damage by different types of physical agents, the authors limit fetal examinations to the second and third trimesters. Rarely, they have found incidental abnormalities on MR examinations (Fig. 4), so they mention the risk of increased anxiety caused by unexpected findings as a risk of the procedure.

Patient positioning

The authors place a patient in the supine position, with feet entering the magnet to minimize the possibility of claustrophobia. A surface coil is centered

Cases illustrated in this article were obtained under NIH grant NS37945. Review of cases was sponsored by a grant from the Carl J. Shapiro Institute for Education and Research.

* Corresponding author.
E-mail address: dlevine@caregroup.harvard.edu (D. Levine).

0033-8389/03/$ – see front matter © 2003 Elsevier Inc. All rights reserved.
doi:10.1016/S0033-8389(03)00043-5

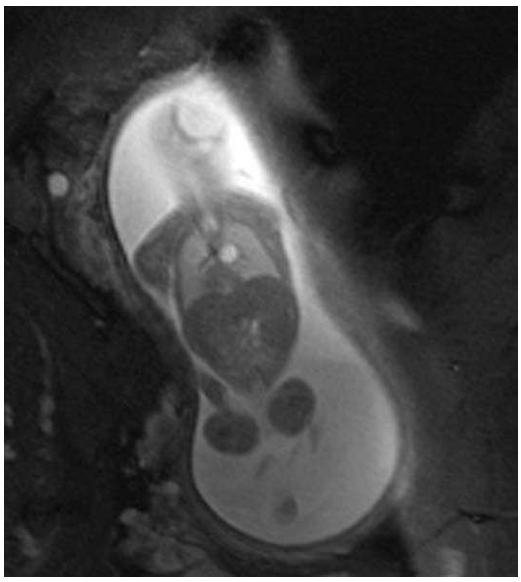

Fig. 1. Coronal MR image of a fetus at 19 weeks' gestation referred for congenital diaphragmatic hernia. Confirmatory sonogram showed an anechoic cyst in the chest, absent stomach below the diaphragm, and no mediastinal shift. Because of the lack of mediastinal shift, the confirmatory sonographic diagnosis was believed to be a combination of foregut duplication cyst and esophageal atresia. MR showed the diaphragm to be intact. Without a confirmatory US, this type of finding would suggest that MR showed increased information compared with US. Because a confirmatory sonogram was performed, the authors concluded that MR showed no new information and did not change patient care.

over the region of interest (established on US performed immediately before the MR study). A pillow is placed below the patient's knees. If the patient is uncomfortable lying on her back for prolonged periods, then she is imaged lying on her side (Fig. 5).

Monitoring the examination

The quality of the fetal MR examination benefits from having an individual who is knowledgeable in fetal anatomy and the clinical question to be answered present during the study. Because the fetus is in nearly constant motion, decisions regarding choice of image plane and whether the anatomy has been evaluated sufficiently must be made relatively quickly.

Protocol

The authors perform a three-plane T1-weighted scout, followed by T2-weighted imaging with half Fourier single shot fast spin echo sequences (SSFSE) in the fetal sagittal, coronal, and axial planes using each sequence as the scout for subsequent imaging. They typically perform additional sequences with thin cuts or higher matrix size through the region of interest. A typical T2-weighted sequence uses echo spacing of 4.2 milliseconds, echo time $(TE)_{effective}$ of 60 milliseconds, echo train length of 72, 4 mm slice thickness, 26×30 cm field of view, 128×256 acquisition matrix, and a refocusing flip angle of 130°.

One T1-weighted sequence is used to look for blood products or hemorrhage. The authors typically use fast low angle shot (FLASH) technique with the following parameters: repitition time (TR)/ TE = 88.5/4.1; flip angle = 80°; 5 mm slice thickness; field of view = 30×35; matrix = 170×256; scan time = 17 seconds (breath-hold).

Viewing the images

When viewing (or filming) fetal MR imaging, one should enlarge the fetus to fill the image and then adjust window and level. This approach provides the best opportunity for evaluating the fetal anatomy.

Examination interpretation

If a second opinion is good, a third opinion is even better. Just as the authors like to perform a

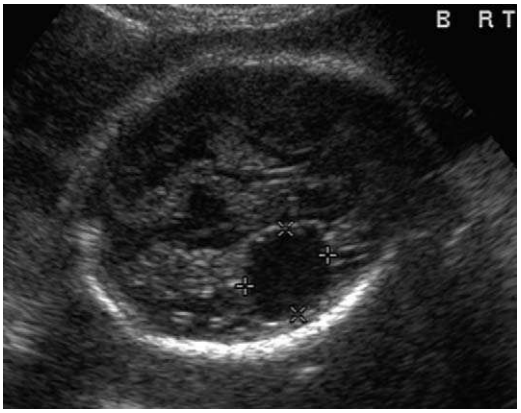

Fig. 2. Ultrasound of fetus at 31 weeks' gestation with a cystic brain lesion (*calipers*). This examination was performed 3 days before the MR examination. This was a fetus from a triamniotic dichorionic triplet pregnancy with demise of one of the monochorionic pair. A repeat US (not shown) performed immediately before the scheduled MR examination showed demise of this fetus, and the MR examination was cancelled.

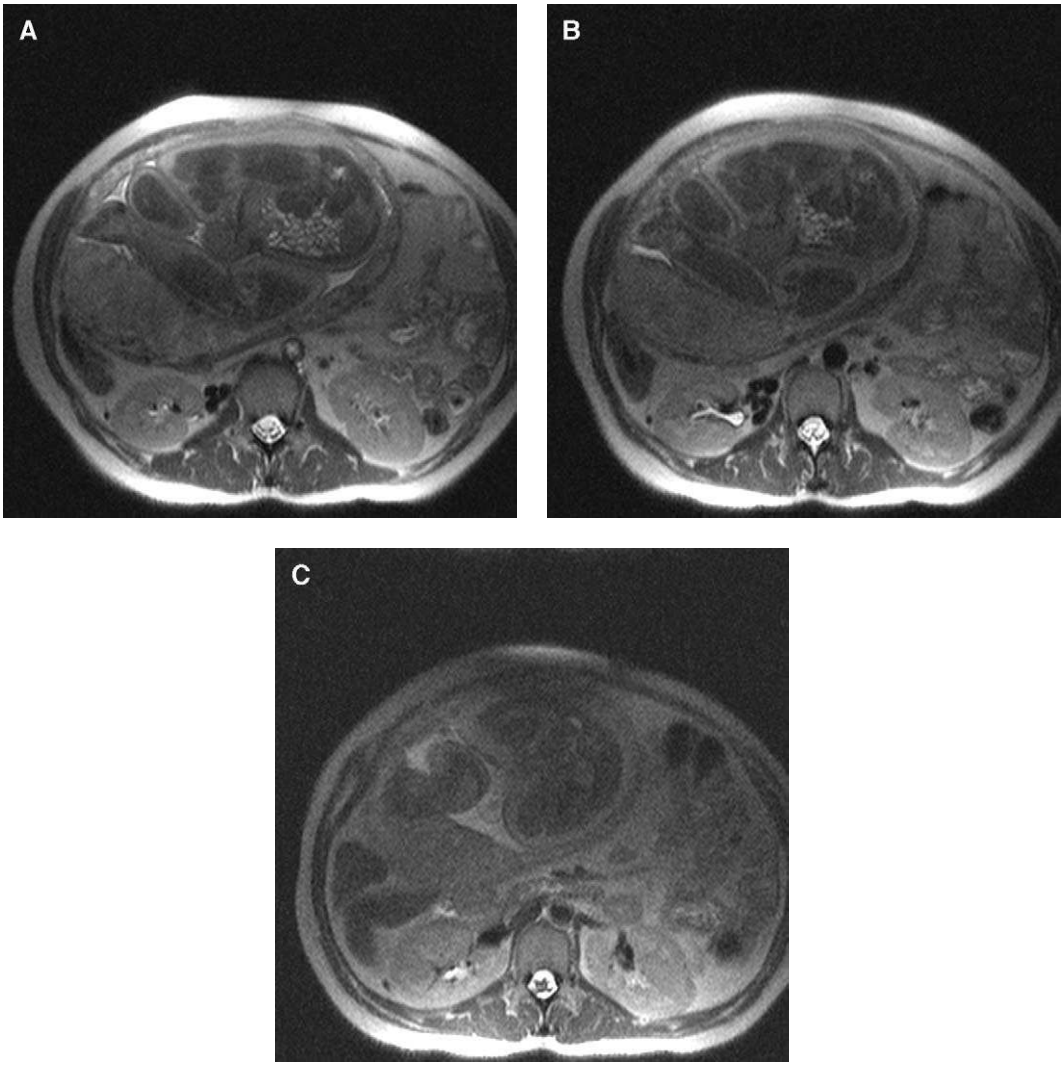

Fig. 3. Three images of a fetus at 35 weeks' gestation with bladder exstrophy. Note the decreased signal in (*B*) and (*C*) relative to (*A*) in the maternal anterior abdominal wall and in the fetal structures, because the images in (*B*) and (*C*) are obtained at the edge of the surface coil.

confirmatory sonogram, they also like to get a second opinion on their reading of the MR examinations. Their experience is in high-risk obstetric imaging. They commonly have fetal MR examinations double read by pediatric radiologists. This is a wonderful trade of information, because pediatric imagers may not be as familiar with fetal diseases but have a wider differential for some of the rare childhood disease processes. This advantage is especially important in assessment of the fetal central nervous system. Having a pediatric neuroradiologist evaluate scans frequently has clarified the diagnosis (Fig. 6).

Anatomy better visualized with MR imaging

Several anatomic areas in the fetus are better visualized with MR imaging than with US. A few examples include the thymus (Fig. 7), major airways (Fig. 8), spleen (Fig. 9), soft palate (Fig. 10), and esophagus (Fig. 11).

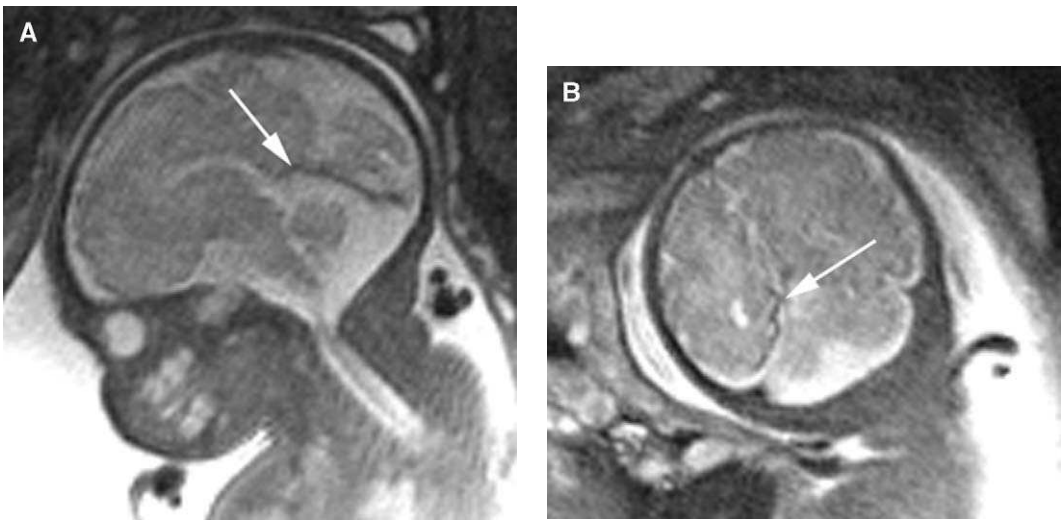

Fig. 4. Fetus at 35 weeks' gestation referred for enlarged cisterna magna. Sonogram was normal (not shown). Sagittal (*A*) and coronal (*B*) MR images show incidental finding of enlarged subtemporal vein (*arrow*). This is an example of the risk of MR showing an unrelated finding that could increase parental anxiety. The patients were counseled that this was a vascular anomaly that would have gone unrecognized if the MR examination had not been performed. Postnatal outcome was normal at 2 years of age.

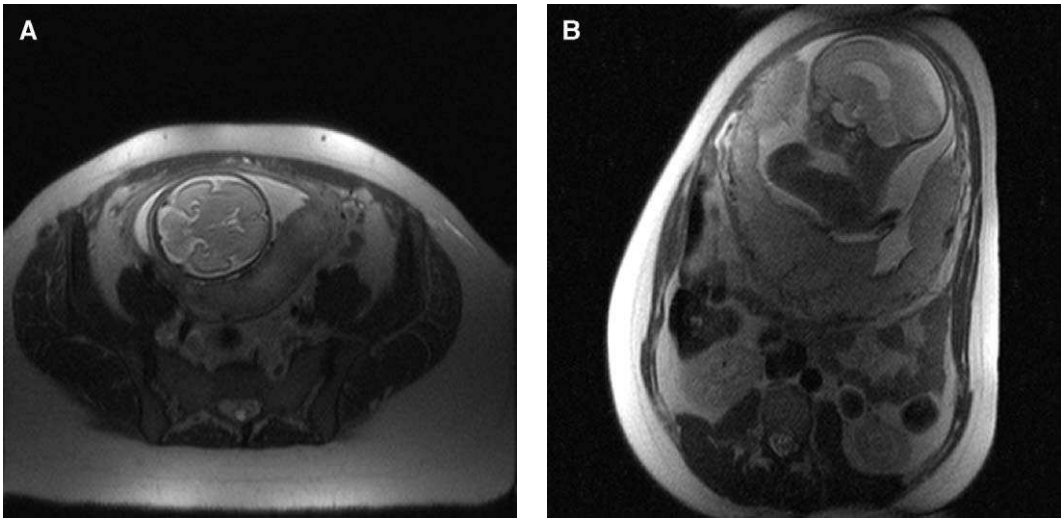

Fig. 5. Two fetuses at 28 weeks' gestation. (*A*) The patient was scanned in supine position. (*B*) The patient was scanned in lateral decubitus position.

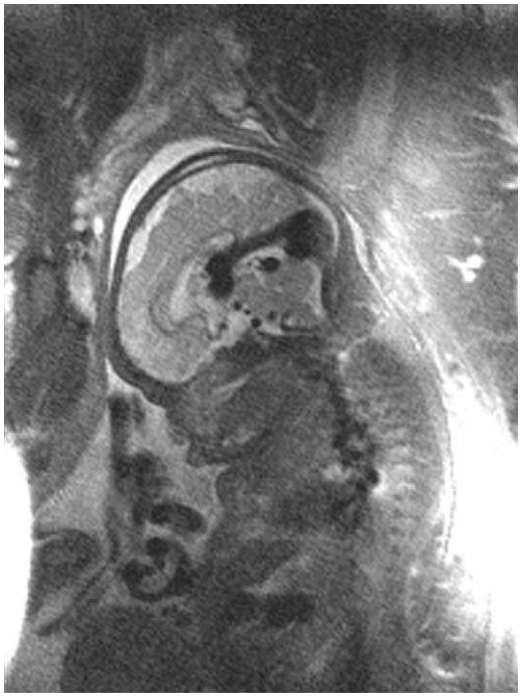

Fig. 6. Sagittal view of the brain of a fetus at 38 weeks' gestation with a vein of Galen malformation. The pediatric neuroradiologist also noted choroidal features of the venous malformation. This put the patient at increased risk for fetal intracranial hemorrhage, and the fetus was delivered by cesarean section.

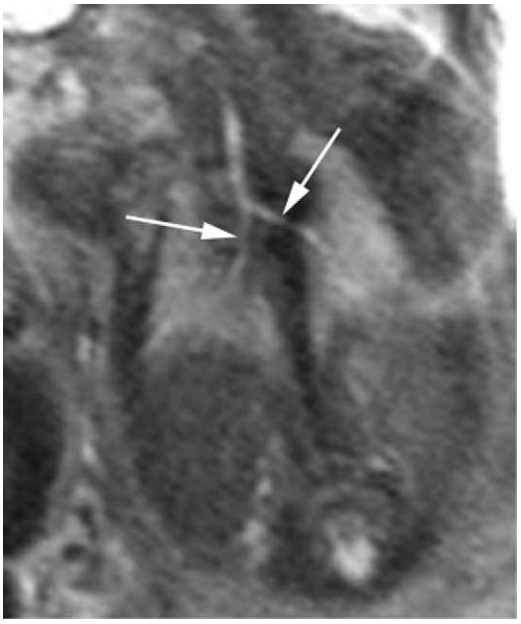

Fig. 8. Trachea and carina. Coronal view of the chest at 33 weeks' gestation shows the trachea, carina, and right and left mainstem bronchi (*arrows*).

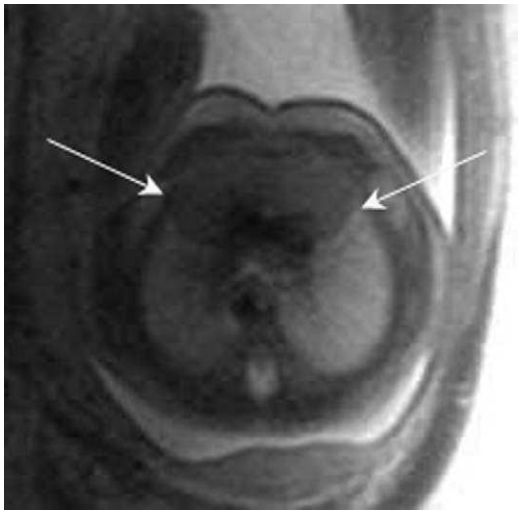

Fig. 7. Axial image of the fetal thymus at 32 weeks' gestation (*arrow*).

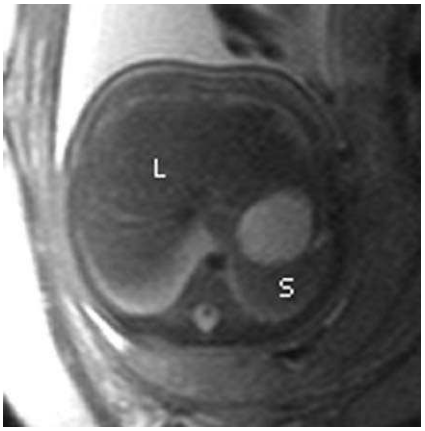

Fig. 9. Fetus at 32 weeks' gestation. Note the spleen (s), which is rarely seen in fetal US but routinely visualized on fetal MR imaging. The liver (l) also is labeled.

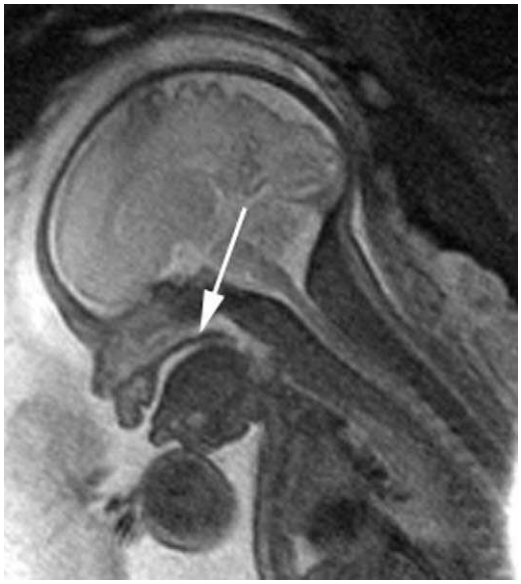

Fig. 10. This midline sagittal view of the face outlines the soft palate (*arrow*) at 33 weeks' gestation. The oropharynx being filled with amniotic fluid aids in evaluation of this structure, which typically cannot be seen by US.

Artifacts: what we see and what we should do

Motion artifact

Motion affects all fetal MR examinations because of the combination of maternal motion (whole body, breathing, bowel peristalis, and arterial pulsations) and fetal motion. Because images are obtained in 300 to 400 milliseconds, SSFSE imaging allows for diagnostic quality imaging despite motion.

Bulk motion

Maternal motion results in motion of the entire field of view during the imaging sequence and generally results in a blurring of the entire image, with ghost images in the phase encoding direction (Fig. 12). Movement of a small portion of the imaged area results in a blurring of that small portion of the object across the image. Bulk motion artifacts can be distinguished from Gibbs or truncation artifacts because they extend across the entire field of view, unlike truncation artifacts, which diminish quickly away from the boundary that causes them. If bulk motion is present, one should remind the patient to keep still. In general, breath-holding is not needed during subsecond imaging sequences, but if the patient is moving during imaging, a breath-hold could be helpful.

Fluid motion

This artifact is characterized by a signal void that occurs in fluid. Fluid motion artifact occurs when

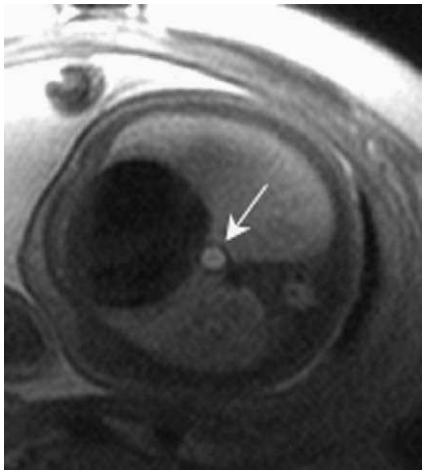

Fig. 11. Distended distal esophagus at 36 weeks' gestation. At times, a distended lower esophagus can be visualized on fetal MR (*arrow*). This was not present on other images in the same region. This is a transient finding, likely caused by reflux.

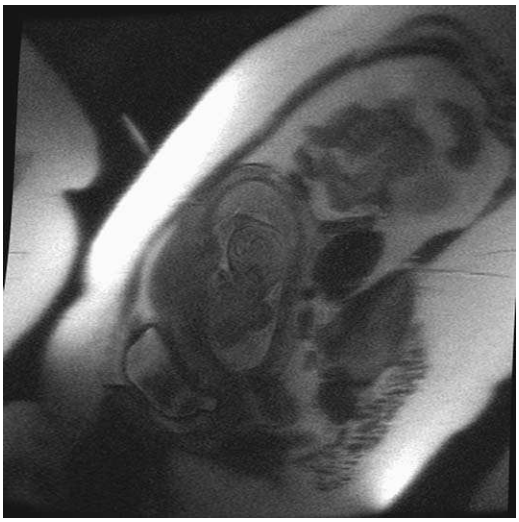

Fig. 12. Bulk movement. Note the blur of the entire image (soft tissues and fetus) because of bulk movement of the patient during the scan.

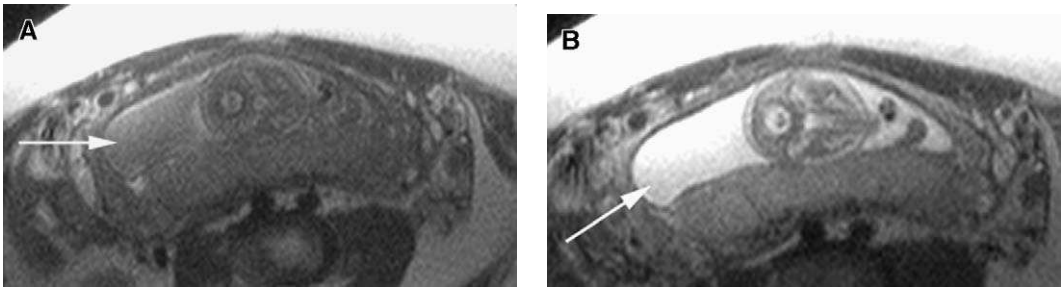

Fig. 13. Fluid motion. Two adjacent images from the same sequence. (*A*) Fluid motion has caused the amniotic fluid (*arrow*) and the fluid around the spinal cord to lose signal. (*B*) The amniotic fluid motion is not visualized (*arrow*), and the amniotic fluid and cerebrospinal fluid around the spinal cord are of high signal intensity.

spins excited by a slice-selective radio frequency pulse change position with respect to the slice or spatial encoding gradients before their signal is recorded. Motion artifact can be seen in amniotic fluid (Figs. 13–15) and in other fetal fluid collections, such as cerebrospinal fluid (Fig. 13) and fetal urine (Fig. 16). Because fetal imaging is typically performed with single shot sequences, only the slice that was obtained during the motion is affected. As long as the fetus is not continuously moving, then typically only one or two slices are degraded by motion during a typical sequence acquisition. If the affected slices are not in the region of interest, then the sequence does not need to be repeated. A pitfall in the assumption that dark fluid on SSFSE imaging is caused by motion is shown in Fig. 17, in which the low signal is caused by blood products.

Repeat visualization of structure or nonvisualization of a structure

If the fetus moves during the sequence and the movement is in plane with imaging, it is possible that a portion of the anatomy will be seen more than once (ie, a leg or arm appears in two places in the same sequence) (Fig. 18). More commonly, an extremity

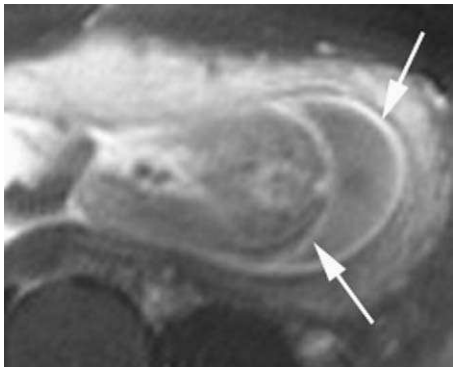

Fig. 14. Fluid motion around a fetus at 20 weeks' gestation. At times, fluid motion is visualized as low signal in the amniotic fluid rimmed by a bright "layer" (*arrows*). This brightness is generally caused by a lack of motion at the periphery of the fluid space. The high signal intensity also may be caused by subcutaneous fat (adjacent to the fetus) or fluid in the subamniotic space, however.

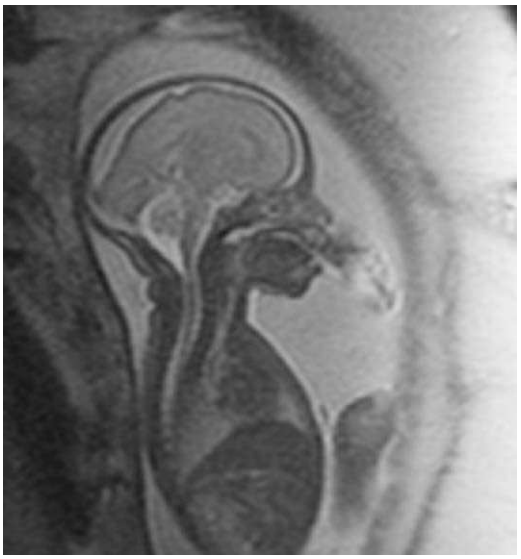

Fig. 15. Fluid motion. Sagittal view of a fetus at 26 weeks' gestation. The fetus was exhaling from the nose during image acquisition, which caused the fluid immediately anterior to the face to lose signal, imitating a mass.

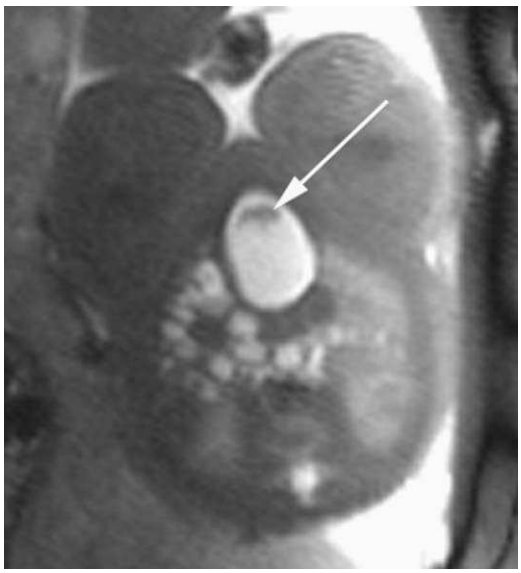

Fig. 16. Fluid motion in the bladder. Transverse view of the bladder in fetus at 22 weeks' gestation. Note loss of signal (*arrow*) caused by jet of urine entering the bladder.

moves out of the image plane during sequence acquisition and is not visualized.

Aliasing (wrap around)

This artifact can be identified when anatomic structures that extend outside the field of view in the phase encode direction appear to "wrap around" into the opposite side of the image. Depending on the anatomy and the placement of the field of view, the "wrapped" anatomy may overlie and obscure other anatomy. This artifact occurs because the tissue outside the field of view is not correctly phase encoded. Any excited tissue outside the field of view still gives signal during readout, but tissue outside the field of view has acquired a phase identical to a position inside the field of view. Because the spatial position is determined from the phase of the signal emitted by the tissue, all signals with the same phase are displayed in the same position inside the field of view [22]. The most straightforward method for eliminating this artifact is to increase the field of view so that it contains all maternal anatomy. This method results in either reduced in-plane resolution or increased scan times. For fetal imaging, it is best to use the smallest field of view that permits imaging of the region of interest (Fig. 19).

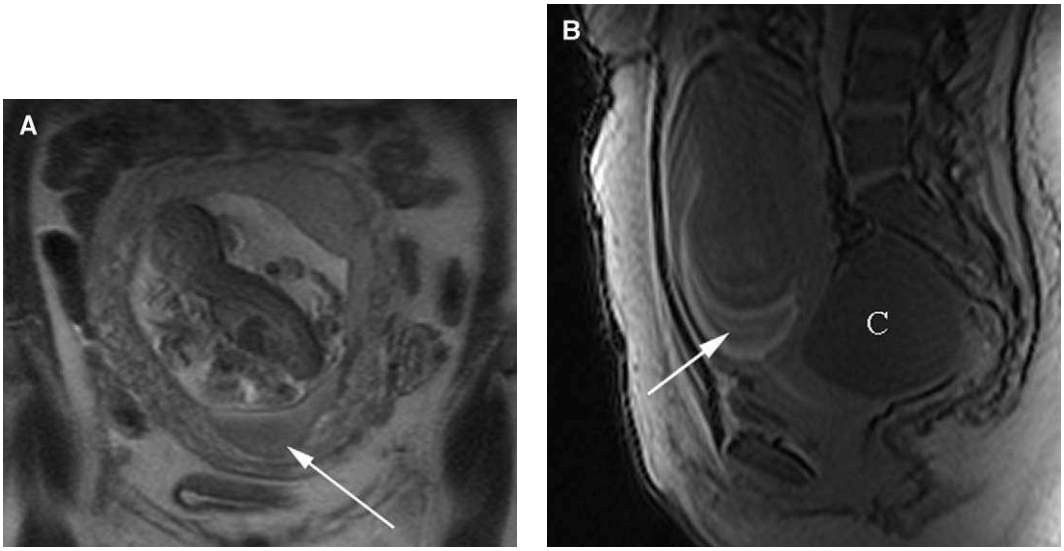

Fig. 17. Pitfall of fluid motion: dark fluid caused by blood products. (*A*) Sagittal T2-weighted image shows dark fluid above the internal os (*arrow*). (*B*) Sagittal T1-weighted image (TR/TE 88.2/1.5) shows this same area to have heterogenous slightly increased signal, consistent with marginal subchorionic hematoma (*arrow*). Also note the adnexal cyst (*C*).

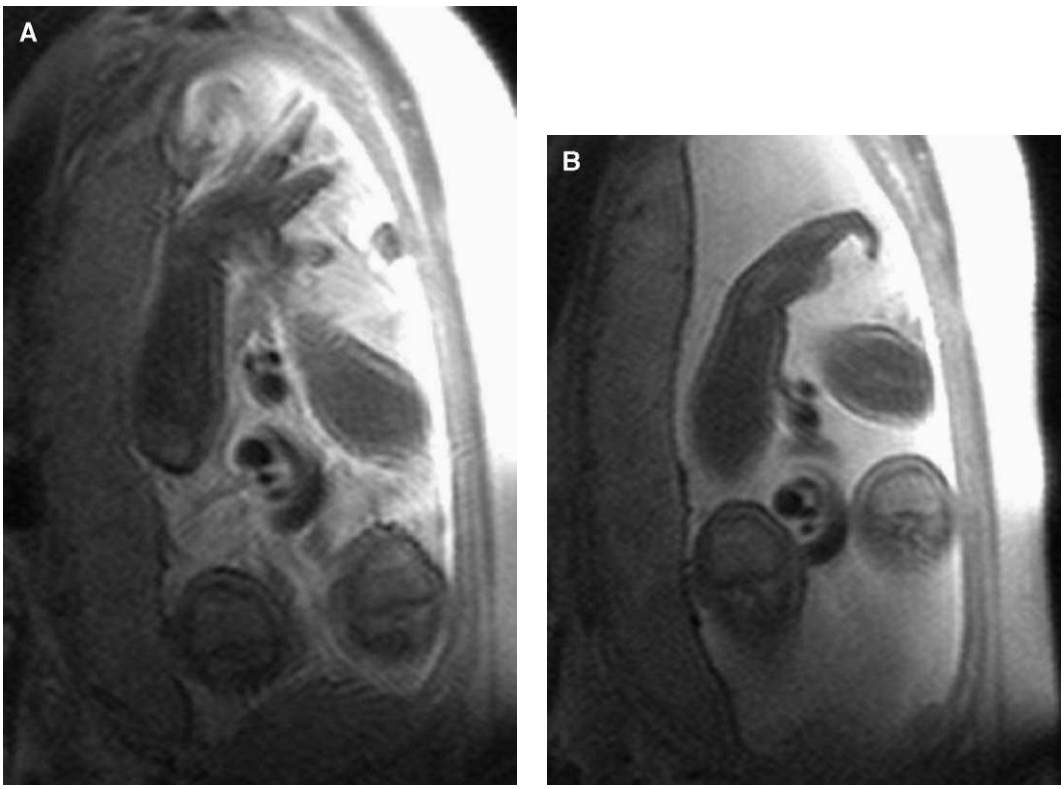

Fig. 18. Two sequential images of the fetal hand at 32 weeks' gestation. Moving extremities can cause a structure to be visualized twice or not at all. In this case the same hand is seen twice: open with fingers extended (*A*) and in a more relaxed position (*B*).

Radio frequency interference

This artifact is characterized by isolated lines or broad bands of lines in the phase encode direction being obscured by "zipper" artifacts (Fig. 20). Often, a single area of high signal-to-noise ratio (SNR) is visualized (Fig. 21). This artifact occurs when unwanted radio frequency signals from outside the magnet are picked up during data reception. Most causes of radio frequency contamination are beyond immediate control. A list of things to do if one sees this artifact follows.

- Ensure scanner room door is closed completely when scanning.
- Shut off extraneous equipment inside the scanner room.
- Ensure no wires from other medical equipment are entering the scanner room from the outside.
- Call service engineer.

Susceptibility artifact

This artifact is characterized by localized distortions of the geometry or intensity of the image caused by inhomogeneities in the main magnetic field (B_o). Spatial distortion results from long-range field gradients, where B_o varies over scales that span many voxels. These changes in B_o cause the spins in different voxels to have slightly different precession frequencies. Because spatial position is encoded by the precessional frequency of the spins, these alterations in frequency can make the signal from spins in one location seem to come from a different position, which results in geometric distortions of the image [22]. Susceptibility artifact is rare with SSFSE imaging, but it can occur (Fig. 22). Things to do if you see this artifact include performing shimming to improve the B_o homogeneity, using shorter TE sequences, and increasing readout bandwidth.

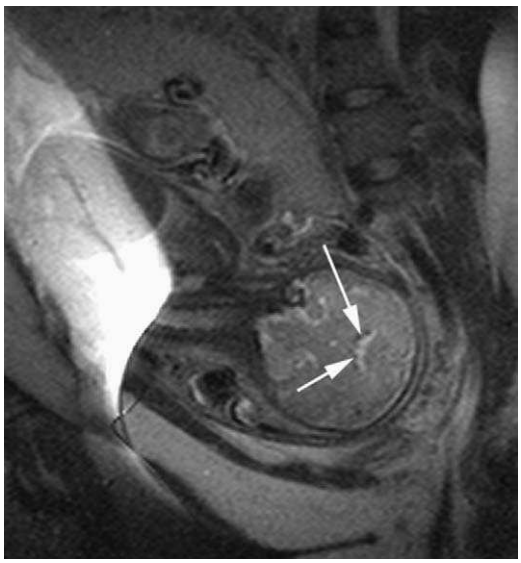

Fig. 19. A fetus with tuberous sclerosis at 34 weeks' gestation. The oblique image plane with respect to maternal anatomy (patient imaged in lateral decubitus position) gives bright wrap around artifact. This artifact does not overlie the area of interest in the fetal brain, because the subependymal tubers (*arrows*) are well visualized.

Gibbs ringing artifact

The Gibbs ringing artifact (also called a truncation artifact) is typified by alternating bright and dark lines running parallel to a sharp signal interface that diminish quickly away from the boundary that causes them (Fig. 23). Gibbs ringing occurs when the echo has not decayed to zero at the edges of the acquisition window [22], so it is most often seen in images when a small acquisition matrix is used. As long as this artifact is recognized and not confused with a real structure, it typically does not limit fetal imaging. This artifact can be reduced by increasing the resolution of the image or by applying a filter to the reconstructed image. Both of these strategies entail tradeoffs. Increasing resolution requires either longer imaging times or reduced image SNR, whereas filtering reduces the resolution of the reconstructed image.

Partial volume artifact

As in all tomographic imaging, if only a portion of an anatomic region is in the slice, partial volume artifact can occur. What is different in obstetric imaging is that this artifact can include structures outside of the fetus, for example, in the placenta (Fig. 24).

Image quality: what we see and what we can do

Signal-to-noise ratio

Because of the relatively small size of the fetus, fetal MR imaging is commonly limited by SNR. Two factors affect the SNR in an MR image: slice thickness and matrix size. The SNR varies directly with the size of the voxels in an image. For example, if the thickness of slices in a two-dimensional image were halved, thereby doubling the resolution in the slice direction, the SNR of that image would be reduced by a factor of two. Most structures in the fetal body are well visualized with 4 mm slice thickness (Fig. 25). Small or thin structures surrounded by fluid may not be visible by MR imaging (Fig. 26).

With the exception of reducing slice thickness in a two-dimensional acquisition, resolution in MR imaging is usually increased by increasing the number of encoding steps (either phase encoding or frequency encoding steps) acquired in (at least) one direction (ie, increasing the matrix size). The SNR of an image varies as the square root of the number of

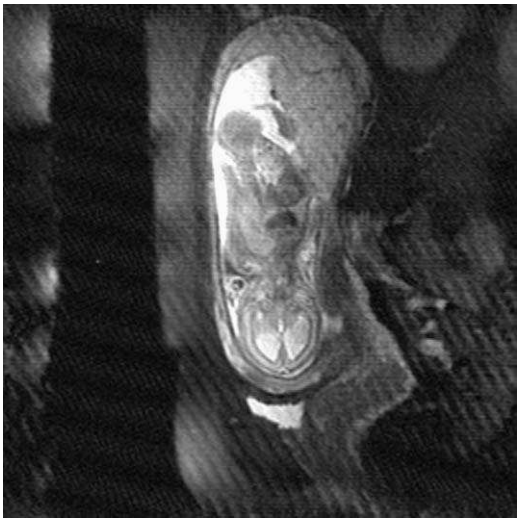

Fig. 20. Radio frequency interference. Coronal image of a fetus with neural tube defect at 19 weeks' gestation. Note the angular appearance of the mildly dilated cerebral ventricles, which is characteristic of a neural tube defect. The image quality is diffusely decreased by lines running through the image.

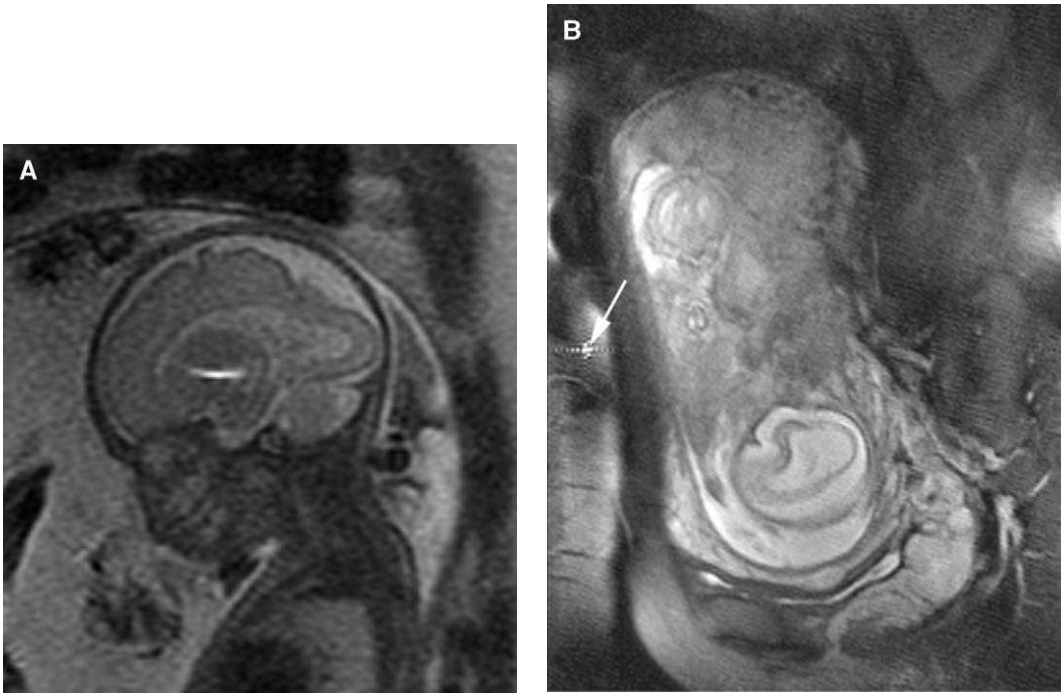

Fig. 21. Radio frequency interference. Image of the fetal head at 22 weeks' gestation (*A*) and twins at 24 weeks' gestation (*B*). In both of these images a bright area is seen that does not correspond to any anatomic structure. (*A*) The artifact is in the fetal brain and could interfere with diagnosis. (*B*) The artifact is in the maternal soft tissues and is not important to making a diagnosis. Note that the entire image is distorted by lines of alternating increased and decreased signal intensity.

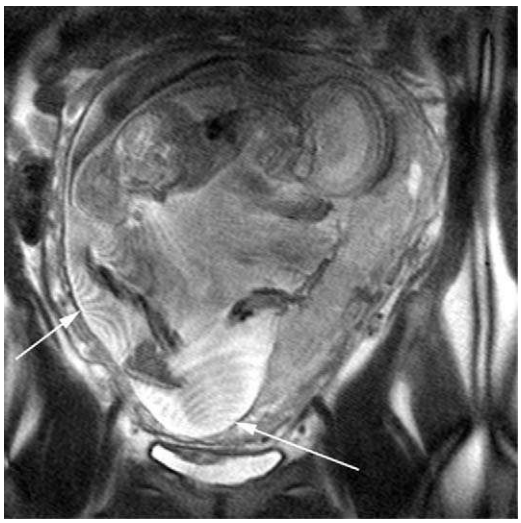

Fig. 22. Susceptibility artifact. Coronal image through the uterus at 20 weeks' gestation shows multiple geographic areas of increased and decreased signal in the amniotic fluid. The pattern of these alternating lines suggests susceptibility artifact.

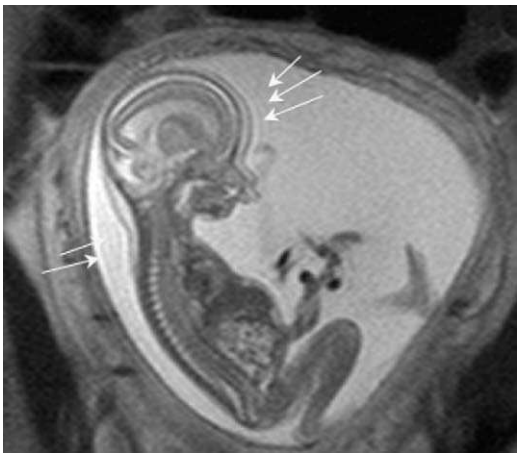

Fig. 23. Gibbs ringing artifact. A fetus with bilateral cleft lip and palate and a pseudomass in the midline face at 18 weeks' gestation. Ripples of high and low signal intensity (*arrows*) radiating away from the fetal amniotic fluid interface are caused by Gibbs artifact.

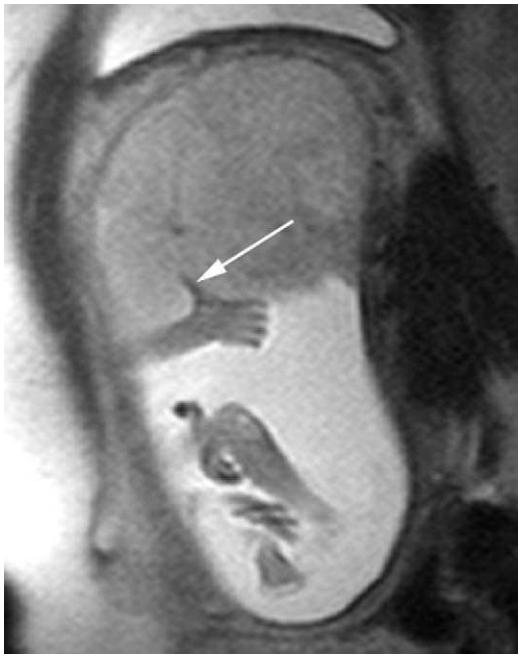

Fig. 24. Partial volume artifact in a fetus at 19 weeks' gestation. This image shows the fetal hand adjacent to the placenta. A prominent vein (*arrow*) in the placenta looks like a hyperextended thumb.

encoding steps. If resolution in the frequency encode direction is increased by doubling the number of frequency encoding steps acquired (and keeping all other imaging parameters the same), there are two competing effects on the SNR of the resulting image. The halving of the voxel size results in a halving of the SNR, but the doubling of the number of encoding steps results in an increase in SNR by a factor of the square root of two. In combination, these two effects result in a reduction in SNR of only a square root of two, rather than the factor of two that might be expected from the reduction in voxel size (Fig. 27). It is important to realize that on some magnets, the longer reconstruction times associated with large matrices allow for more fetal motion between sequence acquisitions.

A final consideration in maximizing SNR is field of view. To ensure the best resolution possible, it is important to keep the field of view as small as possible. Unlike typical abdominopelvic imaging, however, wrap-around artifact into the peripheral maternal anatomy is not a problem (see Fig. 19).

Patient body habitus and use of the surface coil

Because patients in the late stages of pregnancy have larger and more protuberant abdomens than the typical nongravid patient, patient body habitus must be considered. Because the wall of the abdomen can come close to the magnet bore, the surface coils gen-

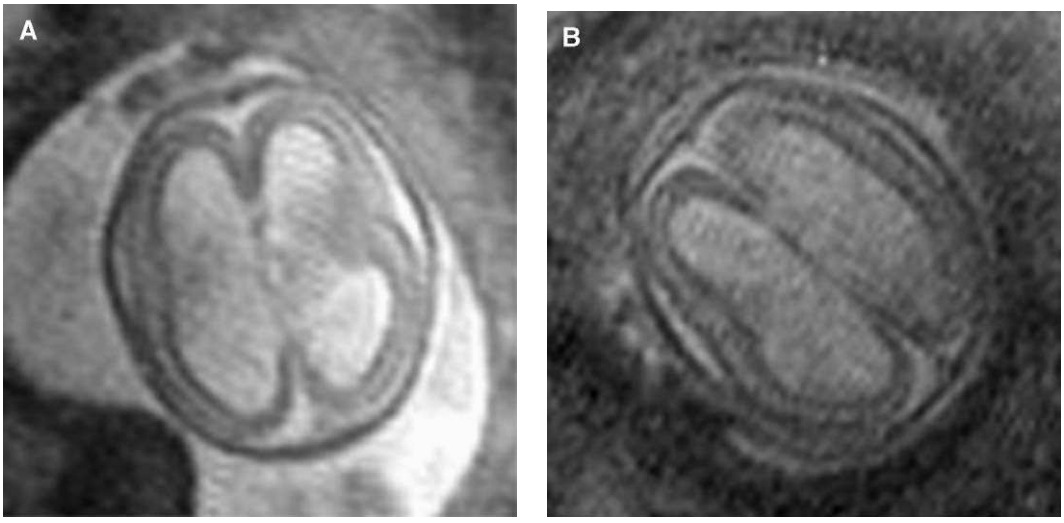

Fig. 25. Slice thickness. A fetus at 19 weeks' gestation with ventriculomegaly. (*A*) Slices are 4 mm thick. (*B*) Slices are 3 mm thick. Note increased signal but increased blur in (*A*) compared with (*B*).

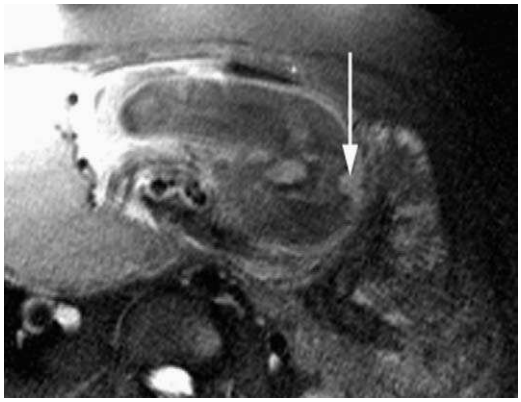

Fig. 26. Difficulty in visualizing thin structures surrounded by fluid. Axial MR in a fetus with an L4 neural tube defect at 26 weeks' gestation. Although the soft tissue defect is well visualized by MR (*arrow*), the sac covering the defect is not seen. The sac was visualized on US (not shown). Nonvisualization of the sac on MR is caused by the thin size of the sac wall and the partial volume averaging that occurs because of cerebrospinal fluid inside the sac and amniotic fluid outside of the sac.

erally used for abdominal and pelvic imaging may be placed closer to the body coil used for radio frequency pulse transmission. The proximity of the surface coil array to the body coil can de-tune the surface coil and result in failure of the magnet to complete its prescan calibration. In these cases it is necessary to remove the surface coils and use the body coil alone for imaging. Surface coils are helpful for increasing the SNR, but if a patient is too large to tolerate a surface coil and still fit in the magnet, imaging can be performed adequately with the body coil (Fig. 28).

Signal inhomogeneity when using a phased array surface coil

It is often advantageous to use a phased array surface coil instead of the magnets built into the body coil for signal reception [23]. Phased arrays give much better SNR than the body coil, in part because the coil array can be placed much closer to the anatomy of interest. Unlike the body coil, however, the signal intensity of an image produced by phased array is not uniform and drops off with distance from the array. A phased array image has high signal intensity at the abdominal wall, but the intensity is significantly lower near the center of the abdomen. This decay in signal intensity results in a heterogeneous appearance to the image, and the varying signal intensity can make the image difficult to interpret. Most magnets have an option to make the image appear more homogenous by applying a surface coil intensity correction that decreases signal intensity near the array and increase it farther away from the array. It should be noted that such corrections cannot

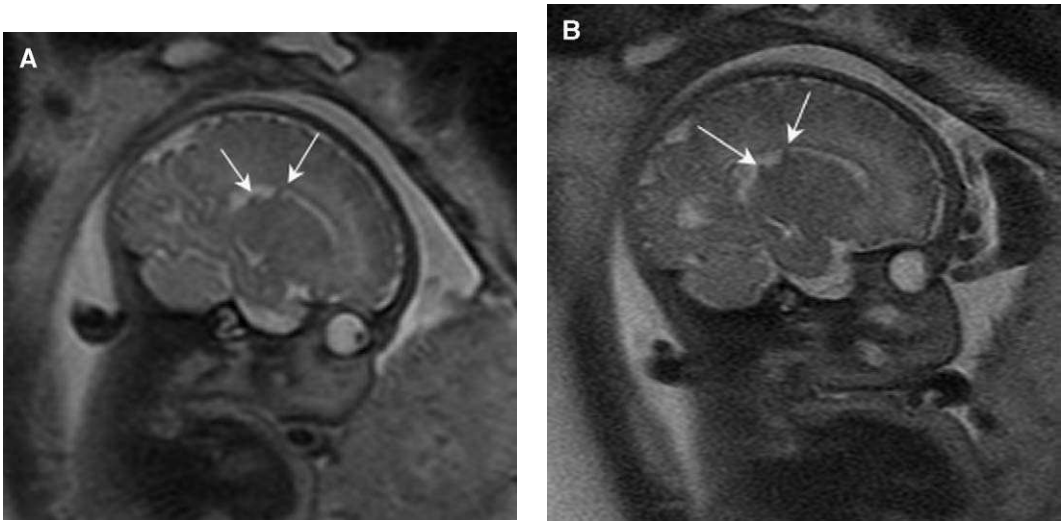

Fig. 27. Sagittal views of the fetal head in fetus with tuberous sclerosis at 36 weeks' gestation. (*A*) Image is taken with a 128×256 matrix. (*B*) Image is taken with a 256×512 matrix. Both images show the small nodules (subependymal tubers, *arrows*) projecting into the ventricle. The image in (*B*) has better resolution than (*A*) but has the same diagnostic information.

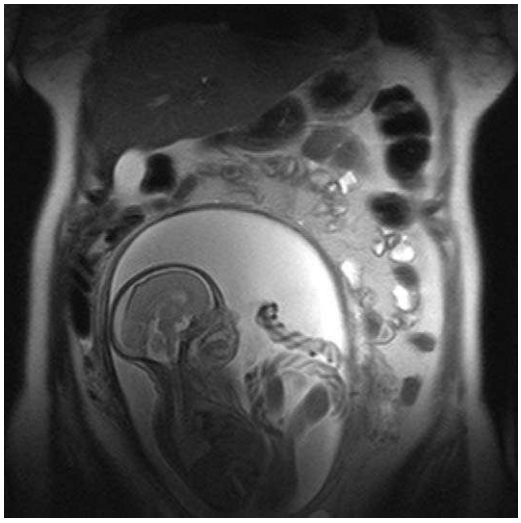

Fig. 28. Coronal image of the maternal abdomen obtained with a body coil at 26 weeks' gestation. This image was obtained during an examination for atypical abdominal pain performed with the body coil rather than a phased array surface coil. The fetal anatomy is still well visualized.

eliminate the falloff in SNR with distance from the array, so that the correction may result in increased conspicuity of noise at large distances from the array.

Fat saturation

Fat saturation is generally of little use in fetal imaging because the fetus has so little fat. Although suppressing the abdominal fat of the mother may be of some use for reducing the intensity of aliasing artifacts in small field of view imaging, this must be reconciled with the increased acquisition time that is usually required for fat suppression.

Pitfalls in image interpretation on MR imaging

Some pathologic conditions have a slightly unexpected appearance on MR imaging. For example, in some cases of nuchal thickening (Fig. 29), the more complex cystic and solid appearance on US corresponds to a simple cystic appearance on MR imaging. Some areas of pathology are better assessed by US than by MR imaging, including small calcifications (Fig. 30), small lesions (Fig. 31), and thin walls of fluid collections (see Fig. 26).

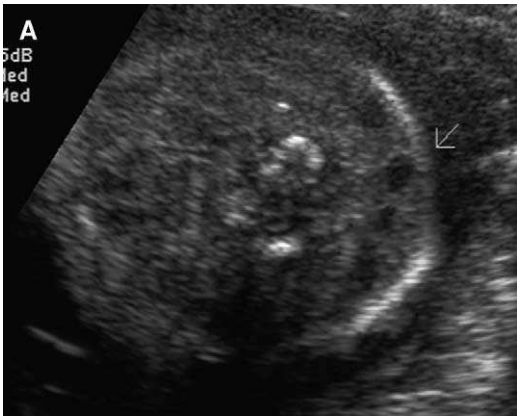

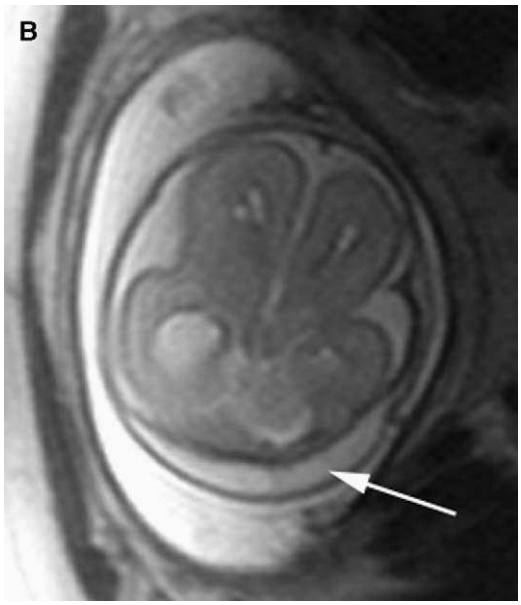

Fig. 29. (*A*) Sonogram and (*B*) MR image of fetus with nuchal thickening. Note the soft tissue with septations behind the neck seen on the sonogram (*arrow*). On MR imaging, the nuchal area has a more simple cystic appearance because of the high fluid content.

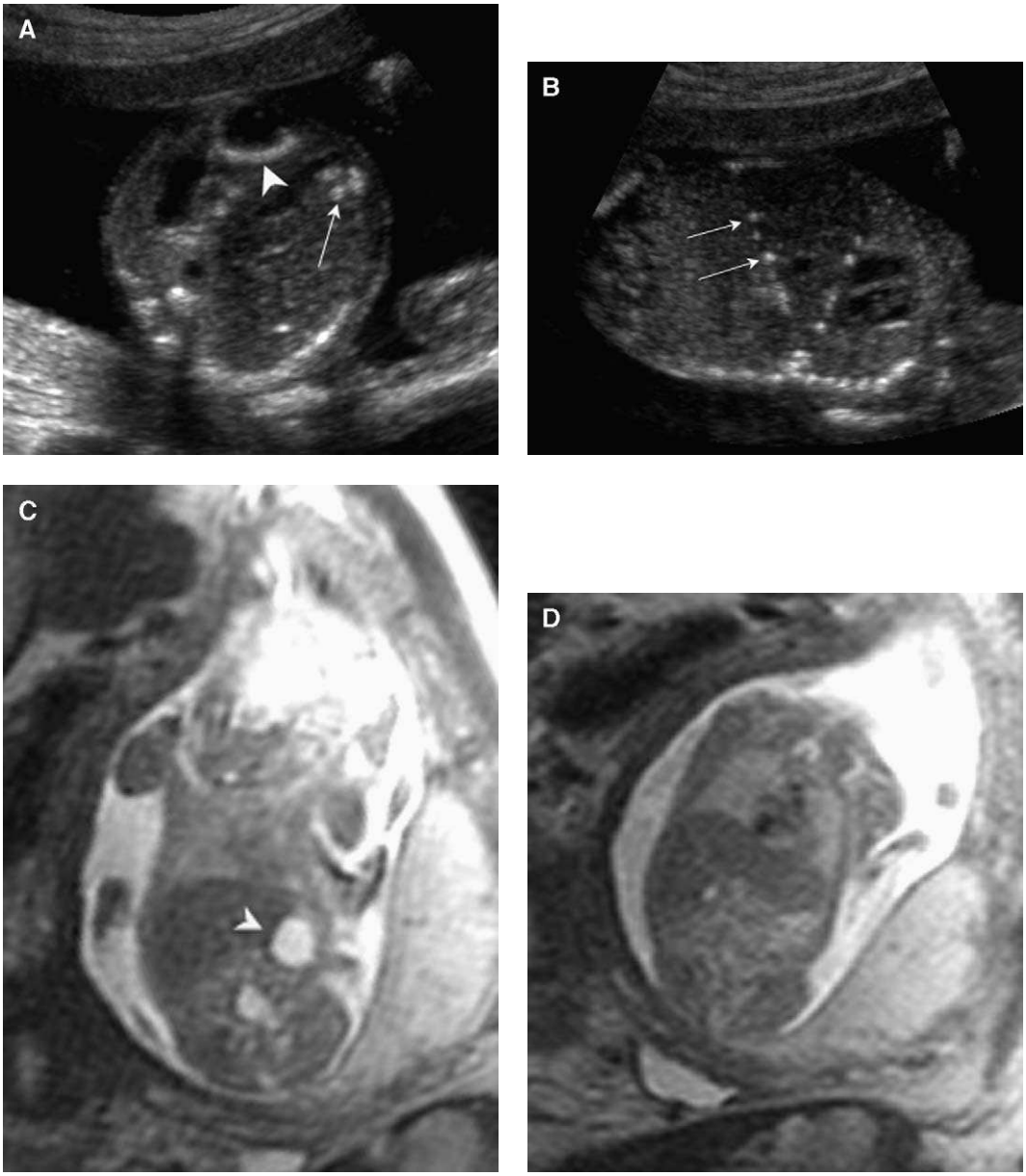

Fig. 30. US (*A,B*) and MR imaging (*C,D*) in a fetus with a meconium pseudocyst (*arrowheads*) and intraabdominal calcifications (*arrows*) at 19 weeks' gestation. Whereas the pseudocyst is well visualized on MR imaging, the punctate calcifications are not visualized.

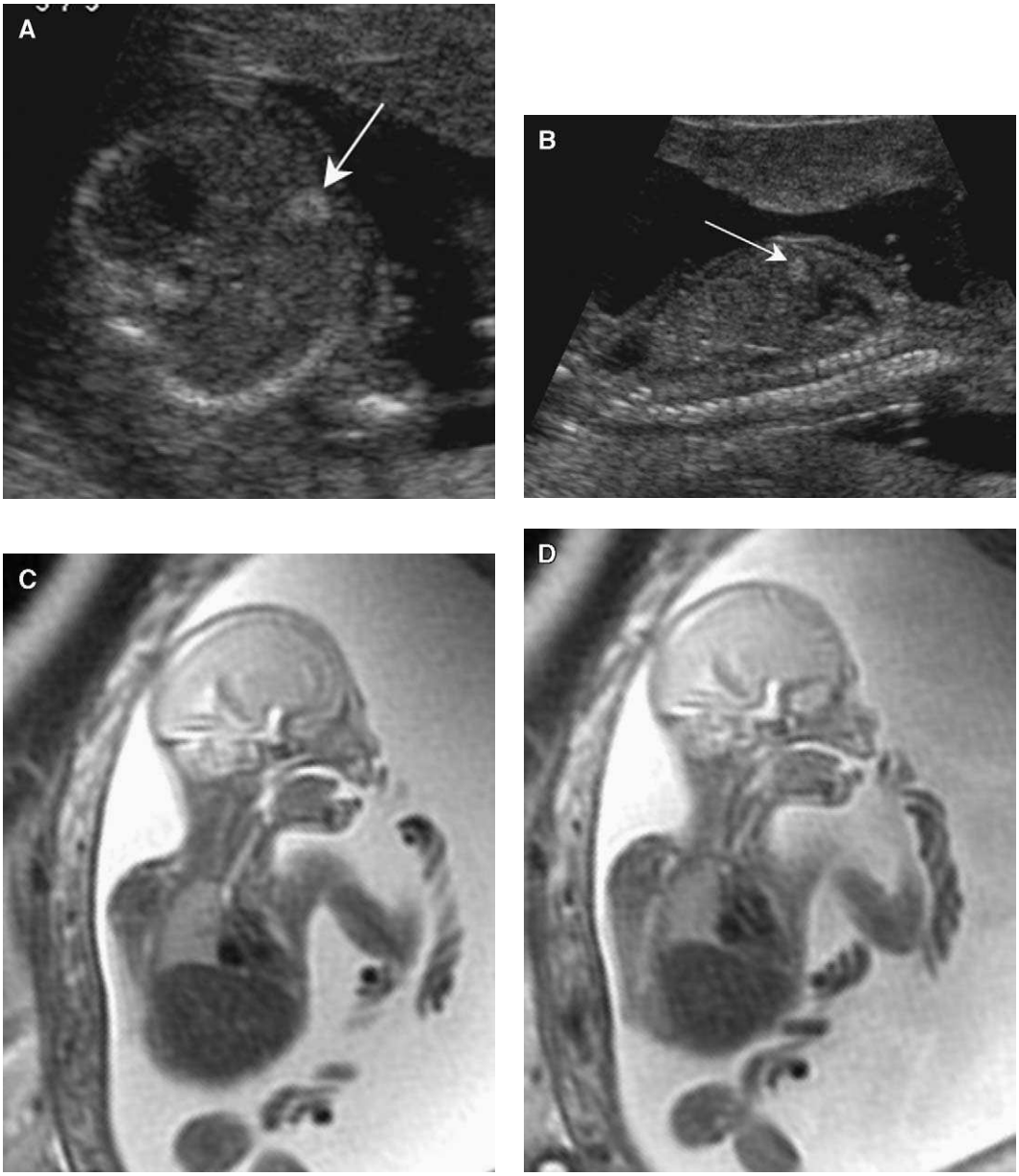

Fig. 31. US (*A,B*) and MR imaging (*C,D*) in a fetus at 21 weeks' gestation with a small echogenic mass in the liver. The mass is well seen on US (*arrows*) but is not visualized on MR imaging.

Summary

The technique of performing fetal MR examinations differs from routine pelvic MR imaging because the fetus is in motion, and image planes must be selected orthogonal to fetal anatomy. The small size of the fetus also increases examination difficulty because thin slices (limited by SNR) are often needed for adequate examination of anatomy and pathology. Knowledge of fetal anatomy and neonatal anatomy/pathology are needed in the assessment of fetal MR imaging. Knowledge of MR artifacts aids in image interpretation.

References

[1] Dinh DH, Wright RM, Hanigan WC. The use of magnetic resonance imaging for the diagnosis of fetal intracranial anomalies. Childs Nerv Syst 1990;6:212–5.

[2] Fusch C, Ozdoba C, Kuhn P, Durig P, Remonda L, Muller C, et al. Perinatal ultrasonography and magnetic resonance imaging findings in congenital hydrocephalus associated with fetal intraventricular hemorrhage. Am J Obstet Gynecol 1997;177:512–8.

[3] Kubik-Huch RA, Wisser J, Stallmach T, Ladd ME, Meier A, Marincek B. Prenatal diagnosis of fetal malformations by ultrafast magnetic resonance imaging. Prenat Diagn 1998;18:1205–8.

[4] Simon EM, Goldstein RB, Coakley FV, Filly RA, Broderick KC, Musci TJ, et al. Fast MR imaging of fetal CNS anomalies in utero. AJNR Am J Neuroradiol 2000;21:1688–98.

[5] Sonigo PC, Rypens FF, Carteret M, Delezoide AL, Brunelle FO. MR imaging of fetal cerebral anomalies. Pediatr Radiol 1998;28:212–22.

[6] Thickman D, Mintz M, Mennuti M, Kressel HY. MR imaging of cerebral abnormalities in utero. J Comput Assist Tomogr 1984;8:1058–61.

[7] Levine D, Mehta T, Trop I, Barnes P. Fast MRI of fetal CNS anomalies with prenatal MRI: results of 149 cases [abstract]. Radiology 2000;217:101.

[8] Levine D, Hatabu H, Gaa J, Atkinson MW, Edelman RR. Fetal anatomy revealed with fast MR sequences. AJR Am J Roentgenol 1996;167:905–8.

[9] Levine D, Barnes PD, Sher S, Semelka RC, Li W, McArdle CR, et al. Fetal fast MR imaging: reproducibility, technical quality, and conspicuity of anatomy. Radiology 1998;206:549–54.

[10] Levine D, Barnes PD, Edelman RR. State of the art: obstetric MR imaging. Radiology 1999;211:609–17.

[11] Levine D, Barnes P, Madsen J, Hulka C, Edelman RR. Evaluation of fetal central nervous system abnormalities with ultrafast MRI. Symposium Neuradiologicum XVI Proceedings 1998;242–3.

[12] Hubbard AM, Crombleholme TM, Adzick NS. Prenatal MRI evaluation of giant neck masses in preparation for the fetal exit procedure. Am J Perinatol 1998;15:253–7.

[13] Hubbard AM, Harty MP, States LJ. A new tool for prenatal diagnosis: ultrafast fetal MRI. Semin Perinatol 1999;23:437–47.

[14] Baker PN, Johnson IR, Harvey PR, Gowland PA, Mansfield P. A three-year follow-up of children imaged in utero using echo planar magnetic resonance. Am J Obstet Gynecol 1994;170:32–3.

[15] Chew S, Ahmadi A, Goh PS, Foong LC. The effects of 1.5T magnetic resonance imaging on early murine in-vitro embryo development. J Magn Reson Imaging 2001;13:417–20.

[16] Kanal E, Gillen J, Evans JA, Savitz DA, Shellock FG. Survey of reproductive health among female MR workers. Radiology 1993;187:395–9.

[17] Kanal E. Pregnancy and the safety of magnetic resonance imaging. Magn Reson Imaging Clin N Am 1994;2:309–17.

[18] Levine D, Zuo C, Faro CB, Chen Q. Potential heating effect in the gravid uterus during MR HASTE imaging. J Magn Reson Imaging 2001;13:856–61.

[19] Myers C, Duncan KR, Gowland PA, Johnson IR, Baker PN. Failure to detect intrauterine growth restriction following in utero exposure to MRI. Br J Radiol 1998;71:549–51.

[20] Schwartz JL, Crooks LE. NMR imaging produces no observable mutations or cytotoxicity in mammalian cells. AJR Am J Roentgenol 1982;139:583–5.

[21] Wolff S, Crooks LE, Brown P, Howard R, Painter RB. Tests for DNA and chromosomal damage induced by nuclear magnetic resonance imaging. Radiology 1980;136:707–10.

[22] Haacke EM, Brown RW, Thompson MR, Venkatesan R. Magnetic resonance imaging: physical principles and design. New York: Wiley-Liss; 1999.

[23] Roemer PB, Edelstein WA, Hayes CE, Souza SP, Mueller OM. The NMR phased array. Magn Reson Med 1990;16:192–225.

RADIOLOGIC
CLINICS OF
NORTH AMERICA

Radiol Clin N Am 41 (2003) 747–756

MR imaging of pelvic floor relaxation

Julia R. Fielding, MD

Department of Radiology, University of North Carolina at Chapel Hill, 101 Manning Drive, Campus Box 7510, Chapel Hill, NC 27599, USA

Pelvic floor relaxation, which is the abnormal descent of the bladder, uterus/vaginal vault, or rectum, is a significant women's health issue that affects primarily parous women older than 50 years. The condition is worsened by obesity and chronic obstructive pulmonary disease. Up to 50% of such women have some degree of genital prolapse. 10% to 20% of this group seek help from a physician. Symptoms range from urinary or fecal incontinence to procidentia, but most women report increased pelvic pain or pressure and protrusion of at least some tissue, usually through the vagina [1–4]. Many women also must use manual pressure on the perineum or vaginal fornices to complete defecation. For severely afflicted women such as these, pelvic floor relaxation becomes a health and significant lifestyle-limiting problem.

Anatomy

The pelvic floor can be divided into three compartments: (1) the anterior compartment, which contains the bladder and urethra, (2) the middle compartment, which contains the vagina, cervix, and uterus, and (3) the posterior compartment, which contains the rectum.

All three compartments are supported by a remarkable collection of fascia and muscle that forms the urogenital diaphragm, or pelvic floor. The muscles that provide the major support of the pelvic organs are two components of the levator ani: the puborectalis and the iliococcygeus (Fig. 1). The puborectalis, a portion of the pubovisceralis, arises and inserts on the parasymphyseal portion of the pubic rami. It extends posteriorly to form a sling around the rectum, which serves two purposes: (1) the orifices of the pelvic floor are kept closed and (2) the bladder neck is elevated and compressed against the pubic symphysis. Both muscles help to maintain a stable position of the pelvic organs and fecal and urinary continence. The iliococcygeus originates from the same fibers as the external anal sphincter. From there it extends laterally to insert at the arcus tendineus, or white line of the pelvic sidewall, and posteriorly to form a firm midline raphe just anterior to the coccyx. The posterior raphe is often called the levator plate. The iliococcygeus provides a physical barrier to organ descent and is the major support of the posterior compartment.

Inferior to this level, the urethra and vagina extend through the urogenital hiatus. The rectum extends beyond the pelvic diaphragm at this level and is separated from the vagina by the perineal body and anal sphincter.

The pelvic organs are also supported by a series of fascial condensations called ligaments. When the muscles of the pelvic floor are damaged, usually during childbirth, support of the pelvic organs falls to the fascia. The pubocervical fascia extends from the anterior vaginal wall to the pubis and supports the bladder. Elastic condensations of the endopelvic fascia, called the parametrium and paracolpium, support the uterus and vagina. The parametria are composed of the cardinal and uterosacral ligaments, both of which elevate and provide superior support to the uterine corpus. The paracolpium have been divided into three levels and extend from the vagina laterally to the sidewalls [5]. The posterior wall of the vagina and rectovaginal fascia supports the rectum, sigmoid colon, and portions of the small bowel. These fascial

E-mail address: julia_fielding@med.unc.edu

0033-8389/03/$ – see front matter © 2003 Elsevier Inc. All rights reserved.
doi:10.1016/S0033-8389(03)00042-3

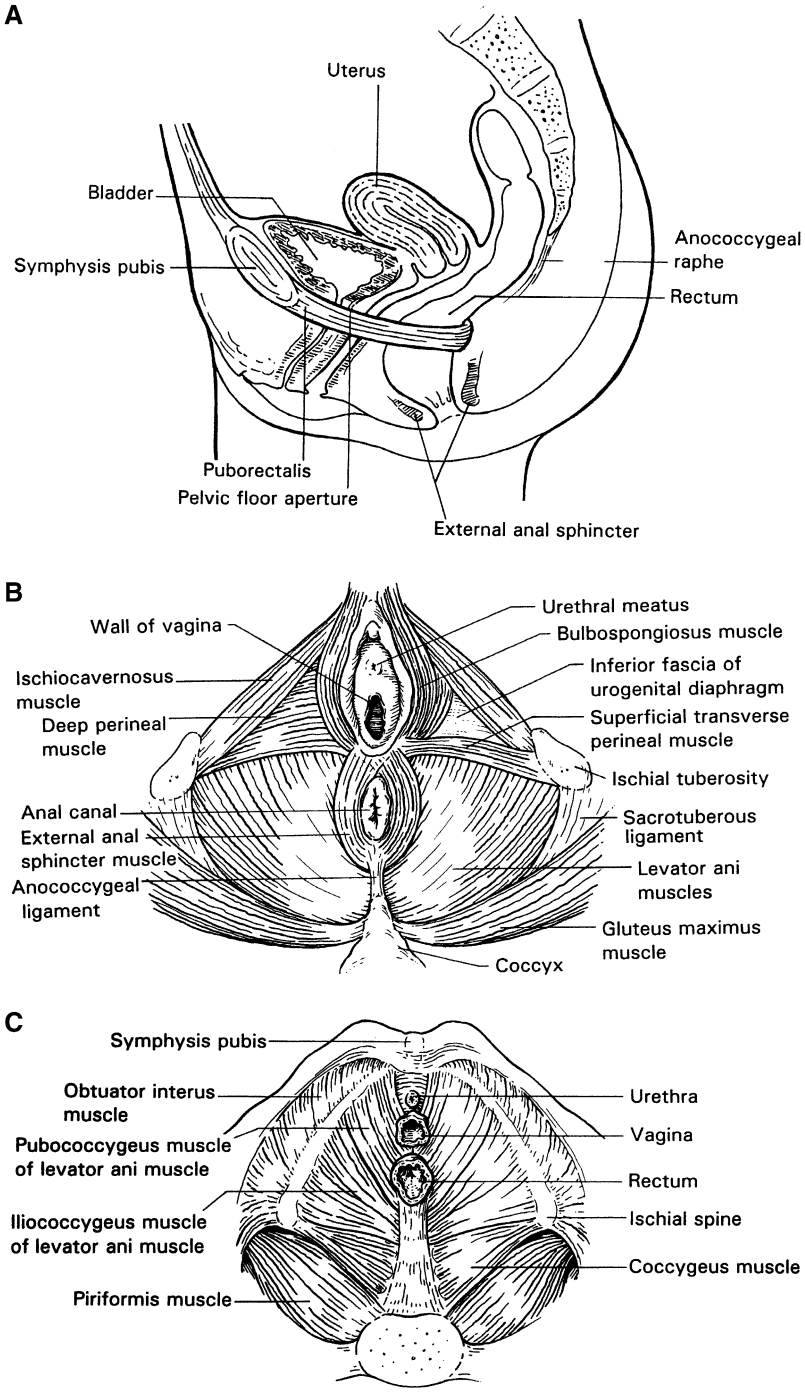

Fig. 1. Sagittal (*A*) and axial (*B*, *C*) line drawings demonstrate the pubococcygeus and the iliococcygeus muscles that are the major components of the levator ani. On sagittal images the pubococcygeal line is drawn from the last joint of the coccyx to the inferior aspect of the symphysis. In contrast to the sagittal drawing, the anococcygeal raphe, or levator plate, usually parallels the pubococcygeal line in women with intact pelvic floors. (*From* Cardozo L. Urogynecology. New York: Churchill-Livingstone; 1997. p. 325–6; with permission.)

condensations are rarely seen using standard methods of imaging but can be identified with MR imaging and an endovaginal coil [6].

Laxity of the supporting muscles and stretching or tearing of the fascial supports lead to pelvic floor relaxation. These deficits become greater in the middle-aged and elderly population likely because of diminished estrogen supply and blood flow to the pelvic floor. Loss of the pubocervical fascia leads to posterior descent of the bladder into the anterior vaginal wall, formation of a cystocele, and associated urinary incontinence. Loss of the paracolpia leads to urethral hypermobility and is often associated with intrinsic urethral sphincter damage. Damage to the parametria and paracolpia causes uterine descent and, in severe cases, procidentia. Tears in the rectovaginal fascia lead to the formation of sigmoidocele and enterocele and, occasionally, rectal intussusception. These women may present with constipation or a feeling of incomplete defecation.

Imaging techniques

For most patients with mild to moderate stress incontinence and pelvic floor relaxation, the combination of physical examination findings and urodynamic pressure readings is diagnostic and no further imaging is required. For patients with severe urinary or fecal incontinence believed to be multifactorial, multiple compartment involvement, or failed prior surgery, imaging can be valuable. Several techniques can be used to evaluate the pelvic organs, including voiding cystourethrography (with or without concurrent video urodynamic tracings), ultrasound of the bladder neck and anal sphincter, colpocystodefecography, and MR imaging.

Voiding cystourethrography

Voiding cystourethrography is often performed during an incontinence evaluation to exclude anatomic abnormalities, such as duplicated collecting systems and ureters, bladder and urethral diverticula, and vesicoureteral reflux. Even when these findings are not present, examination of the bladder can provide useful information. Trabeculation is a sign of urge incontinence or detrusor overactivity (Fig. 2) [7]. The hallmark of this disease is the sudden onset and imminent need to void because of a bladder contraction. This is the most common type of incontinence in elderly persons, and it affects up to 30% of persons living at home and 50% of persons in long-term care institutions [8]. Identification of an unsuspected neurogenic bladder is another significant finding. These patients often have a history of spinal injury. The bladder remains contracted and severely trabeculated during the entirety of the examination and may have a markedly tapered dome. Although voiding cystourethrography is rarely required to diagnose stress incontinence, it can be useful in severe cases in which the bladder extends so far inferiorly that the bladder neck kinks, which masks symptoms [9].

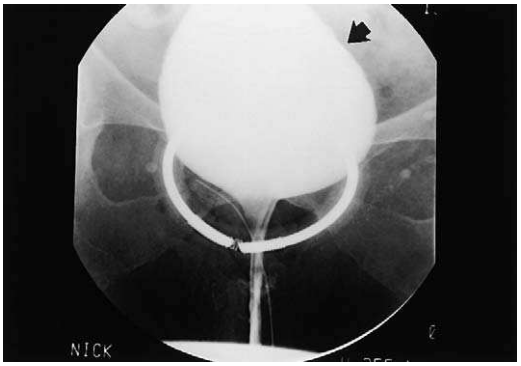

Fig. 2. Coronal image obtained during a voiding cystourethrogram in a 72-year-old woman who complained of urinary incontinence. A pessary is in place. The deformation of the left aspect of the bladder wall (*arrow*) corresponded to a detrusor muscle contraction, which indicated the presence of urge incontinence.

Ultrasound

Ultrasound of the bladder neck or perineum is an alternative way to diagnose stress incontinence. Again it is usually only of clinical use for assessment of bladder neck mobility. Transrectal ultrasound has been shown to be reliable in the identification of rectal sphincter tears and atrophy (Fig. 3) [10,11]. It is often used before surgery to gauge the size and depth of tear and identify adjacent hypoechoic scar tissue. A small probe that provides circumferential images is placed in the rectal canal. Images are obtained at 5-mm intervals along the length of the sphincter, approximately 2.5 cm. The normal internal sphincter is a circumferential black band of uniform thickness. The external sphincter is harder to see because it is echogenic. Tears are defined as areas of discontinuity. Large tears respond poorly even to aggressive surgical intervention.

Defecography

Colpocystodefecography is a method of observing all three compartments of the pelvic floor during rest,

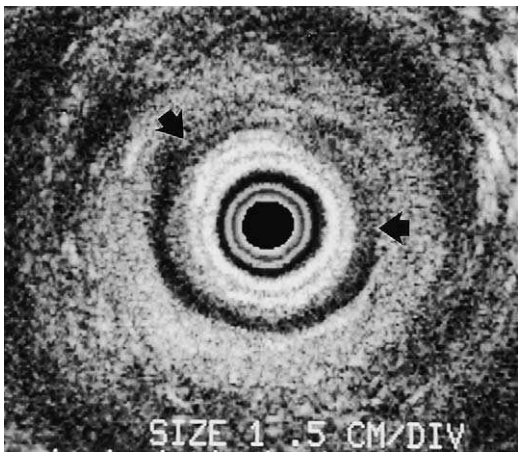

Fig. 3. Axial image obtained during a transrectal ultrasound of a 58-year-old woman with fecal incontinence. The internal anal sphincter becomes increasingly hyperechoic and thin (*between arrows*), which indicates damage to the anterior portion, with a tear at the midline.

upward contraction, and Valsalva maneuver. Because it is done in the sitting position, it most closely mimics the physiologic state [12]. In most institutions it is used primarily to identify posterior compartment abnormalities, so the bladder is not opacified. 1 hour before the study, the patient is a given a barium meal to coat the small bowel loops. Barium paste is placed into the rectum, usually with the aid of a caulking gun, and the patient places a tampon soaked in contrast material in the vagina. In the upright position, multiple spot fluoroscopic images are obtained during pelvic floor maneuvers, concluding with defecation. With pelvic floor contraction, a sharp anorectal angle is an indicator of good muscular support; however, specific measurements have not been found useful. Retained barium within a portion of the anterior rectum that bulges more than 2 cm into the rectovaginal space is defined as an anterior rectocele. Patients often are able to empty the rectocele manually. Descent of small bowel loops into the rectovaginal space is defined as an enterocele and indicates a tear in the rectovaginal fascia (Fig. 4). Many gastroenterologists believe that an enterocele gives a patient the feeling of incomplete defecation despite the presence of an empty rectum, which leads to persistent and ineffectual straining. Intussusception usually involves only the rectum or rectosigmoid and resolves with cessation of Valsalva maneuver.

MR imaging

During the past 10 years, MR imaging has emerged as a competitor to other imaging modalities for evaluation of the female pelvic floor. The main advantages of MR imaging are ability to evaluate the three compartments of the pelvic floor simultaneously during rest and strain and direct visualization of supporting structures [13,14]. Disadvantages include the requirement that the examination be performed in the supine or left lateral decubitus position, although

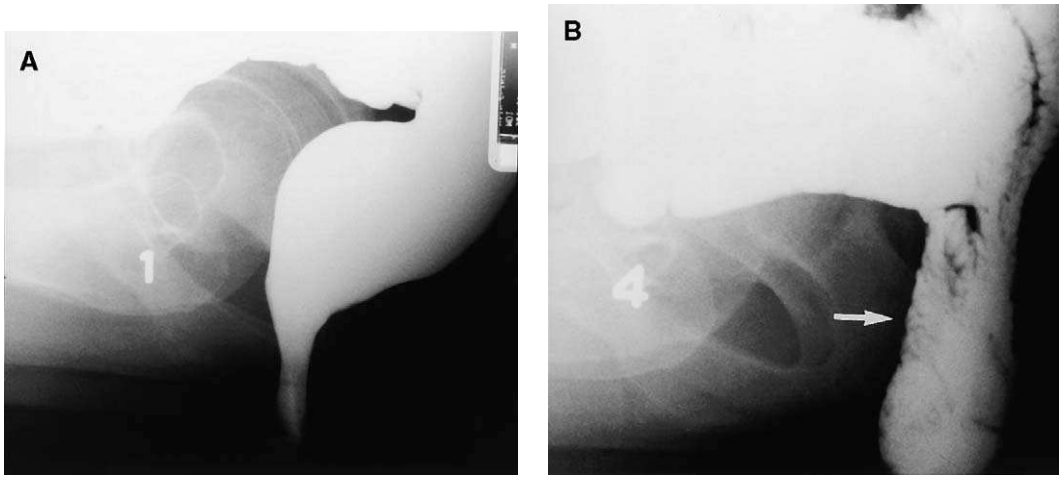

Fig. 4. Sagittal images obtained during defecography performed on a 56-year-old woman who complained of incomplete evacuation. (*A*, *B*) The patient is in the sitting position on a commode chair. (*A*) The patient is evacuating the rectum. No anterior rectocele is identified. (*B*) Multiple loops of small bowel extend posteriorly and inferiorly to the anorectal junction (*arrow*). This is diagnostic of a rare posterior enterocele.

one group working with an open configuration magnet reported no significant difference between upright and supine findings [15]. Because pelvic floor MR imaging is a relatively new technique, the remainder of this article is devoted to a discussion of imaging protocols and interpretation.

MR technique

Obtaining high-quality, useful images requires careful attention to patient preparation and examination technique. Just before imaging, the patient is asked to void, which prevents a distended bladder from distorting adjacent anatomy. If the examination is focused on the posterior compartment, 60 cc of ultrasound gel is placed in the rectum using a small catheter. A multicoil array, either pelvis or torso, is wrapped around the inferior portion of the pelvis and the patient is placed in the supine or left lateral decubitus position. It is important that the coil be placed low enough so that prolapsing structures can be seen.

After a rapid T1-weighted or gradient echo large field-of-view localizer sequence in the sagittal plane, the midline is identified. This image should encompass the symphysis, bladder neck, vagina, rectum, and coccyx. The patient is then coached on how to maintain maximum Valsalva. Most women can maintain maximal pressure for less than 10 seconds. Using an ultrafast T2-weighted imaging sequence, such as single shot fast spin-echo (on GE magnets [General Electric Medical Systems, Milwakee, WI]) or half Fourier acquisition turbo spin echo (on Siemens magnets [Siemens Medical Solutions USA, Malvern, PA]), sagittal midline images 10 mm in thickness are obtained at rest and at maximal Valsalva strain. Table 1 shows typical pulse sequence parameters. Each image is obtained in approximately 3 seconds. The strain images can be repeated after additional verbal coaching if necessary. If a perineal hernia or ballooning of the puborectalis is suspected, these images can be performed in the coronal plane. A standard fast spin-echo or turbo spin-echo (Siemens) sequence is then obtained in the axial view to provide high-resolution images of the supporting structures of puborectalis, pubocervical fascia, and fascial condensations supporting the urethra. T1-weighted and contrast medium-enhanced images are not required. Room time for this examination is approximately 15 minutes. Comparison of this and similar MR techniques with colpocystodefecography has revealed good correlation [16].

MR anatomy

On sagittal images, the pubococcygeal line should be drawn between the last joint of the coccyx and the inferiormost aspect of the symphysis. Urologists and gynecologists use this line as an indicator of the pelvic floor. In early work, Yang et al [17] used gradient echo images to define maximal normal descent of the bladder base (1 cm below), vagina (1 cm above), and rectum (2.5 cm below) with respect to the pubococcygeal line. In practical terms, descent of the bladder or vagina more than 1 cm below the pubococcygeal line indicates some degree of laxity, whereas descent of more than 2 cm in a symptomatic patient often requires surgical therapy. Rectal abnormalities, such as anterior rectocele, intussusception, and enterocele, are identified in the same fashion as with defecography. There are other important findings on sagittal images. The levator plate should remain parallel to the pubococcygeal line at all times. Caudal angulation of the levator plate more than 10° indicates loss of pelvic floor support [18,19].

Measurement of the H and M lines are useful ways to quantify loss of pelvic floor support (Fig. 5) [20]. The H is drawn from the inferior aspect of the

Table 1
Pelvic floor protocol for evaluation of relaxation and incontinence

Sequence	Plane	TR (msec)	TE (msec)	FOV (cm)	Slice thickness/ gap (mm)	Flip angle	Matrix freq × phase	Number excitations
Localizer	Sagittal	15	5	350–400	10 mm / 0	1°	160 × 256	
HASTE[a]	Sagittal	NA	90	300	10 mm / 0 / 1 slice	180°	128 × 256	1 acq/ center low
T2 Turbo SE	Transverse	5000	132	200–400	3 mm / interleaved	180°	270 × 256	2 acq
T2 Turbo SE (optional)	Coronal	5000	132	200–240	5 mm / 1 mm	180°	270 × 256	2 acq

Abbreviations: freq, frequency; HASTE, half Fournier single shot turbo spin echo; NA, not applicable; SE, spin echo.
[a] Repeat this sequence at maximal strain (Valsalva).

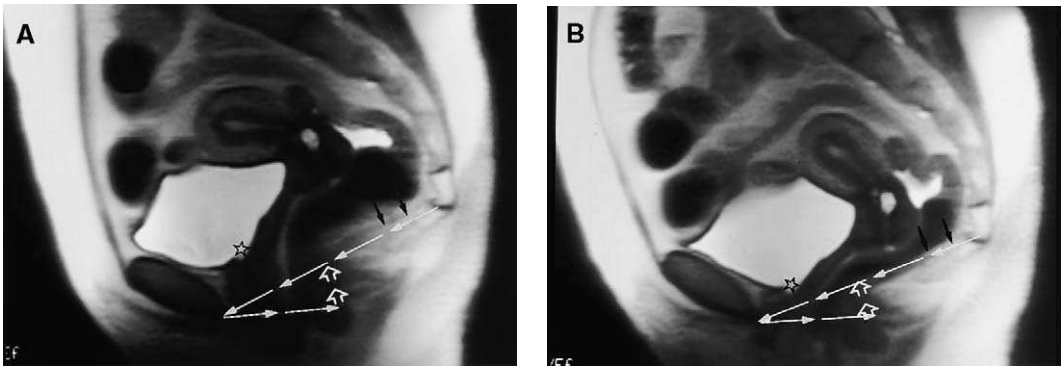

Fig. 5. T2-weighted (2200/96) pelvic MR image of a 46-year-old healthy, continent volunteer. Sagittal images of the subject at rest (*A*) and at strain (*B*) show minimal inferior movement of the pelvic viscera. The bladder neck is marked with a star. The levator plate (*black arrows*) remains parallel with the pubococcygeal line (*upper line of white solid arrows*). The H (*lower line of white solid arrows*) and M (*open arrows*) lines are less than 5 cm and 2 cm, respectively, which indicates an intact levator hiatus. (*From* Fielding JR. Practical MR imaging of female pelvic floor weakness. Radiographics 2002;2:295–304; with permission.)

symphysis pubis to the posterior wall of the rectum and measures the anteroposterior dimension of the pelvic hiatus. The M line is drawn as a perpendicular from the pubococcygeal line to the posteriormost aspect of the H line. It measures the height of the hiatus. In healthy women, the H line should not exceed 5 cm, and the M line should not exceed 2 cm. Values more than these indicate loss of pelvic floor support.

Axial images should be reviewed for muscle integrity and signal intensity and for the vaginal shape and location. The puborectalis should extend from the parasymphysial insertion posterior to the rectum. It should be of similar width along its entire course without evidence of gaps or fraying (Fig. 6). The width of the levator hiatus at the level of the symphysis rarely exceeds 4.5 cm in healthy volunteers; however, there is some overlap with incontinent patients. The vagina normally should be of an H or butterfly shape and be centered in the pelvis [21].

Anterior compartment pathology

Women who present with severe stress incontinence refractory to behavioral, drug, and surgical therapy are good candidates for MR imaging. At strain, the bladder neck extends well below the pubococcygeal line. Because of the strong attachments anteriorly, the posterior wall of the bladder rotates posteriorly and inferiorly, impressing on the vaginal wall. The H and M lines are increased in length. During bladder descent, the urethra sometimes rotates clockwise. This kinking of the urethra at the level of the bladder neck often masks the presence of stress incontinence. The more the patient strains, the less urine leaks out. A mobile urethra is also associated with damage to the internal urethral sphincter (Fig. 7). On axial images, the puborectalis may be avulsed or thinned, which indicates muscle damage. Increased signal intensity of the puborectalis compared with the obturator musculature likely indicates fatty infiltration and has been reported in

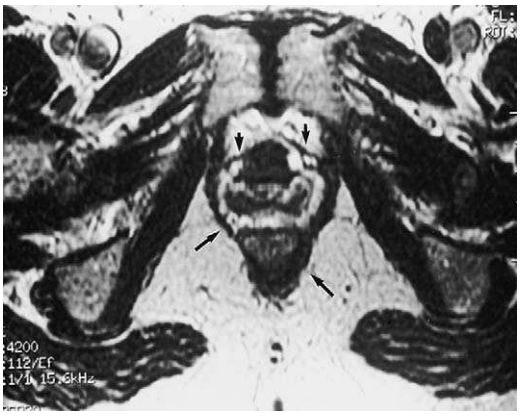

Fig. 6. Axial T2-weighted image (4200/12) shows the vagina to be butterly shaped and centered within the pubococcygeal sling (*long arrows*). Anteriorly the external urethral sphincter and lateral pubovesical ligaments hold the urethra in place and form part of the extrinsic continence mechanism (*short arrows*).

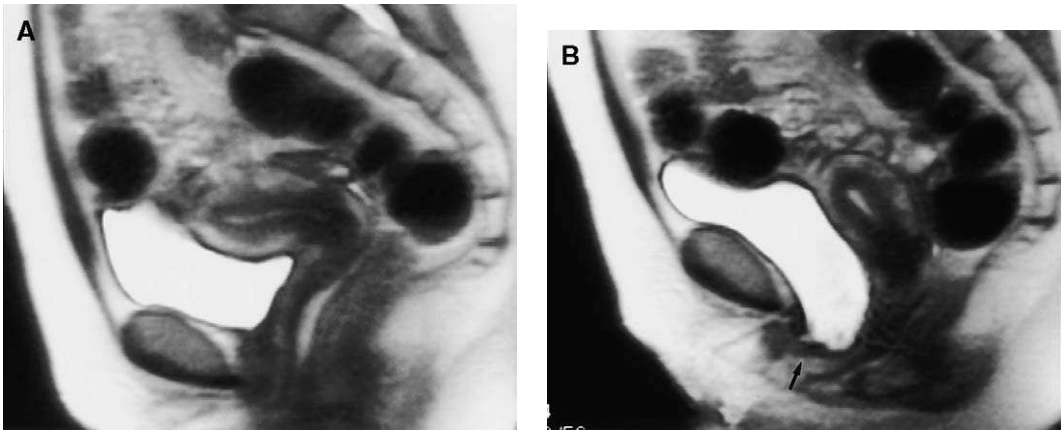

Fig. 7. Stress incontinence and incomplete bladder emptying in a 55-year-old woman. Sagittal T2-weighted images (2200/96) at rest (*A*) and at strain (*B*) show significant descent of the bladder, with rotation of the urethra into the horizontal plane (*arrow*) with strain. This may mask stress incontinence. (*From* Fielding JR. Practical MR imaging of female pelvic floor weakness. Radiographics 2002;2:295–304; with permission.)

association with stress incontinence [22]. Abnormal shape or location of the vagina is a good indication of a paravaginal tear (Fig. 8). These findings are critical to the referring surgeon. Large cystoceles with presumed paravaginal tears are usually treated with a fascial repair and bladder suspension procedure. When physical examination, urodynamics, and MR imaging suggest a mobile urethra, a sling procedure is often performed to increase pressure on the urethra and coaptation of the walls at rest.

Middle compartment pathology

Descent of the reproductive organs is almost always associated with cystocele formation because of the shared fascial supports. Gynecologists grade descent by comparing organ location with bony and soft tissue landmarks. On sagittal MR imaging, descent of the uterus in addition to the vagina and cervix usually indicates rupture of the cardinal or uterosacral ligaments. It is not uncommon to identify a uterine fibroid that prevents descent of the uterus and masks the true degree of pelvic floor and supporting fascial damage (Fig. 9). The H and M lines again are of increased length. In cases of significant middle compartment damage, axial images often show a flattened vagina and a widened hiatus (Fig. 10). Perimenopausal or postmenopausal women with significant anterior and middle compartment relaxation often opt for hysterectomy with paravaginal repair. Younger women who wish to retain their uteri undergo reapproximation of the uterosacral and cardinal ligaments in addition to a paravaginal repair.

Posterior compartment pathology

A rectocele or enterocele can occur alone or in combination with other pelvic floor defects to form

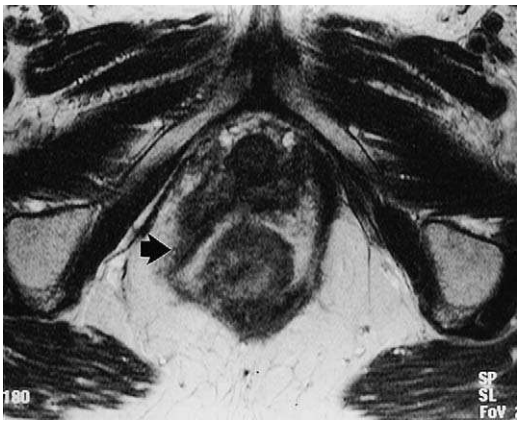

Fig. 8. A 64-year-old woman complained of dyspareunia. Axial T2-weighted image (4400/12) of the pelvic floor shows posterior displacement of the right vaginal fornix and a complete tear of the pubococcygeal sling (*arrow*). (*From* Fielding JR. Practical MR imaging of female pelvic floor weakness. Radiographics 2002;2:295–304; with permission.)

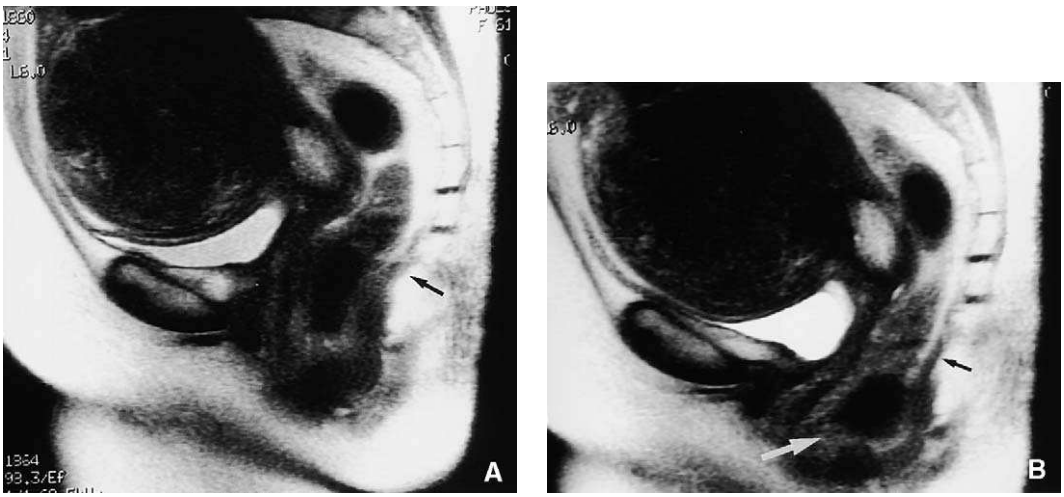

Fig. 9. A 63-year-old woman complained of incomplete bowel evacuation and pelvic pressure. Sagittal T2-weighted (2200/96) MR image at rest (*A*) and at strain (*B*) show a large fibroid that is likely preventing descent of the anterior and middle compartments. The levator plate is vertically oriented (*black arrow*), and there is development of a rectocele (*white arrow*), which indicates significant damage to the posterior compartment. (*From* Fielding JR. Practical MR imaging of female pelvic floor weakness. Radiographics 2002;2:295–304; with permission.)

global pelvic floor relaxation. Many of these patients previously underwent hysterectomies that left them with thinned or torn fascia. On sagittal MR imaging, a rectocele is identified by anterior bulging of the rectal wall, usually into the pouch of Douglas. Enteroceles occur when the rectovaginal fascia is torn, which allows small bowel loops to descend more than 2 cm, again into the cul-de-sac. The levator plate often maintains its normal angulation, and the M and H lines are normal or only minimally elongated with an isolated anterior rectocele or enterocele. The rectocele is treated with a posterior fascial repair. Enterocele repair requires reapproximation of the rectovaginal fascia.

Global pelvic floor relaxation

In severe cases, there is significant descent of the contents of all three compartments of the pelvic floor below the pubococcygeal line [23]. The levator plate is nearly vertical, and there is extreme elongation of the H and M lines (Fig. 11). On axial images there is nearly always increased hiatal width and ballooning of the iliococcygeus. This latter finding and any associated perineal hernias may be identified best on coronal images. Repair of these patients is complex and often includes hysterectomy and an anterior and posterior fascial repair (Fig. 12).

New techniques

Seated imaging

During the past 5 years, several research groups have reported on the feasibility and usefulness of MRI in the upright position [13,24,25]. The primary advantage of this technique is that the seated position

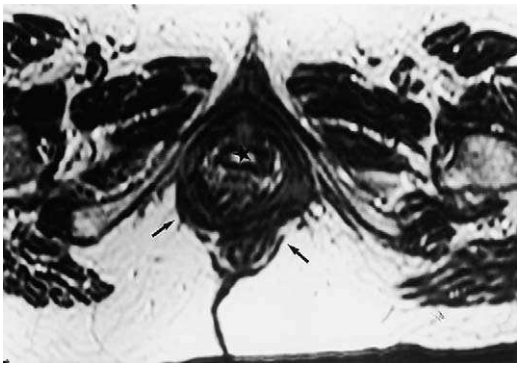

Fig. 10. A 58-year-old woman complained of pelvic pressure and had significant descent of the cervix on physical examination. Axial T2-weighted (4400/12) image shows widening of the hiatus and descent of the pubococcygeal sling (*arrows*). The bladder neck is dilated (*star*).

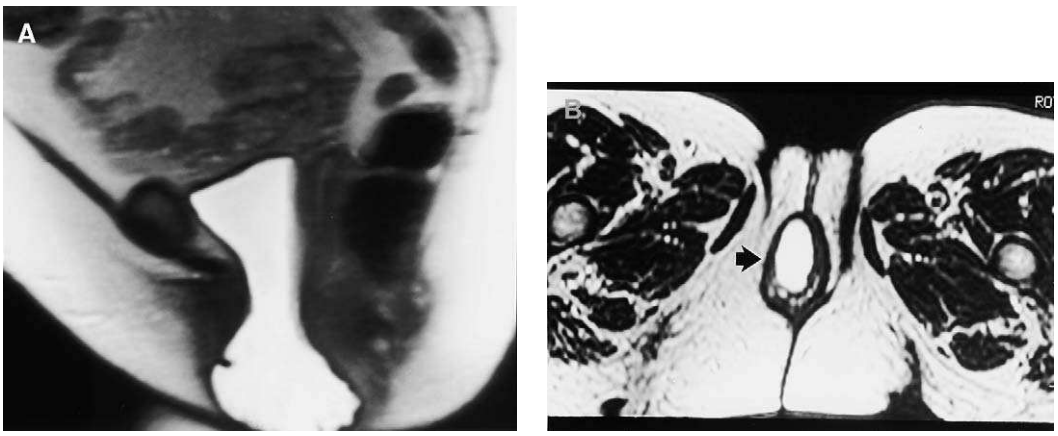

Fig. 11. Pelvic pressure and protrusion of tissue through the pelvic floor in a 68-year-old woman. (*A*) Sagittal T2-weighted image of the patient at strain shows global pelvic floor weakness with a severe cystocele and moderate descent of the uterus and rectum. (*B*) Axial T2-weighted image (4400/12) shows the bladder protruding through the labia (*arrow*). (*From* Fielding JR. Practical MR imaging of female pelvic floor weakness. Radiographics 2002;2:295–304; with permission.)

maximizes symptoms and imaging findings. Disadvantages include the low signal to noise images obtained using available 0.5 T equipment.

Three-dimensional volumetric analysis

The formation of three-dimensional models of the muscular supports of the female pelvic floor is primarily a research tool. The models can be used to quantify muscle volume, simulate lithotomy views, and plan resection of vulvar tumors or repair of the pelvic floor [26]. The technique is based on acquisition of thin (3 mm) axial T2-weighted images that encompass the important soft tissue organs and bony landmarks. A three-dimensional rendering program is then performed that allows various degrees of opacity and, depending on the program used, color. The model pelvis can be rotated at will. This technique has been used to define the volume of the puborectalis in healthy young women and demonstrate that diminished volume correlates well with worsening pelvic floor relaxation [18,26]. It is hoped that in the future this tool can be used to predict surgical outcomes, thereby enabling correct triage of the patient at presentation.

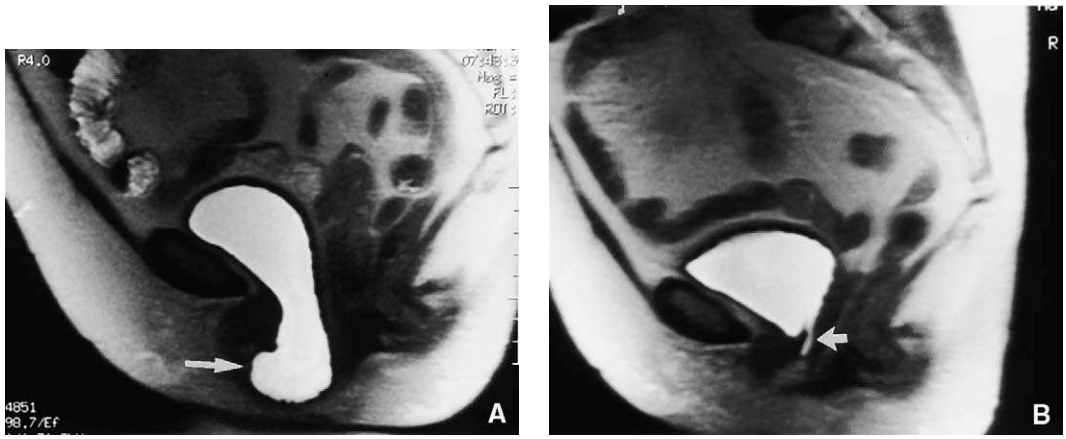

Fig. 12. Cystocele and vaginal vault prolapse in a 74-year-old woman. (*A*) Sagittal T2-weighted MR image (2200/96) obtained at maximal strain shows a large cystocele (*arrow*). (*B*) After surgical repair, midline image obtained with the same MR parameters shows a small residual posterior fascial defect (*arrow*). (*From* Fielding JR. Practical MR imaging of female pelvic floor weakness. Radiographics 2002;2:295–304; with permission.)

Summary

The wide variety of available surface coils, pulse sequences, and post-processing techniques make MR imaging a useful clinical and research tool for evaluation of pelvic floor relaxation. Cases of isolated cystocele do not require imaging; however, in cases in which multiple compartments of the pelvis are involved or the patient has failed prior surgery, MR imaging should be considered for preoperative planning.

References

[1] Molander U, Milsom I, Ekelund P, Mellstrom D. An epidemiological study of urinary incontinence and related urogenital symptoms in elderly women. Maturitas 1990;12:51–60.

[2] Rush CB, Entman SS. Pelvic organ prolapse and stress urinary incontinence. Med Clin North Am 1995;79: 1473–9.

[3] Tapp A, Cardozo L. The effect of epidural anesthesia on postpartum voiding. Neurologic Urodynamics 1987; 6:235–9.

[4] Harris TA, Bent AD. Genital prolapse with and without urinary incontinence. J Reprod Med 1990;35:792–8.

[5] DeLancey JOL. Structural aspects of the extrinsic continence mechanism. Obstet Gynecol 1988;72: 296–301.

[6] Tan IL, Stoker J, Zwamborn AW, Entius KAC, Calame JJ, Lamèris JS. Female pelvic floor: endovaginal MR imaging of normal anatomy. Radiology 1998;206: 777–83.

[7] Fielding JR, Lee JH, Dubeau CE, Zou KH, Resnick NM. Voiding cystourethrography findings in elderly women with urge incontinence. J Urol 2000;163: 1216–8.

[8] Resnick NM, Ouslander JG. Urinary incontinence: where do we stand and where do we go from here? J Am Geriatr Soc 1990;38:263–4.

[9] Pelsang RD, Bonney WW. Voiding cystourethrography in female stress incontinence. AJR Am J Roentgenol 1996;166:561–5.

[10] Gold DG, Halligan S, Kmiot W, Bartram CI. Anal endosonography: inter- and intra-observer agreement. Br J Surg 1999;86:371–5.

[11] Sentovich SM, Wong DW, Blatchford GJ. Accuracy and reliability of transanal ultrasound for anterior anal sphincter injury. Dis Colon Rectum 1998;41: 1000–4.

[12] Kelvin FM, Maglinte DD, Hornback JA, Benson JT. Pelvic prolapse: assessment with evacuation proctography (defecography). Radiology 1992;184:547–51.

[13] Fielding JR, Griffiths DJ, Versi E, Mulkern RV, Lee ML, Jolesz FA. MR imaging of pelvic floor continence mechanisms in the supine and sitting positions. AJR Am J Roentgenol 1998;171:1607–10.

[14] Unterweger M, Marincek B, Gottstein-Aalame N, Debatin JF, Seifert B, Ochsenbein-Imhof N, et al. Ultrafast MR imaging of the pelvic floor. AJR Am J Roentgenol 2001;176:959–63.

[15] Bertschinger KM, Hetzer FH, Roos JE, Treiber K, Marincek B, Hilfiker PR. Dynamic MR imaging of the pelvic floor performed with patient sitting in an open-magnet unit versus with patient supine in a closed-magnet unit. Radiology 2002;223:501–8.

[16] Kelvin FM, Maglinte DDT, Hale DS, Benson JT. Female pelvic organ prolapse: a comparison of triphasic dynamic MR imaging and triphasic fluoroscopic cystocolopoproctography. AJR Am J Roentgenol 2000; 174:81–8.

[17] Yang A, Mostwin JL, Rosenshein NB, Zerhouni EA. Pelvic floor descent in women: dynamic evaluation with fast MR imaging and cinematic display. Radiology 1991;179:25–33.

[18] Hoyte L, Schierlitz L, Zou K, Flesh G, Fielding JR. Two- and 3-dimensional MRI comparison of levator ani structure, volume, and integrity in women with stress incontinence and prolapse. Am J Obstet Gynecol 2001;185:11–9.

[19] Ozasa H, Mori T, Togashi K. Study of uterine prolapse by magnetic resonance imaging: topographical changes involving the levator ani muscle and the vagina. Gynecol Obstet Invest 1992;24:43–8.

[20] Comiter CV, Vasavada SP, Barbaric ZL, Gousse AE, Raz S. Grading pelvic prolapse and pelvic floor relaxation using dynamic magnetic resonance imaging. Urology 1999;3:454–7.

[21] Klutke C, Golomb J, Barbaric Z, Raz S. The anatomy of stress incontinence: magnetic resonance imaging of the female bladder neck and urethra. J Urol 1990;143: 563–6.

[22] Kirschner-Hermanns R, Wine B, Niehaus S, Schaefer W, Jakse G. The contribution of magnetic resonance imaging of the pelvic floor to the understanding of urinary incontinence. Br J Urol 1993;72:715–8.

[23] Healy JC, Halligan S, Reznek RH, Watson S, Phillips RKS, Armstrong P. Patterns of prolapse in women with symptoms of pelvic floor weakness: assessment with MR imaging. Radiology 1997;203:77–81.

[24] Law PA, Danin JC, Lamb GM, Regan L, Darzi A, Gedroyc WM. Dynamic imaging of the pelvic floor using an open-configuration magnetic resonance scanner. J Magn Reson Imaging 2001;13:923–9.

[25] Schoenenberger AW, Debatin JF, Guldenschuh I, Hany TF, Steiner P, Krestin GP. Dynamic MR defecography with a superconducting, open-configuration MR system. Radiology 1998;206:641–6.

[26] Fielding JR, Dumanli H, Schreyer AG, Okuda S, Gering DA, Zou KH, et al. MR-based three-dimensional modeling of the normal pelvic floor in women: quantification of muscle mass. AJR Am J Roentgenol 2000; 174:657–60.

RADIOLOGIC
CLINICS OF
NORTH AMERICA

Radiol Clin N Am 41 (2003) 757–767

Imaging of female infertility

Amy S. Thurmond, MD[a,b,*]

[a]*Tualatin Imaging, 8950 Southwest Nimbus Avenue, Beaverton, OR 97008, USA*
[b]*Department of Obstetrics and Gynecology, Oregon Health Sciences University, 8950 Southwest Nimbus Avenue, Beaverton, OR 97008, USA*

Normal reproduction

The female reproductive tract includes the vagina, uterus and cervix, fallopian tubes, and ovaries and the hypothalamus and pituitary, breasts, and their supporting structures. For the discussion of infertility, the article focuses on the structures of the female pelvis and the monthly physiologic changes that allow conception to occur and are reflected in anatomic changes that can be imaged.

The hypothalamus in the female controls the monthly cycling of hormones responsible for normal ovulation and the readying of the endometrium for embryo implantation. Releasing factors from the hypothalamus stimulate production and release of the anterior pituitary gonadotropins, follicle-stimulating hormone, and luteinizing hormone. Follicle-stimulating hormone and luteinizing hormone cause maturation of ovarian follicles signaled by increase in follicular fluid and follicular estrogen production. The increasing estrogen results in a surge of leuteinizing hormone, which in turn causes rupture of one follicle and expulsion of its ovum, which can then be swept into the fimbriated end of the fallopian tube. The ruptured follicle develops into a corpus luteum, which produces progesterone and estrogen and has a life span of approximately 12 to 13 days. Estrogen and progesterone stimulate growth and development of the secretory endometrium. The follicles that developed, but were not ovulated, become atretic. Sperm are deposited in the vagina and travel up the cervix and uterus into the fallopian tube. Fertilization of the ovum occurs in the ampullary portion of the fallopian tube. As the embryo begins to develop, it travels down the fallopian tube and into the uterine fundus, where it implants in the endometrium. If conception does not occur, the corpus luteum regresses and its hormones are withdrawn, which results in endometrial shedding (menstruation). The cycle is repeated every month, with an average duration of 28 days for the follicular, secretory, and regression phases.

Infertility

Infertility affects one in seven American couples [1]. Approximately 40% of the time the cause is attributable to the woman; 40% of the time the cause is attributable to the man. Approximately 20% of the time there may be combined or unexplained factors. In the past, a radiologist or imaging specialist only encountered the infertile couple at the time of hysterosalpingography, which remains a mainstay in the diagnosis of uterine and tubal causes of infertility. In the past 15 to 20 years, however, there have been advances in treatment for the various causes of infertility, development of new imaging modalities, and improvement of old methods.

* Department of Obstetrics and Gynecology, Oregon Health Sciences University, 8950 Southwest Nimbus Avenue, Beaverton, OR 97008.
E-mail address: amyt@epicimaging.com

0033-8389/03/$ – see front matter © 2003 Elsevier Inc. All rights reserved.
doi:10.1016/S0033-8389(03)00064-2

Traditionally, the causes of infertility are divided into cervical, endometrial/uterine, tubal, peritoneal, ovulatory, and male factor

Cervix

The cervix contains glands that secrete mucus and crypts that harbor sperm. The hospitality of the cervix to sperm is not evaluated by imaging the cervical anatomy but is best determined by the postcoital test. The postcoital test is performed within 24 hours of intercourse and is accomplished by aspiration of the cervical mucus, which is then examined microscopically. The quantity and motility of living sperm are assessed. The most common cause of an abnormal result, also called "hostile mucus," is timing of the test too early or too late in relation to ovulation.

The normal size and appearance of the cervix are variable; therefore, diagnosis based on appearance alone is difficult. An internal os region that is less than 1 mm in diameter by hysterosalpingography (HSG) in a woman with painful periods may indicate cervical stenosis. An internal os wider than 1 cm or a funnel-shaped uterus and cervix in a woman with painless second trimester pregnancy confirms the diagnosis of incompetent cervix [2].

Uterus

Anomalies or defects that affect the size and shape of the uterine cavity and uterine wall also may affect the blood supply and ability of the uterus to support the developing embryo and fetus. The normal shape of the uterine cavity is that of an inverted triangle relative to the cervical canal. The size of the normal cavity can vary, depending on the imaging modality used and whether uterine distention is being used. A subjective sense of normal size and shape, rather than numeric criteria, is most helpful. The uterine wall is usually approximately 2 cm thick. The wall of the uterus is best imaged by sonography or MR imaging, whereas the cavity is best imaged by contrast hysterography (Fig. 1).

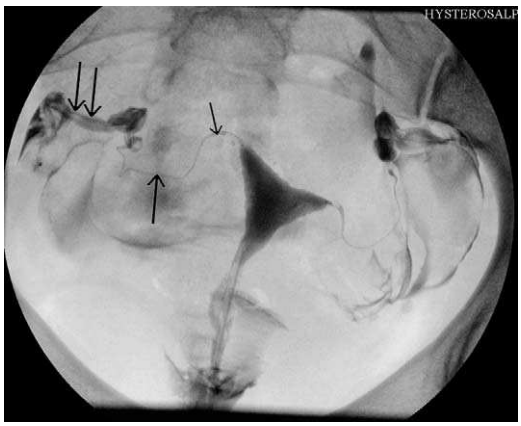

Fig. 1. Normal hysterosalpingogram demonstrates fallopian tube interstitial portion (*short arrow*), isthmic portion (*long arrow*), ampullary portion (*double arrows*).

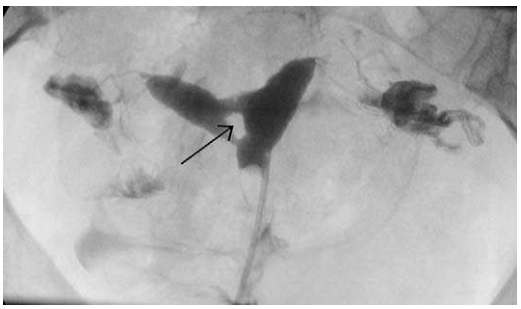

Fig. 2. Small, irregular, well-defined filling defect in the mid uterine cavity (*arrow*) is a synechia from prior miscarriage with dilatation and curettage.

Uterine cavity filling defects

Uterine cavity filling defects encountered during HSG may be caused by synechia, which are scars that result from uterine trauma, such as complications of pregnancy, curettage, uterine surgery, or uterine infection. Synechiae are generally linear and irregular (Fig. 2) and extend from one wall to the opposite wall, which allows contrast agent to flow around them only in one dimension. For this reason, they are more easily defined than polyps, myomas, or other masses that generally allow contrast agent to flow around them in two dimensions. Polyps are small and smooth, do not distort the shape of the cavity, are often multiple, and are echogenic by sonography (Fig. 3). Leiomyomas are usually larger, more vascular, and single and do enlarge and distort the cavity (Fig. 4). Air bubbles are round, smooth, and mobile. Blood clots are lobulated avascular intracavitary masses. Products of conception, if retained from an earlier pregnancy, are usually irregular, unlike the other entities described previously.

All intracavitary masses probably can interfere with embryo implantation. Even small masses may become inflamed and act like an intrauterine device for contraception. Large masses may distort the cavity and the blood supply to the developing embryo. It is important to define the number, size, and

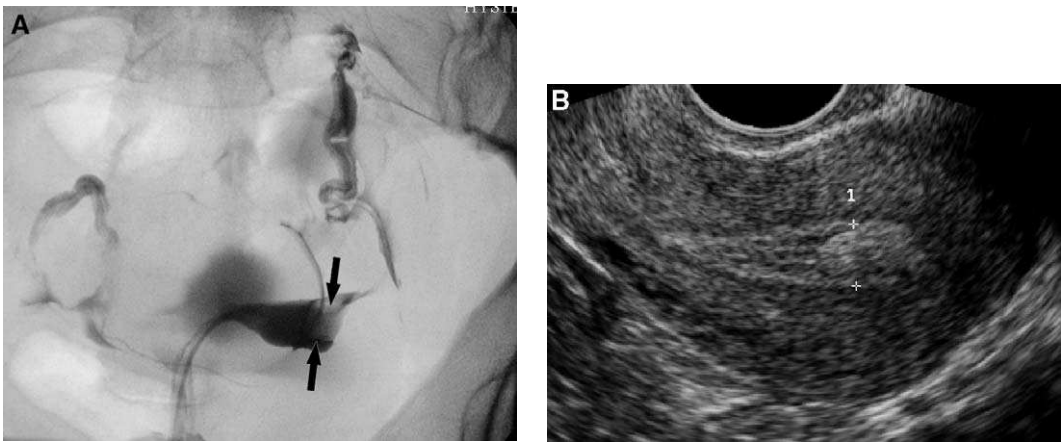

Fig. 3. Endometrial polyp demonstrated by (*A*) hysterosalpingography (*arrows*) and (*B*) transvaginal sonography (*cursors*).

location of uterine masses. Small, mostly intracavitary masses can be removed hysteroscopically. Large myomas with an intramural component may require uterine artery embolization or laparotomy with myomectomy. If surgical resection is planned, MR imaging should be considered to differentiate myomas from adenomyosis [3], because the latter is not resectable (Fig. 5).

Congenital uterine anomalies

Congenital uterine anomalies have been estimated to occur in at least 1% of women [4]. They are a result of defects in paired müllerian duct development, fusion, or resorption and are associated with renal anomalies in 20% to 25%. The anomalies have been classified into seven groups based on their prognosis for future fertility and surgical treatment [4]. Class I (segmental müllerian agenesis) is manifested by variable absence of the uterus or cervix. It presents as absence of menstrual bleeding at puberty and may be associated with pelvic pain because of retrograde menses. It may or may not be surgically correctable depending on the findings. Class II (unicornuate uterus) is caused by absence of development of one of the müllerian ducts (Fig. 6) and is almost always accompanied by absence of the kidney on the same side. There is an association with fertility and pregnancy difficulties; however, there is essentially no treatment. Class III (uterus didelphys) results in two separate uterine horns, cervices, and vaginas. In general, it is not associated with fertility or pregnancy problems and usually is not treated. Class IV (bicornuate uterus) is characterized by two separate uterine horns, usually one cervix and one vagina (Fig. 7). Bicornuate uterus is associated with a low incidence of fertility complications and usually is not treated. An incompetent cervix is associated with bicornuate uterus, and serial scanning during pregnancy to assess cervical length can be helpful. Class V (septate uterus) consists of two uterine cavities and a single fundus. The septum also can involve the cervix and vagina (Fig. 8). Of the correctable lesions, a uterine septum has the highest incidence of fertility and pregnancy problems; therefore the septum is usually removed hysteroscopically (Fig. 8B). Class VI (T-shaped uterus) is caused by diethylstilbestrol exposure in utero. Diethylstilbestrol was an estrogen compound used in the United States in the 1950s, 1960s, and occasionally in the 1970s in women with threatened abortion. In addition to a small, T-shaped uterine cavity, these women may have a mucosal ridge or hood superior to their external cervix and

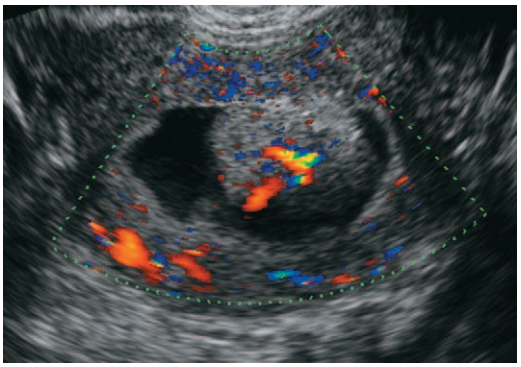

Fig. 4. Intracavitary myoma demonstrated by sonohysterography. Color flow is visualized within the lesion.

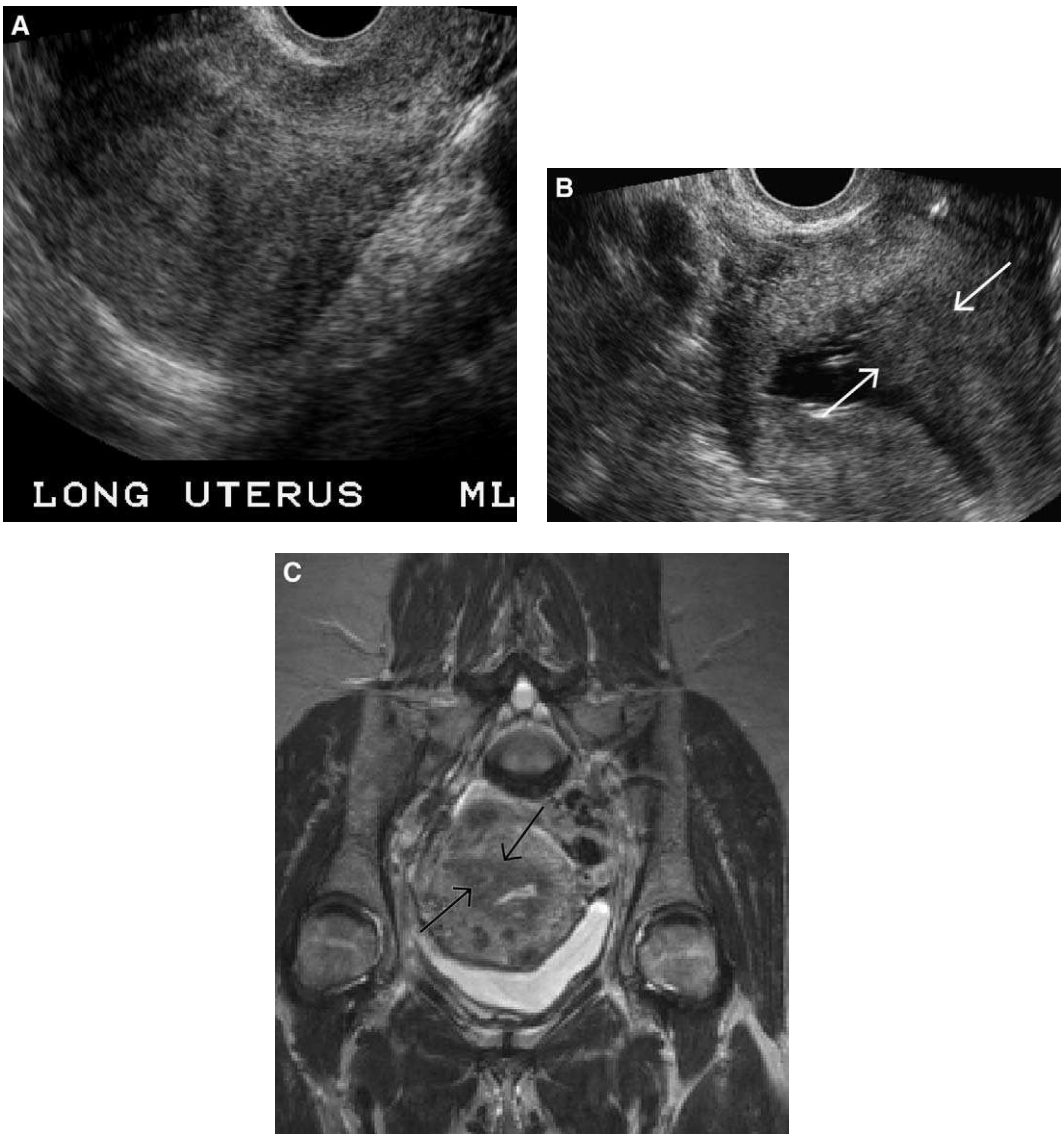

Fig. 5. Uterine myoma suspected by clinical findings. (*A*) Transvaginal sonography demonstrates enlarged uterus with possible mass. (*B*) Sonohysterography outlines ill-defined mass projecting into the cavity (*arrows*). (*C*) MR imaging demonstrates that the mass is adenomyosis and not a myoma (*arrows*).

clear cell adenocarcinoma of the vagina. They do have fertility and pregnancy problems, and no definite treatment is known. Because of high association with cervical incompetence, serial scanning during pregnancy to assess cervical length can be helpful. Finally, and most importantly, many anomalies occur that do not fit neatly into any of these described categories. When in doubt, it is best to describe the anatomy completely without attaching a label to it.

Fallopian tube

The fallopian tubes have a unique status in the body. Via the uterus, cervix, and vagina they connect the peritoneal cavity to the external world [5]. Their function and their anatomy is complex and includes conduction of sperm from the uterine end toward the ampulla, conduction of ova in the other direction from the fimbriated end to the ampulla, and support of the

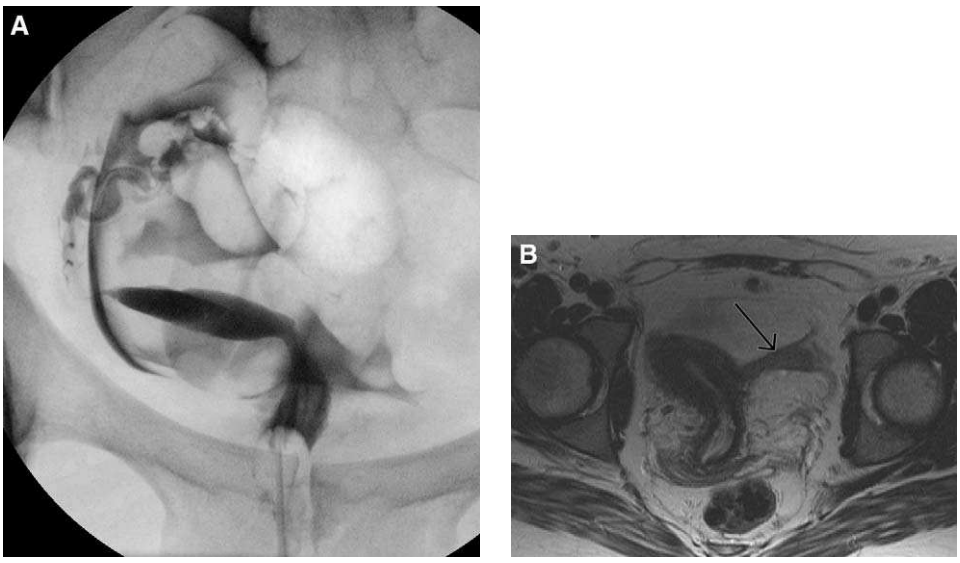

Fig. 6. Unicornuate uterus by hysterosalpingography (*A*) and MR imaging (*B*). Note the nonfunctioning rudimentary horn (*arrow*).

early embryo and conduction of the early embryo from the ampulla into the uterus for implantation. The normal fallopian tube ranges in length from 7 to 16 cm, with an average length of 12 cm. The tube is composed of a ciliated mucosal epithelial layer surrounded by three smooth muscle layers. The tube is divided into four regions (see Fig. 1): (1) the intramural or interstitial portion, which occurs in the wall of the uterine fundus and is 1 to 2 cm long; (2) the isthmic portion, which is approximately 2 to 3 cm long; (3) the ampullary portion, which is 5 to 8 cm long; and (4) the infundibulum, which is the trumpet-shaped distal end of the tube that terminates in the fimbria. Patency of the fallopian tubes is established when contrast medium flows through them and freely around loops of bowel at the time of salpingography, using either fluoroscopic or sonographic guidance.

The interstitial portion of the fallopian tube may be delicate and thread-shaped or may be funnel-shaped, assuming the configuration of a small triangle or diamond. The isthmic portion is normally thread-shaped. Diameter of both regions is approxi-

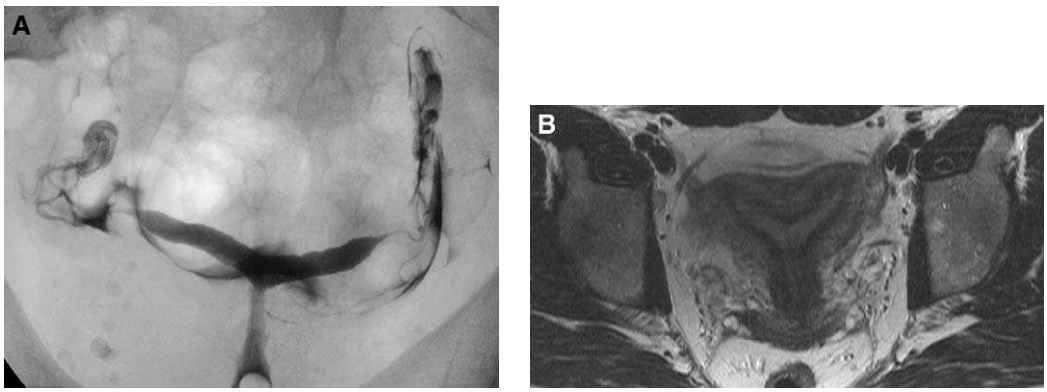

Fig. 7. Bicornuate-septate uterus by hysterosalpingography (*A*) and MR imaging (*B*). The indentation of the serosal contour of the uterine fundus though small makes this technically bicornuate uterus, and likely not clinically significant. Correct categorization and determination of significance of uterine anomalies is debated by fertility specialists.

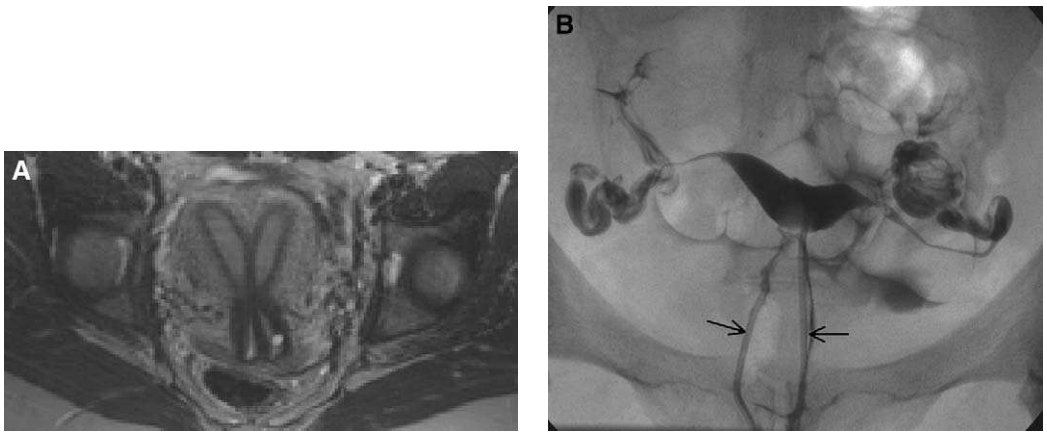

Fig. 8. Septate uterus. (*A*) Complete uterine and cervical septum by MR imaging. (*B*) Postoperative hysterosalpingogram demonstrates normal cavity after resection of uterine septum; cervical septum was not resected to avoid incompetent cervix. Two cervical canals are demonstrated (*arrows*).

mately 1 mm. Proximal tubal obstruction is obstruction in the first 3 to 4 cm of the tube. The cause of proximal tubal obstruction is frequently unclear, but infection and subsequent inflammation are leading causes in all reported series [6]. Histopathologic findings in resected proximal tubal segments include plugs of amorphous debris, chronic inflammation, obliterative fibrosis, and salpingitis isthmica nodosa (SIN) (Fig. 9). Together these lesions account for 70% to 85% of anatomic occlusions at the uterotubal junction. Unusual causes include granulomatous or ''giant cell'' salpingitis from tuberculosis, foreign bodies, and some parasitic infestations. Intraluminal endometriosis occurs in approximately 10% of tubes resected for proximal occlusion and may exist without relation to visible lesions elsewhere in the pelvis. Müllerian anomalies of the fallopian tube are rare, but cornual occlusion is seen with variants of unicornuate uterus, and atresia of tubal segments, including the proximal isthmus, can occur.

Several authors have noted a lack of major histologic findings in patients despite persistent proximal occlusion. It was assumed that the cause of this discrepancy was ''tubal spasm,'' which was estimated to be the cause in up to one third of women with proximal tubal obstruction. No anatomic or functional proximal tubal sphincter was identified, however, and no reliable ''antispasmodic'' was discovered [7]. Careful histologic analysis of tubal specimens resected for proximal occlusion revealed amorphous debris in approximately one third of women [8]. Discrepancy between clinical and imaging diagnosis of proximal tubal occlusion and subsequent pathologic findings may be explained by a temporary or easily dislodged entity, such as amorphous debris in the tubal lumen. Tubal spasm, or some temporary inability to visualize the fallopian tubes, does occur, however, probably much less often than originally proposed. It seems to be a more common cause when the proximal tubal obstruction is unilateral. Placing the patient prone and waiting 5 minutes before slowly reinjecting contrast agent into the uterus may help sort out patients with temporary nonvisualization versus true mechanical obstruction. If the proximal tubal obstruction persists despite these maneuvers, tubal catheterization with selective salpingography can be performed (Fig. 9).

Diverticula in the isthmic segment of the tube are caused by SIN (Fig. 10). SIN was described more than 100 years ago as irregular benign extensions of the tubal epithelium into the myosalpinx associated with reactive myohypertrophy and sometimes inflammation. There is an association between SIN and pelvic inflammatory disease; however, it is not clear whether SIN is caused by pelvic inflammation or whether SIN is congenital and predisposes to inflammation. SIN is focal and located only in the isthmus in most affected women; however, SIN occasionally can be found in the interstitial and ampullary segments. Compared with control populations, SIN has a higher incidence in women with tubal pregnancy and in women with proximal tubal obstruction. SIN associated with tubal obstruction requires treatment to restore tubal patency, which can be accomplished by fluoroscopically guided tubal catheterization and recanalization (see Fig. 9) [9]. If this approach fails, tubal patency can be accomplished by surgical resection and anastomosis.

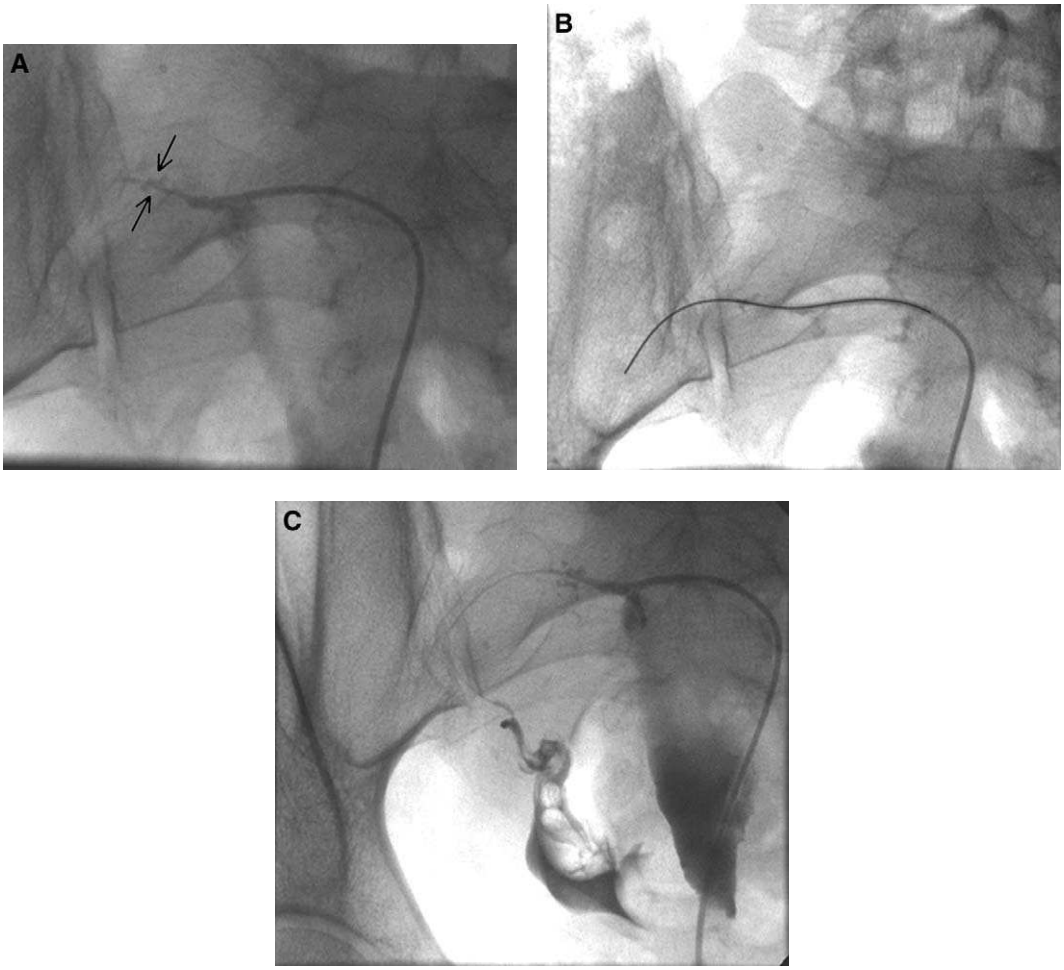

Fig. 9. Fallopian tube catheterization and recanalization in a woman with tubal obstruction associated with SIN. (*A*) Selective salpingography demonstrates the proximal occlusion and isthmic diverticulae of SIN (*arrows*). (*B*) Small guidewire used to recanalize occlusion. (*C*) Repeat selective salpingogram demonstrates a patent tube.

Whether SIN in the absence of tubal obstruction requires surgical resection is debatable.

The ampullary portion is the longest portion of the tube. It gradually widens from 1 to 2 mm at its proximal end to approximately 15 mm, where it joins the fimbriated infundibular portion. Subtle ampullary rugal folds can be demonstrated by salpingography, and occasionally the fimbriae are outlined by contrast material. Abnormal rugal folds imply damage of the epithelium from infection and usually coexist with a dilated and sometimes distally obstructed tube (Fig. 10). Abnormal rugal folds can occur in a patent tube, and they indicate reduced chances for conception. The visualization of abnormal rugal folds requires optimal tubal imaging, because the normal rugal folds are subtle.

Obstruction of the fimbrial portion of the tube is characterized by dilation of the ampullary portion of the tube, which sometimes can be massive, and no free spill of contrast agent into the peritoneal cavity despite adequate filling of the tubes and rolling the patient (see Fig. 10). The amount of dilation of the tube does not necessarily predict surgical results. A dilated tube may be soft and pliable with an intact epithelium and offer an opportunity for surgical correction. An obstructed but minimally dilated tube may have an indurated and thickened wall that cannot be reconstructed. The visualization of normal ampul-

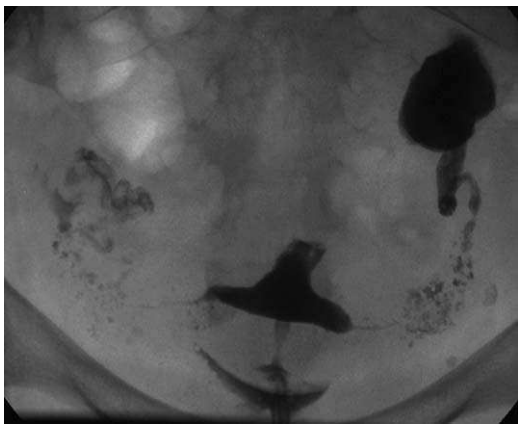

Fig. 10. Woman with untreated chlamydia infection as a teenager has severe bilateral salpingitis isthmica nodosa. The right fallopian tube is patent, and the left fallopian tube is occluded distally and demonstrates a hydrosalpinx.

lary rugal folds probably improves the chances for successful tubal reconstruction.

Dilation of the ampullary portion of the tube in the absence of complete occlusion indicates perifimbrial phimosis, or adhesions around the fimbria that impede egress of fluid. Adhesions around the tube are usually a result of chlamydial or gonococcal infection or endometriosis. It may be difficult to differentiate a dilated tube from loculated spill of contrast agent. Fimbrial phimosis can be mild or severe, but generally the presence of at least a pinpoint opening in the distal tube carries a more favorable surgical prognosis than complete occlusion. It also increases the risk of post-HSG peritonitis, however. Patients with dilated tubes should receive a total of 5 days of antibiotics, usually doxycycline (100 mg) orally twice a day. If the patient is not already taking antiobiotics at the time of the procedure and a dilated tube or tubes are demonstrated, she should receive doxycycline (200 mg) orally before she leaves the department, followed by 100 mg orally twice a day for 5 days [1].

Persistent tortuosity of the tube in all projections is associated with peritubal adhesions (Fig. 11), although some normal tubes can demonstrate this finding.

A woman with severely damaged fallopian tubes but a normal uterine cavity is a good candidate for in vitro fertilization and embryo transfer (see Fig. 10). In vitro fertilization and embryo transfer consist of ovarian stimulation, needle aspiration of the oocytes from the follicles using transvaginal ultrasound guidance, incubation of the oocytes with sperm, and catheter delivery of two to four developing embryos back into the uterine cavity [10]. The ''take home baby rate'' per embryo transfer procedure is approaching 50% in some clinics.

Peritoneal cavity

Laparoscopy is the gold standard for visualizing pelvic adhesions and endometriosis. Ultrasound visualization of adhesions is definitive (Fig. 12), but the sensitivity is poor, and the extent of disease cannot be determined. Indirect evidence about peritubal disease is obtained at the time of HSG from the pattern of spill of contrast agent out the fimbriated end of the tubes and into the peritoneal cavity. When contrast agent flows freely around loops of bowel, one can be confident that no significant pelvic disease exists (see Fig. 1). If contrast agent remains loculated around the tube outlining its wall or in the pelvis despite rolling the patient, one should be suspicious of peritubal and pelvic adhesions (see Fig. 12), although patients with these findings occasionally have a normal pelvis.

Ovary and adnexa

Normal ovary

A follicle is recruited by unknown mechanisms to grow in the follicular phase, and it demonstrates an average increase in diameter of 2 to 3 mm/day. When this ''dominant'' follicle attains an average diameter of 22 mm, it ruptures. Normal rupture can be accompanied by a decrease in size or an increase in size. On sonography echoes in the lumen of the follicle may appear. Fluid around the ovary also may be seen. Ultrasound is considered by some to be the best method for determining when ovulation will occur and documenting when it has occurred [11]. The variable appearance of the event makes the use of ultrasound problematic, however.

After menstruation, the ovaries should contain a few small follicles and sometimes a subtle heterogeneous area that may be the corpus luteum. The presence of one or more cysts larger than approximately 2 cm in diameter—particularly if accompanied by a serum estradiol concentration of more than 100 pg/mL—indicates persistent follicle activity that could interfere with response to ovarian stimulation medication. Suppression of the cyst or cysts with oral contraceptives may be considered [12].

Polycystic ovary syndrome

Polycystic ovary syndrome is often found during evaluation for infertility. The inhibition of release of follicle-stimulating hormone and leutinizing hormone

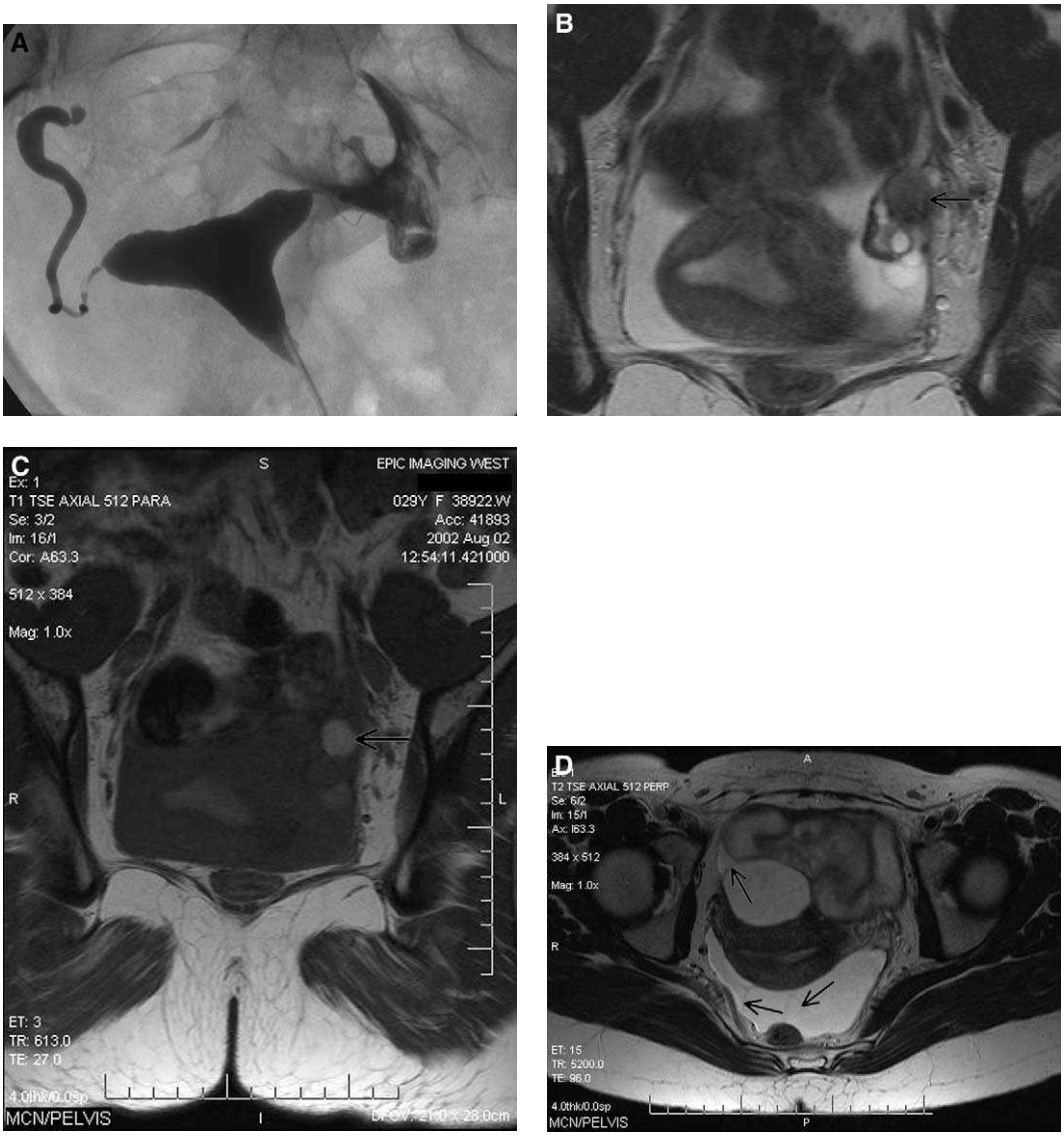

Fig. 11. A 29-year-old woman with infertility. (*A*) Hysterosalpingogram demonstrates occlusion of the right tube in the proximal ampullary portion and tortuosity of the left tube, which is patent. MR imaging demonstrates a left ovarian endometrioma, which is low signal on T2-weighted images (*arrow*) (*B*) and high-signal on T1-weighted images (*arrow*) (*C*). (*D*) T2-weighted MR imaging demonstrates adhesions (*arrows*) that explain the tubal findings.

from the pituitary gland is the underlying mechanism of polycystic ovary syndrome. As a result, follicles in the ovary begin to grow but do not develop properly. The immature follicles produce estrogen and androgen that further inhibit the pituitary gland and prevent normal ovulation. A round ovary with multiple small immature follicles may be evident by ultrasound, and it confirms the diagnosis of polycystic ovary syndrome (Fig. 13) [13]. A woman may have the syndrome as evidenced by low follicle-stimulating hormone and leutinizing hormone and high estrogen and androgen levels, however, and the ovary may appear normal by ultrasound. The chronic elevation of estrogen may cause some women with polycystic ovary syndrome to develop irregular bleeding, a thickened endometrium, or even endometrial carcinoma. The chronic elevation of androgens causes some women to develop hirsutism.

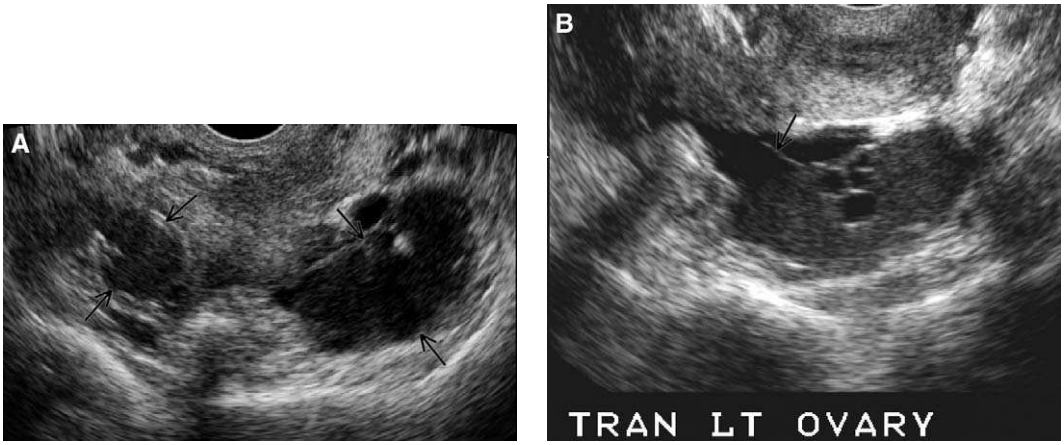

Fig. 12. A 32-year-old woman with pelvic pain and infertility. (*A*) Transvaginal sonography demonstrates bilateral endometriomas (*arrows*) that are composed of low-level echoes. (*B*) On the left side, an adhesion from the ovary to the posterior cervix is demonstrated (*arrow*).

The most common cause of polycystic ovary syndrome is obesity. Fat produces estrogen, which inhibits follicle-stimulating hormone and leutinizing hormone and leads to the cycle described previously. Other causes of polycystic ovary syndrome are diabetes and adrenal, thyroid, or pituitary dysfunction, which affects the delicate hormone balance required for normal ovulation.

Endometriosis

Endometriosis may cause infertility because of anatomic or chemical factors. The most frequent location for endometriotic implants is the ovaries, and endometriomas are often bilateral (see Fig. 12). Endometriosis is the presence of endometrial tissue outside of the endometrial cavity. It usually presents in the reproductive years and is probably caused by retrograde menstruation [14]. Pelvic pain and dyspareunia are associated with endometriosis, although some women with extensive endometriosis may be asymptomatic. Large endometriomas are likely to be diagnosed; however, small implants are not well visualized by any imaging techniques.

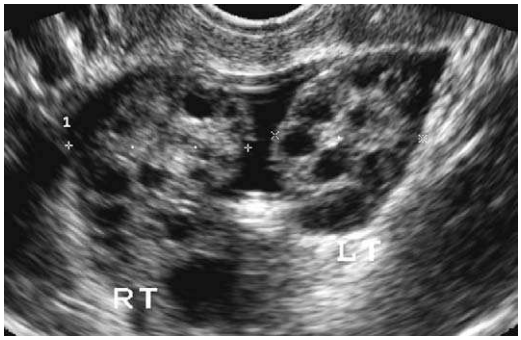

Fig. 13. A 24-year-old woman with infertility and polycystic ovary syndrome. Transvaginal sonography demonstrates that both ovaries are round and contain 10 to 12 small follicles and an echogenic stroma, consistent with the diagnosis.

References

[1] Winfield AC, Wentz AC. Diagnostic imaging in infertility. 2nd edition. Baltimore: Williams and Wilkins; 1992.
[2] Hricak H, Chang YCF, Cann CE, Parer JT. Cervical incompetence: preliminary evaluation with MR imaging. Radiology 1990;174:821–6.
[3] Togashi K, Ozasa H, Konishi I, et al. Enlarged uterus: differentiation between adenomyosis and leiomyoma with MR imaging. Radiology 1989;171: 531–4.
[4] Buttram VC. The American Fertility Society classification of adnexal adhesions, distal tubal occlusion, tubal occlusion secondary to tubal ligation, tubal pregnancies. Müllerian anomalies and intrauterine adhesions. Fertil Steril 1988;49:944–55.
[5] Woodruff JD, Pauerstein CJ. The fallopian tube. Baltimore: Williams and Wilkins; 1969. p. 22–32.
[6] Thurmond AS. Fallopian tube catheterization. In: Thurmond AS, Jones MK, Cohen DJ, editors. Gyne-

cologic, obstetric, and breast radiology. Boston: Blackwell Scientific; 1996. p. 127–31.

[7] Thurmond AS, Novy MJ, Rosch J. Terburaline in diagnosis of interstitial fallopian tube obstruction. Invest Radiol 1988;23:209–10.

[8] Sulak PJ, Letterie GS, Coddington CC, et al. Histology of proximal tubal occlusion. Fertil Steril 1987;48: 437–40.

[9] Thurmond AS, Burry KA, Novy MJ. Salpingitis isthmica nodosa: results of transcervical fluoroscopic catheter recanalization. Fertil Steril 1995;63:715–22.

[10] Bustillo M. Assisted reproductive technology in the United States and Canada: 1992 results generated from the American Fertility Society / Society for Assisted Reproductive Technology Registry. Fertil Steril 1994; 62:1121–8.

[11] Rosen GF. Ultrasound in reproductive endocrinology. In: Schlaff WD, Rock JA, editors. Decision making in reproductive endocrinology. Boston: Blackwell Scientific; 1993. p. 386–91.

[12] Worley RJ. Ovulation induction: clomiphene. In: Schlaff WD, Rock JA, editors. Decision making in reproductive endocrinology. Boston: Blackwell Scientific; 1993. p. 447–52.

[13] Pache TD, Wladimiroff JW, Hop WC, Fauser BC. How to discriminate between normal and polycystic ovaries: transvaginal US study. Radiology 1992;183:421–3.

[14] Klein NA, Olive DL. Management of endometriosis-associated infertility. In: Schlaff WD, Rock JA, editors. Decision making in reproductive endocrinology. Boston: Blackwell Scientific; 1993. p. 488–94.

RADIOLOGIC
CLINICS OF
NORTH AMERICA

Radiol Clin N Am 41 (2003) 769–780

Ultrasonographic evaluation of the endometrium in postmenopausal vaginal bleeding

Katharine G. Davidson, MD[a], Theodore J. Dubinsky, MD[b,*]

[a]*Department of Anesthesiology, University of Iowa Hospitals and Clinics, 6 JCP, Iowa City, IA 52242, USA*
[b]*Departments of Radiology, Obstetrics and Gynecology, Harborview Medical Center, University of Washington, Box 359728, 325 Ninth Avenue, Seattle, WA 98104, USA*

Abnormal vaginal bleeding is a frequent presenting complaint in women in the postmenopausal or perimenopausal period. Postmenopausal bleeding (PMB) may be defined as any vaginal bleeding in a postmenopausal woman not on hormone replacement therapy (HRT) or unscheduled bleeding in a woman on HRT. The differential diagnosis is broad, but irregular or excessive vaginal bleeding can signify an underlying malignancy of the female genital tract. Bleeding occurs in 80% to 90% of women with endometrial cancer, and the prevalence of endometrial cancer among women who present with PMB has been reported to range from 1% to 60%, although a 10% prevalence of endometrial cancer in this population has been accepted by most authors [1]. All women who present with postmenopausal bleeding should be evaluated for potential malignancy, including endometrial cancer, premalignant atypical endometrial hyperplasia, and cervical cancer.

It is well established that women with PMB require further evaluation to exclude carcinoma. To date, however, no universal algorithm exists for proceeding with an evaluation of a woman with PMB. Tissue sampling is the most definitive diagnostic procedure; however, the techniques have variable sensitivity and specificity. In a recent meta-analysis of endometrial sampling methods, the sensitivity rate for detection of endometrial carcinoma ranged from 25% to 100%, with the best results from the Pipelle in postmenopausal women with sample size–weighted sensitivity rate of 99.6% [2].This study was performed by sampling known cases of endometrial carcinoma while the patients were on the operating table. In the authors' own attempt to perform a metaanalysis regarding endometrial biopsy, they found that none of the literature met adequate criteria to be included. The major problem with the biopsy literature is a lack of blinded studies with adequate gold standard proof of outcomes.

Sensitivity rate for detection of atypical hyperplasia varied from 39% to 100%, with weighted sensitivity rate of the Pipelle in postmenopausal women being 88% [2]. The false-negative rates for endometrial biopsy in the office may be more than 15%, whereas even dilation and curettage had up to 11% false-negative rate for endometrial carcinoma [3,4]. One study reported only a 43% sensitivity rate for detecting endometrial carcinoma with endometrial biopsy [5]. The actual sensitivity rate for endometrial biopsy remains unknown, and only when large enough trials using hysteroscopy as the gold standard for evaluating endometrial disease are published will this information become available for accurate evaluation.

Because up to 90% of PMB has a benign cause, questions have arisen regarding the appropriateness of performing biopsies on all patients with bleeding. Subsequently, imaging techniques, mainly transvaginal ultrasound, have been explored to help determine which patients are at higher risk of malignancy and would benefit from tissue sampling and which are more likely to have a benign cause for the bleeding.

* Corresponding author.
E-mail address: tdub@u.washington.edu (T.J. Dubinsky).

0033-8389/03/$ – see front matter © 2003 Elsevier Inc. All rights reserved.
doi:10.1016/S0033-8389(03)00060-5

In 2000, a panel of physicians convened by the Society of Radiologists in Ultrasound met to discuss the role of sonography in women with PMB. The panel members included experts in the fields of radiology, obstetrics and gynecology, gynecologic oncology, epidemiology, and pathology. The panel concluded that PMB demands further evaluation and that either transvaginal sonography or endometrial biopsy could serve as the first diagnostic intervention. The panel also concluded that further studies were needed to determine which approach is more effective [6].

Background

Pelvic ultrasound has been used to evaluate the uterine cavity for fibroids, endometrial thickness, endometrial homogeneity, and the presence of abnormal vascularity within the endometrium. In the absence of visible anomalies (such as fibroids), endometrial thickness has been used as a marker for endometrial pathology. The technique most often used to evaluate the endometrial thickness is a measurement of the anterior and posterior layers of the endometrium in the sagittal plane at the level of the maximal estimated thickness. This technique has been demonstrated to be highly reproducible with high intraobserver (r(I) = 0.96–0.97) and interobserver (r(I) = 0.954) reliability [7]. Some authors have suggested that assessing the morphology of the endometrium based on ultrasonographic appearance may add additional information. The presence of cysts within the endometrium is associated with benign origins of bleeding, such as polyps, whereas endometrial hypoechogenicity and inhomogeneity are associated with an increased risk for malignancy.

Many studies have been conducted on the use of transvaginal sonography to evaluate PMB. In 1997, Smith-Bindman et al [8] published a metaanalysis of the use of transvaginal ultrasound to evaluate endometrial thickness in women with PMB. They included 35 prospective trials with 5892 patients in their analysis. The authors determined that a threshold endometrial thickness of 5 mm had a sensitivity rate of 96% for endometrial carcinoma and 92% for other endometrial disease. The sensitivities were not significantly different in women taking HRT. The specificity of an abnormal thickness was lower (81% for all endometrial disease), however, so that an abnormal ultrasound result still must be followed with either tissue sampling or saline infusion sonography.

Many studies have shown that a threshold of 5 mm for pursuing endometrial sampling reasonably excludes patients with endometrial carcinoma. In a prospective study of 1110 women with PMB, endometrial pathology was found most frequently with endometrial thickness more than 8 mm, and no endometrial cancers were detected in women with thickness of 4 mm or less [9]. Similarly, an evaluation of 419 women with PMB assessed the sensitivity of two thresholds: more than 4 mm and more than 8 mm. The authors reported a sensitivity rate of 95.1% and specificity rate of 54.8% for the 4-mm cutoff and 83.8% and specificity rate of 81.3% for the 8-mm cutoff [10]. Using a threshold of 5 mm or less, a study of 182 women with PMB found no cases of carcinoma, but 3 patients had hyperplasia [11]. Another study concluded that a threshold of 4 mm or less can reliably exclude malignancy in women with PMB [12], with an estimated one case of carcinoma missed for every 250 women scanned with a stripe of less than 5 mm [5].

Some authors reported even a thicker stripe as an adequate threshold for excluding endometrial adenocarcinoma. Mateos et al [13] reported a prospective trial of transvaginal sonography followed by endometrial sampling in 168 women with PMB not on estrogen. Using a cut-off of 6 mm, they reported 88.6% sensitivity rate, 90.6% specificity rate, and 92% positive predictive value (PPV) for any endometrial pathology.

One caution is that cases of endometrial carcinoma have been detected in women with an endometrial stripe as thin as 3 mm [14]. In one study, three of nine cases of carcinoma had a thickness of 3 mm [14]. This study also reported mean thicknesses lower than that of most studies (6 mm for carcinoma), however, which suggested that a difference in technique may partially account for their findings. Some authors have suggested using 3 mm as a threshold to reduce the chance of missing cases of carcinoma at the expense of specificity. The real issue with ultrasound concerns the outcome of symptomatic patients who are evaluated with ultrasound and found to have a thin endometrium or have biopsy that is negative and then are followed on an annual basis. Because it is accepted that both modalities miss some cases of endometrial carcinoma, it becomes relevant to determine which cases are missed and for what reasons and whether these women are ultimately diagnosed correctly in time to treat them successfully.

Atrophic endometrium

Bleeding in postmenopausal women is commonly caused by atrophy of the endometrium and exposure

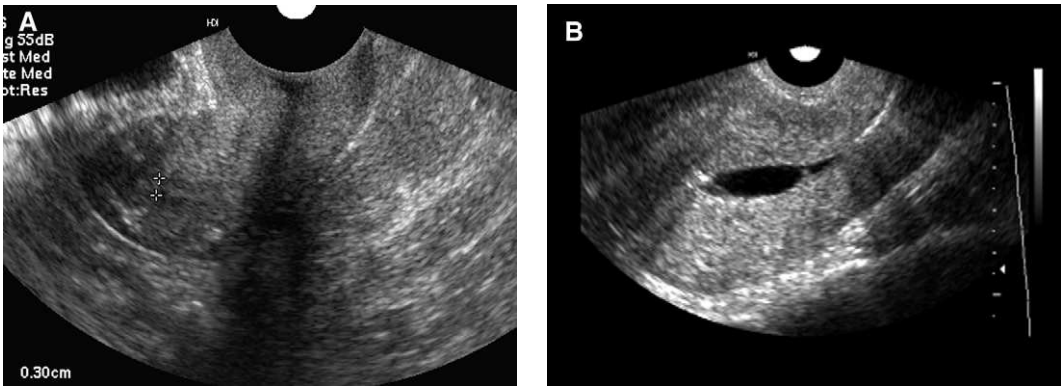

Fig. 1. (*A*) Mid-sagittal ultrasound image demonstrates a thin atrophic endometrium. (*B*) Mid-sagittal image obtained during a saline infusion sonohysterogram demonstrates virtually no endometrium consistent with atrophy.

of the vessels in the underlying myometrium. In the absence of estrogen after menopause, the functional layer is inactive and atrophies, which leaves only the shallow basalis layer. Atrophic endometrium on ultrasound has the appearance of a thin endometrial stripe, often less than 3 mm (Fig. 1). Occasionally, early in menopause the glands may become dilated and have a cystic appearance on ultrasound and histologic evaluation. Biopsy is insensitive in this population because tissue sample is often inadequate for diagnosis, but it is reasonable to follow women who have bleeding and a thin stripe on ultrasound prospectively because of the overall low risk of carcinoma or atypical hyperplasia in that population.

Endometrial polyps

An endometrial polyp is a circumscribed overgrowth of the endometrial mucosa and occasional stromal tissue that protrudes into the uterine cavity on a fibrovascular stalk. The polyps can be singular or multifocal. They are most often benign and, in postmenopausal women, can show the typical atrophic and cystic change of the rest of the endometrium on pathologic evaluation. Adenocarcinomas may grow in a polypoid fashion (Fig. 2), however, or can arise within a polyp. A polyp that appears in a symptomatic postmenopausal woman warrants biopsy.

A recent clinical trial of hysterosonography in PMB found polyps in nearly 50% of the patients [15]. Most polyps are benign proliferation mucosal tissue not clinically relevant except for their association with dysfunctional uterine bleeding.

Sonographic appearance

It may be difficult to detect a distinct polyp on ultrasound examination because the polyp may appear as a diffusely thickened endometrium (Fig. 3). The presence of a polyp also can be suggested by a hyperechoic mass surrounded by hypoechoic endometrium (Fig. 4). Cystic spaces within the polyp may be present. Although not necessary for diagnosis, they are fairly specific for benign endometrial disease (Fig. 5). Polyps may be visualized more readily with the infusion of saline to distend the uterine cavity, saline infusion sonohysterography (SIS). With SIS, a polyp appears as a smoothly marginated focal lesion that protrudes into the endometrial cavity. Not surprisingly, a comparison study of transvaginal sonog-

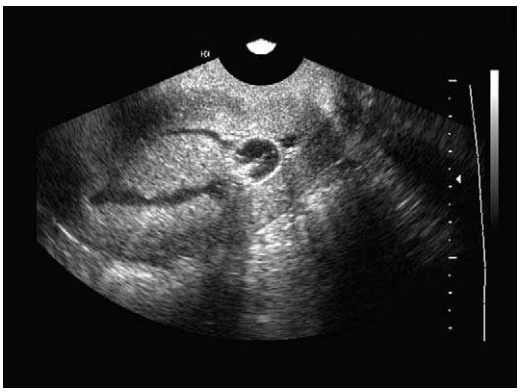

Fig. 2. Mid-sagittal view from a saline infusion sonohysterogram demonstrates a large polypoid lesion. Histology revealed endometrial carcinoma.

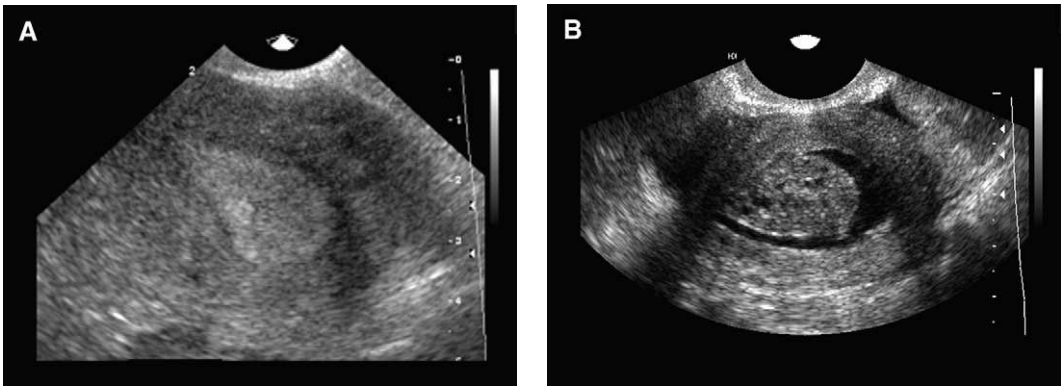

Fig. 3. (*A*) Mid-sagittal ultrasound image demonstrates a slightly heterogeneous thickened endometrium. (*B*) Sonohysterogram image demonstrates a pedunculated heterogeneous mass consistent with a polyp (and less likely a fibroid).

raphy and SIS for detection of endometrial polyps found a significantly greater sensitivity (93% versus 65%) and specificity (94% versus 76%) for SIS over transvaginal sonography alone [16].

Endometrial hyperplasia

Endometrial hyperplasia is a histologic diagnosis characterized by overgrowth of glands with or without stromal proliferation and is believed to result from prolonged estrogen stimulation of the endometrium. Overgrowth of the endometrium is often associated with irregular and heavy vaginal bleeding. There are many different classifications based on the appearance of the glands and stroma, but the most significant form is hyperplasia with atypia that is believed to be a precursor to endometrial cancer. 30% to 40% of all carcinomas are noted to have coexisting atypical hyperplasia [17]. The atypical hyperplasia is often focal, however, and may be found in the background of simple hyperplasia or normal endometrium.

Sonographic appearance

On ultrasound, hyperplasia appears as a thickened endometrial stripe (Fig. 6). In a complete scan of the uterus, the thickening is more likely to be focal but may involve the entire endometrium. It has a similar appearance to an endometrial malignancy on ultra-

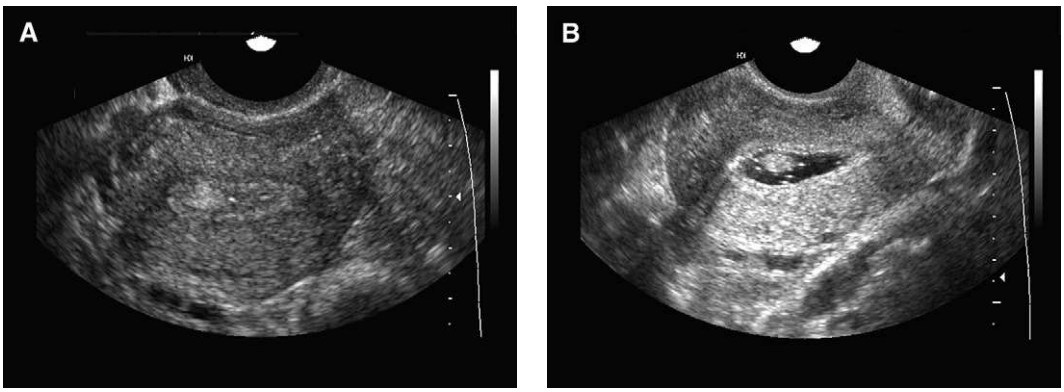

Fig. 4. (*A*) Transverse ultrasound image demonstrates a small focal echogenicity within the endometrium consistent with a small polyp. (*B*) The corresponding saline infusion sonohysterogram image demonstrates the small sessile polyp seen on the transvaginal ultrasound image.

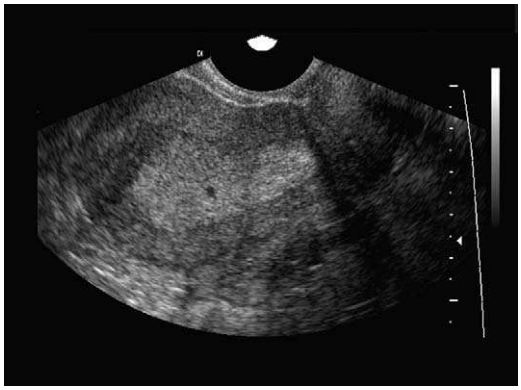

Fig. 5. Transverse ultrasound image demonstrates a small cyst within the endometrium. A large polyp was demonstrated at saline infusion sonohysterography, and it was removed at hysteroscopy.

sound, but the endometrial-myometrial interface is not disrupted.

Uterine leiomyomas

Uterine leiomyomas, frequently referred to as fibroids, are common benign neoplastic growths of smooth muscle cells within the myometrium. They occur in up to 40% of women over the age of 35 [18] and are seen on 75% of hysterectomy specimens [19]. These benign tumors regress with estrogen withdrawal. They are overgrowth of muscle tissue and are pseudoencapsulated and noninvasive. They can be subserosal (arising from the exterior surface of the uterus), intramural (completely within the myometrium), submucosal (protruding into the uterine cavity and distorting the endometrial cavity), or pedunculated (arising from a stalk, similar to a polyp). Fibroids with submucosal extent are believed to cause vaginal bleeding by increasing the surface area of the endometrium and disrupting the normal sloughing process (Fig. 7). In postmenopausal women, these benign tumors usually regress, and malignant degeneration is rare. In the presence of continued hormonal stimulation, however, they may continue to be symptomatic.

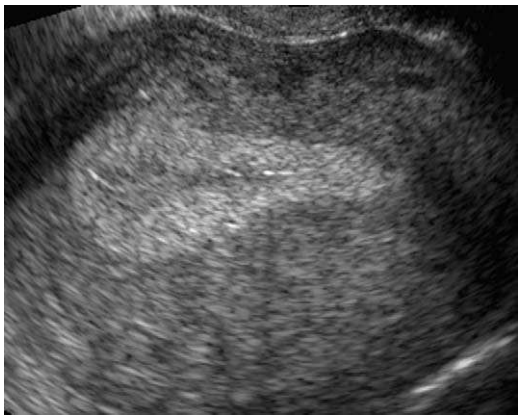

Fig. 6. Mid-sagittal view of a thickened endometrium in a postmenopausal woman. Biopsy revealed hyperplasia.

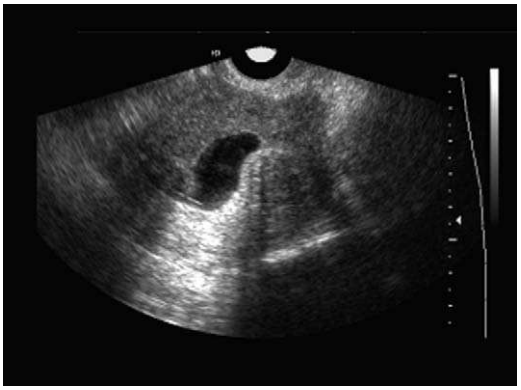

Fig. 7. Mid-sagittal view during saline infusion sonohysterography of an intramural fibroid with submucosal extension.

Sonographic appearance

Leiomyomas have a varied appearance on ultrasound depending on location within the uterus. A generalized enlargement of the uterus, irregularities in the external surface or endometrial cavity, and areas of hyperechogenicity or hypoechogenicity within the surrounding myometrium all suggest leiomyomas. Calcifications also may form within the leiomyomas and be visualized sonographically. Submucosal leiomyomas are the most likely to cause vaginal bleeding and may appear as an area of increased echogenicity bulging into the endometrial cavity with echogenicity similar to that of the myometrium. It can be difficult to distinguish a leiomyoma from a blood clot or a polyp [20]. Leiomyomas also may obscure the endometrium on imaging or cause an overestimation of endometrial thickness, which would lead to further evaluation.

Endometrial carcinoma

Endometrial carcinoma, which arises within the glandular cells of the uterine lining, is most common in postmenopausal women, with 70% of cases occur-

ring in women more than 50 years of age. It is the most common gynecologic malignancy in the United States. In postmenopausal women who present with abnormal vaginal bleeding, the risk of cancer is approximately 10%. The disease is surgically staged. In early stages there is a high cure rate; survival decreases once the malignancy has spread to adjacent organs or lymph nodes. The mainstay of treatment is surgical staging, with hysterectomy and lymph node dissection as indicated, followed by radiation therapy if there is evidence of extrauterine spread.

Sonographic appearance

Signs suggestive of endometrial carcinoma on ultrasound include a distended or fluid-filled uterine cavity, an enlarged or lobular uterus, and prominent echogenicity of the endometrium (Fig. 8). A normal postmenopausal uterus usually measures less than 50 cc [21], and uterine enlargement is seen in at least 71% of women with endometrial adenocarcinoma [22]. A recent study reported a 0.6% prevalence rate of endometrial cancer in women with PMB and endometrial thickness of 4 mm or less. This prevalence increased to 19% in women a with thickness of 5 mm or more [23]. The authors concluded that in women with endometrial thickness less than 4 mm, endometrial biopsy may not be required. Many other authors agree with this threshold [24]. Others suggest an even thicker threshold of 6 mm [14]. Several studies suggested that an endometrial thickness of more than 15 mm is highly specific for the diagnosis of endometrial carcinoma [24].

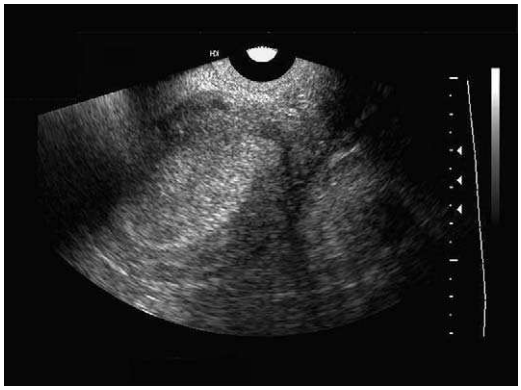

Fig. 8. Diffusely thickened endometrium in a postmenopausal woman. Because the risk for endometrial carcinoma is high in this group of patients, she underwent endometrial biopsy immediately, which confirmed endometrial carcinoma.

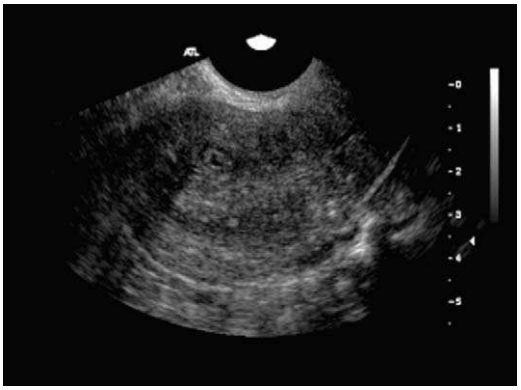

Fig. 9. Mid-sagittal view of the endometrium in a postmenopausal woman shows a thickened endometrium with ill-defined margins. Histology revealed endometrial carcinoma.

Qualitative markers have been reported as suggestive of malignancy, including endometrial cavity fluid collection, irregularity of the myometrial-endometrial interface (Fig. 9), and inhomogeneity of the endometrium. In 1995, Weigel et al [25] suggested that the addition of assessment of the endometrium for homogeneity, presence of a central echo, and echogenecity would be most useful in assessing women whose endometrial stripe is in the "gray area" of 4 to 10 mm. They calculated 100% sensitivity of irregular endometrial interface in predicting endometrial carcinoma. In cases in which intrauterine fluid is found, the measurement of endometrial thickness is calculated to exclude the fluid and measure only the endometrium itself.

The sonographic texture of the endometrium also has been studied as a marker of endometrial pathology. In a retrospective study of 68 postmenopausal women who underwent vaginal sonography, Hulka et al [26] reported that cystic spaces within the endometrium were predictive of polyps, endometrial hyperplasia often appeared hyperechoic, and endometrial carcinoma appeared heterogeneous. There was also significant overlap in the diagnoses [26]. In a more recent study of 207 women with PMB, the morphology of the endometrium was categorized as homogenous, focally increased echogenicity, diffusely increased echogenicity, or diffusely inhomogeneous in addition to measurement of endometrial thickness. The authors reported that in three of three cases of endometrial cancer with a thickness of less than 6 mm, all had inhomogeneity. 10 of 11 cases of endometrial cancer with a thickness of more than 6 mm also had an inhomogeneous endometrium [27]. Adding morphologic characteristics increased the

specificity and negative predictive value and decreased the sensitivity rate from 100% to 77.8% [28]. The combination of quantitative and qualitative findings may improve the predictive value of transvaginal sonography.

A study of SIS found that difficulty with distension of the uterus at the time of saline infusion was associated with a sevenfold increased risk of malignancy, although in this study the sensitivity rate for detecting carcinoma was less than that of conventional transvaginal sonography (44% versus 60%) [29]. Sensitivity also may be improved by careful attention to technique. Fleischer [30] recommends (1) surveying the entire endometrium in the sagittal and coronal planes before measuring the anteroposterior double-layer thickness in the sagittal plane near the fundus, (2) assessing the texture of the endometrium, (3) measuring uterine volumes, and (4) measuring endometrial blood flow.

Research has suggested that ultrasound may be valuable in the staging of endometrial cancers [31] with regard to depth of invasion into the myometrium. Surgical staging is currently the gold standard and the standard of care. Distant metastases and lymph node involvement and myometrial extension are better evaluated with CT and MR imaging. Once a diagnosis of endometrial carcinoma is established, these are better imaging methods than ultrasound for staging the disease.

Additional techniques

Other techniques have been proposed to add accuracy to the imaging of the endometrium. Saline infusion sonohysterography has been applied to the evaluation of PMB because the infusion of saline into the endometrial cavity may improve the differentiation of intraluminal masses and shape of the endometrium. Dubinsky and colleagues correlated SIS findings with pathologic diagnosis on curettage or hysterectomy in 88 women with vaginal bleeding. The authors defined a suspicious endometrial appearance as either focal endometrial thickening (>4 mm) or a focal inhomogeneous endoluminal mass. For detection of carcinoma using this definition, they found a sensitivity rate of 89% and specificity rate of 46%. One case of carcinoma in situ was associated with a benign-appearing endoluminal mass on SIS. The authors concluded that all endoluminal masses require further evaluation to exclude carcinoma [32]. More recently, Bree et al [15] estimated a sensitivity rate of 98% and specificity of 88% for SIS and estimated that the use of SIS added certainty to the diagnosis in 88% of patients and resulted in a change in patient treatment in 80%.

One study suggested that SIS may be as effective as hysteroscopy in evaluation of the endometrium. In a prospective study of 105 women with PMB and an endometrial stripe of more than 5 mm, all patients were evaluated with SIS followed by hysteroscopy. The authors found a 96% agreement between SIS and hysteroscopy in the diagnosis of focal lesions and a similar sensitivity rate (80%) for diagnosing polyps. Hysteroscopy distinguishes between benign and malignant lesions primarily because tissue sampling can be performed during hysteroscopy. Hysteroscopy is the gold standard because of the ability to perform directed biopsy. The limitations of hysteroscopy are the invasive nature, requirement for expensive equipment, and general anesthesia. Office-based hysteroscopy instruments that held the promise of increased convenience and affordability have not lived up to expectations. A small study compared transvaginal sonography, SIS, and hysteroscopy and found that patients rated transvaginal sonography as significantly less painful than the other two procedures [33].

Modalities such as color flow and power Doppler imaging have been reported to increase the sensitivity and specificity rates of ultrasound in detecting endometrial pathology. Amit et al [34] reported on a prospective study of 60 women with PMB and reported a sensitivity rate of 86% and sensitivity rate of 89% for power Doppler (pulsatility index point cutoff 1.0). On the other hand, Sheth et al [35] evaluated color duplex Doppler in postmenopausal women with thickened endometrial stripes and found that low-impedence arterial flow in benign and malignant lesions was not significantly different. The presence of a single draining vessel is highly indicative of the presence of a polyp (Fig. 10), whereas more diffuse flow with multiple areas of aliasing increases the risk of carcinoma (Fig. 11). Lack of flow does not exclude the presence of an endoluminal lesion, however.

Three-dimensional ultrasound is a technique with emerging applications that has been studied for evaluation of PMB. In particular, the ability to produce coronal images of the cornua may increase the sensitivity of SIS slightly for lesions in this location that may be difficult to appreciate fully otherwise. Abnormalities of the endometrium that occur in women with congenital variants of the uterus also may be imaged to greater advantage with three-dimensional ultrasound techniques. In general, however, the actual benefit of three-dimensional imaging in most patients is probably limited as long as careful attention is paid to imaging technique.

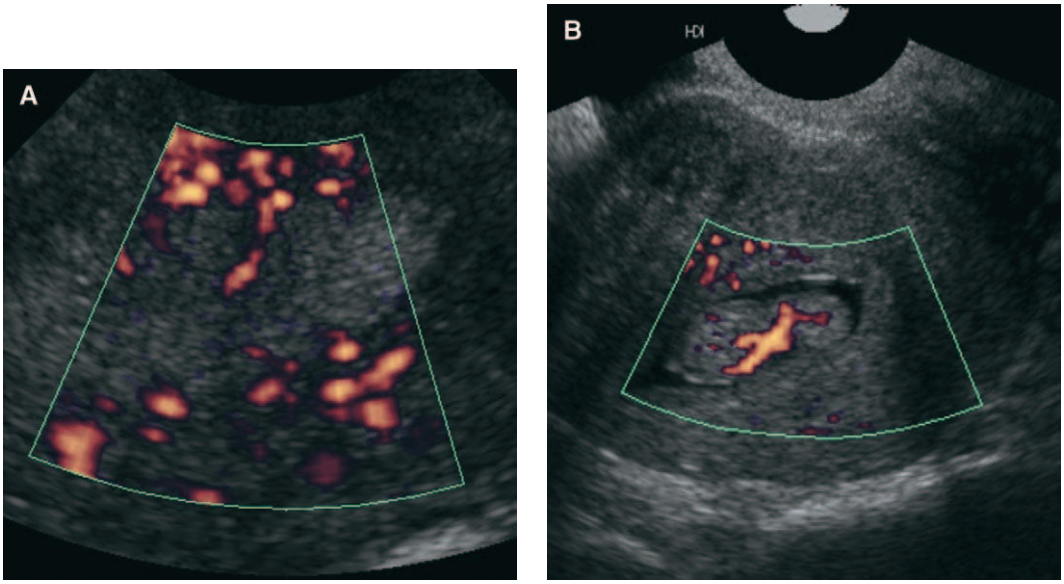

Fig. 10. (*A*) Color flow image of the endometrium demonstrates a solitary feeding vessel. The presence of such a vessel significantly increases the probability that a polyp is present. (*B*) In another patient with a polyp, during saline infusion sonohysterography one large branching vessel is seen.

Yaman et al [36] demonstrated good reproducibility with three-dimensional technique in assessing endometrial volume with mean interobserver correlation of 0.95, which was superior to that of two-dimensional thickness measurements (0.76).

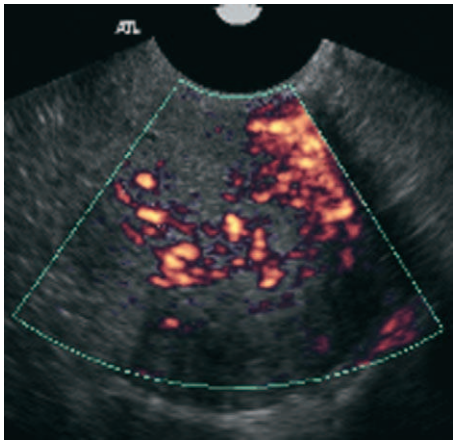

Fig. 11. Color flow image of the same patient as in Fig. 6, which demonstrates scattered flow aliasing throughout the endometrium. Angiogenesis and microarteriovenous fistula formation occur as a part of endometrial carcinoma development. Although not of high sensitivity for detecting carcinoma, the presence of this pattern of flow is highly predictive for carcinoma.

Three-dimensional ultrasound also has been demonstrated to be a valid measurement technique in assessing volume [37]. In one study, using a cutoff volume of 13 mL had a sensitivity rate and PPV of 100% and 91.7%, respectively, in diagnosing endometrial cancer in women not on HRT with PMB [38]. In the latter study, the mean endometrial thickness and volume in women later found to have endometrial carcinoma were 29.5 mm and 39 mL, respectively, whereas women with atrophic endometrium had a mean thickness of 5.3 mm and volume of 0.9 mm. Patients with hyperplasia or polyps were in between, with a mean thickness of 15.6 mm and volume of 5.5 mL [38].

Special populations

Certain populations present added difficulties in the assessment of PMB. Women who are on tamoxifen therapy for breast cancer are one example. Tamoxifen is a competitive inhibitor of the estrogen receptor and is well documented to increase the risk of endometrial hyperplasia and carcinoma [39]. Oncologists have investigated the optimal strategy for following these patients to detect endometrial anomalies in the earliest stage possible. Transvaginal sonography has been used for this purpose in asymptomatic women because tamoxifen therapy may alter the

sonographic appearance of the endometrium. Recent studies suggest a high false-positive rate from screening of asymptomatic women on tamoxifen because a physiologic thickened myometrium may be mistaken for endometrial hypertrophy by transvaginal sonography [40]. This is probably better evaluated with SIS; however, there is reluctance to subject all women on tamoxifen to annual SIS examinations. Current American College of Obstetrics and Gynecology recommendations for screening women on tamoxifen therapy include annual gynecologic examination with Pap tests and bimanual examination.

Women on sequential HRT also present a diagnostic challenge because most women continue to have monthly bleeding and the primary symptom of endometrial cancer may be disguised. In a premenopausal menstruating woman, endometrial thickness varies from a mean of 4 mm in the early follicular phase to 11.5 mm just before menses [41]. Even long after menopause, the uterus retains the capacity to grow in response to hormonal administration. Research has demonstrated that vaginal sonography is accurate is assessing endometrial thickness in this population [42]. The mean endometrial thickness increases significantly with therapy, however, with a mean of 4.3 mm in one study. Another study of women with PMB reported that women on HRT had a mean thickness of 5.7 mm and increased the threshold for thickened endometrium in their study from 4 mm or less in women not on HRT to 8 mm or less in women in HRT [43].

The optimal timing for evaluation of the endometrium in women on HRT is during the period immediately after withdrawal bleeding to avoid false-positive results. Another trial that evaluated endometrial thickness in postmenopausal women on HRT found a mean thickness of 3.2 to 3.6 mm. The authors also reported that 9% of these patients with an endometrial thickness of more than 4 mm had abnormal endometrial findings on hysteroscopy with endometrial biopsy [44]. A thickened endometrium was a more sensitive predictor of pathologic condition than irregular bleeding. Although it is not practical or cost effective to screen all postmenopausal women on HRT for endometrial pathologic conditions, this study provided further evidence that irregular bleeding in the absence of ultrasonographic findings of endometrial proliferation is most like secondary to benign atrophic changes rather than abnormal cellular proliferation.

In most gynecology training programs, students are taught that biopsy always should be performed in women with high pretest probability for endometrial cancer. Such risk factors include hyperestrogenic states (obesity, chronic anovulation, unopposed estrogen therapy), personal history of breast cancer with or without tamoxifen therapy, and family history of endometrial, ovarian, breast, or colon cancer. No studies in the literature actually provide any evidence for this practice, and a recent cost analysis by Medverd and Dubinsky [45] indicated that the prevalence of carcinoma would have to be higher than is actually present in any of these populations to make biopsy more cost minimizing than ultrasound.

Summary

Transvaginal ultrasound with SIS is a cost-minimizing screening tool for perimenopausal and postmenopausal women with vaginal bleeding. Its use decreases the need for invasive diagnostic procedures for women without abnormalities, and ultrasound increases the sensitivity of detecting abnormalities in women with pathologic conditions. Vaginal sonography is preferred over uniform biopsy of postmenopausal women with vaginal bleeding because it (1) is a less invasive procedure, (2) is generally painless, (3) has no complications, and (4) may be more sensitive for detecting carcinoma than blind biopsy. Transvaginal sonography is rarely nondiagnostic. Endometrial sampling is less successful in women with a thin endometrial stripe on ultrasound than in women with real endometrial pathologic condition.

A limitation of ultrasound is that an abnormal finding is not specific: ultrasound cannot always reliably distinguish between benign proliferation, hyperplasia, polyps, and cancer. Although ultrasound may not be able to distinguish between hyperplasia and malignancy, the next step in the clinical treatment requires tissue sampling. Because of the risk of progression of complex hyperplasia to carcinoma, patients with this finding may benefit from hormonal suppression, dilatation and curettage, endometrial ablation, or hysterectomy, depending on the clinical scenario. The inability to distinguish these two entities based on ultrasound alone should not be seen as a limitation because tissue sampling is required in either case. Occasionally (in 5% to 10% of cases), a woman's endometrium cannot be identified on ultrasound, and these women also need further evaluation.

Ultrasonography also may be used as a first-line investigation in other populations with abnormal uterine bleeding. In a multicenter, randomized, controlled trial of 400 women with abnormal uterine bleeding, the investigators found that transvaginal sonography combined with Pipelle endometrial bi-

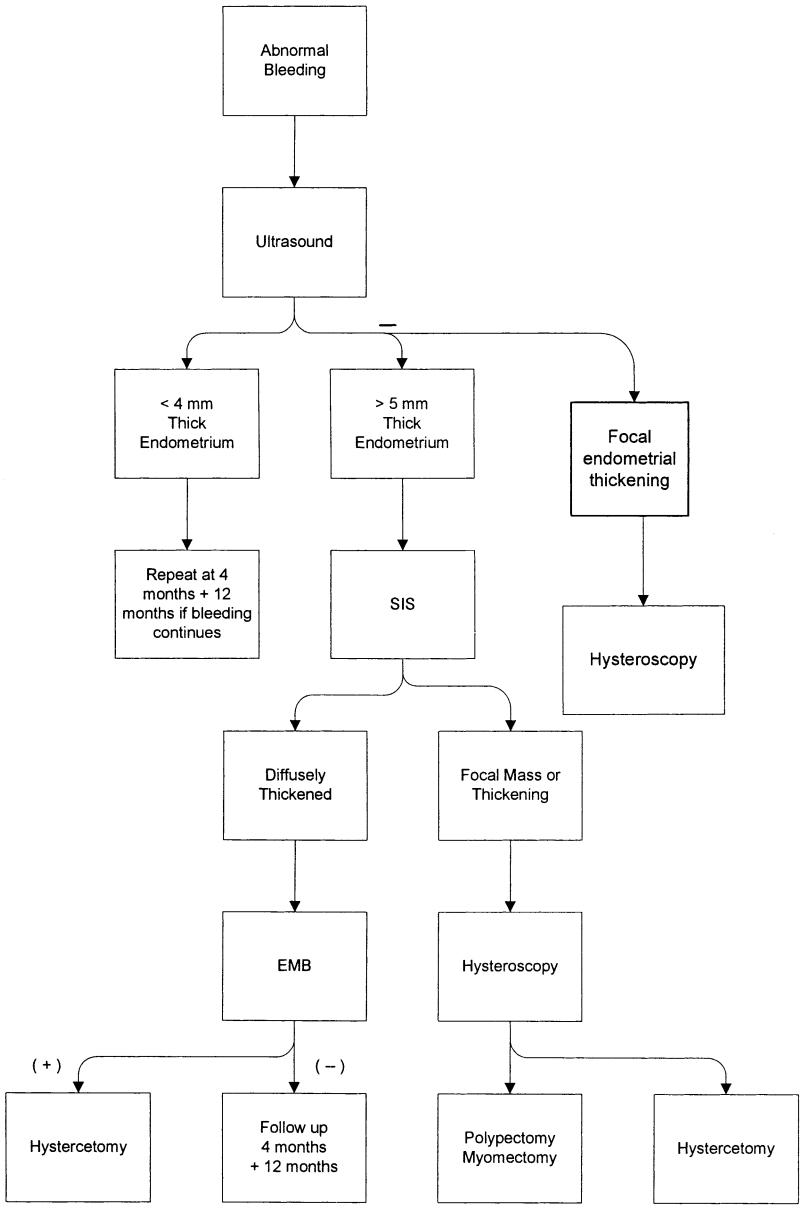

Fig. 12. Proposed algorithm for evaluating women with abnormal vaginal bleeding.

opsy and outpatient hysteroscopy was as effective as inpatient hysteroscopy and curettage [4,8]. The subjects included women older than 35 years with PMB, menorrhagia, intermenstrual bleeding, postcoital bleeding, or irregular menses. Transvaginal sonography may be a cost-effective, sensitive, and well-tolerated method to evaluate most women with abnormal bleeding in combination with physical examination and endometrial biopsy and hysteroscopy as indicated [46].

Hysteroscopy is likely to become the new gold standard in the future because of its ability to visualize directly the endometrium and perform directed biopsies as indicated. As office-based hysteroscopy becomes more practical and widespread, the technique may become more cost effective. An evaluation

plan using transvaginal sonography as the initial screening evaluation followed by endometrial biopsy or, more likely, hysteroscopy is likely to become the standard of care (Fig. 12).

It remains unproven whether certain patients at higher risk for carcinoma should proceed directly to invasive evaluation. Women on tamoxifen with persistent recurrent bleeding, women with significant risk factors for carcinoma, and women with life-threatening hemorrhage comprise this group. Further studies are still necessary to evaluate high-risk patients and determine whether ultrasound or biopsy is really the most cost-effective initial test.

References

[1] Hawwa ZM, Nahhas WA, Copenhaver EH. Post-menopausal bleeding. Lahey Clinic Foundation Bulletin 1970;19:61–70.

[2] Dijkhuizen FP, Mol BW, Brolmann HA, Heintz AP. The accuracy of endometrial sampling in the diagnosis of patients with endometrial cancer and hyperplasia. Cancer 2000;89:1765–72.

[3] Stowall TG, Solomon SK, Ling FW. Endometrial sampling prior to hysterectomy. Obstet Gynecol 1989;73: 405–9.

[4] Epstein E, Ramirez A, Skoog L, Valentin L. Dilation and curettage fails to detect most focal lesions in the uterine cavity in women with postmenopausal bleeding. Acta Obstet Gynecol Scand 2001;80:1131–6.

[5] Dubinsky TJ, Parvery HR, Maklad N. The role of transvaginal sonography and endometrial biopsy in the evaluation of peri- and postmenopausal bleeding. AJR Am J Roentgenol 1997;169:145–9.

[6] Goldstein RB, Bree RL, Benson CB, Benaceraf BR, Bloss JD, Carlos R, et al. Evaluation of the woman with postmenopausal bleeding: Society of Radiologists in Ultrasound-Sponsored Consensus Conference Statement. J Ultrasound Med 2001;20:1025–36.

[7] Alcazar JL, Zornoza A. Transvaginal ultrasonographic measurement of endometrial thickness: an intra-observer and interobserver reproducibility study. Radiography 2001;7:101–4.

[8] Smith-Bindman R, Kerlikowske K, Feldstein VA, Subak L, Scheidler J, Segal M, et al. Endovaginal ultrasound to exclude endometrial cancer and other endometrial abnormalities. JAMA 1998;280:1510–7.

[9] Granberg S, Ylostalo P, Wikland M, Karlsson B. Endometrial sonographic and histologic findings in women with and without hormonal replacement therapy suffering from postmenopausal bleeding. Maturitas 1997;27:35–40.

[10] Garuti G, Sambruni I, Cellani F, Garzia D, Alleva P, Lueti M. Hysteroscopy and transvaginal ultrasonography in postmenopausal women with uterine bleeding. Int J Gynaecol Obstet 1999;65:25–33.

[11] Briley M, Lindsell DR. The role of transvaginal ultrasound in the investigation of women with post-menopausal bleeding. Clin Radiol 1998;53:502–5.

[12] Bakour SH, Dwarankanath LS, Khan KS, Newton JR, Gupta JK. The diagnostic accuracy of ultrasound scan in predicting endometrial hyperplasia and cancer in post-menopausal bleeding. Acta Obstet Gynecol Scand 1999;78:447–51.

[13] Mateos F, Zarauz R, Seco C, Rayward JR, del Barrio P, Aguirre J, et al. Assessment with transvaginal ultrasonography of endometrial thickness in women with post-menopausal bleeding. Eur J Gynaecol Oncol 1997; 18:504–7.

[14] Buyuk E, Durmusoglu F, Erenus M, Karakoc B. Endometrial disease diagnosed by transvaginal ultrasound and dilation and curettage. Acta Obstet Gynecol Scand 1999;78:419–22.

[15] Bree RL, Bowerman RA, Bohm-Velez M, Benson CB, Doubilet PM, DeDreu S, et al. Ultrasound evaluation of the uterus in patients with post-menopausal bleeding: a positive effect on decision-making. Radiology 2000;216:260–4.

[16] Kamel HS, Darwish AM, Mohamed SA. Comparison of transvaginal ultrasonography and vaginal sonohysterography in the detection of endometrial polyps. Acta Obstet Gynecol Scand 2000;79:902.

[17] Sherman ME, Silverberg SG. Advances in endometrial pathology. Clin Lab Med 1995;15:517.

[18] Gompel C, Silverberg SG. Pathology, gynecology and obstetrics. 2nd edition. Philadelphia: JB Lippincott; 1977.

[19] Agorastos T, Dinas K, Patsiaoura K. Cystic degenerated angioleiomyoma mimicking ovarian pathology. Acta Obstet Gynecol Scand 2001;80:863–5.

[20] Dodson MG. Use of transvaginal ultrasound in diagnosing the etiology of menometrorrhagia. J Reprod Med 1994;39:262–72.

[21] Chambers CB, Unis JS. Ultrasonographic evidence of uterine malignancy in the postmenopausal uterus. Am J Obstet Gynecol 1986;161:549.

[22] Requard CK, Wicks JD, Mettler Jr FA. Ultrasonography in the staging of endometrial adenocarcinoma. Radiology 1981;140:781.

[23] Gull B, Carlsson SA, Karlsson B, Ylostalo P, Milsom I, Granberg S. Transvaginal ultrasound of the endometrium in women with post-menopausal bleeding: is it always necessary to perform an endometrial biopsy? Am J Obstet Gynecol 2000;182:509–15.

[24] Loverro G, Bettocchi S, Cormio G, Nicolardi V, Greco P, Vimercati A, et al. Transvaginal sonography and hysteroscopy in postmenopausal uterine bleeding. Maturitas 1999;33:139–44.

[25] Weigel M, Friese K, Strittmatter HJ, Melchert F. Measuring the thickness: is that all we have to do for sonographic assessment of endometrium in postmenopausal women? Ultrasound Obstet Gynecol 1995;6: 97–102.

[26] Hulka CA, Hall DA, McCarthy K, Simeone JF. Endometrial polyps, hyperplasia, and carcinoma in post-

menopausal women: differentiation with endovaginal sonography. Radiology 1994;191:755–8.
[27] Sheikh M, Sawhney S, Khurana A, Al-Yatama M. Alteration of sonographic texture of the endometrium in post-menopausal bleeding: a guide to further management. Acta Obstet Gynecol Scand 2000;79:1006–10.
[28] Sousa SR, Lilvestre M, Almeida e Sousa L, Falcao F, Dias L, Silva T, et al. Transvaginal ultrasonography and hysteroscopy in postmenopausal bleeding: a prospective study. Acta Obstet Gynecol Scand 2001;80: 856–62.
[29] Epstein E, Ramirez A, Skoog L, Valentin L. Transvaginal sonography, saline contrast sonohysterography and hysteroscopy for the investigation of women with postmenopausal bleeding and endometrium > 5 mm. Ultrasound Obstet Gynecol 2001;18:157–62.
[30] Fleischer AC. Optimizing the accuracy of transvaginal ultrasonography of the endometrium. N Engl J Med 1997;337:1839–40.
[31] Fleischer AC, Dudley BS, Entmas SS, et al. Myometrial invasion by endometrial carcinoma: sonographic assessment. Radiology 1987;162:307.
[32] Dubinsky TJ, Stroehlein K, Abu-Ghazzeh Y, Parvey HR, Maklad N. Prediction of benign and malignant endometrial disease: hysterosonographic-pathologic correlation. Radiology 1999;210:393–7.
[33] Cameron ST, Walker J, Chambers S, Critchley H. Comparison of transvaginal ultrasound, saline infusion sonography and hysteroscopy to investigate postmenopausal bleeding and unscheduled bleeding on HRT. Aust N Z J Obstet Gynaecol 2001;41:291–4.
[34] Amit A, Weiner Z, Ganem N, Kerner H, Edwards CL, Kaplan A, et al. The diagnostic value of power Doppler measurements in the endometrium of women with postmenopausal bleeding. Gynecol Oncol 2000;77:243–7.
[35] Sheth S, Hamper UM, McCollum ME, Caskey CI, Rosenshein NB, Kurman RJ. Endometrial blood flow analysis in post-menopausal women: can it help differentiate benign from malignant causes of endometrial thickening? Radiology 1995;195:661–5.
[36] Yaman C, Ebner T, Jesacher K, Obermayr G, Polz W, Tews G. Reproducibility of three-dimensional endometrial volume measurements in patients with post-menopausal bleeding. Ultrasound Obstet Gynecol 2002;19: 282–6.
[37] Riccabona M, Nelson TR, Pretorius DH. Three-dimensional ultrasound: accuracy of distance and volume measurements. Ultrasound Obstet Gynecol 1996;7: 429–38.
[38] Gruboeck K, Jurkovic D, Lawton F, Savvas M, Tailor A, Campbell S. The diagnostic value of endometrial thickness and volume measurements by three-dimensional ultrasound in patients with post-menopausal bleeding. Ultrasound Obstet Gynecol 1996;8: 272–6.
[39] Fornander T, Cedarmark B, Mattson A, et al. Adjuvant tamoxifen in early breast cancer: occurrence of new primary cancers. Lancet 1989;1:117–20.
[40] Liedman R, Lindahl B, Andolf E, Willen R, Ingvar C, Ranstam J. Disaccordance between estimation of endometrial thickness as measured by transvaginal ultrasound compared with hysteroscopy and directed biopsy in breast cancer patients treated with tamoxifen. Anticancer Res 2000;20:4889–91.
[41] Wiczyk HP, Janus CL, Richards CJ, et al. Comparison of magnetic resonance imaging and ultrasound in evaluating follicular and endometrial development throughout the normal cycle. Fertil Steril 1988;49:969.
[42] Affinito P, Palomba S, Pellicano M, Sorrentino C, Di Carlo C, Morgera R, et al. Ultrasonographic measurement of endometrial thickness during hormone replacement therapy in postmenopausal women. Ultrasound Obstet Gynecol 1998;11:343.
[43] Affinito P, Palomba A, Sammartino A, Bonifacio M, Nappi C. Ultrasonographic endometrial monitoring during continuous-sequential hormone replacement regimen in post-menopausal women. Maturitas 2001; 39:239–44.
[44] Omodei U, Ferrazzia E, Ruggeri C, Palai N, Fallo L, Dordoni D, et al. Endometrial thickness and histological abnormalities in women on hormone replacement therapy: a transvaginal ultrasound/hysteroscopic study. Ultrasound Obstet Gynecol 2000;15:317–20.
[45] Medverd JR, Dubinsky TJ. Cost analysis of ultrasound versus endometrial biopsy in the evaluation of abnormal vaginal bleeding. Radiology 2002;222: 619–27.
[46] Goldstein SR, Nachtigall M, Snyder JR, Nachtigall L. Endometrial assessment by vaginal ultrasonography before endometrial sampling in patients with postmenopausal bleeding. Am J Obstet Gynecol 1999;163: 119–23.

RADIOLOGIC
CLINICS OF
NORTH AMERICA

Radiol Clin N Am 41 (2003) 781–797

Sonohysterography

Mary Jane O'Neill, MD

Division of Abdominal Imaging and Interventional Radiology, Massachusetts General Hospital, Harvard Medical School, White Building Room 270, 55 Fruit Street, Boston, MA 02114, USA

Sonohysterography (SHG) is a valuable, minimally invasive, sonographic examination that plays a crucial role in the triaging of abnormal uterine bleeding. SHG augments the traditional transvaginal ultrasound (TVUS) examination by distending the endometrial canal with saline, which allows each individual layer of the endometrial lining to be evaluated separately. The single-layer evaluation made possible with SHG significantly improves detection and characterization of focal and diffuse endometrial processes over that of TVUS alone [1–3]. Focal lesions involve less than 25% of the endometrial surface area and are unlikely to be diagnosed without hysteroscopically guided biopsy. Although the ability to accurately detect focal endometrial lesions noninvasively with SHG has had the largest impact on the management of abnormal bleeding in postmenopausal patients, the diagnosis and management of dysfunctional bleeding and infertility in premenopausal patients also have improved significantly. The improvement is largely because of the detailed evaluation that the study provided regarding the location and extent of subendometrial processes that affect the endometrium and endometrial cavity. This article reviews the technique, indications, and diagnostic findings during SHG.

Technique

Patient preparation

All premenopausal patients and all postmenopausal patients on sequential estrogen replacement therapy should be examined during the proliferative phase of the menstrual cycle (days 0–14) to decrease the likelihood of false-positive findings [4]. During the secretory phase, the endometrium not only is thicker but also tends to appear more heterogeneous and irregular in contour (Fig. 1). This appearance leads to increased rates of false-negative and false-positive diagnoses during SHG for endometrial pathology and decreases overall sensitivity and specificity of the examination. During the proliferative phase, the normal endometrium is thin and homogeneous (Fig. 2), which allows much more definitive evaluation of endometrial and subendometrial processes.

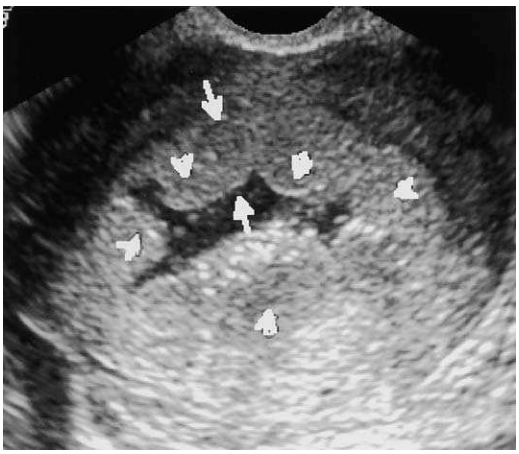

Fig. 1. Coronal SHG in 33-year-old woman with intermenstrual bleeding preformed at day 23 of menstrual cycle. The secretory endometrium is thick and heterogeneous (*arrows*). The lobulated contour (*arrowheads*) can cause false-positive and false-negative findings at SHG.

E-mail address: Moneill@partners.org

0033-8389/03/$ – see front matter © 2003 Elsevier Inc. All rights reserved.
doi:10.1016/S0033-8389(03)00038-1

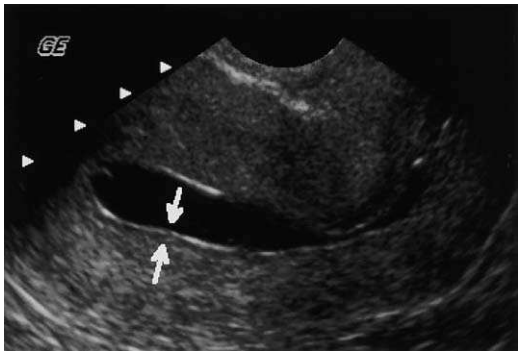

Fig. 2. Repeat SHG in same patient performed at day 5 of menstrual cycle. During the proliferative phase, the premenopausal endometrium is thin and homogeneous (*arrows)*. Note the slight hypoechoic appearance to the single layer of the premenopausal endometrium during this phase.

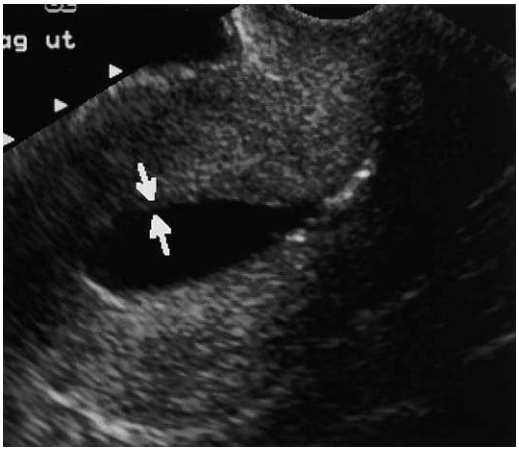

Fig. 4. Sagittal SHG in 54-year-old woman with postmenopausal bleeding demonstrates a normal single endometrial layer. The postmenopausal endometrium is thin and almost imperceptible (*arrows*). Pathology in this case was endometrial atrophy.

Few reports of pelvic infections have been related to SHG. Patients who are at increased risk of stasis of saline within the pelvis because of tubal occlusion or peritubal adhesions are at higher risk, however, and they may benefit from antibiotic prophylaxis. Before catheter insertion, a preliminary TVUS should be performed to assess for preexisting ovarian or adnexal pathology and document the current appearance of the endometrial lining. The adnexa also should be assessed after the procedure to identify the presence of any new adnexal collections.

Catheter insertion

The study can be performed through a balloon-tipped catheter placed in either the cervical or endometrial canal or a nonocclusive straight catheter placed in the endometrial canal. Balloon catheters are less likely to become dislodged during ultrasound probe insertion. If the balloon is initially inflated in the endometrial canal, the balloon should be deflated and the catheter retracted under sonographic guidance into the proximal cervical canal to ensure that the

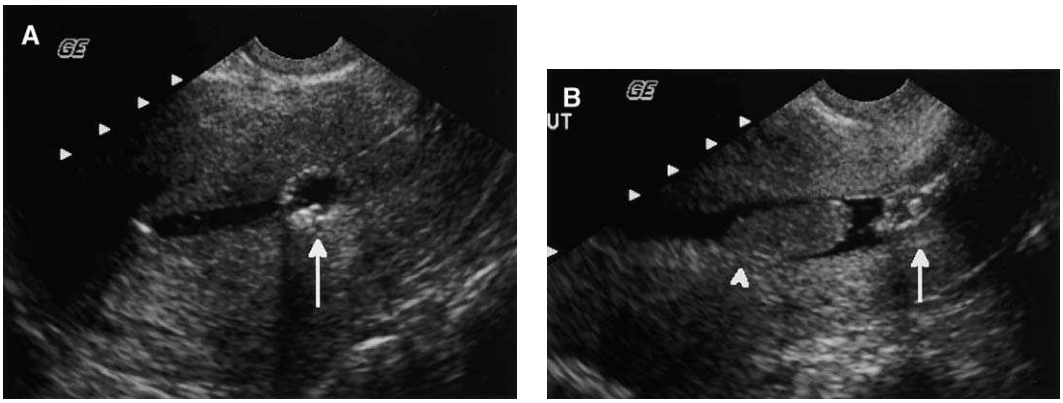

Fig. 3. Sagittal SHG in 63-year-old woman with postmenopausal bleeding. (*A*) Initial saline infusion reveals no focal abnormalities. The catheter (*arrow*) is in the inferior aspect of the endometrial cavity. (*B*) After retraction of the catheter into the superior portion of the cervical canal (*arrow*), a focal endometrial lesion arising from the posterior endometrial surface in the lower uterine segment is revealed (*arrowhead*). Pathology showed a benign endometrial polyp.

entire single layer thickness of the endometrium is completely evaluated without interference from the catheter (Fig. 3).

If the cervical os is stenotic and cannot be accessed with the 5 Fr catheter, access can be achieved using the Seldinger technique. This technique involves a 0.038 glide wire (Cook, Bloomington, IN) to gain initial access into the endometrial cavity. Once this wire has been introduced, a small 5 Fr tapered dilator (Cook, Bloomington, IN) can be advanced over the wire. The study can be performed through the dilator after the wire has been removed. Using this technique when routine catheter placement fails significantly improves the technical success rate of SHG.

Normal endometrium by sonohysterography

Premenopausal

The normal single layer of the premenopausal endometrium during the early proliferative phase is slightly hypoechoic, thin, and homogeneous in thickness (see Fig. 2). There is no widely accepted limit to the single layer thickness in premenopausal patients, but a single layer thickness more than 6 mm is unusual and should be evaluated carefully and possibly biopsied in symptomatic women. Regardless of the absolute thickness, the endometrium should be homogeneous in echotexture and smooth in contour [4].

Postmenopausal

The normal single layer of the postmenopausal endometrium is homogeneously echogenic, smooth in contour, and uniform in thickness (Fig. 4). The absolute thickness is considered normal or atrophic if less than 2 mm in symptomatic women and 2 to 3 mm in asymptomatic women on estrogen replacement or tamoxifen [5–7].

Indications

Triage of postmenopausal bleeding

Until recently, triage of patients with abnormal uterine bleeding was based primarily on the findings of office endometrial biopsy and TVUS [1,2]. With the advent of hysteroscopy and SHG, however, it is evident that most causes of postmenopausal bleeding (PMB) are secondary to focal endometrial or subendometrial processes, such as endometrial polyps or submucosal fibroids. These entities involve only a

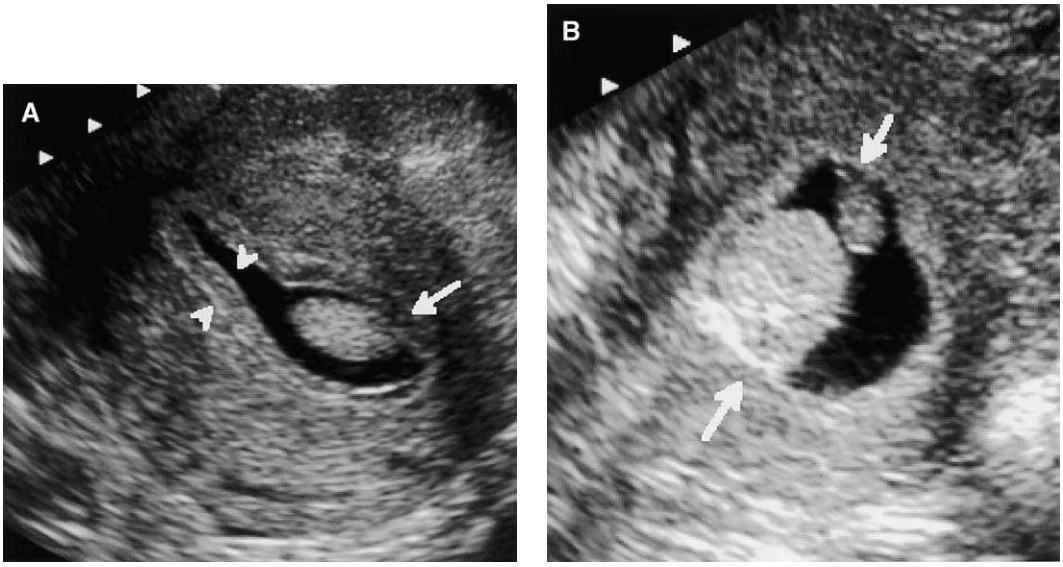

Fig. 5. (*A*) Sagittal SHG in 54-year-old woman with postmenopausal bleeding (PMB) demonstrates the typical appearance of an endometrial polyp. The lesion is homogeneously echogenic and arises from a narrow stalk from the posterior endometrial surface in this retroverted uterus (*arrow*). Note the normal thin remaining single layer of the endometrium (*arrowheads*). (*B*) Multiple polyps identified (*arrows*) on coronal SHG in 52-year-old woman with PMB. It is not unusual to identify more than one endometrial lesion at SHG. Each lesion should be localized accurately.

small proportion of the endometrial lining and are significantly underdiagnosed by office endometrial biopsy secondary to sampling error [5–8].

Because patient management is dictated by the presence or absence of focal endometrial lesions, the primary goal of SHG is not to diagnose specific endometrial lesions accurately but rather to determine whether the abnormality that affects the endometrium is focal or diffuse. If there is a focal abnormality, it must be localized accurately so that the hysteroscopic surgeon can remove it reliably. Although imaging features suggest particular diagnoses, none is sensitive or specific enough to dictate patient care in the setting of PMB [9,10]. In principle, all focal lesions in symptomatic PMB should be investigated with hysteroscopic sampling.

Triage of abnormal endometrium in asymptomatic postmenopausal patients on estrogen replacement therapy or tamoxifen

Patients on estrogen replacement therapy and tamoxifen have a higher risk of focal and diffuse endometrial pathology and commonly have abnormally thick or heterogeneous endometrial stripes without symptoms. SHG plays an important role in detecting potential focal endometrial lesions in this subgroup of asymptomatic patents.

Dysfunctional uterine bleeding

Sonohysterography in the premenopausal patient population serves a more specialized role. Endome-

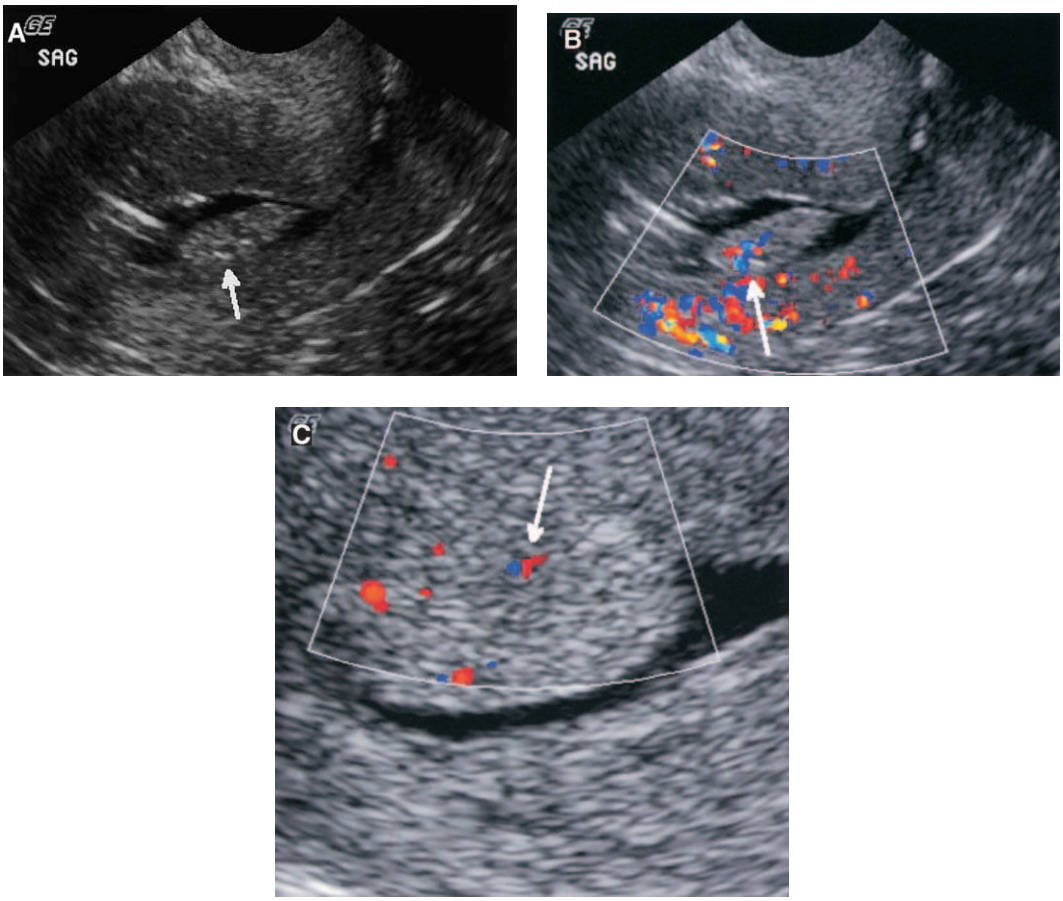

Fig. 6. (*A*, *B*) Doppler interrogation of the stalk of the polyp arising form the posterior endometrial surface in this 51-year-old woman with postmenopausal bleeding (PMB) demonstrates the characteristic prominent color Doppler flow (*arrows*). (*C*) Doppler interrogation of the base of a submucosal fibroid in a 56-year-old woman with PMB demonstrates a similar vascular pedicle (*arrow*). This feature is most often seen in endometrial polyps but is nonspecific and is occasionally observed in other endometrial and subendometrial pathologies.

trial polyps are less common in these patients but can cause intermenstrual bleeding and infertility [1]. SHG plays an important role in defining the extent of submucosal extension in patients with abnormal vaginal bleeding and suspected submucosal fibroids. Assessing the extent of submucosal component can help guide the mode of resection chosen by the gynecologic surgeon.

Infertility and pregnancy complications

Because of the cross-sectional view of the cavity, SHG plays an important role in the diagnosis and staging of intrauterine adhesions in patients with infertility. Another more limited role of SHG in the premenopausal patient is the diagnosis of small foci of retained placental tissue in patients who remain symptomatic after failed dilatation and curettage for retained products of conception.

Pathology

Focal lesions

Endometrial polyps

Endometrial polyps are the most common focal endometrial lesions and account for approximately 30% of cases of PMB [1]. Histologically, polyps represent hyperplastic growths of endometrial glands,

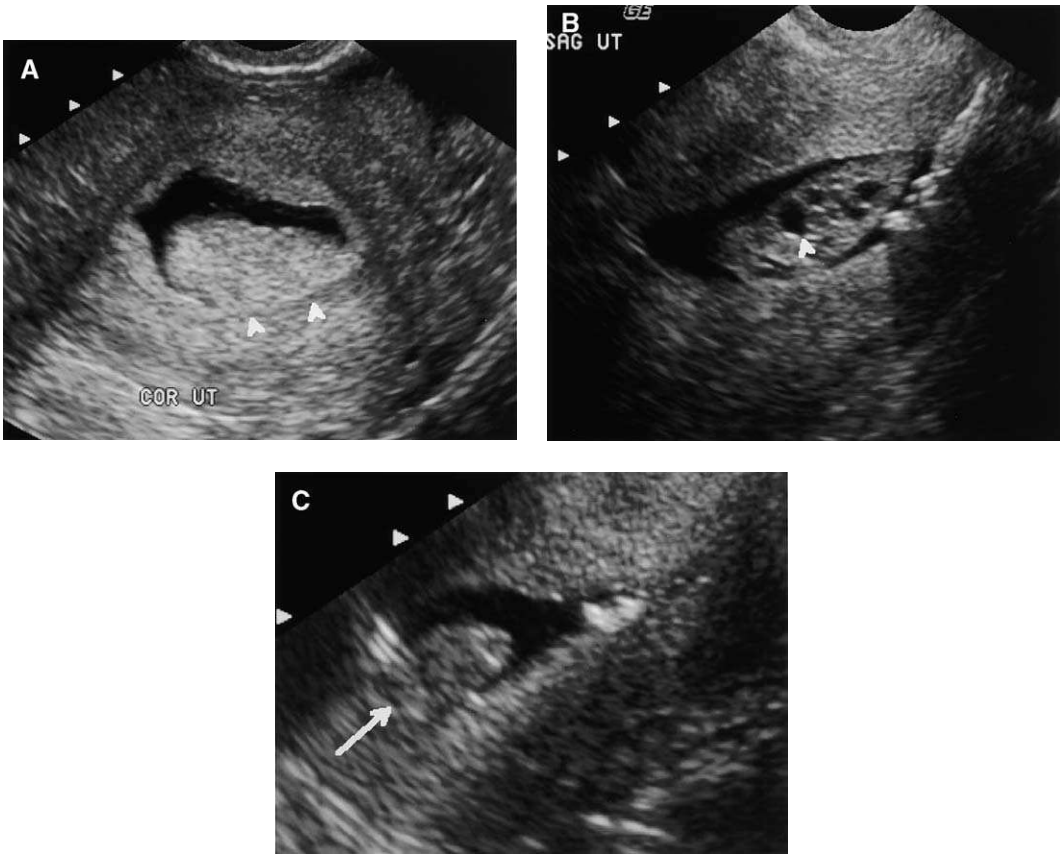

Fig. 7. (*A*) Coronal SHG in 57-year-old woman with postmenopausal bleeding (PMB) demonstrates an endometrial polyp with a broad base of attachment (*arrowheads*). When this finding is observed, the interface between the base of the polyp and the underlying myometrium should be scrutinized closely for any irregularities or evidence of invasion. (*B*) Sagittal SHG in a 57-year-old woman on tamoxifen reveals a large polyp with multiple intralesional cysts (*arrowheads*). This polyp had foci of severe atypia at histopathology. (*C*) Sagittal SHG in a 61-year-old woman with PMB shows a broad-based, hypoechoic, heterogeneous polypoid lesion arising form the endometrial surface in the fundus (*arrow*). Although this polyp represented a benign polyp on pathology, this feature indicates a higher likelihood of more aggressive histology.

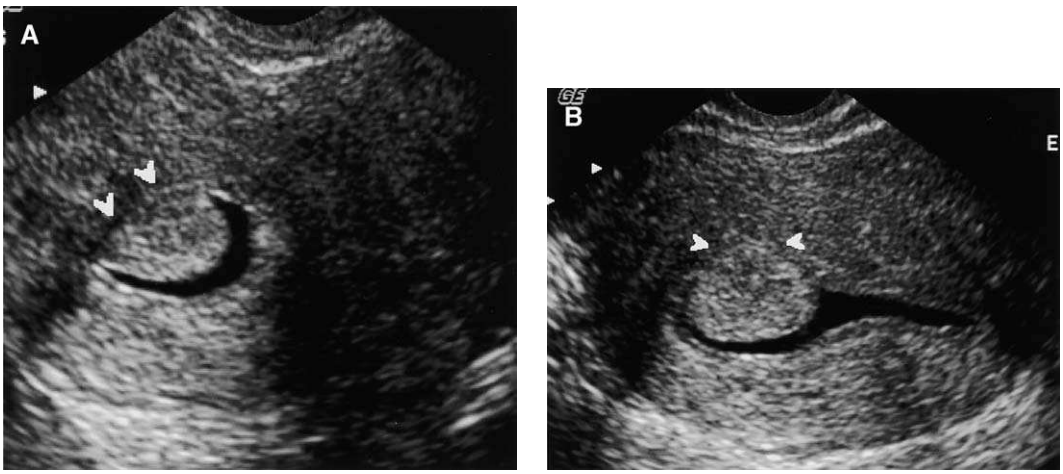

Fig. 8. (*A*) Coronal SHG in a 61-year-old woman on estrogen replacement therapy shows a benign broad-based endometrial polyp with a normal distinct endometrial myometrial interface (*arrowheads*). (*B*) Coronal SHG in a 52-year-old woman with postmenopausal bleeding shows a broad-based endometrial polyp with disruption of the smooth endometrial myometrial interface (*arrowheads*). This finding suggests myometrial invasion. A benign polyp was found at histology with no myometrial invasion or cytologic atypia.

and stroma and can be found in premenopausal and postmenopausal patients. Common presentations include PMB, intermenstrual bleeding, metorrhagia, and infertility [11].

On SHG, polyps typically are well-defined, homogeneous, echogenic solid lesions with a narrow base of attachment to the underlying endometrium (Fig. 5). There is often a well-defined vascular pedicle within the stalk when Doppler evaluation is performed, but this is not a feature specific to polyps [12] (Fig. 6). It is not unusual to identify more than one endometrial polyp during SHG. This is one reason to perform SHG for localization even in patients with strong suspicion for focal endometrial lesions at TVUS. Accurate detection and localization of the lesions before operative hysteroscopy increase the success rate of surgical resection.

Less commonly, polyps can have a broad base of attachment, contain cystic components, and contain areas of hypoechogenicity/heterogeneity within the polyp (Fig. 7). The heterogeneity within endometrial polyps most likely indicates prior hemorrhage, infarction, or inflammation [13]. The interface between the endometrium and the underlying myometrium should be interrogated closely in all focal endometrial lesions, particularly when the point of attachment is broad based or other atypical features are present (Fig. 8). If the interface is distorted or poorly visualized, the likelihood of a more aggressive process is significantly increased [14,15].

Most polyps, even those with typical benign features, are eventually removed hysteroscopically because continued PMB complicates future clinical patient management and because foci of hyperplasia or carcinoma in situ cannot be excluded sonographically.

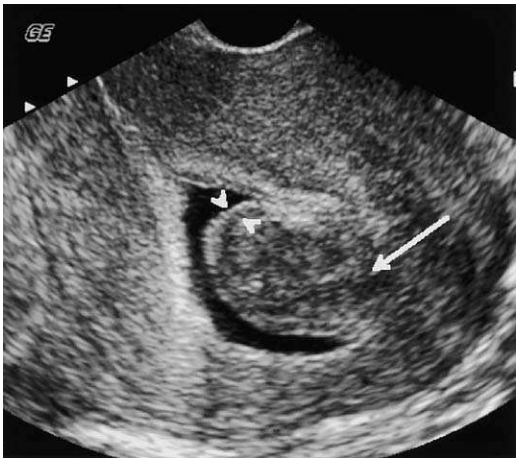

Fig. 9. Sagittal SHG in 37-year-old patient with severe menorrhagia shows a large submucosal fibroid (*arrow*). Submucosal fibroids tend to be more heterogeneous, hypoechoic, and larger than endometrial polyps. Note the thin layer of normal endometrium covering this mass, which indicates the submucosal location of the lesion (*arrowheads*).

Submucosal leiomyomas

Submucosal fibroids are a common source of dysfunctional premenopausal bleeding. They also can interfere with implantation and cause recurrent miscarriage, infertility, and premature labor [16]. Although fibroids are most often associated with dysfunction bleeding, they do play a role in the etiology of PMB and account for approximately 10% of cases [1].

During SHG, submucosal fibroids appear as broad-based, hypoechoic, submucosal masses that lift up the normal endometrium and project to various degrees into the endometrial canal (Fig. 9). When the endometrium can be seen lining the surface of the mass, the submucosal origin can be determined; however, this feature is not always present (Fig. 10). In these cases, distinguishing submucosal from mucosal lesions is not as definitive.

One of the more important functions of SHG in patients with suspected submucosal fibroids is to assess accurately the percent of protrusion of the volume of the fibroid into the endometrial canal. This information assists in triaging the patient to the most appropriate means of fibroid resection. Hysteroscopic resection is generally reserved for fibroids that project more than 50% of their volume into the endometrial canal. Open or laparoscopic myomectomy is required for lesions with less than 50% protrusion [16–18] (Fig. 11).

Pedunculated submucosal fibroids are completely endoluminal in location and are attached by only a small stalk to the subendometrium. These lesions are more difficult to distinguish sonographically from endometrial polyps and can be misdiagnosed as endometrial lesions (Figs. 11D, 12).

Adenomyosis in patients with suspected fibroids is occasionally seen during SHG (Fig. 13). Mild displacement of the endometrial lining can be seen in this entity, but intraluminal extension is rare.

Endometrial hyperplasia

Endometrial hyperplasia accounts for 4% to 8% of cases of endometrial bleeding and is defined as a proliferation of endometrial glands of irregular size and shape, with an increase in the gland/stroma ratio when compared with the normal proliferative endometrium [11]. Endometrial hyperplasia ranges in severity from simple hyperplasia without atypia, to hyperplasia with mild/ moderate atypia, to hyperplasia with severe atypia. Mild/moderate atypia has little or no malignant potential and is usually treated with removal of the exogenous agent or induction of menses with a progesterone analog. Severe atypia has a 20% risk of developing into endometrial carcinoma and is managed more aggressively with dilatation and curettage [8,19,20]. Risk factors for endometrial hyperplasia include exposure to unopposed estrogen,

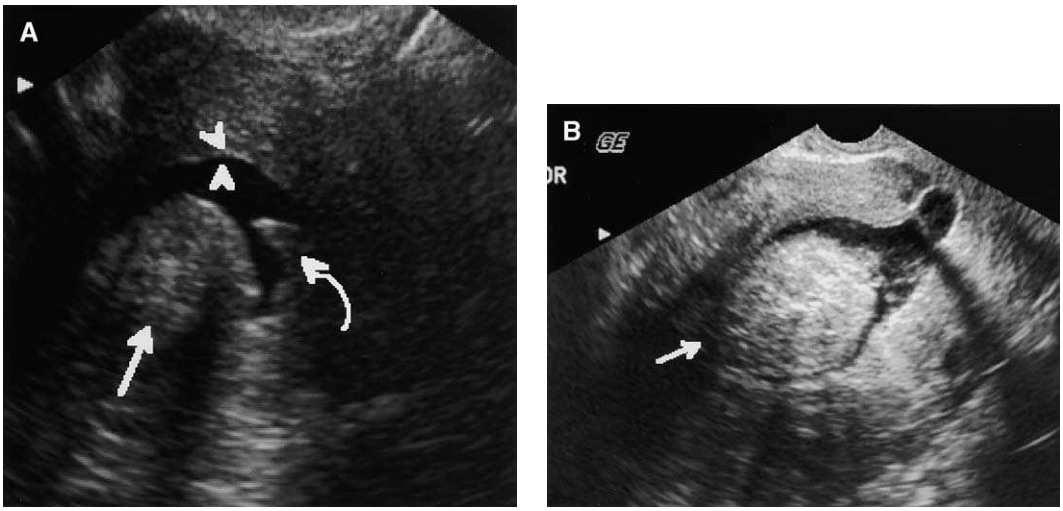

Fig. 10. (*A*, *B*) Coronal and sagittal SHG in two different postmenopausal patients with bleeding demonstrates submucosal fibroid (*arrows*). These lesions could not be distinguished sonographically from polyps because the endometrial layer over the lesions is atrophic and is not visualized. Definitive characterization with biospy proved that these lesions were fibroids. A more typical appearing endometrial polyp also was found in the first patient (*curved arrow*).

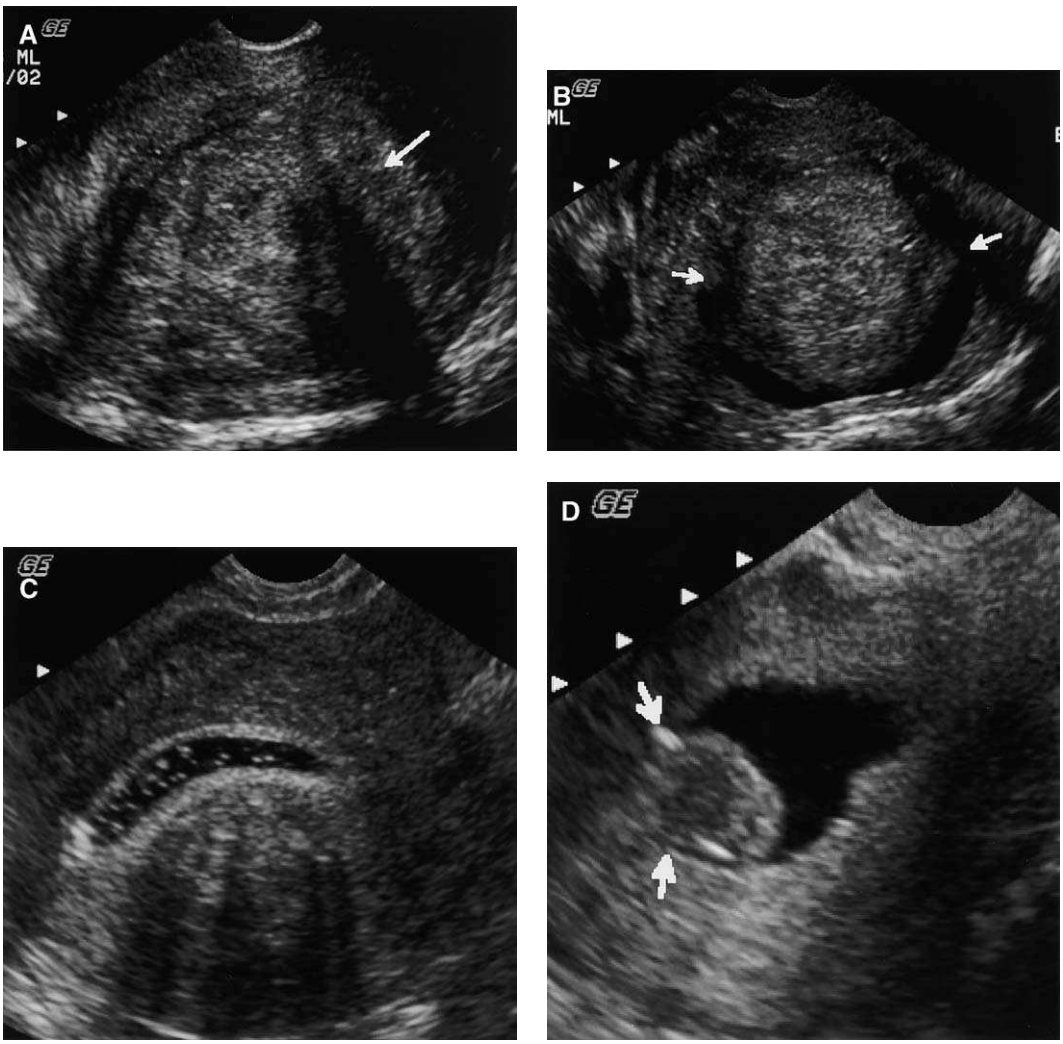

Fig. 11. (*A*) Coronal transvaginal ultrasound in 47-year-old woman with heavy menses demonstrates a centrally located fibroid (*arrow*). (*B*) SHG shows that this fibroid projects approximately 50% of its total volume into the endometrial cavity (*arrows*). (*C*) Coronal SHG in a 32-year-old woman with dysfunctional uterine bleeding shows a submucosal fibroid with less than 50% protrusion into the endometrial canal (*arrows*). (*D*) Sagittal SHG in a 47-year-old woman with postmenopausal bleeding demonstrates a submucosal fibroid with more than 50% protrusion into the endometrial cavity (*arrows*).

tamoxifen usage, nulliparity, obesity, and hypertension and diabetes.

Endometrial hyperplasia is usually a diffuse thickening of the echogenic endometrial stripe; however, focal areas of endometrial hyperplasia occasionally can be seen. The focal form of hyperplasia is more difficult to differentiate from endometrial polyps during SHG because of the considerable overlap of sonographic characteristics of the two lesions. Hyperplasia and carcinoma in situ also can be contained within otherwise benign endometrial polyps [21] (Fig. 14). Focal endometrial hyperplasia is most commonly a broad-based, echogenic mass that does not distort the endometrial-myometrial interface (Fig. 15). When only focal thickening is observed, the lesion should be sampled hysteroscopically to avoid the possibility of sampling error during office biopsy.

Endometrial cancer

Endometrial carcinoma is the most common gynecologic malignancy in the United States, and it affects predominantly postmenopausal women. Although endometrial cancer is the most prevalent gynecologic cancer, because of early detection, it accounts for

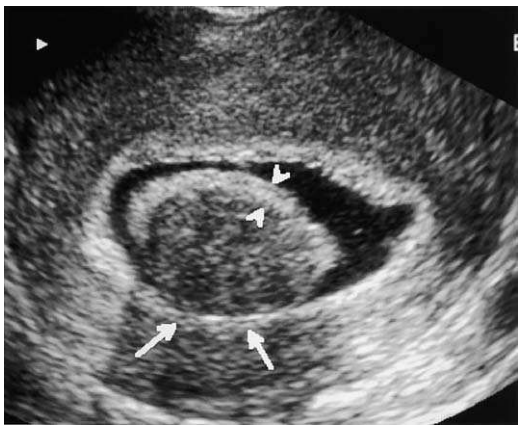

Fig. 12. Coronal SHG in a 31-year-old woman with severe bleeding demonstrates a large endoluminal submucosal fibroid (*arrow*). Note the thin layer of endometrium on the surface of this lesion (*arrowheads*).

just 1.5% of cancer deaths [11]. PMB is a common symptom of endometrial cancer and leads to early detection in most cases. Only 4% to 5% of cases of PMB are caused by endometrial cancer, however [1,4]. Endometrial cancer usually involves a large percentage of the endometrial lining and is readily diagnosed with office endometrial biopsy. Lesions can be small and polypoid, however, and may require a specific hysteroscopic biopsy for diagnosis (Fig. 16).

There is a wide variability in the SHG appearance of endometrial cancer. Large, broad-based, heterogeneous lesions should be viewed with increased concern for carcinoma, particularly if distortion of the endometrial-myometrial interface suggests myometrial invasion or inability to distend the endometrial cavity adequately (Fig. 17) [22,23].

Intrauterine adhesions

Patients who present with infertility or recurrent pregnancy loss are at increased risk for intrauterine adhesions. Adhesions are poorly detected by TVUS because they are compressed within the cavity and the endometrium often appears normal. Occasionally adhesions may be suspected when small echogenic foci or linear hypoechoic bands are detected in the endometrial lining [24].

Sonohysterography is highly sensitive in detecting and grading the severity of intrauterine adhesions [23,25]. SHG is more sensitive than even hysterosalpingography because of the improved cross-sectional capabilities associated with ultrasound. Adhesions appear as mobile, thin or thick echogenic bands that bridge the endometrial cavity (Fig. 18) [25]. As the severity of adhesions progresses, the endometrial cavity becomes less distensible during saline infusion (Fig. 19) [26]. Adhesions are often associated with echogenic endometrial scars, but either entity can be seen without the other (Fig. 20).

Retained products of conception

Retained products of conception are usually completely managed with TVUS and dilatation and curettage without routine need for SHG. A small

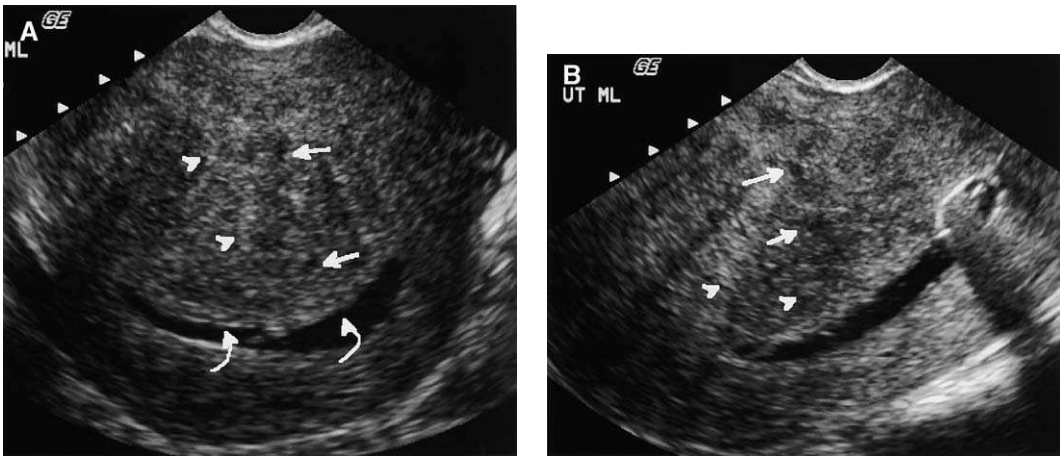

Fig. 13. Coronal (*A*) and sagittal (*B*) SHG in a 36-year-old woman with heavy menses and suspected submucosal fibroid shows the classic sonographic findings of adenomyosis. Note the presence of myometrial cysts (*arrows*), myometrial echogenic nodules (*arrowheads*), and asymmetric anterior wall swelling causing a slight impression on the endometrial lining and cavity (*curved arrows*).

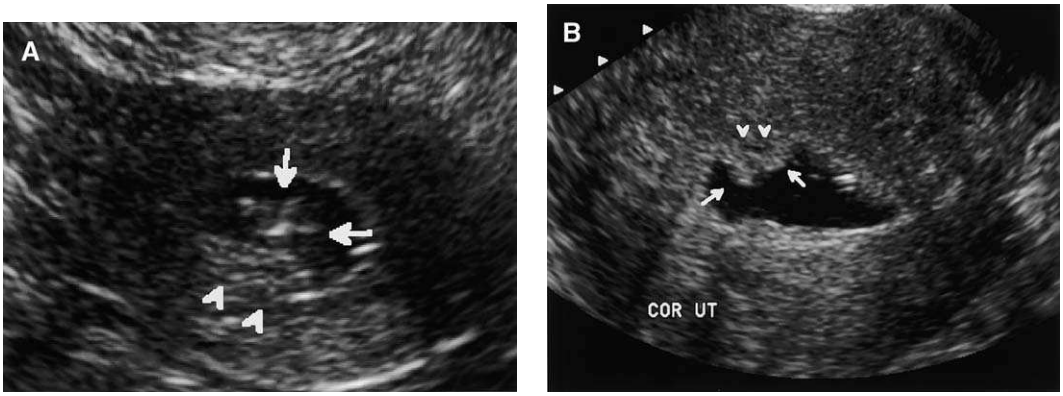

Fig. 14. (*A*) Coronal SHG in a 73-year-old woman with postmenopausal bleeding (PMB) shows a lobulated polypoid mass (*arrows*) arising from the posterior endometrial surface. The interface between the polyp and myometrium is normal (*arrowheads*). Pathology demonstrated an endometrial polyp with foci of endometrial hyperplasia with severe atypia. (*B*) Coronal SHG in a 53-year-old woman with PMB demonstrates a broad-based, hypoechoic, lobulated polypoid lesion (*arrows*) with a poorly defined interface with myometrium (*arrowheads*). Pathology revealed an endometrial polyp with foci of endometrial carcinoma.

percentage of patients remain symptomatic despite repetitive dilatations and curettage because of undetected foci of retained placental tissue. SHG is the ideal test to identify and localize the residual tissue in these problematic cases. Retained products of conception can have a wide variety of appearances during SHG, but they tend to be more irregular in contour and less homogeneous than typical endometrial polyps [27] (Fig. 21).

Diffuse lesions

Endometrial hyperplasia

Diffuse endometrial hyperplasia has a similar appearance and etiology to that described for focal hyperplasia, except the abnormality involves a larger percentage of the endometrial lining (Fig. 22).

Endometrial cancer

Diffuse endometrial cancer has a similar appearance and etiology to that described for focal cancer, except the abnormality involves most of endometrial lining. Interrogation of the myometrial-endometrial interface along the entire base of attachment is crucial in assessing the invasiveness of a lesion suspected to represent endometrial carcinoma (Fig. 23).

Tamoxifen-induced subendometrial changes

Tamoxifen is a nonsteroidal compound used in prophylaxis and therapy of breast cancer in premenopausal and postmenopausal women. Tamoxifen inhibits estrogen-dependent tumor growth by competing with estrogen at its receptor sites. The effect of drug binding at the estrogen receptor has either proestrogenic or antiestrogenic effects depending on the cell type. Both effects are seen within the endometrium, as evidenced by the increased rates of focal and diffuse endometrial pathology and endometrial atrophy that have been reported in patients on tamoxifen [28,29]. When endometrial abnormalities are detected, there is an increased risk for more aggressive histology within the lesion (Fig. 24) [24].

Tamoxifen also can cause cystic changes in the inner myometrium just beneath the endometrium that lead to pseudo-thickening of the endometrium on

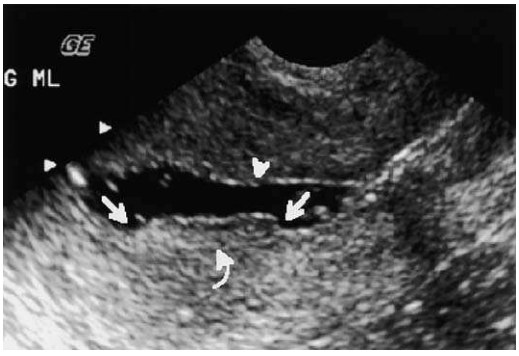

Fig. 15. Sagittal SHG in a 61-year-old woman with postmenopausal bleeding shows a long segment of focal endometrial thickening in the posterior endometrial surface (*arrows*). The remainder of the endometrium is normal in thickness (*arrowhead*). The interface with the myometrium is normal (*curved arrows*). Pathology revealed endometrial hyperplasia with mild atypia.

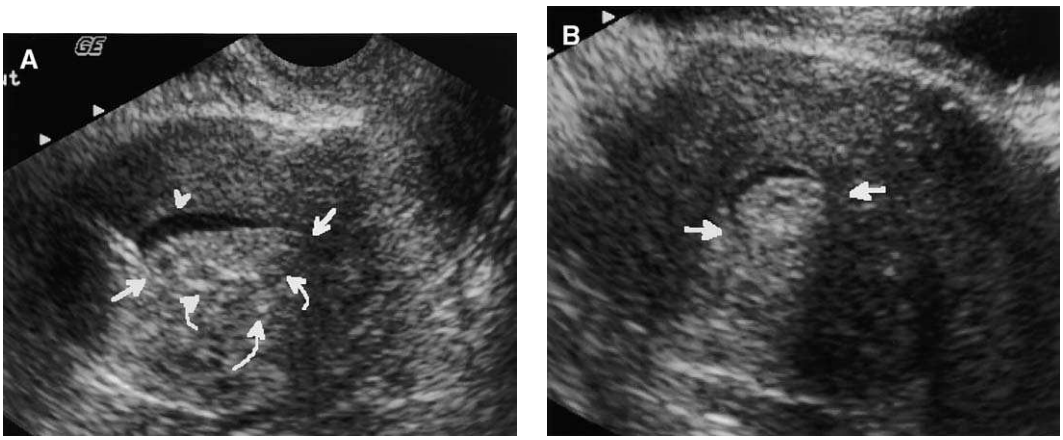

Fig. 16. Sagittal (*A*) and coronal (*B*) SHG in a 65-year-old patient with postmenopausal bleeding shows a broad-based heterogeneous polypoid mass (*arrows*) with a poorly defined endometrial-myometrial interface (*curved arrows*). The anterior endometrium is normal (*arrowhead*). Office biopsy suggested endometrial atrophy, but hysteroscopic biopsy revealed invasive endometrial carcinoma.

TVUS (Fig. 25) [30]. This subendometrial process is poorly understood, and different theories exist for the pathophysiolgy of this lesion. The most widely accepted theory is that tamoxifen causes a reactivation of preexisting adenomyosis with the inner layer of the myometrium [31,32]. This process of cystic degeneration of the inner myometrial layer is often associated with endometrial atrophy, further complicating diagnosis. If the endometrium is not clearly distinct from the cystic lesions, it is not possible to distinguish this process from other causes of true endometrial thickening, such as endometrial cancer and hyperplasia and aggressive tissue sampling must be performed (Fig. 26) [30].

Sonohysterography triage of postmenopausal bleeding

Postmenopausal patients can be divided into three specific clinical categories: patients with PMB, patients on estrogen replacement therapy, and patients

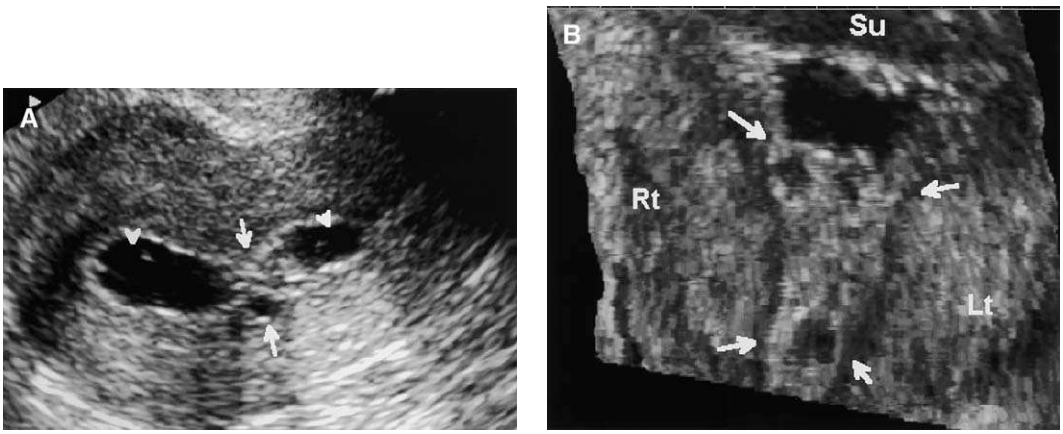

Fig. 17. Sagittal (*A*) and three-dimensional reformatted long axis (*B*) SHG in a 66-year-old woman on tamoxifen for breast cancer. The endometrial cavity is nondistensible in the region of the heterogeneous, annular mass (*arrows*). The cavity above and below the mass is filled with saline (*arrowheads*). Pathology revealed noninvasive endometrial carcinoma.

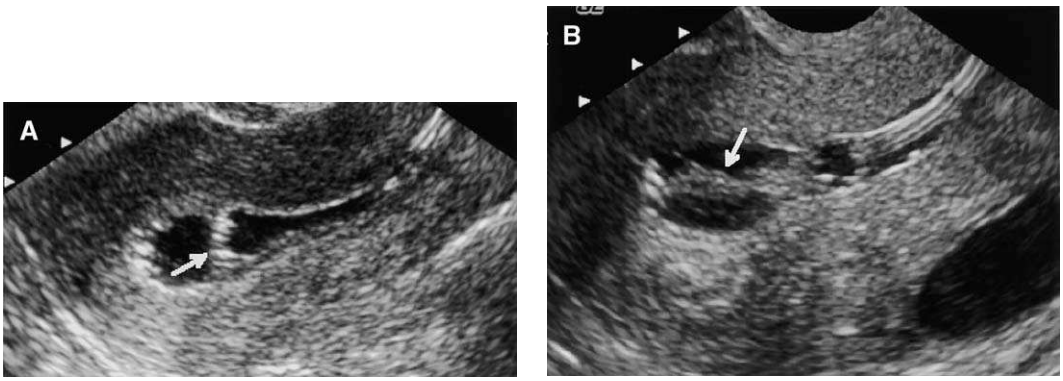

Fig. 18. Sagittal SHG in two different patients, both after hysteroscopic myomectomy, with mild (*A*) and moderate (*B*) uterine adhesions (*arrows*). The cavity is still distensible in both cases. The thickness of the bridging band is thicker and more irregular in the case of moderate adhesions.

on tamoxifen. In patients with PMB, TVUS is the initial examination performed. If the endometrium measures less than 4 mm by TVUS, endometrial atrophy is likely to be the cause of the PMB, and continued follow-up or one-time biopsy confirmation of atrophic endometrium is generally performed. The likelihood of endometrial carcinoma arising in a homogeneous endometrium with a double layer of 4 mm is negligible [22]. If the endometrium measures more than 4 mm, is heterogeneous in echotexture, or is not visualized by TVUS, SHG is required to assess for focal versus diffuse endometrial pathology. Some authors propose a more aggressive approach and recommend SHG for evaluation of all cases of PMB, even in cases in which the TVUS is normal [9].

With SHG, a single layer thickness of the endometrium of less than 2 mm is considered diagnostic of endometrial atrophy. Thickening of the endometrium more than 2 mm by SHG suggests diffuse endometrial pathology, and office endometrial biopsy should be performed to obtain a specimen for diagnosis. When focal endometrial abnormalities are identified, hysteroscopic-guided resection of the abnormality is required to avoid sampling error related to the nonspecific office endometrial biopsy [23,25].

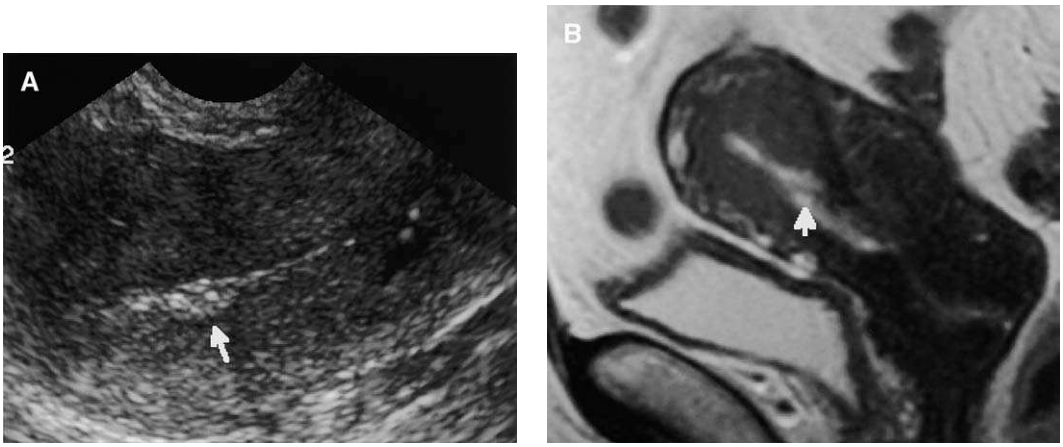

Fig. 19. (*A*) Sagittal SHG in a 42-year-old woman with secondary infertility demonstrates a nondistensible cavity and irregular endometrial lining with an echogenic, nonshadowing focus in the body of the uterus (*arrow*). (*B*) Sagittal T2-weighted MRI reveals presence of hypointense linear adhesion within the T2 bright endometrium in the same location (*arrow*).

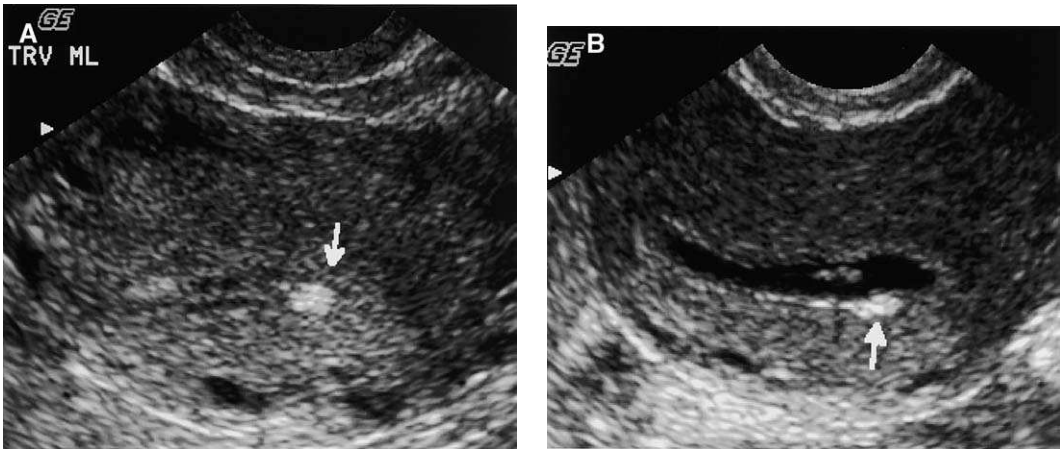

Fig. 20. (*A*) Coronal TVUS and SHG (*B*) in a 53-year-old woman with perimenopausal bleeding. The echogenic focus initially believed to represent a polyp on TVUS (*arrows*) was shown after SHG to represent an area of fibrosis within the posterior endometrial surface. No polypoid mass was detected on SHG, and endometrial biopsy revealed atrophy.

Asymptomatic postmenopausal patients who undergo TVUS for the purpose of surveillance because of hormone replacement therapy or tamoxifen therapy are managed slightly differently from patients with PMB. In patients on estrogen replacement therapy, many observers allow the double-layer thickness of the endometrium to be up to 6 mm before more specific evaluation with biopsy or SHG is attempted, provided the stripe remains smooth and homogeneous. In cases in which the stripe appears thicker than 6 mm but otherwise seems normal, reimaging earlier in the hormonal cycle may eliminate the need for additional evaluation [33]. Some observers suggest SHG and histologic sampling in asymptomatic patients on hormone replacement therapy when the endometrial thickness is more than 4 mm [23].

Patients on tamoxifen therapy who have abnormally thick or heterogeneous endometrial stripes are managed more aggressively than patients in the two other groups because of the higher incidence of neoplasia in this group of patients [30]. Dilatation and curettage provides a more complete method of endometrial sampling in the cases of diffuse endometrial pathology or abnormalities of the endometrial/myometrial interface than office endometrial biopsy alone.

Sonohysterography versus hysteroscopy

Office hysteroscopy provides another minimally invasive means of diagnosing focal and diffuse endometrial lesions. SHG and office hysteroscopy demonstrate high sensitivity and specificity for the diagnosis of focal and diffuse endometrial lesions and can be used effectively in the triage of PMB. Reported sensitivity and specificity rates of SHG for focal and diffuse endometrial lesions are 80% to 90%, similar to rates reported for hysteroscopy [10,16,17,23,25]. Both methods are well tolerated by patients and have high technical success rates. Because of the smaller size of the SHG catheters and the ability of the fluid to pass by proximal lesions, fewer failures related to cervical stenosis

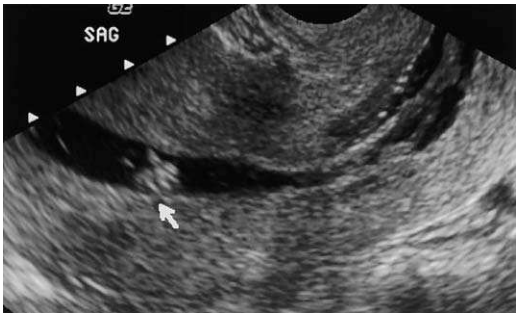

Fig. 21. Sagittal SHG in a 27-year-old woman with persistent bHCG elevation and bleeding despite repeat dilatation and curettage. A small focus of placental tissue is identified along the posterior endometrial surface (*arrow*) and resected hysteroscopically. Pathology revealed retained products of conception.

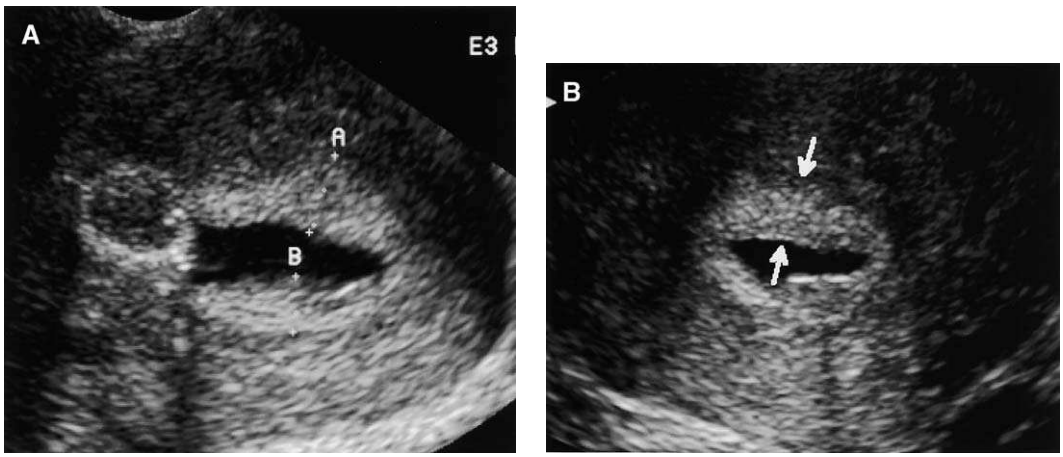

Fig. 22. Sagittal (*A*) and coronal (*B*) SHG in a 67-year-old woman with postmenopausal bleeding. There is diffuse thickening of each endometrial layer (*calipers*). The anterior endometrial surface demonstrates an irregular interface with the underlying myometrium. Pathology revealed hyperplasia without atypia.

and proximal adhesions are encountered with SHG when compared with hysteroscopy.

Summary

Sonohysterography can distinguish focal from diffuse pathology reliably and has become a crucial imaging test in the triage of PMB and in premenopausal patients with dysfunctional uterine bleeding or infertility. Polyps and submucosal fibroids are the most common focal findings during SHG. In postmenopausal patients, detection and accurate localization of findings, rather than lesion characterization, are the primary goals of the procedure. Most, if not all, focal lesions in this patient popula-

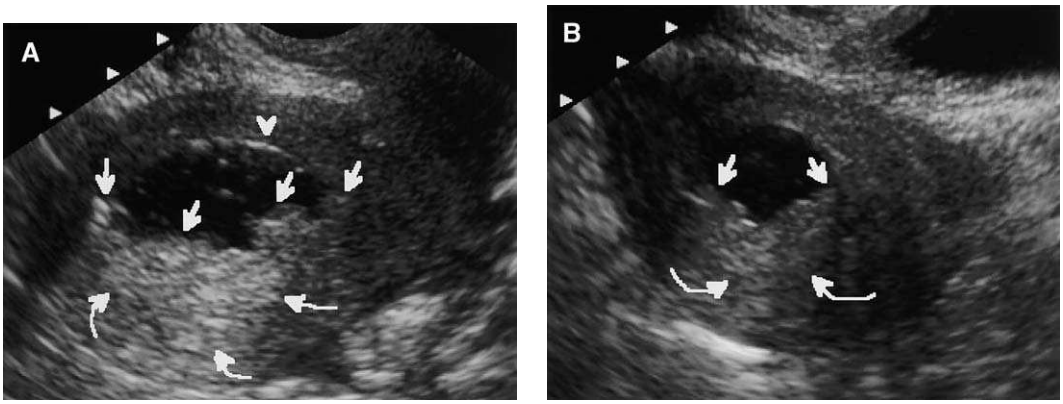

Fig. 23. Sagittal (*A*) and coronal (*B*) SHG in a 72-year-old woman with postmenopausal bleeding. There is diffuse irregular thickening of the posterior endometrial layer (*arrows*). The anterior endometrial surface is normal (*arrowheads*). The endometrial-myometrial interface is highly irregular (*curved arrows*). Pathology revealed invasive endometrial carcinoma.

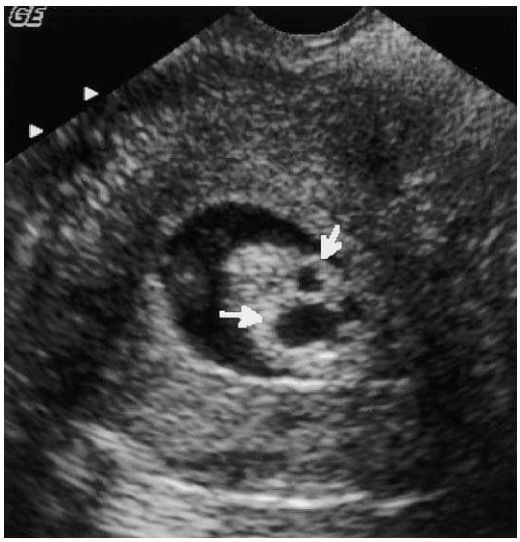

Fig. 24. Coronal SHG in a 65-year-old asymptomatic patient on tamoxifen shows a large polypoid lesion that contains multiple cysts that arise from the lateral endometrial surface (*arrow*). Pathology revealed an endometrial polyp with foci of carcinoma in situ.

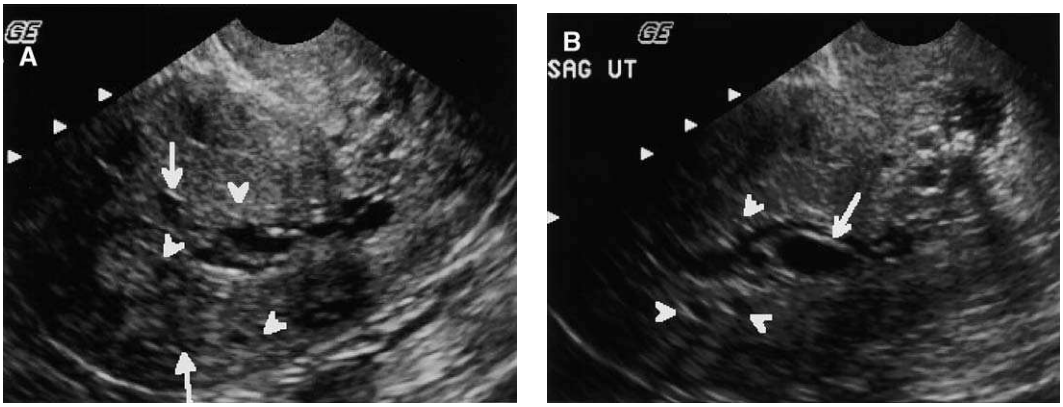

Fig. 25. (*A*) Sagittal TVUS in a 68-year-old asymptomatic patient on tamoxifen shows a markedly thickened endometrial stripe (*arrows*). Multiple cysts are seen at the central and peripheral portions of the endometrial stripe (*arrowheads*). (*B*) Sagittal SHG in same patient demonstrates that all of the cysts are subendometrial (*arrowheads*). The thin atrophic endometrial can be seen overlying the largest of the subendometrial cysts (*arrow*). Endometrial biopsy performed under hysteroscopic guidance revealed endometrial atrophy.

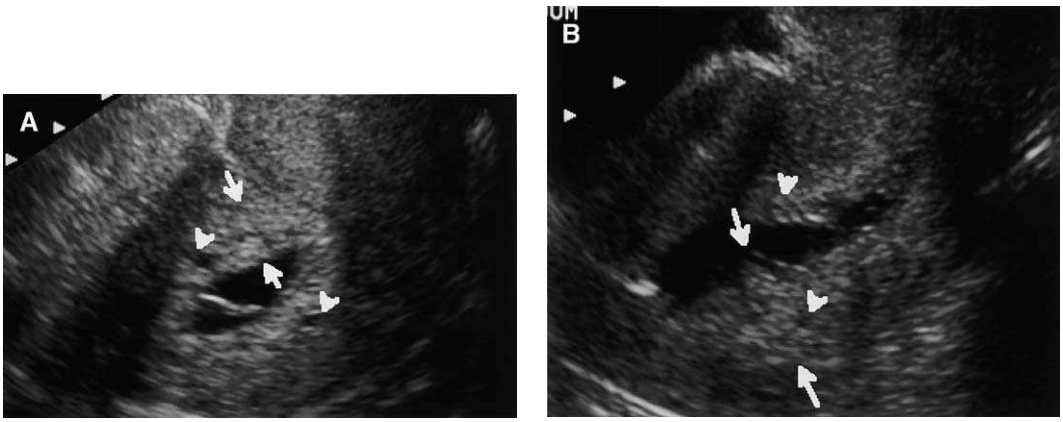

Fig. 26. (*A*) Sagittal SHG in a 76-year-old woman with postmenopausal bleeding on tamoxifen. Multiple peripheral cysts are present (*arrowheads*), but the endometrial lining cannot be seen distinctly (*arrows*). Histology revealed endometrial atrophy. (*B*) Sagittal SHG in a 69-year-old asymptomatic patient on tamoxifen demonstrates peripheral cysts (*arrowheads*) but no distinct endometrial lining (*arrow*). The interface between the endometrium and myometrium also is indistinct. Histology revealed noninvasive endometrial cancer.

tion require tissue diagnosis, even when the imaging features suggest benign lesions.

References

[1] O'Connoll LP, Fries MH, Aeringue E, Brehm W. Triage of abnormal postmenopausal bleeding: a comparison of endometrial biopsy and transvaginal sonohysterography versus fractional curettage with hysteroscopy. Am J Obstet Gynecol 1998;178: 956–61.

[2] Bree RL, Bowerman RA, Bohm-Velez M, et al. US evaluation of the uterus in patients with postmenopausal bleeding: a positive effect on diagnostic decision making. Radiology 2000;216:260–4.

[3] Dueholm M, Forman A, Jensen ML, Laursen H, Kracht P. Transvaginal sonography combined with saline contrast sonohysterography in evaluating the uterine cavity in premenopausal patients with abnormal uterine bleeding. Ultrasound Obstet Gynecol 2001;18: 54–61.

[4] Sohaey R, Woodward P. Sonohysterography: technique, endometrial findings, and clinical applications. Semin Ultrasound CT MR 1999;20:250–8.

[5] Vuento MH, Pirhosen JP, Makinen JI, et al. Screening for endometrial cancer in asymptomatic postmenopausal women with conventional and colour Doppler sonography. Br J Obstet Gynaecol 1999;106: 14–20.

[6] Bakour SH, Dwarakanath LS, Khan KS, Newton JR, Gupta JK. The diagnostic accuracy of ultrasound scan in predicting endometrial hyperplasia and cancer in postmenopausal bleeding. Acta Obstet Gynecol Scand 1999;78:447–51.

[7] Gull B, Carlsson SA, Karlsson B, Ylostalo P, Milsom T, Granberg S. Transvaginal ultrasonography of the endometrium in women with postmenopausal bleeding: is it always necessary to perform an endometrial biopsy. Am J Obstet Gynecol 2000;182:509–15.

[8] Goldstein SR, Zeltser I, Horan CK, Snyder JR, Schwartz LB. Ultrasonography-based triage for perimenopausal patients with abnormal uterine bleeding. Am J Obstet Gynecol 1997;177:102–8.

[9] Laifer-Narin S, Ragavendra N, Parmenter EK, Grant EG. False-normal appearance of the endometrium on conventional transvaginal sonography: comparison with saline hysterosonography. AJR Am J Roentgenol 2002;178:129–33.

[10] Bonnamy L, Marret H, Perrotin F, Body G, Berger C, Lansac J. Sonohysterography: a prospective survey of results and complications in 81 patients. Eur J Obstet Gynecol Reprod Biol 2002;102:42–7.

[11] Kurman RJ. Blaustein's pathology of the female genital tract. 4th edition. New York: Springer-Verlag; 1994.

[12] Gaucherand P, Piacenza JM, Salle B, et al. Sonohysterography of the uterine cavity: preliminary investigations. J Clin Ultrasound 1995;23:339–48.

[13] Bradley LD, Falcone T, Magen AB. Radiographic imaging techniques for the diagnosis of abnormal uterine bleeding. Obstet Gynecol Clin 2000;27: 245–76.

[14] Artner A, Bosze P, Gonda G. The value of ultrasound in preoperative assessment of the myometrial and cervical invasion in endometrial carcinoma. Gynecol Oncol 1994;54:147–51.

[15] Fishman A, Altaras M, Bernheim J, Cohen I, Beyth Y,

Johnson LA. The value of transvaginal sonography in the preoperative assessment of myometrial invasion in high and low grade endometrial cancer and in comparison to frozen section in grade 1 disease. Eur J Gynaecol Oncol 2000;21:128–30.

[16] Gronlund L, Hertz J, Helm P, Colov NP. Transvaginal sonohysterography and hysteroscopy in the evaluation of female infertility, habitual abortion, or metrorrhagia: a comparative study. Acta Obstet Gynecol Scand 1999;78:415–8.

[17] Fleischer AC, Vasquez JM, Cullinan JA, Eisenberg E. J. Sonohysterography combined with sonosalpingography: correlation with endoscopic findings in infertility patients. Ultrasound Med 1997;16:381–4.

[18] Fernandez H, Sefrioui O, Virelizier C, Gervaise A, Gomel V, Frydman R. Hysteroscopic resection of submucosal myomas in patients with infertility. Hum Reprod 2001;16:1489–92.

[19] Marsden DE, Hacker NF. Optimal management of endometrial hyperplasia. Best Pract Res Clin Obstet Gynaecol 2001;15:393–405.

[20] Lev-Toaff A, Toaff ME, Liu JB, Merton DA, Goldberg BB. Value of sonohysterography in the diagnosis and management of abnormal uterine bleeding. Radiology 1995;201:179–84.

[21] Goldstein SR, Monteagudo A, Popiolek D, Mayberry P, Timor-Tritsch I. Evaluation of endometrial polyps. Am J Obstet Gynecol 2002;186:669–74.

[22] Karlsson B, Granberg S, Wikland M, et al. Transvaginal ultrasonography of the endometrium in women with postmenopausal bleeding: a Nordic multicenter study. Am J Obstet Gynecol 1995;172:1488–94.

[23] Epstein E, Ramirez A, Skoog L, Valentin L. Transvaginal sonography, saline contrast sonohysterography and hysteroscopy for the investigation of women with postmenopausal bleeding and endometrium >5 mm. Ultrasound Obstet Gynecol 2001;18:157–62.

[24] Fedele L, Bianchi S, Dorta M, et al. Intrauterine adhesions: detection with transvaginal US. Radiology 1996;199:757–9.

[25] Soares SR, Barbosa dos Reis MM, Camargos AF. Diagnostic accuracy of sonohysterography, transvaginal sonography, and hysterosalpingography in patients with uterine cavity diseases. Fertil Steril 2000;73:406–11.

[26] Parsons AK, Lense JJ. Sonohysterography for endometrial abnormalities: preliminary results. J Clin Ultrasound 1993;21:87–95.

[27] Bronz L, Suter T, Rusca T. The value of transvaginal sonography with and without saline instillation in the diagnosis of uterine pathology in pre- and postmenopausal women with abnormal bleeding or suspect sonographic findings. Ultrasound Obstet Gynecol 1997;9:53–8.

[28] Fisher B, Costantino JP, Redmond CK, et al. Endometrial cancer in tamoxifen-treated breast cancer patients: findings from the National Surgical Adjuvant Breast and Bowel Project (NSABP B-14). J Natl Cancer Inst 1994;86:527–37.

[29] Van Leeuwen FE, Benraadt TH, Coebergh JW, et al. Risk of endometrial cancer after tamoxifen treatment of breast cancer. Lancet 1994;343:448–52.

[30] Elhelw B, Ghorab MN, Farrag SH. Saline sonohysterography for monitoring asymptomatic postmenopausal breast cancer patients taking tamoxifen. Int J Gynaecol Obstet 1999;67:81–6.

[31] McCluggage WG, Desai V, Manek S. Tamoxifen-associated postmenopausal adenomyosis exhibits stromal fibrosis, glandular dilatation and epithelial metaplasias. Histopathology 2000;37:340–6.

[32] Cohen I, Beyth Y, Tepper R, Figer A, Shapira J, Cordoba M, et al. Adenomyosis in postmenopausal breast cancer patients treated with tamoxifen: a new entity? Gynecol Oncol 1995;58:86–91.

[33] Levine D, Gosnick BB, Johnson LA. Change in endometrial thickness in postmenopausal women undergoing hormone replacement therapy. Radiology 1995;997:603–8.

RADIOLOGIC
CLINICS OF
NORTH AMERICA

Radiol Clin N Am 41 (2003) 799–811

MR imaging of the ovaries: normal appearance and benign disease

Kaori Togashi, MD, PhD

Department of Diagnostic and Interventional Imageology, Graduate School of Medicine, Kyoto University, 54 Shogoin Kawaharacho, Sakyo-ku, Kyoto 606-01, Japan

The noninvasive nature of MR imaging is beneficial in evaluations of what are probably benign diseases in young women of reproductive age. Although MR imaging is believed to be safe even during pregnancy, a cautious approach that involves waiting until after 12 weeks' gestation is recommended [1,2]. Disadvantages of MR imaging are its high cost and long scanning time. Its excellent tissue contrast underscores its importance in the evaluation of adnexal masses, however, because it allows specific diagnoses of fat, blood, and fibrous tissue. Even if normal in size, an ovary may present with tiny foci of endometrial implants or dermoid cysts that are only identifiable on MR imaging; however, MR imaging is generally used as a problem-solving modality. When ultrasound results are inconclusive, the use of MR imaging may alter treatment decisions, eliminate the need for surgery, and result in reduced overall costs [3,4].

MR imaging technique

Fasting for several hours and the administration of an anticholinergic agent are mandatory conditions when imaging the pelvis in nonpregnant patients. With the use of a phased array multicoil, T1-weighted images are obtained using a spin-echo technique, and T2-weighted images are obtained using a fast spin-echo technique. Currently, ultrafast imaging techniques are not accepted as an alternative for fast spin-echo technique [5]. In evaluations of pelvic masses, postcontrast and fat suppression or chemical shift images may be required. Chemical shift imaging helps to distinguish fat from blood [6]. Postcontrast images are highly accurate for detection and characterization of complex adnexal masses [7].

Normal and function related masses

Normal ovaries on MR imaging

In women of reproductive age, normal ovaries were identified in 82 of 84 of cases on MR imaging [8,9]. T2-weighted images reveal the zonal anatomy of the ovary, which consists of lower intensity cortex and higher intensity medulla. Many cysts that exhibit high intensity are embedded in the cortex. When less than 25 mm in diameter, these cysts are called physiologic cysts and include follicles at various stages of development, corpus luteum, and surface inclusion cysts [8,9]. The size and number of cysts in ovaries of women of reproductive age change during their menstrual cycle. A dominant follicle can enlarge by 20 to 25 mm [10]. The corpus luteum may present as a cyst with a thick, enhancing, and occasionally convoluted wall or as an enhancing nodule. A hemosiderin deposit along the inner aspect of the cyst wall may be observed as a line of high intensity on T1-weighted images and as a line of low intensity on T2-weighted images (Fig. 1) [8,9]. The presence of an enhancing nodule may cause a problem in differentiating a hemorrhagic corpus luteum cyst from a malignant cyst. The corpus luteum gradually involutes into the corpus albicans, which is not perceptible on imaging findings. In postmenopausal

E-mail address: ktogashi@kuhp.kyoto-u.ac.jp

0033-8389/03/$ – see front matter © 2003 Elsevier Inc. All rights reserved.
doi:10.1016/S0033-8389(03)00041-1

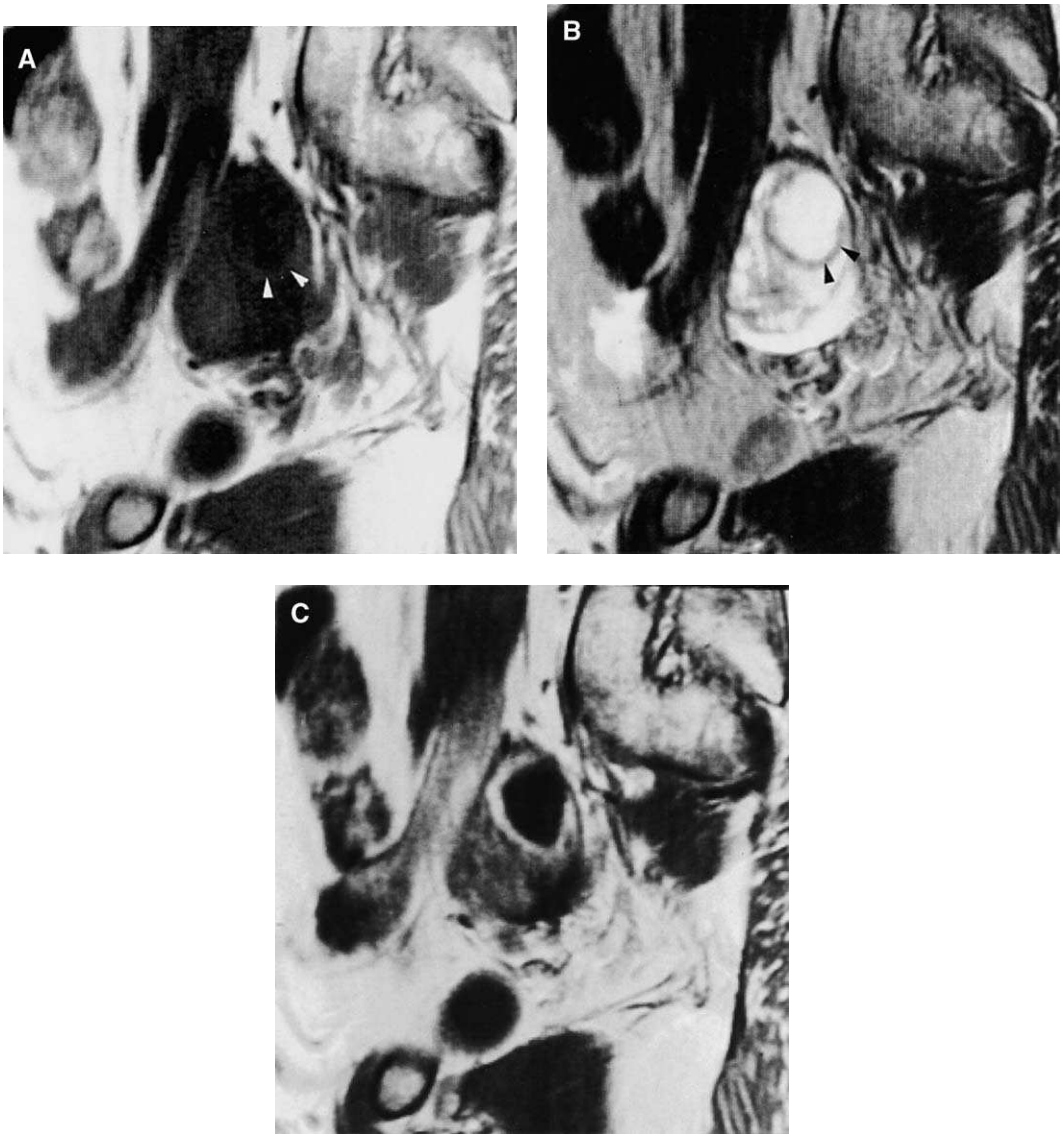

Fig. 1. Normal ovary with a corpus luteum; a cyst distinctly larger than others. (*A*) T1-weighted image shows thin line of high intensity that represents a hemosiderin deposit along the wall (*arrowheads*). (*B*) T2-weighted image shows a line of relatively low intensity along the wall (*arrowheads*). (*C*) Postcontrast image shows a thick, enhancing, and convoluted wall.

women, ovaries show more homogeneous low signal intensity and are hardly identifiable because of their fewer ovarian cysts. The hilum of the ovary and the mesovarium may be identified as a well-enhancing structure.

Functional cysts

Functional cysts are common. When a follicle fails to involute or ovulate, a follicular cyst develops. These cysts usually range from 3 to 8 cm and have a thin wall filled with a simple fluid or a small amount of blood. Luteal cysts have a thick and enhancing wall. Luteal cysts are the masses most commonly encountered during pregnancy, and they typically regress after 7 to 8 weeks' gestation [10]. A small amount of hemorrhage is common in a luteal cyst and presents as a layer of low intensity at the bottom of the fluid content on T2-weighted images. It is called a ''hematocrit effect'' [11]. With a larger amount of

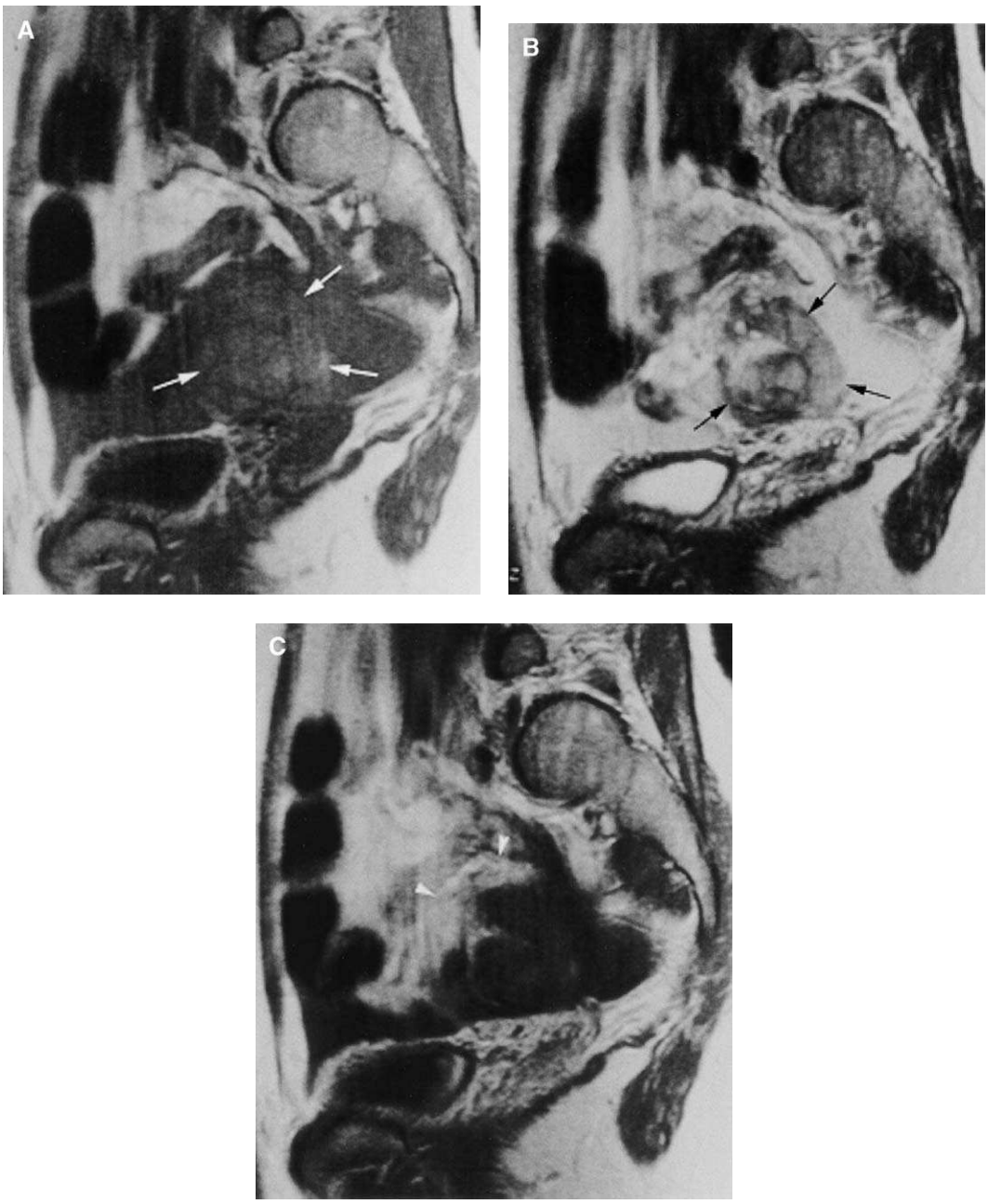

Fig. 2. Ovarian bleeding from luteal hematoma in acute phase. (*A*) T1-weighted image shows free peritoneal fluid of intermediate signal and a mass (*arrows*) of mixed signal intensity that contains slightly higher signal intensity. (*B*) T2-weighted image shows mass (*arrows*) of mixed signal intensity that consists of high and distinct signal intensity within a free fluid that shows a lower signal than urine. (*C*) The wall of luteal hematoma is enhancing (*arrowheads*).

hemorrhage, a hemorrhagic corpus luteum cyst develops. The signal intensity of hemorrhagic cyst varies according to the age of the blood products [12]. The most frequently encountered hemorrhagic corpus luteum cyst is in the subacute phase, and it displays high intensity on T1- and T2-weighted images. Caution is needed so as not to misdiagnose such a hemorrhagic corpus luteum cyst as an endometrioma. Follow-up studies show that hemorrhagic corpus luteum cysts soon regress, whereas endometriotic cysts persist [10].

Theca lutein cysts are less common because they result from excessive human chorionic gonadotropic levels produced by multiple gestations or by gestational trophoblastic disease.

Complications of functional cysts: ovarian bleeding

Probably the most common complication of a functional cyst is hemorrhage, which may be a small amount and be limited to within the cyst or may cause external bleeding and present with severe abdominal pain. Hemorrhagic corpus luteum cysts are the most common cause of ovarian bleeding. Acute hemorrhage is of intermediate signal on T1-weighted images and of distinct low intensity on T2-weighted images (Fig. 2) [12,13]. Hemoperitoneum appears as a higher signal than simple fluid on T1-weighted images and as a lower signal on T2-weighted images [13]. The treatment option for ovarian bleeding is usually just observation. Based on signal intensity, MR imaging allows the accurate distinction of ovarian bleeding from other adnexal masses, such as torsion or rupture, that require immediate surgical intervention.

Development of multiple functional cysts

Functional cysts can be multiple and simulate multiloculated cystic neoplasia. Ovarian hyperstimulation syndrome and hyperreactio luteinalis may present with extremely enlarged ovaries [14]. The former condition is associated with induction of ovulation (Fig. 3). The latter condition is usually associated with gestational trophoblastic disease with excessive human chorionic gonadotropin, but occasionally it is associated with an otherwise normal pregnancy. Both conditions may be mistaken for a malignancy, but the clinical history and their rapid growth usually assist in leading to the correct diagnosis. The enlarged ovaries in these conditions consist of multiple cysts of uniform size. In contrast, multiloculated cystic neoplasia show variable size and shape of loculi separated by septa [15].

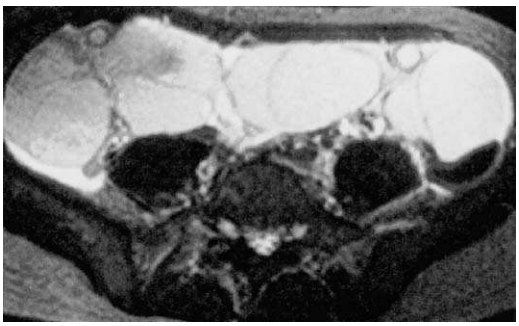

Fig. 3. Ovarian hyperstimulation syndrome. T2-weighted image shows a huge mass composed of multiple uniformly sized cysts.

The so-called ‘‘polycystic ovarian syndrome’’ indicates a primary ovarian insufficiency, which may be associated with oligomenorrhea, obesity, and hirsutism. Polycystic ovaries are also encountered in various hormonal disorders, however, which reflects anovulation or infrequent ovulation. Imaging findings alone are not specific, but identification of multiple peripheral cysts beneath the capsule may help in the consideration of this condition [16].

Peritoneal inclusion cysts

Peritoneal inclusion cysts are a physiologic condition closely related to the function of ovaries. Normal peritoneum absorbs fluid produced by active ovaries. Inflammation or adhesions deprive the peritoneum of this ability, however, and as a result, fluid retention develops adjacent to active ovaries in women with a history of pelvic surgery or pelvic inflammatory disease. A peritoneal inclusion cyst shows a peculiar configuration surrounded by the pelvic wall, pelvic organs, and bowel loops (Fig. 4) [17]. Imaging findings are characteristic enough to make a preoperative diagnosis. An accurate diagnosis of this condition based on imaging findings helps to obviate multiple surgeries that arise from suspicion of a recurrent ovarian tumor. Conservative treatment is the rule for this condition in contrast to other cystic masses, which basically require surgery.

Endometriomas

After exclusion of a physiologic enlargement of the ovary or functional cysts, one can consider the differential diagnosis of adnexal masses. Endometriomas are unique retention cysts and are benign

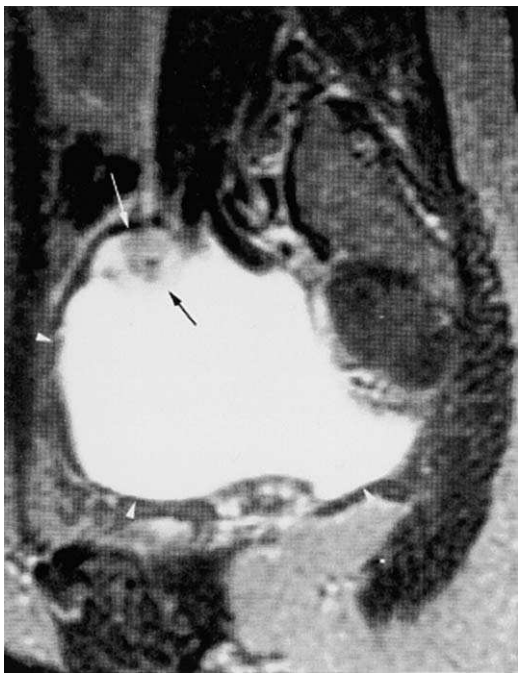

Fig. 4. Peritoneal retention cyst in a woman with a history of pelvic surgery. T2-weighted image shows a cystic mass (*arrowheads*) adjacent to the ovary (*arrows*). The pelvic wall and the ovary bound the border of the lesion.

lesions. Because the lesion is filled with aged blood, endometriomas typically exhibit high signal intensity on T1-weighted images and fat saturation images [18]. The lack of reduction of signal intensity on fat saturation images is important in the distinction between endometriomas and dermoid cysts (Fig. 5) [6]. A diagnosis of an endometrioma can be reliable if the lesion consists of multiple high-intensity cysts on fat saturation T1-weighted images. Another reliable sign of endometriotic cysts is a cyst that exhibits high signal intensity on a T1-weighted image and is of heterogeneous low intensity on a T2-weighted image. This pattern of signal intensity is called shading [18].

Even if the signal intensity is typical for an endometrioma, a benign diagnosis should be abandoned if vegetations are identified in a lesion. There is a rare benign condition called a decidualized endometrial cyst, however [19,20]. Clear cell carcinoma is known to develop in an otherwise normal endometrioma, with an incidence of 0.04%. One should search carefully for small vegetations and distinguish them from clots adherent to the wall [21].

Benign neoplasia

Primary ovarian tumors arise from surface epithelium, gonadal stroma, and primordial germ cells. Surface epithelial tumors are the most common ovarian tumors and are further subclassified into serous, mucinous, clear cell, endometrioid, and transitional cell tumors. Among these histologic subtypes, serous, mucinous, and transitional cell tumors may present as benign lesions. Although most ovarian tumors should be evaluated surgically, to improve the prognosis of patients, preoperative distinction between benign and malignant tumors is mandated for appropriate subspecialty referrals for possible malignant ovarian tumors [22].

Surface epithelial tumors

Serous and mucinous tumors are the most common surface epithelial tumors. They can vary from entirely cystic to entirely solid, but benign diagnosis should be applied only for lesions that do not have solid tissue on imaging findings [7]. The serous cystadenoma is usually unilocular and contains fluid similar to that of simple fluid. The mucinous cystadenoma is typically multiloculated and shows a stained-glass appearance (with compartments of varying signal intensity) or daughter cysts. Thick, mucinous content that occasionally exhibits low intensity on T2-weighted images is also common in mucinous tumors.

A Brenner tumor is a benign transitional cell tumor and is a rare exception to the rule that the presence of solid tissue in a cystic mass indicates malignancy [23]. A Brenner tumor presents as a solid nodule usually with another cystic mass (typically a mucinous cystadenoma) (Fig. 6). The signal intensity of the solid nodule is distinct low signal intensity on T2-weighted images, which reflects its fibrocollagenous nature, and helps make an accurate diagnosis. MR imaging findings are essential for making a preoperative diagnosis of this benign tumor.

Sex-cord stromal tumors

A solid component in an ovarian tumor usually suggests malignancy. Fibromas and thecomas are an exception to this rule, however. Such tumors are predominantly solid but are benign. Fibromas and thecomas typically show distinct low signal intensity on T2-weighted images, which reflects abundant collagen [24,25]. Their signal intensity may change in the presence of edema and cyst formation, however, which are other common findings of these

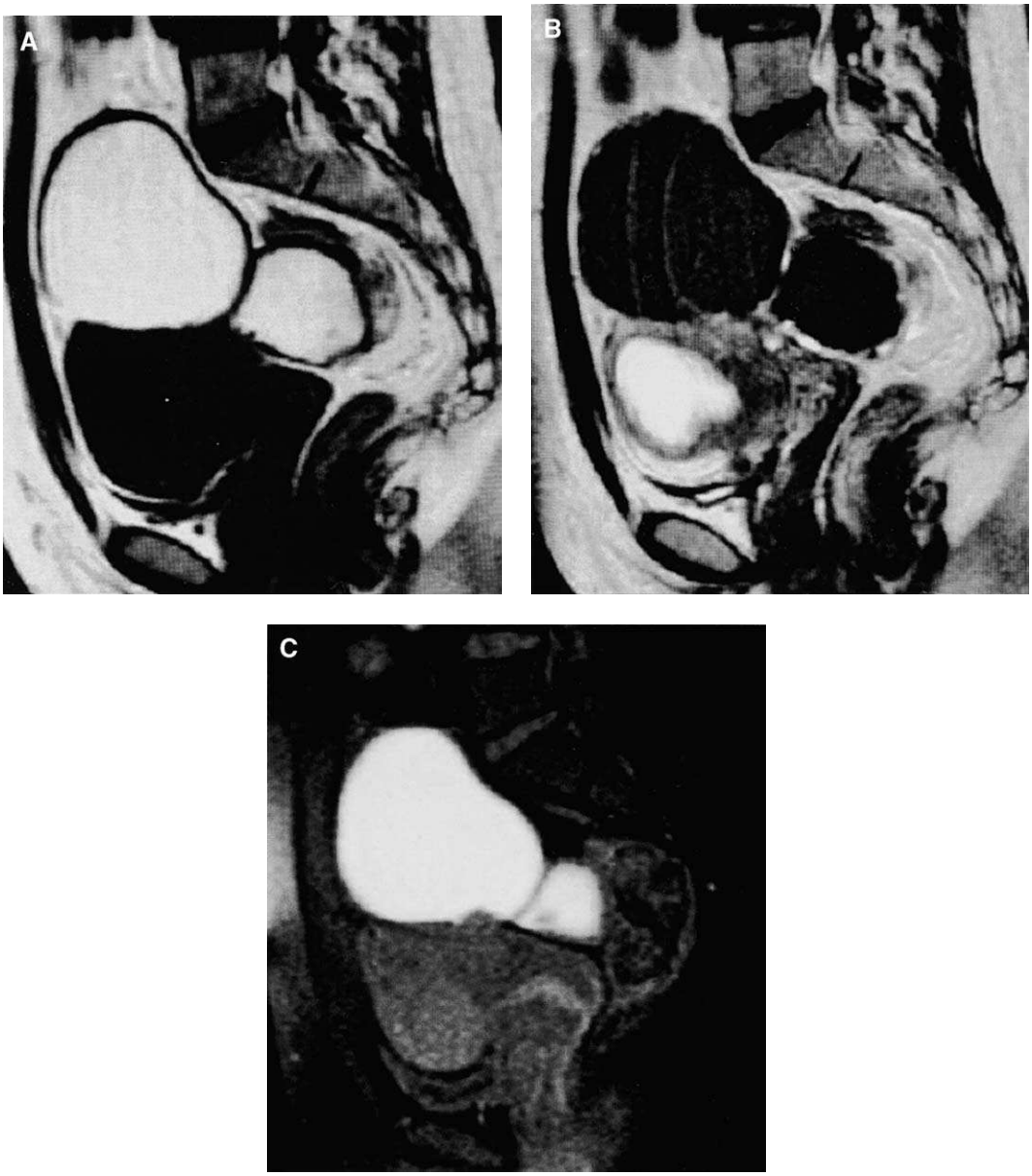

Fig. 5. Endometriomas. (*A*) T1-weighted image shows two cysts of high signal intensity. (*B*) T2-weighted image shows the cysts to be of heterogeneous low signal intensity. The dorsal cyst shows a lower signal than that of the ventral one. If the lesion exhibits high signal on T1-weighted image and low signal on T2-weighted image, the diagnosis of endometriotic cyst is reliable. (*C*) Fat suppressed image shows no reduction in signal intensity of the lesion. The diagnosis of an endometrioma is reliable if the lesion consists of multiple high intensity cysts on T1-weighted and fat sat images.

tumors [24]. Cysts may be central or eccentric and should be distinguished from necrosis by their thin walls and smooth inner surfaces. Benign ovarian tumors, such as fibromas and thecomas, occasionally are associated with ascites and hydrothorax, which usually indicate malignancy. Such a condition is called Meigs' syndrome and can be a diagnostic pitfall. The hypointense signal of the tumor on T2-weighted images is a diagnostic clue.

Although low signal intensity of solid tissue is usually a reliable indicator of benignancy, it should be noted that Krukenberg tumors also can exhibit low

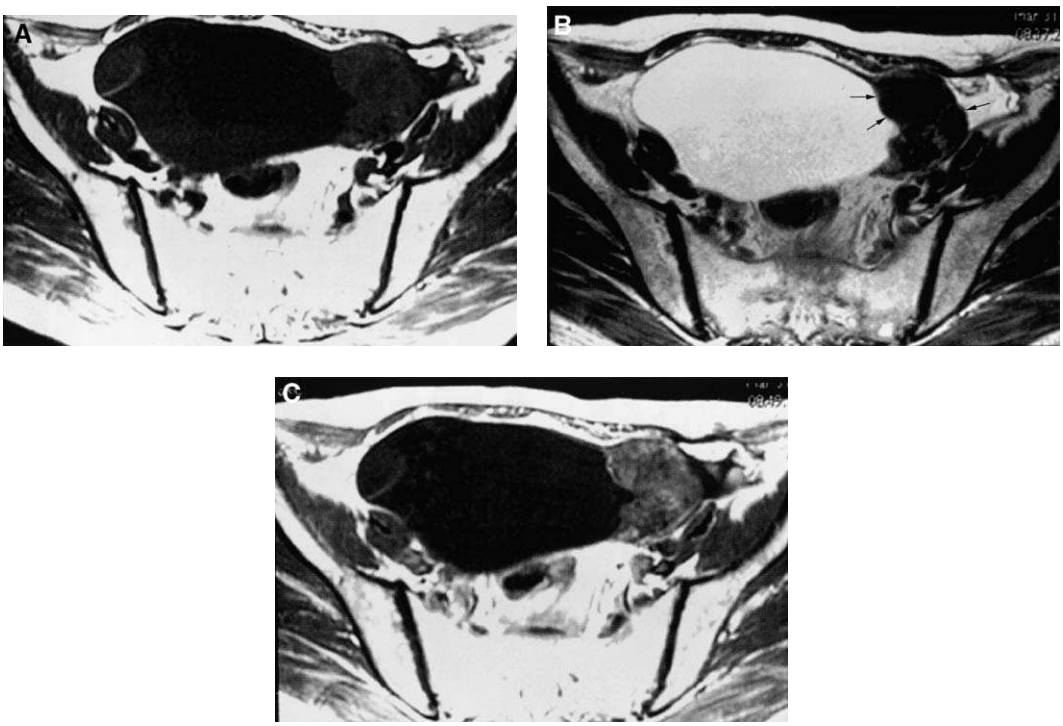

Fig. 6. Brenner tumor associated with mucinous cystadenoma. (*A*) T1-weighted image shows two components that exhibit low signal and intermediate signal intensities. (*B*) T2-weighted image shows a cystic component (representing the mucinous tumor) and solid tissue (representing the Brenner tumor) that exhibits distinct low signal intensity. (*C*) Postcontrast image shows a weak enhancement in the solid tissue.

signal intensity [26]. Bilaterality and prominent enhancement favor diagnosis of Krukenberg tumors [26,27].

Sclerosing stromal tumors differ clinically from fibrothecomas by being most common in young women. Important MR imaging findings are striking enhancement, higher than that of the uterus, pseudolobulation that consists of low intensity nodules set against high intensity background on T2-weighted images, and a peripheral rim [28]. Preoperative diagnosis of this benign tumor may help to offer a less invasive treatment option, such as laparoscopic surgery. Because this tumor easily can be mistaken as a Krukenberg tumor on histologic studies, the role of imaging is important.

Germ cell tumors

Germ cell tumors are the most commonly encountered tumors in children and young adults. More than 95% of germ cell tumors are benign dermoid cysts, which are referred to as mature cystic teratomas. Dermoid cysts are usually filled with sebaceous fluid that exhibits prominent high signal intensity on T1- and T2-weighted images and reduced signal on fat saturation images (Fig. 7) [6,29]. Reduced signal intensity on fat saturation image is a diagnostic sign for a dermoid cyst and distinguishes it from an endometrioma. Rokitansky protuberances are frequently identifiable and may resemble solid protrusions on precontrast images. Contrast enhancement is usually absent in these protrusions, however. Although dermoid cysts are typically filled with sebaceous fluid, huge dermoid cysts in younger age groups may be filled with simple fluid and have scant fatty tissue [30].

Immature teratomas, malignant counterparts of dermoid cysts, also present as huge cystic masses filled with simple fluid and scant fatty tissue. As with other germ cell tumors, dermoid cysts are commonly associated with an elevated level of serum marker CA 19-9. If the lesion is associated with a slightly elevated level of alpha-fetoprotein, an immature teratoma should be considered, because the two conditions are not distinguishable on imaging findings alone.

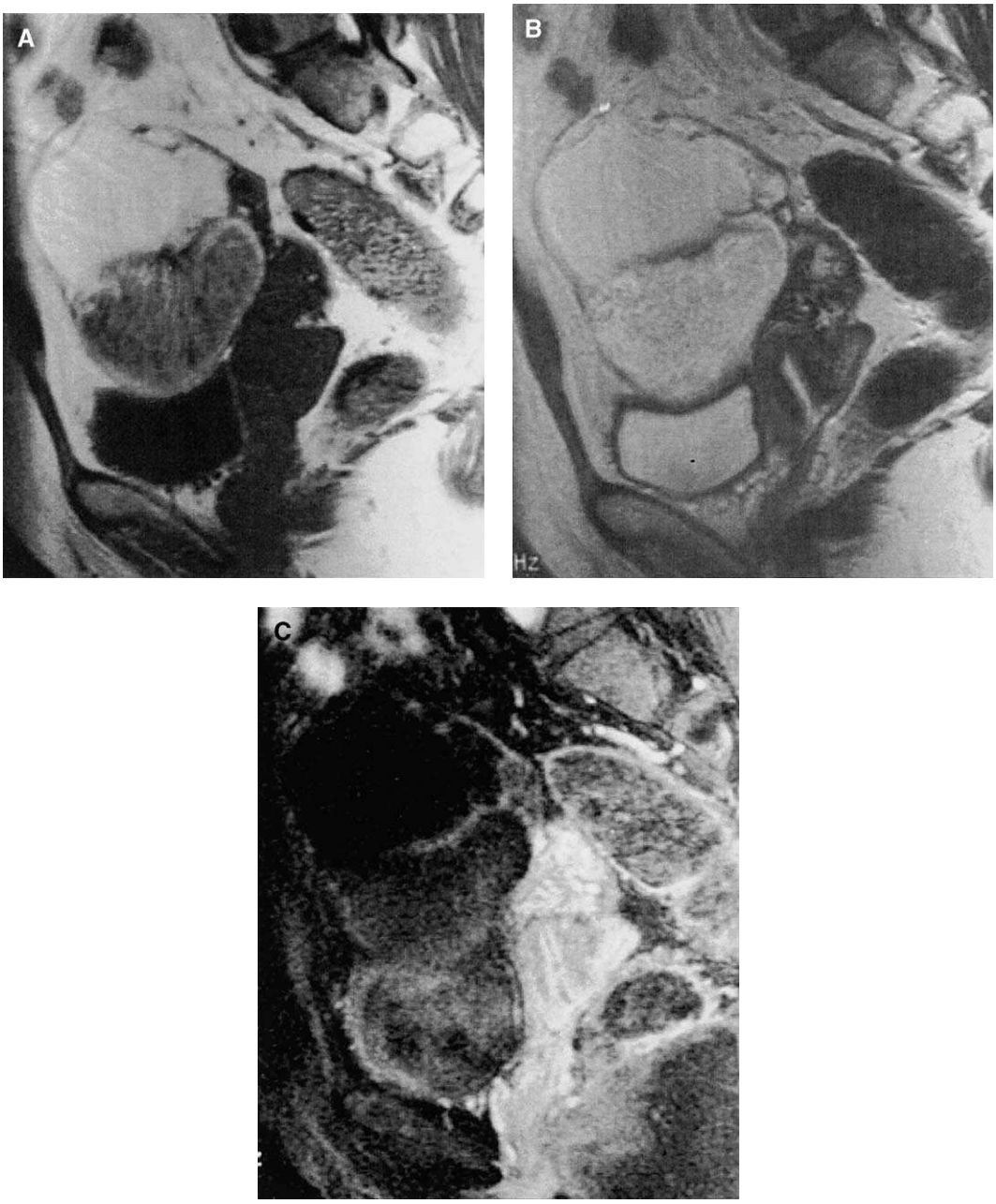

Fig. 7. Dermoid cyst. (*A*) T1-weighted image shows a cyst that contains a layer of high and intermediate signal intensities. (*B*) T2-weighted image shows that both contents exhibit high signal intensity. (*C*) Fat suppressed image shows reduced signal intensity of both contents, indicating fatty fluid. The upper layer represents pure sebaceous fluid, and the lower layer represents sebaceous fluid mixed with hair or desquamated epithelium.

Struma ovarii is a germ cell tumor but consists of a monodermal component with thyroid tissue, in contrast to other teratomas, which have three dermal layers. MR imaging findings may be diagnostic of this condition. Typical findings include a multiloculated cystic mass with numerous minute loculi, thick content that exhibits low signal intensity on T2-weighted images, and striking enhancement [31]. A thyroid scintigram may confirm a diagnosis.

Inflammatory masses

Chronic inflammatory masses develop as sequelae of acute pelvic inflammatory diseases or granulomatous diseases. These conditions are occasionally mistaken as gynecologic malignancies because they frequently involve multiple pelvic organs and show no obvious inflammatory signs. In some clinical settings, MR imaging may offer an accurate diagnosis of these problematic conditions.

Chronic stage of tubo-ovarian abscesses

Acute pelvic inflammatory disease typically presents with acute inflammatory symptoms, and ultrasound is the modality of choice to evaluate this condition. If an acute condition is inadequately treated, however, the lesion progresses insidiously to a chronic inflammatory mass. This progression usually results in a mixed solid and cystic lesion having a thick wall with variable signal intensity of the fluid. Hydrosalpinx and pyosalpinx are frequently identifiable. Because of associated edema and a tendency to adhere to the adjacent tissue, the lesion is usually ill defined and associated with prominent "mesh-like" linear stranding that radiates from the mass to the adjacent pelvic structures [32]. Lymphadenopathy may be observed.

Actinomycosis

Granuloma may be caused by an actinomycosis infection. Actinomycotic granulomata may lack typical clinical findings of inflammation from the beginning. The lesion may have a cystic component, but it predominantly presents as a solid mass that exhibits low signal intensity on T2-weighted imaging. The mass tends to show diffuse and widespread involvement of the uterus, bilateral adnexa, and muscles of pelvic girdles, and it resembles extensive invasion by uterine cancer [33]. Aggressive transfascial extension is an important characteristic of actinomycosis, and the presence of transfascial extension should indicate actinomycosis in the absence of any known pelvic malignancy. Identification of a foreign body, such as an intrauterine contraceptive device, further favors a diagnosis of actinomycosis. Diagnosis is established with identification of a sulfur granule within the mass (Fig. 8).

Tuberculosis

Tuberculosis typically presents as adnexitis, lymphadenitis, or peritonitis. Prominent lymphadenopathy associated with endometritis resembles an advanced uterine cancer, whereas massive ascites and peritoneal enhancement mimic ovarian cancer with peritoneal carcinomatosis. Diagnosis is difficult because symptoms are vague. Massive ascites, lymph

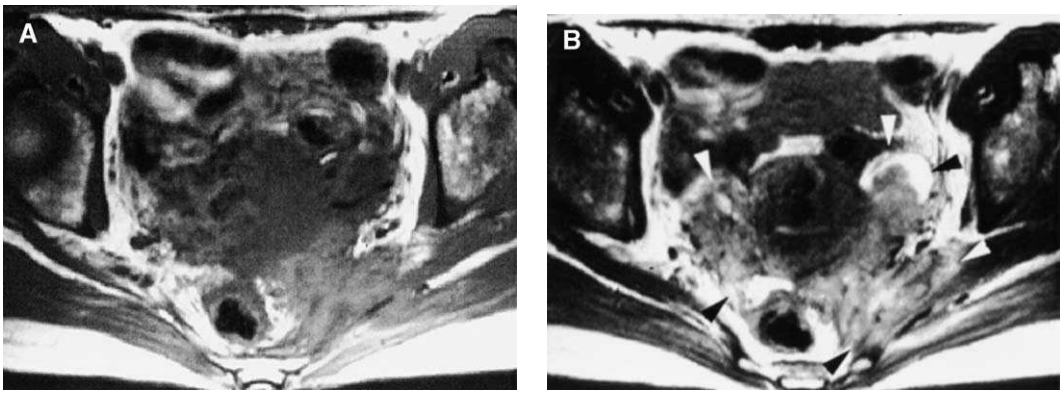

Fig. 8. Pelvic actinomycosis. (*A*) T1-weighted image shows a lesion that involves bilateral adnexa, the uterus, and left pyriform muscle. This pattern of extension is called transfascial extension. (*B*) T2-weighted image reveals a predominantly solid mass of relatively low signal intensity with a small cystic component (*arrowheads*).

node enlargement, and adnexal masses should indicate tuberculosis if the usual clinical evaluation has failed to identify gynecologic malignancies. Culture of abscess fluid or polymerase chain reaction analysis is necessary to confirm the diagnosis.

Other uncommon benign adnexal masses

Magnetic resonance findings occasionally help to make an accurate diagnosis of uncommon benign conditions that may resemble gynecologic malignancies. Examples discussed in this section include hematocele caused by ectopic pregnancy, torsed adnexal masses, massive ovarian edema, and solid adnexal masses caused by endometriosis.

Hematosalpinx and hematocele caused by ectopic pregnancy

Typical presentation of ectopic pregnancy is acute abdominal pain and bleeding in a patient with a positive test result for β-human chorionic gonadotropin. With the advent of imaging findings and more sensitive laboratory tests, most patients are identifiable while in an asymptomatic status. Sonographic findings in association with elevated human chorionic gonadotropin and clinical findings, such as abnormal vaginal bleeding after amenorrhea, are diagnostic in many cases. If sonographic findings are inconclusive, however, MR imaging helps to make a more confident diagnosis of ectopic pregnancy, because MR imaging is sensitive for blood elements. Acute hematoma exhibits intermediate signal intensity on T1-weighted images and distinct low signal intensity on T2-weighted images [13]. The wall in hematosalpinx is prominently enhanced, which represents increased blood flow because of implantation. Rarely, an undiagnosed ectopic pregnancy proceeds to chronic stage hematocele and shows prominent high signal intensity on T1- and T2-weighted images.

Ovarian torsion

Acute abdominal pain is a typical presentation of torsion, but it also frequently presents with vague

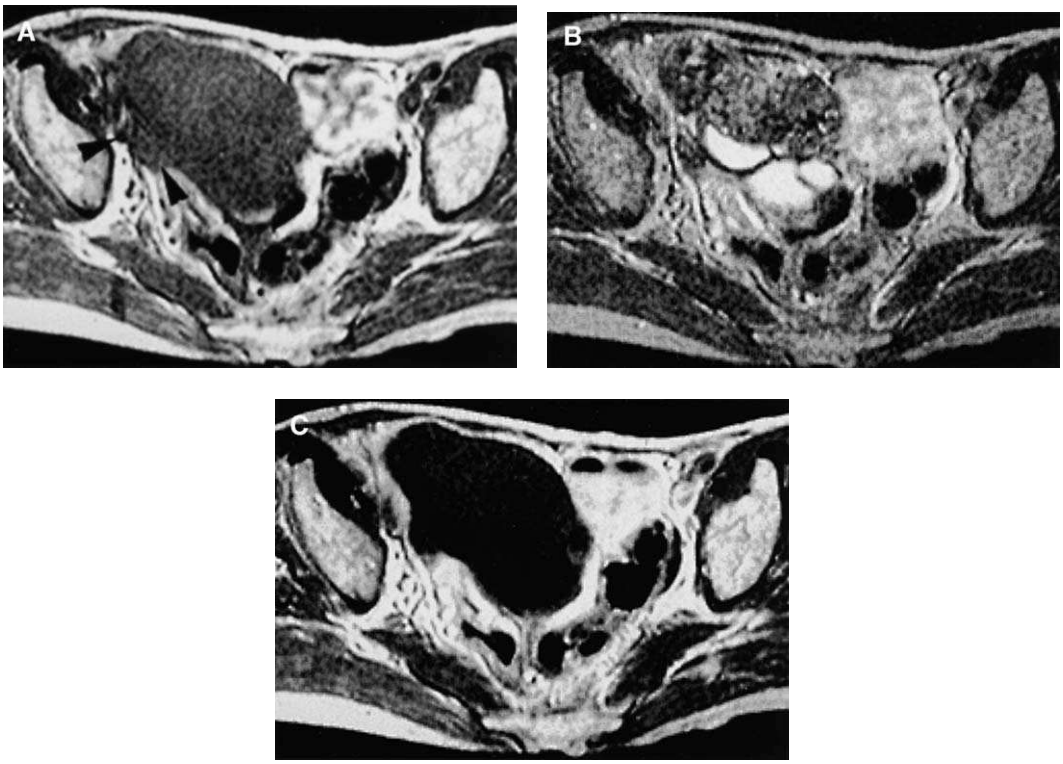

Fig. 9. Torsed ovary with massive hemorrhagic infarction. (*A*) T1-weighted image shows a mass of intermediate signal associated with a beaked protuberance, which indicates a pedicle (*arrowheads*). (*B*) T2-weighted image shows distinct low intensity, which indicates necrosis. (*C*) Postcontrast image reveals complete absence of any enhancement.

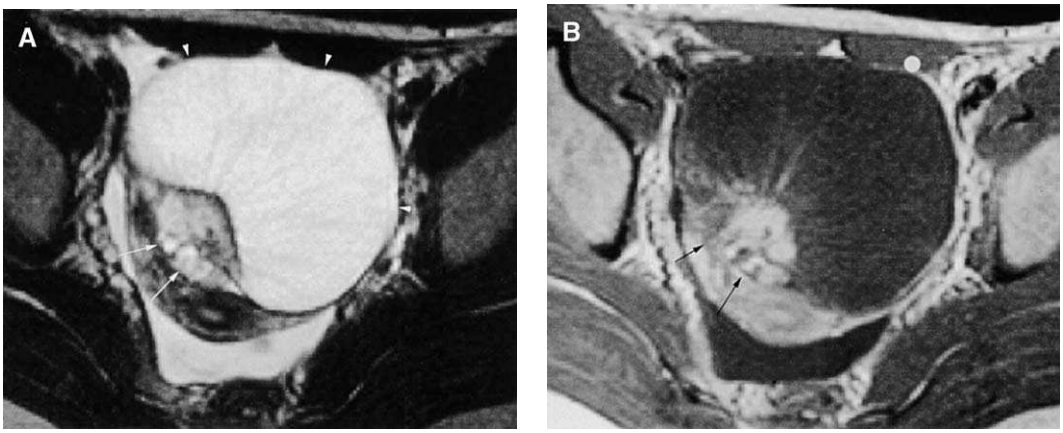

Fig. 10. Massive ovarian edema. (*A*) T2-weighted image shows the ovary (*arrowheads*), which is extremely swollen but still keeps the shape of a fava been, and the ovarian hilum (*arrows*). Within the ovary, fine radiations from the hilum can be seen. (*B*) Postcontrast image shows strong enhancement of the ovarian hilum (*arrows*) and a lack of enhancement of the entire ovary, except for weak enhancement in the radiations.

symptoms that make clinical diagnosis difficult. Imaging findings vary according to the stage of torsion (eg, the extent of edema and ischemia). With hemorrhage and necrosis, torsion presents as a necrotic mass that lacks enhancement. At an early stage, a torsed ovary is swollen with multiple follicles separated by edematous stroma. In both stages, the common finding is the presence of a thick pedicle between the mass and the uterus [34,35]. Another important finding that favors a diagnosis of torsion is an absence or diminished enhancement of the mass. If one can make an early diagnosis of an incomplete torsion with vague symptoms based on imaging findings, prompt surgical intervention helps to salvage ovaries (Fig. 9).

Massive ovarian edema

Massive ovarian edema likely occurs with incomplete and intermittent torsion of the ovaries, which causes partial and recurrent obstruction of venous drainage. Reported MR imaging findings vary, which probably reflects different stages of this condition. Findings include masses that are not distinguishable from ovarian cancer and a prominently enlarged ovary embedded with multiple cysts (Fig. 10) [36,37].

Solid endometriosis

Solid endometriosis is typically found in the rectovaginal septum and in other fibromuscular pelvic structures, but it occasionally appears in an adnexa. Because of a hard consistency of the lesion, this condition may be mistaken for ovarian cancer on palpation. MR imaging may be helpful in obtaining an accurate diagnosis of endometriosis [38,39]. The solid mass exhibits distinct low signal intensity on T2-weighted images, which reflects its fibrocollagenous nature. Punctate foci of high signal intensity on T1-weighted images are frequently identifiable within the solid mass. The presence of an endometriotic cyst further progresses a diagnosis of endometriosis.

Summary

MR imaging enables a physician to make an accurate diagnosis of various benign adnexal masses and helps to obviate unnecessary surgery.

References

[1] Levine D, Barnes PD, Edelman RR. Obstetric MR imaging. Radiology 1999;211:609–17.
[2] Smith FW, Kent C, Abramovich DR, Sutherland HW. Nuclear magnetic resonance imaging: a new look at the fetus. Br J Obstet Gynaecol 1985;92:1024–33.
[3] Scoutt LM, McCarthy SM, Lange R, Bourque A, Schwartz PE. MR evaluation of clinically suspected adnexal masses. J Comput Assist Tomogr 1994;18:609–18.
[4] Schwartz LB, Panageas E, Lange R, Rizzo J, Comite F, McCarthy S. Female pelvis: impact of MR imaging on

treatment decisions and net cost analysis. Radiology 1994;192:55–60.
[5] Niitsu M, Tanaka YO, Anno I, Itai Y. Multishot echo-planar MR imaging of the female pelvis: comparison with fast spin-echo MR imaging in an initial clinical trial. AJR Am J Roentgenol 1997;168:651–5.
[6] Stevens SK, Hricak H, Campos Z. Teratomas versus cystic hemorrhagic adnexal lesions: differentiation with proton-selective fat-saturation MR imaging. Radiology 1993;186:481–8.
[7] Hricak H, Chen M, Coakley FV, Kinkel K, Yu KK, Sica G, et al. Complex adnexal masses: detection and characterization with MR imaging–multivariate analysis. Radiology 2000;214:39–46.
[8] Outwater EK, Talerman A, Dunton C. Normal adnexa uteri specimens: anatomic basis of MR imaging features. Radiology 1996;201:751–5.
[9] Outwater EK, Mitchell DG. Normal ovaries and functional cysts: MR appearance. Radiology 1996;198: 397–402.
[10] Russell DJ, Fleischer AC, Cullinan JA, Kepple DM, et al. Adnexal mass: detection and evaluation. In: Fleischer AC, Javitt MC, Jeffrey RB, Jones III HW, editors. Clinical gynecologic imaging. Philadelphia: Lippincott-Raven; 1997. p. 43–106.
[11] Nyberg DA, Porter BA, Olds MO, Olson DO, Andersen R, Wesby GE. MR imaging of hemorrhagic adnexal masses. J Comput Assist Tomogr 1987;11: 664–9.
[12] Gomori JM, Grossman RI, Goldberg HI, Zimmerman RA, Bilaniuk LT. Intracranial hematomas: imaging by high-field MR. Radiology 1985;157:87–93.
[13] Kataoka ML, Togashi K, Kobayashi H, Inoue T, Fujii S, Konishi J. Evaluation of ectopic pregnancy by magnetic resonance imaging. Hum Reprod 1999; 14:2644–50.
[14] Ghossain MA, Buy JN, Ruiz A, Jacob D, Sciot C, Hugol D, et al. Hyperreactio luteinalis in a normal pregnancy: sonographic and MRI findings. J Magn Reson Imaging 1998;8:1203–6.
[15] Seong CK, Won HJ, Sim JS, Yeon KM. Simplified morphological criteria of multiloculated cystic adnexal masses: usefulness in the differentiation between tumorous and nontumorous conditions. In: Supplement to Radiology: 85th Annual Meeting of the Radiological Society of North America. Chicago: Radiological Society of North America; 1999. p. 219.
[16] Mitchell DG, Gefter WB, Spritzer CE, Blasco L, Nulson J, Livolsi V, et al. Polycystic ovaries: MR imaging. Radiology 1986;160:425–9.
[17] Kurachi H, Murakami T, Nakamura H, Hori S, Miyake A, Kozuka T, et al. Imaging of peritoneal pseudocysts: value of MR imaging compared with sonography and CT. AJR Am J Roentgenol 1993;161:589–91.
[18] Togashi K, Nishimura K, Kimura I, Tsuda Y, Yamashita K, Shibata T, et al. Endometrial cysts: diagnosis with MR imaging. Radiology 1991;180:73–8.
[19] Tanaka YO, Shigemitsu S, Nagata M, Shindo M, Okamoto Y, Yoshikawa H, et al. A decidualized endometrial cyst in a pregnant woman: a case observed with a steady-state free precession imaging sequence. Magn Reson Imaging 2002;20:301–4.
[20] Tanaka YO, Yoshizako T, Nishida M, Yamaguchi M, Sugimura K, Itai Y. Ovarian carcinoma in patients with endometriosis: MR imaging findings. AJR Am J Roentgenol 2000;175:1423–30.
[21] Komatsu T, Konishi I, Mandai M, Togashi K, Kawakami S, Konishi J, et al. Adnexal masses: transvaginal US and gadolinium-enhanced MR imaging assessment of intratumoral structure. Radiology 1996;198: 109–15.
[22] Carney ME, Lancaster JM, Ford C, Tsodikov A, Wiggins CL. A population-based study of patterns of care for ovarian cancer: who is seen by a gynecologic oncologist and who is not? Gynecol Oncol 2002;84: 36–42.
[23] Outwater EK, Siegelman ES, Kim B, Chiowanich P, Blasbalg R, Kilger A. Ovarian Brenner tumors: MR imaging characteristics. Magn Reson Imaging 1998; 16:1147–53.
[24] Troiano RN, Lazzarini KM, Scoutt LM, Lange RC, Flynn SD, McCarthy S. Fibroma and fibrothecoma of the ovary: MR imaging findings. Radiology 1997;204: 795–8.
[25] Outwater EK, Siegelman ES, Talerman A, Dunton C. Ovarian fibromas and cystadenofibromas: MRI features of the fibrous component. J Magn Reson Imaging 1997;7:465–71.
[26] Ha HK, Baek SY, Kim SH, Kim HH, Chung EC, Yeon KM. Krukenberg's tumor of the ovary: MR imaging features. AJR Am J Roentgenol 1995;164:1435–9.
[27] Kim SH, Kim WH, Park KJ, Lee JK, Kim JS. CT and MR findings of Krukenberg tumors: comparison with primary ovarian tumors. J Comput Assist Tomogr 1996; 20:393–8.
[28] Ihara N, Togashi K, Todo G, Nakai A, Kojima N, Ishigaki T, et al. Sclerosing stromal tumor of the ovary. J Comput Assist Tomogr 1999;23:555–7.
[29] Togashi K, Nishimura K, Itoh K, Fujisawa I, Sago T, Minami S, et al. Ovarian cystic teratomas: MR imaging. Radiology 1987;162:669–73.
[30] Yamashita Y, Hatanaka Y, Torashima M, Takahashi M, Miyazaki K, Okamura H. Mature cystic teratomas of the ovary without fat in the cystic cavity: MR features in 12 cases. AJR Am J Roentgenol 1994;163: 613–6.
[31] Dohke M, Watanabe Y, Takahashi A, Katayama T, Amoh Y, Ishimori T, et al. Struma ovarii: MR findings. J Comput Assist Tomogr 1997;21:265–7.
[32] Ha HK, Lim GY, Cha ES, Lee HG, Ro HJ, Kim HS, et al. MR imaging of tubo-ovarian abscess. Acta Radiol 1995;36:510–4.
[33] Hawnaur JM, Reynolds K, McGettigan C. Magnetic resonance imaging of actinomycosis presenting as pelvic malignancy. Br J Radiol 1999;72:1006–11.
[34] Kimura I, Togashi K, Kawakami S, Takakura K, Mori T, Konishi J. Ovarian torsion: CT and MR imaging appearances. Radiology 1994;190:337–41.

[35] Haque TL, Togashi K, Kobayashi H, Fujii S, Konishi J. Adnexal torsion: MR imaging findings of viable ovary. Eur Radiol 2000;10:1954–7.
[36] Kramer LA, Lalani T, Kawashima A. Massive edema of the ovary: high resolution MR findings using a phased-array pelvic coil. J Magn Reson Imaging 1997;7:758–60.
[37] Lee AR, Kim KH, Lee BH, Chin SY. Massive edema of the ovary: imaging findings. AJR Am J Roentgenol 1993;161:343–4.
[38] Siegelman ES, Outwater E, Wang T, Mitchell DG. Solid pelvic masses caused by endometriosis: MR imaging features. AJR Am J Roentgenol 1994;163: 357–61.
[39] Gougoutas CA, Siegelman ES, Hunt J, Outwater EK. Pelvic endometriosis: various manifestations and MR imaging findings. AJR Am J Roentgenol 2000;175: 353–8.

RADIOLOGIC CLINICS OF NORTH AMERICA

Radiol Clin N Am 41 (2003) 813–839

Osteoporosis imaging

Thomas M. Link, MD[a,*], Sharmila Majumdar, PhD[b,c]

[a]*Department of Radiology, Technische Universität München, Ismaninger Straße 22, Munich D-81675, Germany*
[b]*Departments of Radiology, Orthopedic Surgery and Growth and Development, University of California at San Francisco, MRSC, Box 1290, AC 109, 1 Irving Street, San Francisco, CA 94143, USA*
[c]*Department of Bioengineering, University of California at Berkeley, Evans Hall, Berkeley, CA 94720, USA*

What is osteoporosis?

Osteoporosis was defined at the National Institutes of Health consensus conference as a disease that is associated with a loss of bone mass and a deterioration of bone structure, both of which result in an increased bone fragility and susceptibility to fracture [1]. In 2000, this definition was modified to osteoporosis being defined as a skeletal disorder characterized by compromised bone strength that predisposes to an increased risk of fracture [2,3]. Because this definition seems abstract, the following statements were added: Bone strength reflects the integration of two main features: bone density and bone quality. Bone density is expressed as grams of mineral per area or volume. In any given individual, bone density is determined by peak bone mass and amount of bone loss. Bone quality refers to architecture, turnover, damage accumulation (eg, microfractures), and mineralization.

Because bone density is the parameter that can be determined best in vivo, has a high precision, and correlates well with the biomechanically determined bone strength (it explains approximately 70% of bone strength [2,3]) the World Health Organization (WHO) defined osteoporosis on the basis of bone mineral density (BMD) [4]. BMD that is more than 2.5 standard deviations below that of a white, young, healthy female adult reference population (T-score) is defined as osteoporosis. BMD that is 1 to 2.5 standard deviations below that of the young and healthy reference population is defined as osteopenia (Box 1). This definition, however, originally was established only for BMD of the proximal femur (and later of the anteroposterior [AP] spine) determined using dual-energy X-ray absorptiometry (DXA) but has been applied to define diagnostic thresholds at other skeletal sites and for other technologies. Because of the difficulty in accurate measurement and standardization between instruments and sites, controversy exists among experts regarding the continued use of this diagnostic criterion [2,3]. It is also not clear how to apply this diagnostic criterion to ethnic groups and children and men.

Box 1. World Health Organization definition of osteoporosis, based on bone mineral density and T-scores using dual x-ray absorptiometry of the proximal femur and spine [4]

T-score > -1	Normal
T-score < -1, > -2.5	Osteopenia
T-score < -2.5	Osteoporosis
T-score < -2.5 and osteoporotic fractures	Severe Osteoporosis

Parts of this article have been adapted from Magnetic resonance imaging of trabecular bone structure. Topics in Magnetic Resonance Imaging 2002;13:5.

* Corresponding author.
E-mail address: tmlink@roe.med.tu-muenchen.de (T.M. Link).

0033-8389/03/$ – see front matter © 2003 Elsevier Inc. All rights reserved.
doi:10.1016/S0033-8389(03)00059-9

As populations age, the incidence of osteoporosis and subsequent fractures increases. In Western civilization—the United States and Europe—osteoporosis is already the most prevalent bone disease and will generate major problems for public health institutions [5]. In California, osteoporosis accounted for more than $2.4 billion in direct health care costs in 1998 and more than $4 million in lost productivity because of premature death [6]. Most of the cost results from hip fractures and other fractures. Only 15% of costs are for people with a diagnosis of ''osteoporosis'' per se, and of this group, most of the costs are associated with a secondary—not a primary—diagnosis. According to the International Osteoporosis Foundation, more than 40% of middle-aged women will suffer one or more osteoporotic fractures during their remaining lifetime. The most important fracture sites are the proximal femur, spine, and distal radius. Hip fractures are the worst complication of osteoporosis, with substantial morbidity and high 1-year mortality rates. The rate of hip fractures is expected to triple over the next three decades [7,8]. Vertebral fractures occur with a higher incidence earlier in life than other types of osteoporotic fractures [9]. It is difficult to determine the exact number of fractures that occur annually, however, because many cases are clinically undetected [10].

Several therapies are available to prevent osteoporosis and osteoporotic fractures. In addition to calcium and vitamin D bisphosphonates, selective estrogen receptor modulators, estrogen, and calcitonin are effective drugs in preventing osteoporotic fractures. Research has shown recently that an estrogen/progestin replacement therapy has substantial side effects, including an increased risk of breast cancer that increases with the duration of use [11]. Because of these side effects and to limit the substantial costs associated with these medications, sensitive and specific diagnostic techniques are required to assess the risk of osteoporotic fractures. Therapy also must be initiated at a relatively early stage before fractures occur.

The best established diagnostic techniques to assess osteoporosis focus on BMD (ie, DXA and QCT). Several newer emerging techniques are quantitative ultrasound and high-resolution tomographic techniques that analyze bone structure, such as high-resolution MRI and CT. Conventional radiographs are not suited for determining bone mass but are essential for assessing osteoporotic fractures, which are particularly important in the spine.

Imaging of fracture and deformity

Osteoporosis-related vertebral fractures have important health consequences for older women, including disability and increased mortality [12]. Because these fractures can be prevented with appropriate medications, recognition and treatment of high-risk

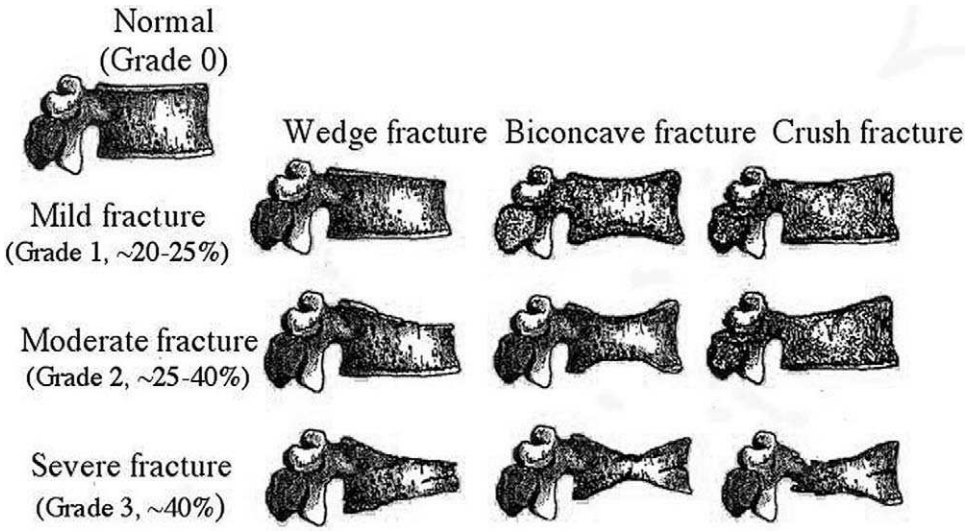

Fig. 1. The spinal fracture index is a semiquantitative score that was developed by Genant et al [16] and differentiates four grades of fracture. (*From* Genant HK, Wu CY, van Kuijk C, Nevitt MC. Vertebral fracture assessment using a semiquantitative technique. J Bone Miner Res 1993;8:1137–1148; with permission of the American Society for Bone and Mineral Research.)

patients are warranted. In a cross-sectional survey, Gehlbach et al [13] analyzed 934 women aged 60 years and older who were hospitalized and had a chest radiograph obtained. Moderate or severe vertebral fractures were identified for 132 (14.1%) study subjects. Only 50% of the contemporaneous radiology reports identified a fracture as present, however, and only 17 (1.8%) of the 934 participants had a discharge diagnosis of vertebral fracture. Few hospitalized older women with radiographically demonstrated vertebral fractures were identified or treated by clinicians. The results of this study should increase the awareness of the radiologist in diagnosing vertebral fractures. The presence of one vertebral fracture increases the risk of any subsequent vertebral fracture fivefold [14], and 20% of the women who have a recent diagnosis of a fracture will sustain a new fracture within the next 12 months [15].

Because most vertebral fractures do not come to clinical attention, the radiographic diagnosis is important. The severity of vertebral fractures may be visually determined from radiographs using a semiquantitative score, the so-called ''spinal fracture index,'' which was previously developed by Genant et al (Fig. 1) [16]. In this score, four grades are differentiated: grade 0 = no fracture; grade 1 = mild fracture (reduction in vertebral height 20%–25%); grade 2 = moderate fracture (reduction in height 25%–40%); grade 3 = severe fracture (reduction in height more than 40%). Fig. 2 shows examples of different grades of osteoporotic fractures in the thoracic and lumbar spine in postmenopausal patients. Several other scores have been developed, such as the ''spine deformity index'' and the ''radiological vertebral index'' [17–19], but these scores are used less frequently.

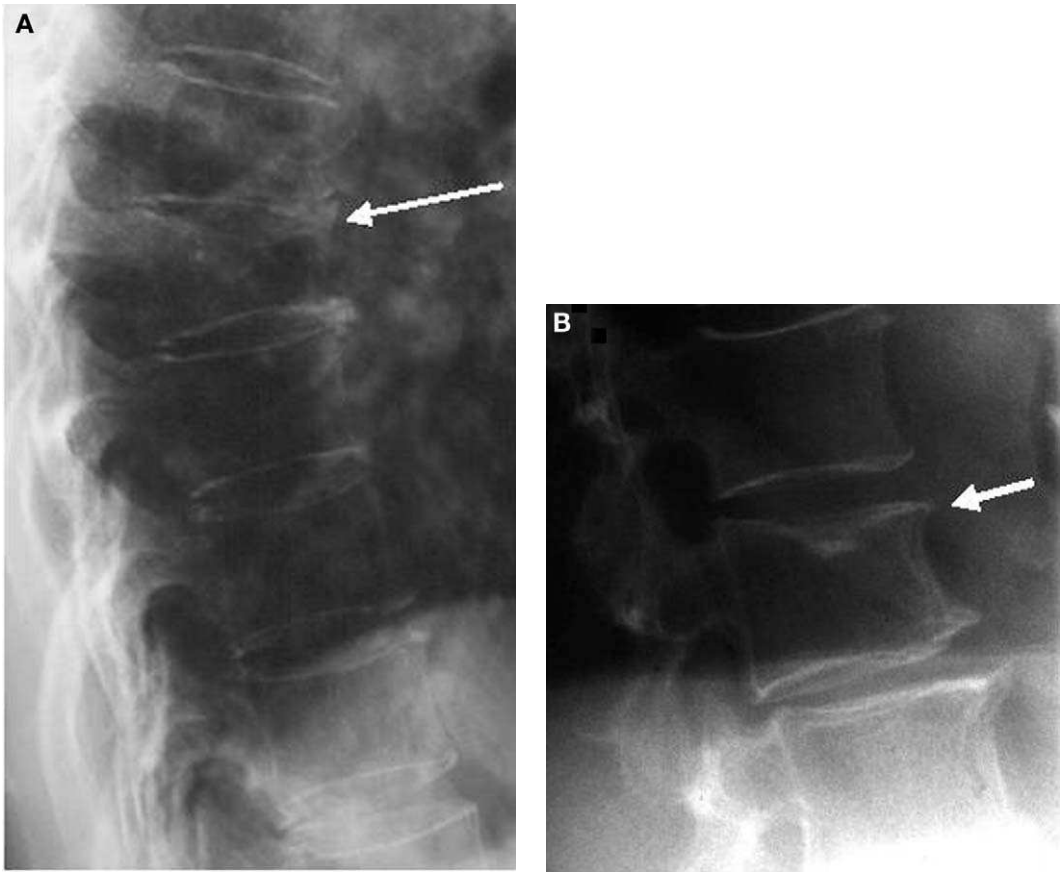

Fig. 2. Spine radiographs. (*A*) Moderate grade 2 fracture of a thoracic vertebra (T9) with a height reduction of nearly 40% (*arrow*). (*B*) Grade 1 fracture of a lumbar vertebra (L2) with a wedge-like deformity and a maximum height reduction of 20% to 25% (*arrow*).

Conventional radiographs of the spine are not suited to determine BMD in the early diagnosis of osteoporosis because it takes a bone loss of more than 20% to 40% before osteoporosis is visualized in the radiographs [20]. Morphologic signs described on spine radiographs, such as a coarse trabecular structure and a frame-like appearance of the vertebrae, are also not reliable [21].

Conventional radiographs are important in the differential diagnosis of osteoporosis, however, because several other diseases may present with bone loss and fractures. In rare cases, osteoporosis may present with a coarse trabecular structure with thick vertical trabeculae suggestive of vertebral hemangioma. This so-called "hypertrophic atrophy," however, is generalized and the trabecular bone structure appears more coarse than in hemangioma (Fig. 3A). Important differential diagnoses in osteoporosis are osteomalacia, hyperparathyroidism, renal osteopathia, and malignant bone marrow disorders (eg, plasmocytoma and diffuse metastatic disease). Endplate fractures are found in Scheuermann's disease (Fig. 3B) and malignant lesions (Fig. 4). The differential diagnosis of osteoporotic and malignant pathologic fractures may be difficult. Fractures located above the T7 level, associated with a soft tissue mass or osseous destruction and involving the posterior part of the vertebrae in conventional radiographs, most likely are malignant. CT and MRI may be helpful in differentiating osteoporotic and malignant fractures and depicting multiple lesions, soft tissue masses, or destructive changes (Fig. 4). Diffusion-weighted MR sequences and iron oxide contrast media in MRI have been used successfully to differentiate malignant and benign bone marrow pathologic conditions [22,23].

Conventional radiographs of the proximal femur and the distal radius are usually obtained after a low impact trauma with persistent symptoms in postmenopausal elderly individuals. In many cases, fractures may be occult in conventional radiographs. Bogost et al showed that 37% of proximal femur fractures were not detected in conventional radiographs, which were demonstrated in MR scans of these patients [24]. Non-enhanced T1-weighted and short T1 inversion recovery or spectrally fat saturated T2-weighted sequences are recommended in patients

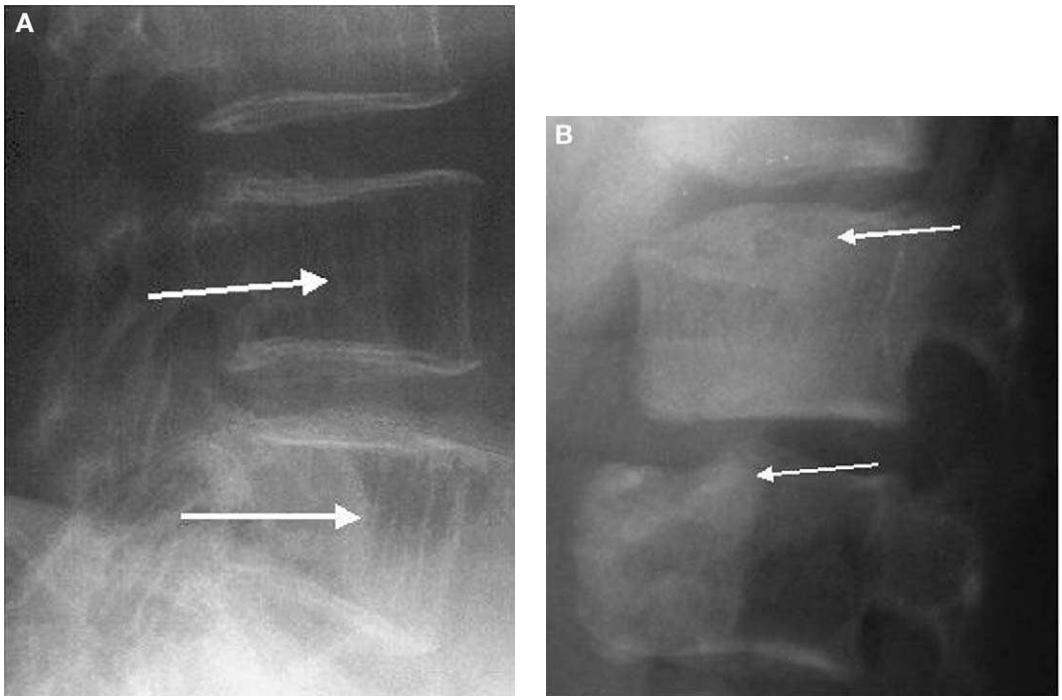

Fig. 3. Differential diagnosis, conventional spine radiographs. (*A*) Osteoporosis presents with a coarse trabecular bone structure similar to vertebral hemangioma (hypertrophic atrophy) (*arrows*). (*B*) Deformity of multiple vertebrae caused by Scheuermann's disease with fractured endplates and nonossified apophyses (*arrows*).

with a high clinical suspicion of fracture but negative radiographs (Fig. 5).

Osteodensitometry

Several techniques have been used to measure bone density. Photo densitometry was one of the first quantitative techniques that was used to determine bone mass of the calcaneus, metacarpals, and phalanges [25]. Digital x-ray radiogrammetry is a new method that automatically identifies regions in radius, ulna, and the three middle metacarpals and measures bone density [26]. This method has a high precision and reliability and may be used in standard radiographs of the forearm to predict hip, vertebral, and wrist fracture risk [27].

Single-photon absorptiometry is another technique for measuring peripheral BMD that uses a highly collimated photon beam from a radionuclide source (such as iodine-125) to measure photon attenuation [28]. This technique measures BMD of the distal radius and the calcaneus. Because single-photon absorptiometry is a single energy technique, a standardized water bath is required. This method has a high precision and low exposure dose, but the use of a radionuclide source is a limitation of this technique. The same applies to dual-photon absorptiometry, which may be used for the spine, hip, and total body because of the dual energy technique (typically gadolinium-153 with energies of 44 and 100 keV), which reduces the soft tissue contribution substantially [29]. This technique has a high precision and a low exposure dose, but the scanning time is

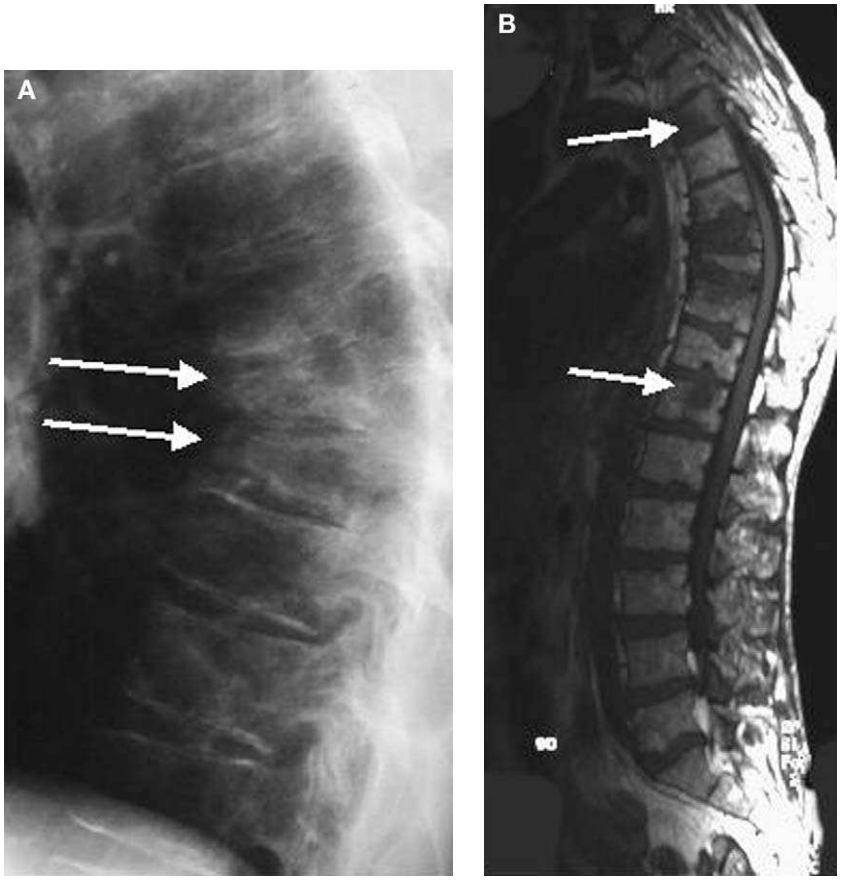

Fig. 4. Pathologic vertebral fracture caused by bone metastasis. (*A*) Conventional spine radiograph depicts fractures of two thoracic vertebrae (*arrows*). Sagittal T1-weighted (*B*) and short T1 inversion recovery MR images (*C*) show multiple neoplastic lesions (*arrows*) of the spine in addition to the vertebral fractures.

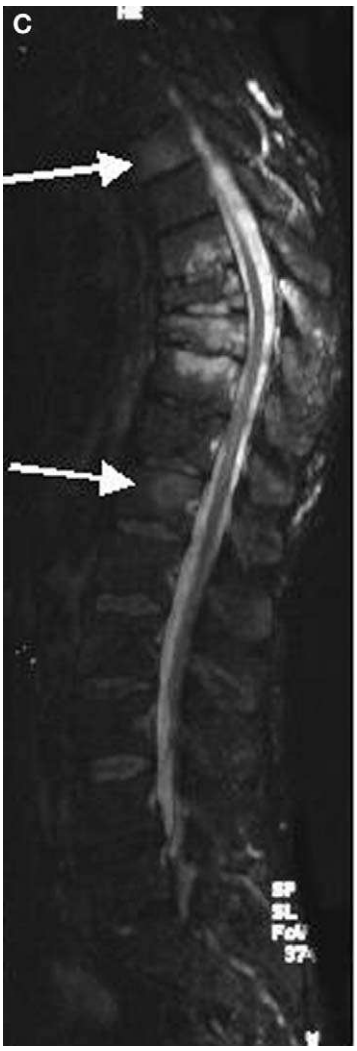

Fig. 4 (*continued*).

relatively long. Because of isotope source changes, single-photon absorptiometry and dual-photon absorptiometry are of limited clinical significance and have been replaced by DXA, which uses an x-ray tube instead of a radionuclide source. Currently the most important techniques in osteodensitometry are DXA and QCT.

Dual X-ray Absorptiometry

As in dual-photon absorptiometry, the principal of DXA is a dual-energy measurement that is based on the fact that radiation of distinct energies is attenuated by tissues to different extents. In soft tissue and bone, a low-energy beam is attenuated to a greater degree than a high-energy beam. Contrast in attenuation between bone and soft tissue is greater for the low-energy beam than for the high-energy beam, such that the attenuation profile of bone may be determined by subtracting the low- and high-energy attenuation profiles. Compared with dual-photon absorptiometry, DXA has several advantages, including increased precision, shorter examination time, finer collimation with a better spatial resolution, and lack of radionuclide source decay [30,31]. The correlation between BMD data obtained from dual-photon absorptiometry and DXA of the spine and hip was excellent ($r = 0.98$ and $= 0.95$) [32]. DXA scanners provide either pencil or fan beam techniques. Fan beam techniques are faster. Precision of DXA is high and radiation exposure is low (Table 1).

Using DXA, BMD is most frequently determined at the spine (AP or lateral) (Fig. 6) and at the proximal femur (Fig. 7). Whole body measurements and measurements at the distal radius and the calcaneus also may be obtained. The AP examination of the lumbar spine is a standard procedure with a precision in vivo of 1%, a radiation exposure effective dose of 1 to 50 μSv (the higher dose is required for digital high-resolution images), and a high accuracy (4%–10%) (see Table 1) [30,33,34]. For monitoring BMD, the precision alone, however, is not the only parameter required to assess the diagnostic performance of a technique. One also must know the annual rate of BMD loss in normal patients using this technique and the least significant change between two measurements, which for DXA and QCT are shown in Table 2.

Using automated software, areal BMD (g/cm^2) is determined usually in L1-4. These projection images, however, have several limitations: (1) Vertebrae with a larger size have a higher BMD. (2) Aortic calcification and all other soft tissue calcifications in the regions of interest (ROIs) increase BMD. (3) Degenerative changes of the spine, including osteophytes, facet sclerosis, and degenerative disc disease, also may increase BMD falsely (Fig. 6). In elderly patients with substantial degenerative changes of the lumbar spine, AP DXA of the lumbar spine may not be a suitable technique. Lateral DXA is less influenced by these changes because it assesses only the vertebral bodies and focuses more on trabecular bone. Drawbacks of this technique are lower precision, higher radiation exposure, and superimposition of the pelvis and the ribs, however, which may limit analysis of the lumbar spine to L3 [35–37]. So far, AP DXA is the standard DXA procedure to assess the lumbar spine.

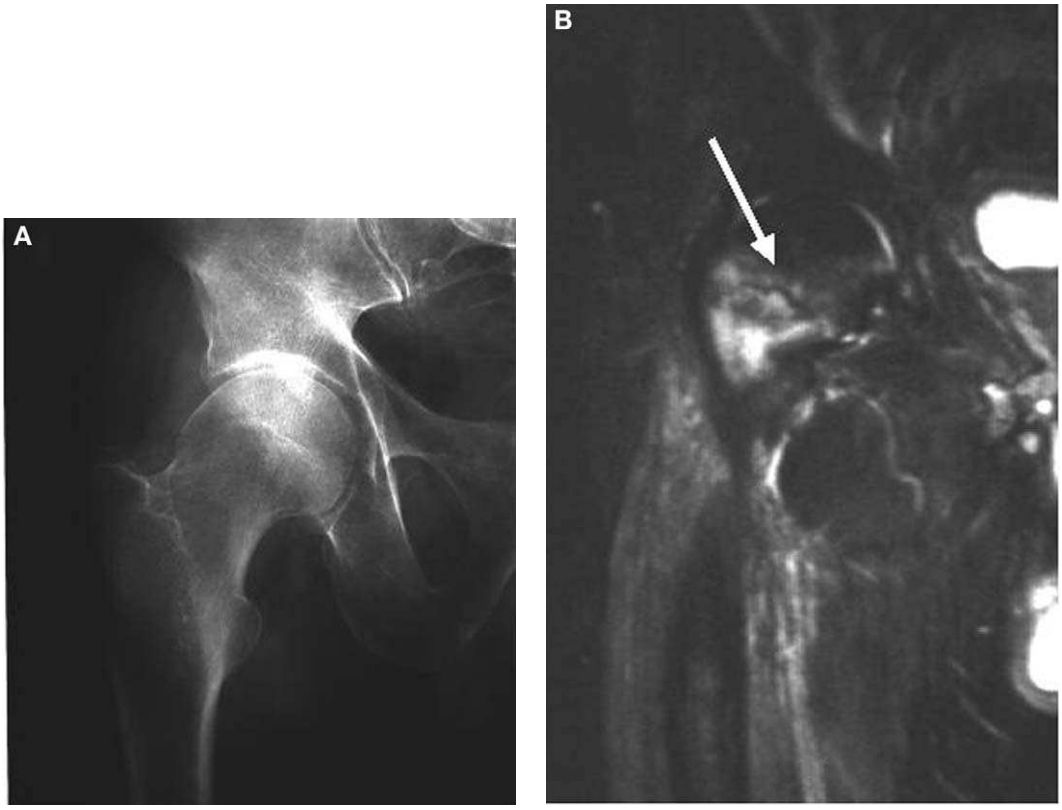

Fig. 5. Osteoporotic proximal femur fracture caused by minor trauma. The femoral neck fracture was not depicted on the conventional radiograph (*A*) but is clearly shown in the coronal short T1 inversion recovery MR image (*arrow*) (*B*). The MR examination was performed because of persistent pain 4 days after the initial trauma.

When analyzing DXA scans, several pitfalls that may be operator dependent must be considered, such as mislabeled vertebrae, misplaced disk space markers, wrong sized ROIs, use of a fractured or deformed vertebra for measurement, and opaque artifacts in the analysis region. These analysis errors are of greater magnitude than the machine's intrinsic precision errors [38]. DXA of the proximal femur is a particularly important examination because it is currently one of the best techniques to assess fracture risk of the hip (Fig. 7). The examination of the hip, however, is more demanding than that of the spine [39]. The proximal femur must be positioned in a standardized fashion and several ROIs must be placed correctly. The correct location of these ROIs varies according to the manufacturer. Standard ROIs are the neck region, the trochanteric region, and the intertrochanteric region and Ward's ROI (the square of 1 × 1 cm with the lowest density within the proximal femur). The ROI that is used most frequently is the total femur. The total femur ROI consists of the neck region, the trochanteric region, and the intertrochanteric region. Ward's ROI has an inferior precision compared with the other ROIs and is currently not used as a standard ROI. The precision for hip BMD and the annual rate of loss are lower compared with AP spine DXA and the least significant change is higher (Tables 1, 2).

As in DXA of the lumbar spine, several operator-dependent errors may occur in the proximal femur and should be detected by the radiologist [38,40]. Most of these errors are caused by improper positioning of the patient and the ROIs. Correct positioning of the patient includes internal rotation of the hip with a straight femoral shaft (the lesser trochanter should not or just barely be visualized). Correct positioning and size of the ROIs, in particular the neck box, may vary according to the manufacturer (eg, Lunar/GE systems have a standardized size of the neck box that is placed automatically in the region of the neck with the smallest diameter). Osteoarthritis, Paget's disease, fracture, vascular calcifications, calcific tendinitis,

Table 1
Accuracy, precision, and radiation exposure of techniques used for bone mineral density measurement

Techniques	Location	Accuracy [%]	Precision [%]	Radiation exposure, effective dose [μSv]
Older techniques				
Photo densitometry	Phalanx, metacarpals	10	5	< 5
DPA	Lumbar spine, proximal femur	2–11	2–3	5
			2–5	3
SXA	Radius, calcaneus	4–6	1–2	< 1
Dual energy QCT	Lumbar spine	3–6	4–6	~ 500[a]
Standard techniques: axial skeleton				
DXA	Lumbar spine			
	AP	4–10	1	1–50[b]
	lateral	5–15	2–6	3–50[b]
	Proximal femur	6	1.5–3	~ 1–2[c]
	Whole body	3	1	~ 3[c]
QCT (single energy)	Lumbar spine	5–15	1.5–4	60–500[d]
Standard techniques: peripheral skeleton				
DXA	Radius	4–6	1	< 1
Peripheral QCT	Radius	2–8	1–2	~ 1

Abbreviations: DPA, dual photon absorptiometry; QCT, quantitative CT; SPA, single photon absorptiometry; SXA, single x-ray absorptiometry.

[a] 125 kV/ 85 kV and 410mAs.

[b] The low values apply for pencil beam scanners, whereas fan beam scanners have an effective dose that is threefold to fivefold higher. The highest exposure doses were measured using a fan beam scanner with a high image quality.

[c] For pencil beam scanners.

[d] 60μSv are obtained using a low dose protocol (80kV, 125mAs).

enostosis, and avascular necrosis of the hip are also potential sources of error. Conventional radiographs may be required if an atypical density profile is shown. If these lesions are too large or developmental dysplasia of the hip is found, BMD must be determined at a different site.

Recently an upper neck region has been introduced that is supposed to predict the risk of femur neck fractures better than the complete neck ROI (Fig. 8) [41]. The thickness and porosity in the upper neck region are believed to be critical to maintaining femoral strength. The upper neck region also demonstrates a more rapid age-related decline than the standard femoral neck region [42]. An automated hip axis length measurement also is included in one of the manufacturer's newest software analysis packages, which is supposed to improve the prediction of proximal femur fracture (Fig. 8) [43–46]. Dual femur measurements are recommended to reduce precision error and facilitate the evaluation of skeletal response to therapy at the femur [47,48].

Peripheral DXA techniques include those that analyze the distal radius and the calcaneus. These techniques have high precision and low radiation exposure, but annual BMD loss at these sites is low, which is a potential limitation for monitoring BMD. Dedicated devices have been developed that are portable and inexpensive and have shorter scan times [49]. It has been shown that these techniques may be useful in assessing osteoporosis and fracture risk [50]. In comparison with spine and hip DXA measurements, however, the peripheral BMD measurements are less suited to predicting fracture risk of the spine and proximal femur. They may be useful in reducing the cost of detection of osteoporosis, however, and provide a greater opportunity for identification of women at risk for fracture [49].

Quantitative computed tomography

Standard QCT is performed on the lumbar spine; usually the first to third lumbar vertebrae are analyzed. In contrast to DXA, QCT allows a true densitometric, volumetric measurement (in mg/mL) of trabecular bone, whereas DXA gives an areal BMD (in mg/cm^2), which includes trabecular and cortical bone. Because the trabecular bone has a substantially higher metabolic turnover, it is more sensitive to changes in BMD (annual rate of bone loss in QCT 2%–4% versus 1% in AP DXA of the spine). On the

other hand, the precision of QCT is lower than that of DXA (1.5%–4% versus 1%), and significant longitudinal changes must be larger (6%–11% versus 3%–4%) (Tables 1, 2). A big advantage of QCT is that it is not as susceptible to degenerative changes of the spine as DXA. Osteophytes, facet joint degeneration, and soft tissue calcifications (particularly aortic calcification) do not falsely elevate the BMD in QCT. As in DXA, however, fractured or deformed vertebrae must not be used for BMD assessment because these vertebrae usually have an increased BMD.

QCT may be performed at any CT system; however, a calibration phantom is required and dedicated software improves the precision of the examination. The patient is examined supine, lying on the phantom usually with a water- or gel-filled cushion in between to avoid artifacts caused by air gaps. A lateral digital radiograph respectively scout view is used to select mid-vertebral slice positions of L1-3 parallel to the

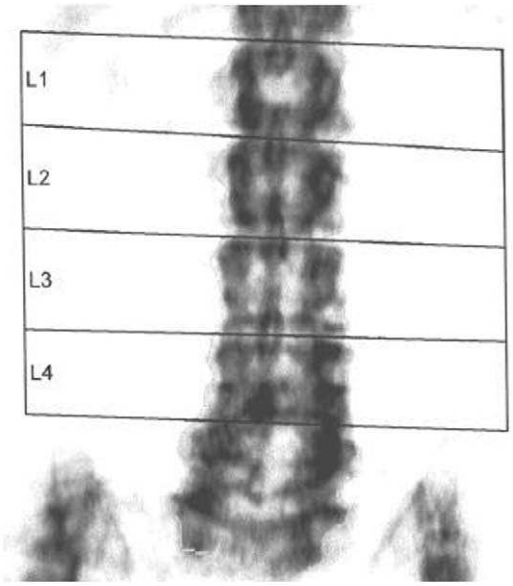

A

location	BMD in g/cm²	T-score	Z-score
L1	1,064	-0,5	1,0
L2	1,108	-0,8	0,8
L3	1,011	-1,6	0,0
L4	1,163	-0,3	1,3
L1-L4	1,087	-0,8	0,8

B

Fig. 6. DXA. Anteroposterior spine of a 79-year-old postmenopausal, white woman. (*A*) The DXA scan of the lumbar spine with L1-4 ROIs. Note that the areas of the facet joints in L1, L2, and L4 appear denser than in L3, which corresponds to degenerative changes (osteoarthritis of the facet joints). (*B*) This is reflected in the absolute BMD data, in which the areal density in L1, L2, and L4 is higher than in L3. Applying the WHO guidelines to the T-scores, L3 would be evaluated as osteopenic (T-score = −1.6), whereas the other vertebrae would be considered as normal. (*B*) The age-matched standard deviations (Z-scores) also are shown, which are in or above the normal range. (*C*) The BMD of L3 is presented in relation to patient age, the absolute BMD values (*left*), the T-scores (*right*), and the Z-score (*gray areas*).

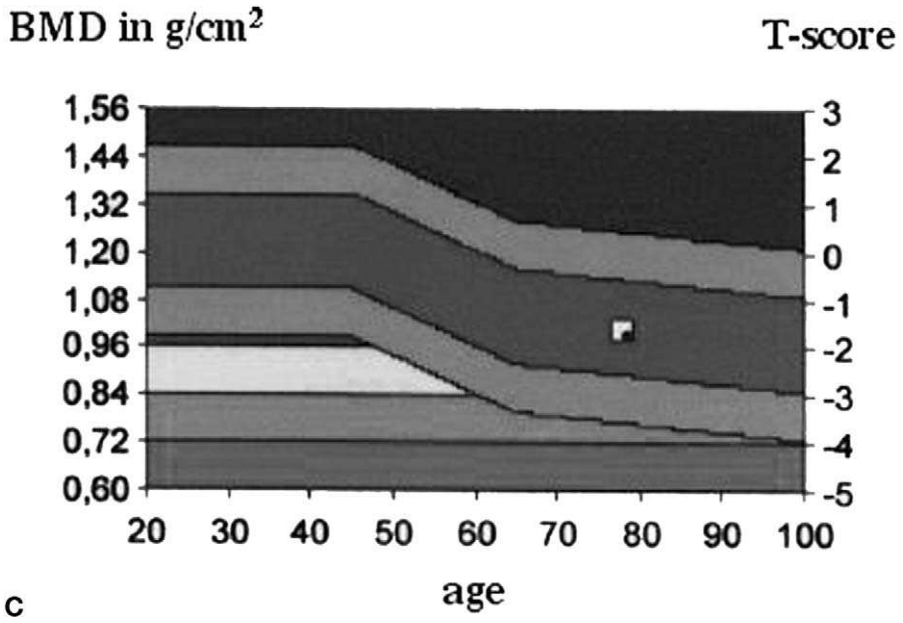

Fig. 6 (*continued*).

vertebral endplates (Fig. 9). Automated software that selects the mid-vertebral planes may be useful in reducing the precision error [51]. Usually a slice thickness of 8 to 10 mm is used (Fig. 9). A low-energy, low-dose protocol (eg, 80 kVp and 146 mAs) is recommended to minimize radiation exposure (down to an effective dose of 50–60 μSv, including the digital radiograph) [52]. Bone marrow fat increases with age and may decrease BMD falsely. The actual BMD may be underestimated by 15% to 20%. Because of age-matched databases, however, the clinical relevance of this fat error is small [53]. A dual-energy QCT technique was described to reduce the fat error. Because this technique has increased radiation exposure and decreased precision, however, its use is limited to research purposes [52,54].

To transform the attenuation measured in Hounsfield units into BMD (mg/mL), calibration phantoms are required. The patient and the phantom are examined at the same time, which is defined as simultaneous calibration. The Cann-Genant phantom with five cylindrical channels filled with K_2HPO_4 solutions (of known concentrations) was the first phantom in clinical use [55,56]. Because of the limited long-term stability of these solutions, however, solid-state phantoms with densities expressed in milligrams of calcium hydroxyapatite/mL were developed, which do not change with time and are more resistant to damage. Two phantoms are currently used: (1) the solid-state "Cann-Genant" phantom (Fig. 10A) [57] and (2) the phantom developed by Kalender et al (Fig. 10B) [58,59]. The latter phantom has a small cross-section and is constituted of only two density phases: a 200 mg/mL calcium hydroxyapatite phase and a water equivalent.

Several ROIs have been used to determine the BMD in the axial sections of the vertebrae. Manually placed elliptical ROIs (Fig. 11A) and automated image evaluation with elliptical and peeled ROIs (Fig. 11B) have been described [58,60]. The ROI developed by Kalender et al uses an automatic contour tracking of the cortical shell to determine a ROI analyzing trabecular and cortical (as visualized by CT) BMD separately [58]. The use of automated ROIs improves the precision of BMD measurements [59,61]. Steiger et al [60] have shown that elliptical and peeled ROIs yield similar results and have a high correlation ($r = 0.99$).

Data obtained by QCT are compared with an age-, sex-, and race-matched database (Fig. 12) [62,63]. T-scores used for the assessment of osteoporosis according to the WHO definition have been established for DXA but not for QCT, although they may be given by the software of the manufacturers. If these T-scores are used to diagnose osteoporosis, a substantially higher number of individuals compared with DXA will be diagnosed as osteoporotic, because BMD measured with QCT shows a faster decrease with age than

DXA (Fig. 12). Researchers have advocated using BMD measurements analogous to the WHO definition but with thresholds corresponding to lower T-scores. Felsenberg et al [52] classify BMD values from 120 to 80 mg/mL as osteopenic and BMD values less than 80 mg/mL as osteoporotic, which corresponds to a T-score of approximately −3.

With spiral and multislice CT, acquisition of larger bone volumes, such as entire vertebrae and the proximal femur, is feasible within a few seconds. These data sets can be used to obtain three-dimensional images, which provide geometric and volumetric density information. A drawback of these techniques, however, is a relatively high exposure dose, which has been estimated as high as 350 μSv for the spine and 1200 μSv for the hip using software developed by Kalender et al [64]. The primary advantage of volumetric QCT of the spine is an improved precision

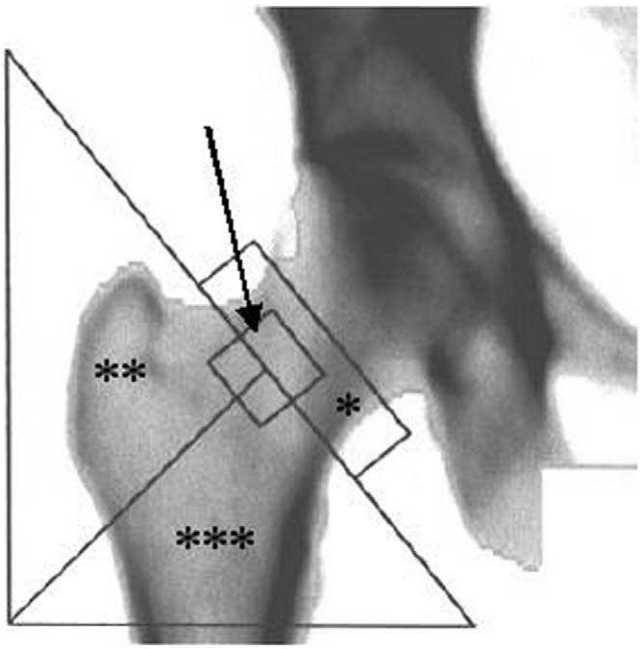

A

location	BMD in g/cm²	T-score	Z-score
Neck	0.988	0.1	0.5
Ward's	0.727	-1.4	-0.6
Trochanter	0.820	0.3	0.2
total	1.048	0.4	0.6

B

Fig. 7. DXA. Proximal femur of a 53-year-old postmenopausal, white woman. (*A*) The DXA scan of the proximal femur with the ROIs: the neck ROI (*), the trochanteric ROI (**), Ward's ROI (*arrow*), and the intertrochanteric ROI (***). The total BMD is determined from the measurements in the neck ROI, the trochanteric ROI, and the intertrochanteric ROI. Note that the lesser trochanter is only barely depicted. Applying the WHO guidelines to the T-scores, the total proximal femur ROI is in the normal range (*B*). This ROI also should be used for the diagnosis, although Ward's ROI is within the osteopenic range. (*C*) The BMD of the total femur ROI is presented in relation to patient age, the absolute BMD values (*left*), the T-scores (*right*), and the Z-score (*gray areas*).

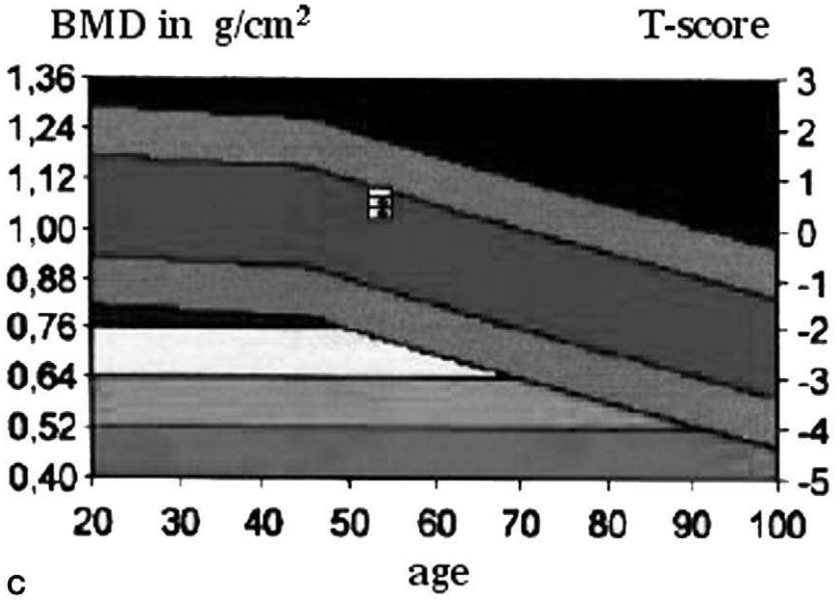

Fig. 7 (*continued*).

for trabecular BMD measurements, which was 1.3% as determined during an in vivo study [65]. An algorithm developed by Lang et al [66] processes volumetric CT images of the proximal femur to measure BMD in the femoral neck, total femur, and trochanteric regions. This technique has a high precision rate of 0.6% to 1.1% for trabecular bone and may be used to determine geometric measures, such as the cross-sectional area of the femur neck and the hip axis length. These measurements may be useful in optimizing fracture prediction of the proximal femur.

Dedicated peripheral QCT scanners have been developed to assess the BMD of the distal radius [67]. These scanners have a low radiation dose and a high precision with a short examination time but have the same limitations as peripheral DXA in the monitoring of patients with osteoporosis. Although this technique is potentially suited to predict fracture risk, studies have shown the limitations of this technique in predicting spine fractures and proximal hip fractures compared with other bone densitometry techniques [68–70].

Quantitative ultrasound

Quantitative ultrasound techniques recently have been proposed for the assessment of osteoporosis, in particular at peripheral skeletal sites such as the calcaneus, tibia, and the phalanges [71–75]. The underlying basis of this method is the attenuation of sound waves as they pass through bone and the time taken for a sound wave to propagate through bone. A transducer is placed close to an easily accessible bone with little soft tissue overlying it, and as the signal travels through the bone it is attenuated. The attenuation increases with frequency, and the rate of attenuation over a given frequency range is measured and provides a measure of broadband ultrasonic attenuation. The speed of sound is also measured by many commercial ultrasound devices, and this measure is obtained by the time

Table 2
Least significant change for quantitative CT and dual x-ray absorptiometry and average annual bone mineral density loss and monitoring time interval in healthy women after menopause

	LSC (%)	Rate of BMD loss (%/y)	MTI (y)
DXA, femur	4–8	0.5–1	5–6
DXA, AP spine	3–4	0.5–2	3
DXA, radius	3	1	3
QCT	6–11	2–4	3
Peripheral QCT (radius)	3	1	3

Abbreviations: AP, anteroposterior; LSC, least significant change; MTI, monitoring time interval; QCT, quantitative CT; y, year.

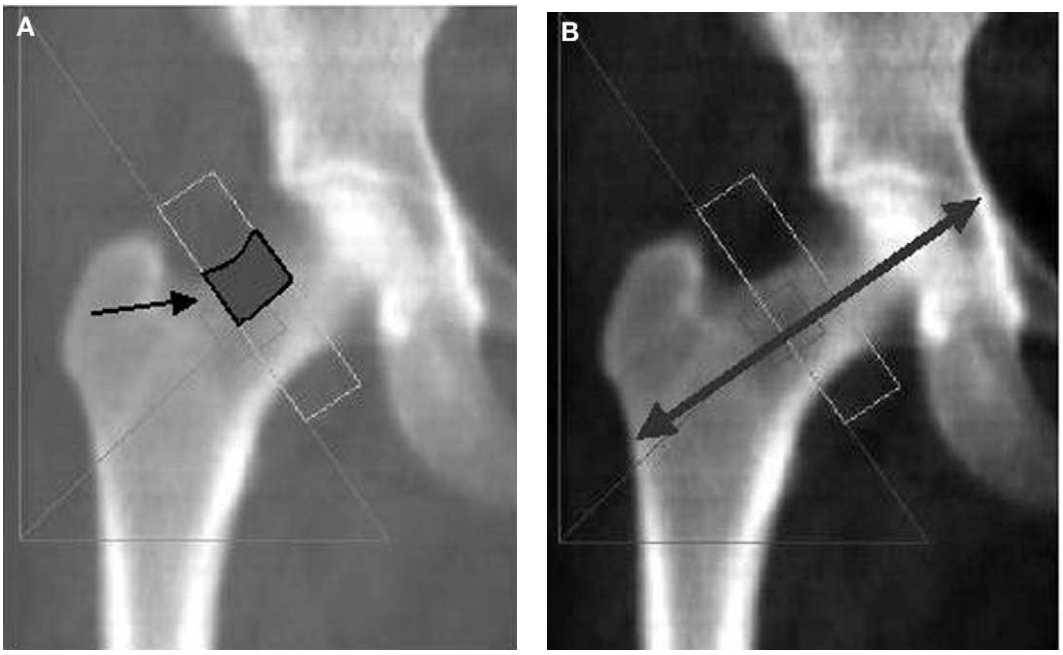

Fig. 8. (*A*) Advances in DXA of the proximal femur show the upper neck region (*arrow*), which constitutes the upper half of the neck region and (*B*) the hip axis line, which includes a femoral and an acetabular part.

taken for the sound waves to travel between two transducers. The attenuation of the sound waves is reduced when the number of attenuating elements—in the case of bone, the number of trabeculae—is reduced. From physical principles, the speed of sound in a given medium depends on the density and elastic modulus of the medium.

Ultrasound methods are attractive for the assessment of osteoporosis because the cost of the equipment is low, there is no ionizing radiation, and the equipment is portable. Initial scanners required the foot be immersed in a water bath; however, the newer systems are dry and use an ultrasound gel for contact.

In vitro and in vivo studies have shown that speed of sound decreases, and broadband ultrasonic attenuation is reduced with reductions in bone density and trabecular number, and hence in osteoporosis. Large retrospective and prospective studies have shown that quantitative US measures provide a relative risk comparable to bone density measures in hip fracture [75,76] and vertebral fracture [77]. The clinical issues associated with the reliability and reproducibility of the ultrasound measures include reproducible placement of the transducers and temperature variations of the foot [78]. Research is ongoing to improve the performance of this technique.

MR imaging

The three-dimensional, noninvasive imaging capabilities of MR imaging have been used clinically to assess and diagnose osteoporotic and vertebral fractures [79–81]. In recent years, however, MR imaging also has been developed to assess the characteristics of trabecular bone. MR imaging permits not only the depiction but also the quantification of trabecular bone structure; hence its biomechanical properties. MR imaging can be used to assess the properties of trabecular bone in two different ways. Cortical bone and trabecular bone have short intrinsic T2 (spin-spin relaxation time) values and low water content, and they have relatively low MR detectable magnetization. The presence of bone in proximity to bone marrow results in a modification of the marrow relaxation times, T1 and T2. The magnitude of T1 modification depends on the surface area to volume ratio of this bone marrow interface, increases at higher magnetic field strengths, and increases when the number of bone and marrow interfaces increase, that is, as bone density increases. The magnitude of T2 relaxation time changes are also governed by similar mechanisms as T1 relaxation but are also affected by processes such as diffusion. Magnetic susceptibility of trabecular bone is substantially different from that of bone marrow.

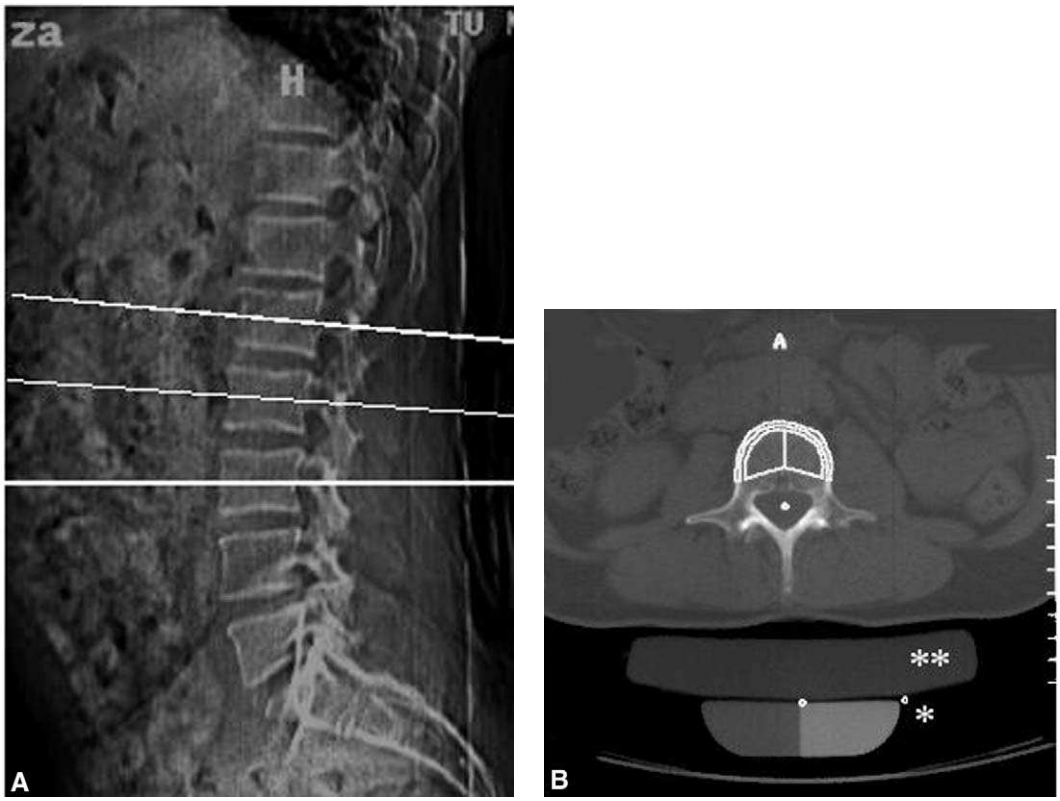

Fig. 9. QCT of the lumbar spine. (*A*) A lateral digital radiograph is shown with the mid-vertebral slice positions of L1-3 that are aligned parallel to the vertebral endplates. (*B*) Depiction of a 10-mm thick section of L2 with the calibration phantom (*) and the gel cushion (**). An automated, peeled ROI (which determines cortical and trabecular bone mineral density separately) was used.

This gives rise to localized inhomogeneities in the magnetic field that depend on the number of trabecular bone marrow interfaces, the size of the individual trabeculae, and the field strength. The diffusion of water in these magnetic field inhomogeneities results in an irreversible loss of magnetization and shortens the marrow relaxation time T2. This effect also depends on magnetic field strength and is greater at higher magnetic field strength. In addition to these effects on marrow relaxation, an effect may occur in the presence of trabeculae, that is, the modification of the marrow relaxation time T2*. In specific types of MR imaging sequences (eg, gradient-echo sequences) in addition to diffusion-mediated loss of magnetization, the magnetization is further lost irreversibly as a result of the field inhomogeneities. This loss results in a characteristic relaxation time T2*, which includes the additional contribution caused by field inhomogeneities and the T2 relaxation properties. This effect forms the basis of quantitative MR imaging.

The impact of bone on the MR properties of marrow was first investigated in an in vitro experiment in 1986 by Davis et al [82] at a field strength of 5.8 T. The investigators found that as bone density increased, there were concomitant increases in the magnetic field inhomogeneities and decreases in T2*. At a field strength of 0.6 T, Rosenthal et al [83] showed that in excised cadaveric specimens the relaxation time T2* of saline present in the marrow spaces was shorter than that of pure saline. Calibration of T2* with measures of BMD have been undertaken in vitro [83–89] and in vivo [90–94]. Investigators also have found that T2* variations with bone density depend on the spatial resolution at which the images are obtained [90] and on the three-dimensional distribution of the trabecular bone, or structure, as shown in computer studies [85,95] and phantom experiments [83,96–98].

In the area of osteoporosis, the biomechanical properties of trabecular bone are of ultimate impor-

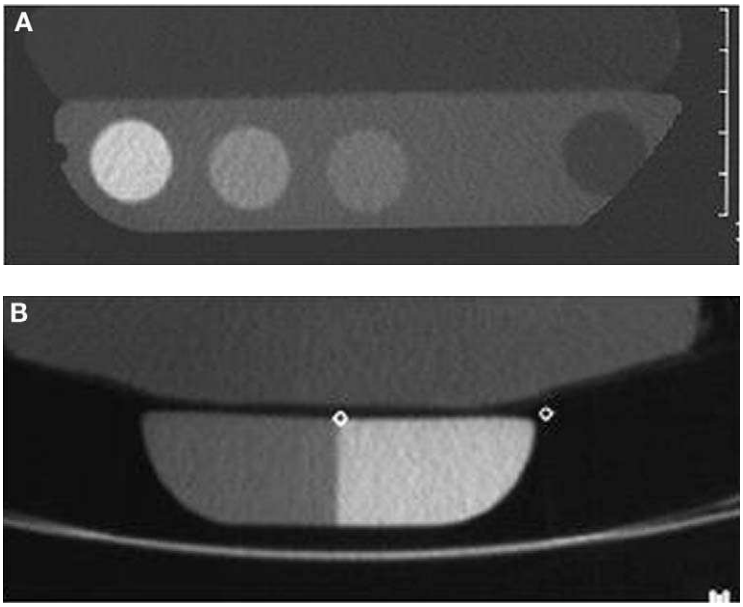

Fig. 10. (*A*) QCT calibration phantoms show a solid-state "Cann-Genant" phantom, comprised of five density phases. (*B*) The phantom developed by Kalender et al with a small cross-section, is comprised of two density phases.

tance. Using specimens from the human tibia [99] and vertebrae [100], it has been shown that T1/T2* increases linearly as the elastic modulus increases. Correlations between ultimate compressive strength and T2* have been studied in porcine bone [86] and human vertebral samples [101].

Clinically, Sebag et al [102] showed qualitatively that bone marrow in the presence of trabecular bone showed increased signal loss in gradient-echo images, where T2* effects predominate. Subsequently, quantitative estimates of T2* in regions of varying bone density, such as in the epiphysis, metaphysic, and diaphysis, were measured by Ford et al [92] using a technique known as *interferometry* and localized proton spectroscopy. In a small sample size, researchers also have shown that T2* values potentially may distinguish osteoporotics from normals [91]. In vivo calibration of T2* with trabecular bone density has been obtained from coincident measurements in the forearm, distal-femur, and proximal tibia using MRI and QCT [103].

Fransson et al [94] correlated T2* in the tibia with measures of BMD in the proximal femur and calcaneal ultrasound. The investigators found good correlations between T2* with BMD but relatively lower correlation with ultrasound measures. This could be caused by the significant heterogeneity of bone structure in the calcaneus and in the tibia and the fact that the ultrasound measure is a single point measure and could be measuring a small and variable region between subjects. The heterogeneity in the bone density and its impact on T2* in the calcaneus was quantified in vivo by Guglielmi et al [104], who showed that the shortest relaxation time occurs in the superior talar region that corresponds to the highest BMD. They also demonstrated a linear correlation between MRI and DXA measurements (r = 0.66 for T1/T2* versus BMD). In a case control study, T2* measures of the proximal femur distinguished between subjects with hip fractures and normal subjects [105]. A combination of relaxation time measures and BMD improved the ability to discriminate persons with vertebral fractures from individuals without [106].

Imaging of trabecular bone structure

In the context of osteoporosis, in addition to the quantity (mass) or the density of bone mineral, other factors such as the extent of mineralization, the macro-architecture of the bone, the trabecular bone micro-architecture, and bone turnover play a role in defining bone strength. Several methods to assess these parameters are under study, and they aim to extend knowledge in the area of bone biology.

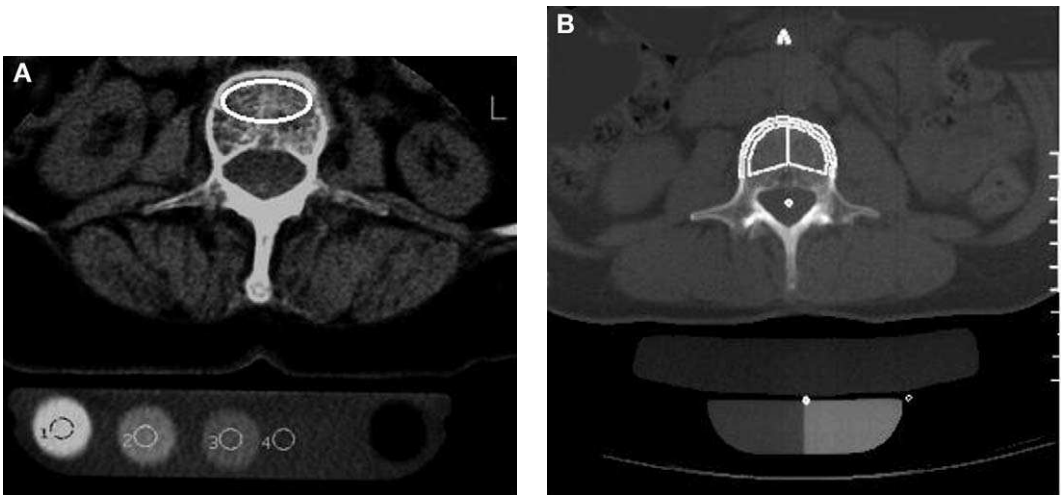

Fig. 11. Different ROIs used for the analysis in QCT. (*A*) An elliptical ROI that was placed manually. (*B*) An automatically placed "peeled" ROI, which determines trabecular and cortical BMD separately.

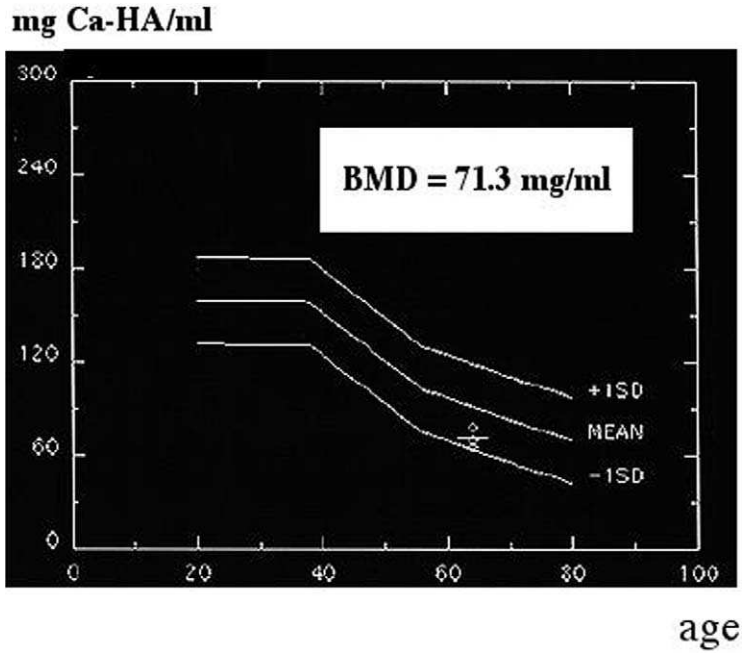

Fig. 12. Age-related decrease of BMD in QCT, which is more substantial than that found in DXA of the lumbar spine. The BMD of L3 in an individual patient is shown in relation to age and age-matched normal BMD. Although manufacturers give T- and Z-scores (in this 62-year-old female patient the T-score would be −3.2 SD and the Z-score −0.7), these are not established for QCT.

Radiographic assessment

The three-dimensional micro-architecture of a cube of trabecular bone (Fig. 13) and radiographs obtained at different orientations depict the anisotropy of the micro-architecture of the trabecular network (Fig. 13B–D) and reflect different radiographic patterns depending on the orientation. Several computer-based methods have been applied in the study of radiographic patterns of trabecular bone and the relationship of these measures with respect to biomechanical properties of bone and osteoporotic status in vivo [107–112]. Caligiuri et al [113–115] used projection lateral radiographs (nonmagnified medial-lateral) of the lumbar spine and determined Fourier transform and fractal analysis based texture measures. The investigators found that the texture measurements appeared more successful than BMD

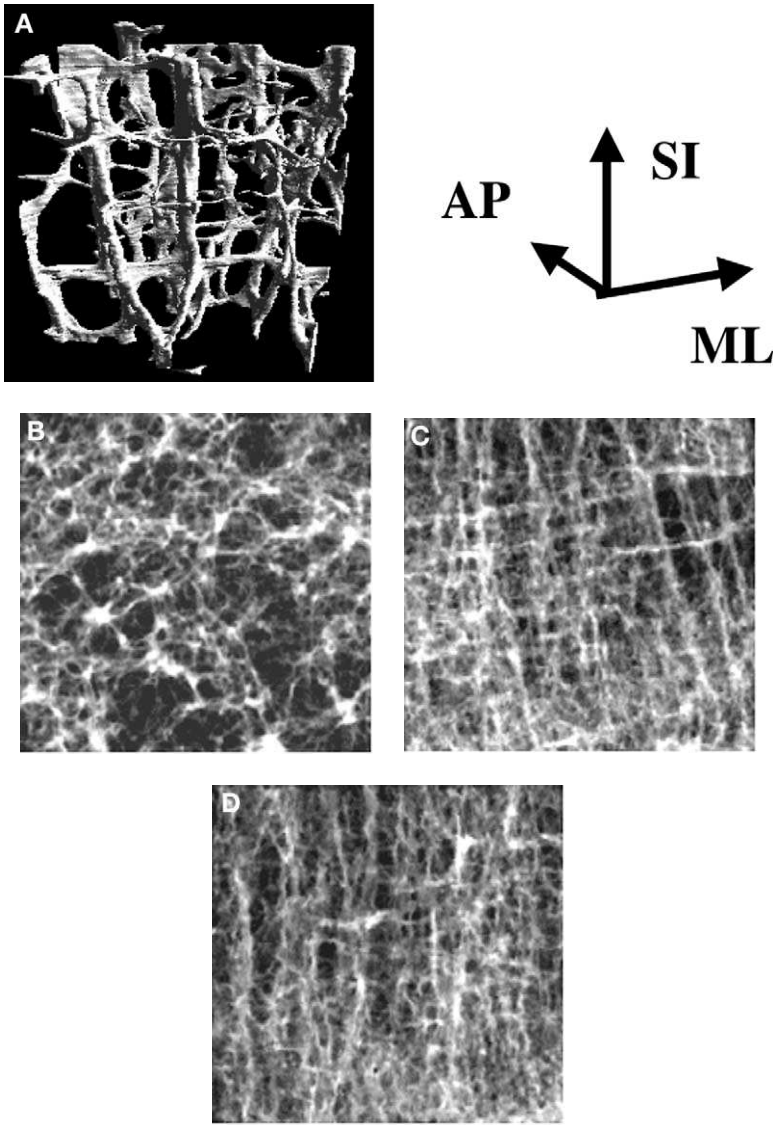

Fig. 13. (*A*) Three-dimensional rendering of trabecular bone specimen imaged after photographing 5 μm thick layers in sequence, using a serial grinder to reveal the subsequent layers. The radiographs in *B–D*, which were obtained using different orthogonal projections, reveal differences in trabecular pattern caused by the anisotropy and orientation of the three-dimensional trabecular network.

obtained with DXA in predicting the presence or absence of fractures elsewhere in the spine. Buckland-Wright et al [116] analyzed magnification radiographs of lumbar vertebrae in an experimental and clinical study using fractal signature analysis. Similar analysis by Link et al [117] using morphometric texture parameters and direct magnification radiographs have shown that texture measures may have some relevance in predicting biomechanical properties. In the study by Veenland et al [118] on direct magnification radiography of human cadaveric vertebrae, texture parameters based on mathematical morphology were assessed. Multivariate regression of fracture stress versus BMD and the textural parameters showed that for the female vertebrae, a combination of one texture parameter and BMD gave a better prediction of fracture stress than BMD alone.

Several authors used calcaneus radiographs to analyze bone structure with fractal dimension. Lespessailles et al [119–121] performed in vitro and in vivo studies and compared fractal dimension derived from a fractional Brownian motion model with biomechanical stability, bone histomorphometry, and osteoporotic status. The authors found a significant correlation between this texture measure and biomechanical strength; however, BMD performed substantially better. In an in vivo study, Pothuaud et al [122] used the same technique and found significant differences between patients with osteoporotic spine fracture and age-matched controls.

Quantitative ultrasound assessment

In early studies, quantitative US was found to depend on the orientation of trabecular bone [123] and researchers postulated that it provided a measure that was a combination of trabecular bone density and structure, especially in the calcaneus. Subsequent studies questioned the role of quantitative US in the assessment of trabecular bone structure and have shown that in the commercial ultrasound devices, ultrasound measures seem to depict bone density alone [124].

Assessment from three-dimensional tomographic images

In addition to projection radiographs, new emerging micro-CT methods and MR imaging methods are being used in the study of bone structure. Fig. 14 shows a representative micro-CT image of an iliac crest biopsy of trabecular bone, and similar images of the distal radius also may be obtained in vivo using a prototype device [125–128].

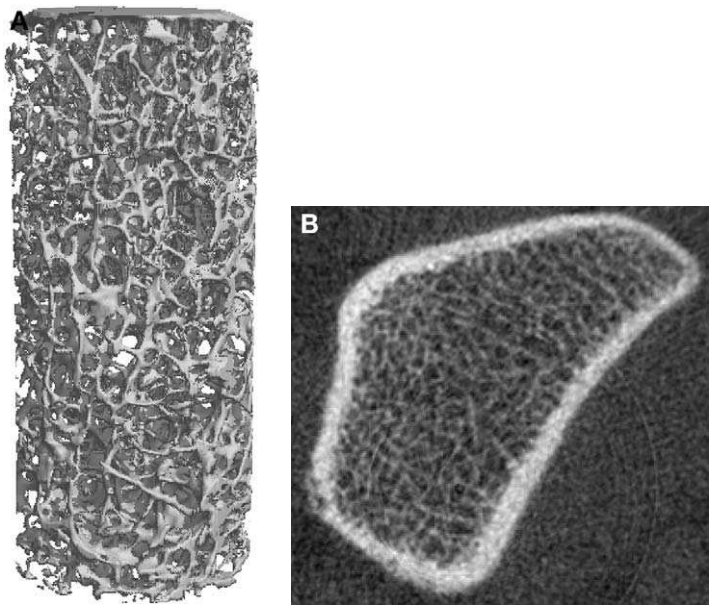

Fig. 14. (*A*) A three-dimensional rendering of a micro-CT image of trabecular bone obtained from an iliac crest biopsy. The image resolution was 34 × 34 × 34 μm obtained using a Scanco, μCT 20 (Scanco, Switzerland). (*B*) An in vivo image obtained through the distal radius using a prototype scanner. (Courtesy of Andres Laib, Scanco, Switzerland.)

With the advent of phased array coils and improved software and hardware, it has been possible to push the frontiers of MR imaging. The three-dimensional imaging capability, along with the fact that MR imaging is a nonionizing modality, makes it potentially attractive as a tool for imaging trabecular bone structure. The marrow surrounding the trabecular bone network, if imaged at high resolution, reveals the trabecular network (Fig. 15). Using such μCT and MR images, multiple different image processing and image analysis algorithms have been developed to quantify the trabecular bone structure in two or three dimensions. The measures that have been derived so far are many, and some of them are synonymous with the histomorphometric measures such as trabecular bone volume fraction, trabecular thickness, trabecular spacing, trabecular number, connectivity, fractal dimension, tubularity, and maximal entropy.

Several calibration and validation studies have been undertaken in which MR-derived measures of structure are compared with measures derived from other modalities, such as histology, micro-μCT, and BMD, and with biomechanical parameters. One of the primary issues in MR-derived visualization and quantitation of structure arises from the fact that the spatial resolution of the MR images is often comparable to the thickness of the trabecular bone itself, which gives rise to partial volume effects in the image. The image may not depict thin trabeculae or may represent an average or a projection of a few trabeculae. Recognizing that MR-derived measures are not identical to histologic dimensions—a major focus in the field—has been used to establish measures to investigate the resolution dependence of MR-based measures and then calibrating MR-derived measures of bone structure.

Hipp et al [129] compared the morphologic analysis of 16 specimens of bovine trabecular bone using three-dimensional MR reconstruction ($92 \times 92 \times 92$ μm^3) and two-dimensional optical images (23×23 μm^2) of the six faces of the samples. Recognizing that it is not possible to reconstitute accurately the ''true'' trabecular bone structure from high-resolution MR imaging, Majumdar et al [130] introduced the notion of ''apparent'' trabecular bone network. Whereas the ''apparent'' network is not identical to the ''true'' histologic structure, it still reflects some ''apparent'' morphologic and topologic properties that are highly correlated to the ''true'' structure [130,131]. These studies and others [132] show good correlation between the MR-derived and other high-resolution imaging–derived measures, such as trabecular separation and number, moderate correlation for trabecular bone volume fraction, and poor correlation for trabecular thickness. These correlations indicate that MR imaging can depict trabecular bone structure, although the absolute measures differ from the measures obtained at higher resolution. The poorer correlation of trabecular thickness is explained by the fact that the image resolution is comparable to the dimensions of the trabeculae being measured, and a small sampling error, or a partial volume effect, in the estimation leads to a large percentage error.

The effect of slice thickness on standard morphologic measurements has been investigated by Kothari et al [131]. Vieth et al [133] compared standard

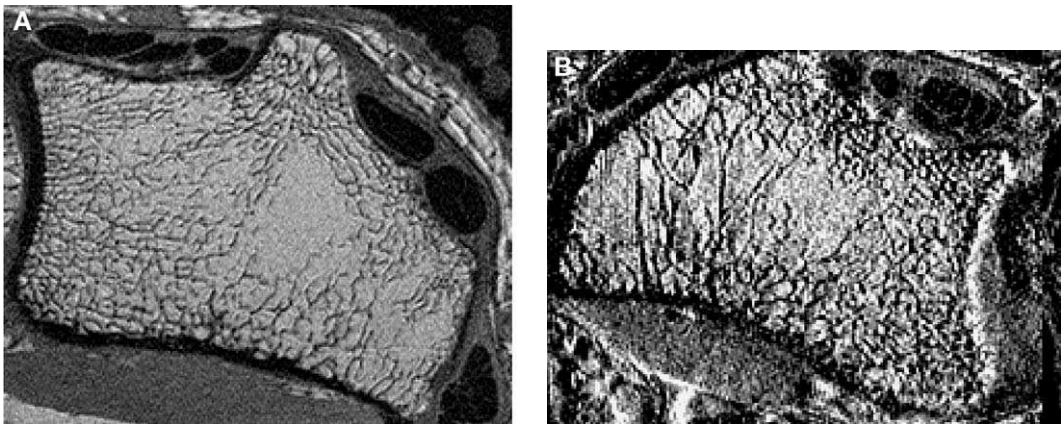

Fig. 15. Axial images of the distal radius obtained at 1.5 T (*A*) spin-echo and (*B*) gradient echo. The dark network represents the trabecular bone network, whereas the higher intensity background represents marrow-equivalent material in the trabecular spaces.

morphologic measurements of 30 calcaneus specimens using MR imaging (195 × 195 μm^2 in-plane resolution and 300/900 μm slice thickness) and contact radiographs (digitized with 50 × 50 μm^2 in-plane spatial resolution) of sections obtained from the same specimens. The results of this study showed that MR-based measurements were significantly correlated with those obtained from digitized contact radiographs. Partial volume effects caused by slice thickness and image post-processing (thresholding) had substantial impact on these correlations, however: the thicker the slice, the poorer the correlation.

Lin et al [134] confirmed correlation between structure parameters derived from MR imaging and serial grinding images and established that the heterogeneity of calcaneal bone structure, as determined from MR imaging, is real and is correlated to the magnitude of the spatial heterogeneity using higher resolution microscopic images.

The accuracy of a new model-independent morphologic measure, based on the distance transformation technique applied to high-resolution MR imaging of human radius specimens with in vivo resolution of 156 × 156 μm^2 in plane and 300 or 500 μm in slice thickness, has been investigated by Laib et al [135]. These measures were compared with high-resolution μCT images (34 × 34 × 34 μm^3), and good correlation was found between the two sets of measurements, with the best $R^2 = 0.91$ for TbN.

The feasibility of using MR imaging at the resolution of 117 × 117 × 300 μm^3 to better predict mechanical properties was established by Majumdar et al [132] using a set of 94 specimens of several skeletal sites, with a wide range of bone densities and structures. Among several results reported in this study, it was shown that MR-based structural measures, used in conjunction with BMD (evaluated from quantitative CT measures), enhanced the prediction of bone strength. Using a stepwise regression model, including structural parameters in addition to BMD, resulted in an improvement of the prediction of the mean elastic modulus (evaluated from nondestructive testing). The adjusted correlation coefficient increased from 0.66 to 0.76 for all specimens, 0.71 to 0.82 for vertebral specimens, and 0.64 to 0.76 for femoral specimens.

MR imaging (117 × 117 × 300 μm^3) of vertebral midsagittal sections of lumbar vertebrae and standard morphological parameters were calculated by Beuf et al [101]. Ultimate stress was estimated in two perpendicular directions (horizontal/vertical) using compression testing applied to two cylindrical samples drilled in each vertebra close to the midsagittal section. All the morphologic parameters were correlated to horizontal and vertical ultimate stresses ($r > 0.8$, $P < 0.001$).

Link et al [136] used texture parameter measures on high-resolution MRI (156 × 156 × 300 μm^3) of proximal femur and spine specimens. Whereas the correlation between elastic modulus and BMD was $R^2 = 0.66$ for the spine specimens and $R^2 = 0.61$ for the femur specimens, a multivariate regression model that combined BMD and texture parameters increased the correlation to $R^2 = 0.83$ for spine and $R^2 = 0.72$ for femur.

In vivo, the skeletal sites most commonly imaged are the radius [130,137–142] and calcaneus [143–146]. The distal radius is a site with a large quantity of trabecular bone and is a common site for osteoporotic fractures. It is easily accessible with localized surface (detection) coils, and subjects are able to tolerate immobilization comfortably for the period required for high-resolution imaging. The calcaneus, although not a typical site for osteoporotic fractures, has been used with success to predict fracture at other sites, and this skeletal site is well adapted to high-resolution MR imaging. The phalanges recently have been of increased interest as a site for bone density measurement [147,148] and can be imaged by high-resolution MRI.

The image contrast can be manipulated in MR imaging based on the specific pulse sequence used, and the appearance of trabecular bone can be varied based on whether a spin-echo or gradient-echo sequence is used [149]. The high susceptibility difference between bone and marrow induces susceptibility artifacts at their boundary, which in the case of in vivo imaging could have a high impact on the bone structure quantification [149]. Although spin-echo images may be preferable to reduce this effect, gradient-echo images acquire an equivalent volume in considerably less time and can be exploited in vivo at several skeletal sites. By the optimization of the pulse sequence timing (short echo time) in gradient-echo imaging, one can attempt to minimize the susceptibility artifact. Fig. 15A shows a representative axial scan through the distal radius using a spin-echo–based method, whereas Fig. 15B shows a representative scan using a gradient-echo–based technique. The quantitative evaluation of structure from these images also constitutes a major area of research. The processing of high-resolution MR images generally consists of several stages [140]. Newitt et al [140] have shown that each stage must be standardized and normalized to ensure a high degree of reproducibility. In particular, these authors described a standardized analysis system with considerable reduction of human interaction. The efficiency of

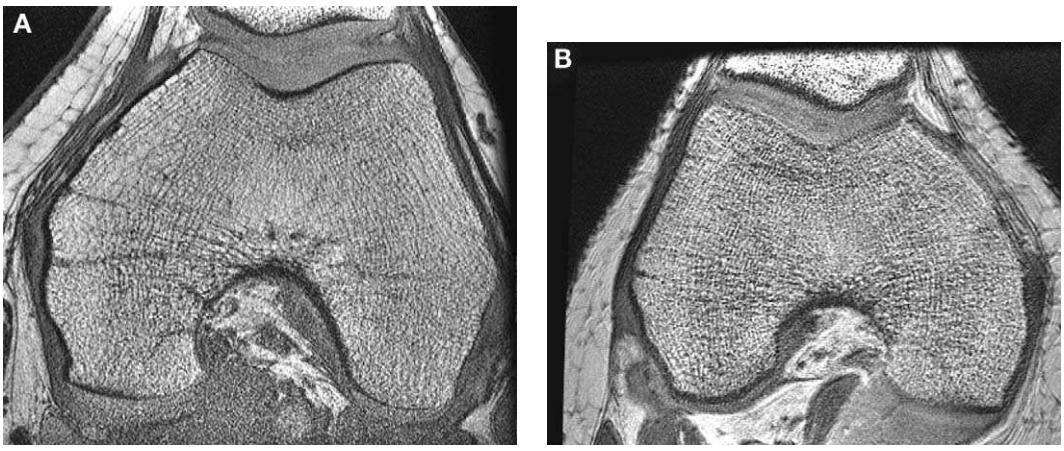

Fig. 16. Axial images through the distal femur at (*A*) 1.5 T and (*B*) 3 T. (Image obtained by David Newitt, UCSF, and Ann Shimakawa, GE Medical.) The spatial resolution is 195 × 195 × 1000 μm for both, and the imaging time at 3 T is half the time taken at 1.5 T.

this system was evaluated in terms of reproducibility (2%–4%) and has been applied successfully in several cross-sectional [139,146,150–152] and longitudinal studies [153,154].

Some noise reduction–based preprocessing techniques have been applied before the binarization stage, such as low pass filtering [137] or histogram deconvolution [155]. The use of some postprocessing schemes after the binarization, based on either morphologic criterion relative to the shape and morphology of the trabeculae [156] or topologic criterion relative to the numbers of bone and marrow components [157], have been applied. Wu et al [158] proposed a sophisticated histogram model taking into account the partial volume effect characterizing MR imaging using a probabilistic approach. Hwang et al [159] used spatial correlation analysis and deduced parameters such as intertrabecular spacing, contiguity, and tubularity. A combination of some of these parameters was predictive of the vertebral deformity [160].

More recently, distance transformation technique was applied to high-resolution in vivo MR imaging of the distal radius (156 × 156 × 500 μm^3) in postmenopausal women [161]. Morphology-based parameters were evaluated without assumption of any structure model, and the most significant parameter in distinguishing subjects with vertebral fracture (n = 88) from those without vertebral fracture (n = 60) was the intraindividual distribution of separation (standard deviation of the trabecular bone separation parameter). Using receiver operating curve analysis, the competence of this parameter was comparable to radius or spine BMD measures but was not as pertinent as the competence of hip BMD alone.

With the advent of higher field magnets for clinical imaging (Figs. 16,17) and computerized image processing, MR imaging promises to provide an important complement to standard methods of assessing osteoporosis and response to therapy. Slices can be obtained at a resolution of 195 × 195 × 1000 μm. With higher field, improved coils, there is potential for

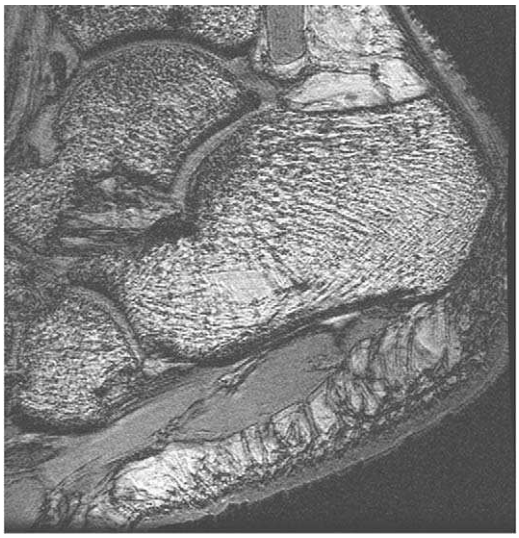

Fig. 17. A sagittal image through the calcaneus obtained at 195 × 195 × 500 μm at 3 T. (Image obtained by Ann Shimakawa, GE Medical.)

improving resolution, improving signal-to-noise ratio of the images, or reducing imaging time. Clearly with the proliferation of high field systems and further research in the area of imaging trabecular bone structure, optimized protocols will emerge.

Not only is the use of MR imaging an attractive alternative for assessing trabecular bone structure but also its potential for quantifying bone marrow composition [162–165] makes it an attractive modality for the comprehensive characterization of age-related or therapy-related metabolic changes in the skeleton.

Summary

Because osteoporotic fractures may be prevented, diagnostic techniques are essential in the assessment of osteoporosis. Conventional radiographs of the spine are not suited for diagnosing early osteoporosis, but they show fractures that may have no clinical symptoms. The radiologist should be aware of the enormous significance of these fractures for future osteoporotic fractures. Bone mass measurements are standard techniques in the diagnosis of osteoporosis, which are the basis of the WHO definition of osteoporosis. In this article the authors presented these standard techniques and newer diagnostic techniques that provide insights in the structure of trabecular bone.

References

[1] Consensus. Development, conference: diagnosis, prophylaxis, and treatment of osteoporosis. Am J Med 1993;94:646–50.
[2] NIH Consensus Development Panel on Osteoporosis Prevention and Therapy. Osteoporosis prevention, diagnosis, and therapy. JAMA 2001;285:785–95.
[3] NIH Consensus Statement Online. Osteoporosis prevention, diagnosis, and therapy. 2000;17:1–36.
[4] WHO. Technical report: assessment of fracture risk and its application to screening for postmenopausal osteoporosis. A report of a WHO study group. Geneva: World Health Organization; 1994.
[5] Melton L, Kan S, Frye M, Wahner H, O'Fallon W, Riggs B. Epidemiology of vertebral fractures in women. Am J Epidemiol 1989;129:1000–10.
[6] Max W, Sinnot P, Kao C, Sung H, Rice D. The burden of osteoporosis in California, 1998. Osteoporos Int 2002;13:493–500.
[7] Kannus P, Niemi S, Parkkari J. Hip fractures in Finland between 1970 and 1997 and predictions for the future. Lancet 1999;353:802–5.
[8] Willig R, Keinanen-Kiukaaniemi S, Jalovaara P. Mortality and quality of life after trochanteric hip fracture. Public Health 2001;115:323–7.
[9] Meunier P, Delmas P, Eastell R, et al. Diagnosis and management of osteoporosis in postmenopausal women: clinical guidelines. International Committee for Osteoporosis Clinical Guidelines 1999;21:1025–44.
[10] Riggs B, Melton LR. The worldwide problem of osteoporosis: insights afforded by epidemiology. Bone 1995;17:505S–11S.
[11] Nelson H, Humphrey L, Nygren P, Teutsch S, Allan J. Postmenopausal hormone replacement therapy: scientific review. JAMA 2002;288:872–81.
[12] Ensrud K, Thompson D, Cauley J, et al. Prevalent vertebral deformities predict mortality and hospitalization in older women with low bone mass: Fracture Intervention Trial Research Group. J Am Geriatr Soc 2000;48:241–9.
[13] Gehlbach S, Bigelow C, Heimisdottir M, May S, Walker M, Kirkwood J. Recognition of vertebral fracture in a clinical setting. Osteoporos Int 2000;11:577–82.
[14] Melton LR, Atkinson E, Cooper C, O'Fallon W, Riggs B. Vertebral fractures predict subsequent fractures. Osteoporos Int 1999;10:214–21.
[15] Lindsay R, Silverman S, Cooper C, et al. Risk of new vertebral fracture in the year following a fracture. JAMA 2001;285:320–3.
[16] Genant HK, Wu CY, van Kuijk C, Nevitt MC. Vertebral fracture assessment using a semiquantitative technique. J Bone Miner Res 1993;8:1137–48.
[17] Leidig-Bruckner G, Genant HK, Minne HW, et al. Comparison of a semiquantitative and a quantitative method for assessing vertebral fractures in osteoporosis. Bone 1994;15:437–42.
[18] Minne H, Leidig G, Wüster C, et al. A newly developed spine deformity index (SDI) to quantitate vertebral crush fractures in patients with osteoporosis. J Bone Miner Res 1988;3:335–49.
[19] Meunier P, Bressot C, Vignon E, et al. Radiological and histological evolution of post-menopausal osteoporosis treated with sodium fluoride-vitamin D-calcium: preliminary results. In: Baud C, editor. Fluoride and bone. Bern: Hans Huber Publishers; 1978. p. 263–76.
[20] Lachmann E, Whelan M. The roentgen diagnosis of osteoporosis and its limitations. Radiology 1936;26:165–77.
[21] Doyle F, Gutteridge D, Joplin G, Fraser R. An assessment of radiologic criteria used in the study of spinal osteoporosis. Br J Radiol 1967;40:241–50.
[22] Baur A, Stabler A, Bruning R, et al. Diffusion-weighted MR imaging of bone marrow: differentiation of benign versus pathologic compression fractures. Radiology 1998;207:349–56.
[23] Daldrup-Link HE, Rummeny EJ, Ihβen B, Kienast K, Link TM. Iron oxide enhanced MR imaging of bone marrow in patients with non-Hodgkin's lymphoma: differentiation of tumor infiltration and hypercellular bone marrow. Eur Radiol 2002;12:1557–66.

[24] Bogost G, Lizerbram E, Crues J. MR imaging in evaluation of suspected hip fracture: frequency of unsuspected bone and soft-tissue injury. Radiology 1995;197:263–7.
[25] Heuck F, Schmidt E. Die quantitative Bestimmung des Mineralgehalts des Knochens aus dem Röntgenbild. Fortschr Röntgenstr 1960;93:523–54.
[26] Rosholm A, Hyldstrup L, Backsgaard L, Grunkin M, Thodberg H. Estimation of bone mineral density by digital X-ray radiogrammetry: theoretical background and clinical testing. Osteoporos Int 2001;12:961–9.
[27] Bouxsein M, Palermo L, Yeung C, Black D. Digital X-ray radiogrammetry predicts hip, wrist and vertebral fracture risk in elderly women: a prospective analysis from the study of osteoporotic fractures. Osteoporos Int 2002;13:358–65.
[28] Vogel JM. Application principles and technical considerations in SPA. In: Genant HK, editor. Osteoporosis update 1987. San Francisco: Radiology Research and Education Foundation; 1987. p. 219–31.
[29] Mazess RB, Wahner HM. Nuclear medicine and densitometry. In: Melton LJI, editor. Osteoporosis: etiology, diagnosis, and management. New York: Raven Press; 1988. p. 251–95.
[30] Pacifici R, Rupich R, Vered I, et al. Dual energy radiography (DER): a preliminary comparative study. Calcif Tissue Int 1988;43:189–91.
[31] Mazess RB, Barden HS. Measurement of bone by dual-photon absorptiometry (DPA) and dual-energy x-ray absorptiometry (DEXA). Ann Chir Gyn 1988; 77:197–203.
[32] Borders J, Kerr E, Sartoris DJ, et al. Quantitative dual energy radiographic absorptiometry of the lumbar spine: *in vivo* comparison with dual-photon absorptiometry. Radiology 1989;170:129–31.
[33] Glüer CC, Steiger P, Selvidge R, Elliesen-Kliefoth K, Hayashi C, Genant HK. Comparative assessment of dual-photon-absorptiometry and dual-energy-radiography. Radiology 1990;174:223–8.
[34] Mazess RB, Collick B, Trempe J, Barden H, Hanson J. Performance evaluation of a dual energy x-ray bone densitometer. Calcif Tissue Int 1989;44:228–32.
[35] Larnach TA, Boyd SJ, Smart RC, Butler SP, Rohl PG, Diamond TH. Reproducibility of lateral spine scans using dual energy x-ray absorptiometry. Calcif Tissue Int 1992;51:255–8.
[36] Rupich R, Pacifici R, Griffin M, Vered I, Susman N, Avioli LV. Lateral dual energy radiography: a new method for measuring vertebral bone density. A preliminary study. J Clin Endocrinol Metab 1990;70: 1768–70.
[37] Rupich RC, Griffin MG, Pacifici R, Avioli LV, Susman N. Lateral dual-energy radiography: artifact error from rib and pelvic bone. J Bone Miner Res 1992;7: 97–101.
[38] Staron R, Greenspan R, Miller T, Bilezikian J, Shane E, Haramati N. Computerized bone densitometric analysis: operator-dependent errors. Radiology 1999; 211:467–70.
[39] Engelke K, Glüer CC, Genant HK. Factors influencing short-term precision of dual x-ray bone absorptiometry (DXA) of spine and femur. Calcif Tissue Int 1995;56:19–25.
[40] Theodorou D, Theodorou S. Dual-energy X-ray absorptiometry in clinical practice: application and interpretation of scans beyond the numbers. Clin Imaging 2002;26:43–9.
[41] Duboeuf F, Hans D, Schott A, et al. Different morphometric and densitometric parameters predict cervical and trochanteric hip fracture: the EPIDOS Study. J Bone Miner Res 1997;12:1895–902.
[42] Crabtree N, Lunt M, Holt G, et al. Hip geometry, bone mineral distribution, and bone strength in European men and women: the EPOS study. Bone 2000; 27:151–9.
[43] Reid I, Chin K, Evans M, Jones J. Relation between increase in length of hip axis in older women between 1950s and 1990s and increase in age specific rates of hip fracture. BMJ 1994;309:508–9.
[44] Peacock M, Turner C, Liu G, Manatunga A, Timmerman L, Johnston CJ. Better discrimination of hip fracture using bone density, geometry and architecture. Osteoporos Int 1995;5:167–73.
[45] Glüer CC, Cummings SR, Pressman A, et al. Prediction of hip fractures from pelvic radiographs: the study of osteoporotic fractures. J Bone Miner Res 1994;9:671–7.
[46] Faulkner KG, McClung M, Cummings SR. Automated evaluation of hip axis length for predicting hip fracture. J Bone Miner Res 1994;9:1065–70.
[47] Faulkner K, Genant H, McClung M. Bilateral comparison of femoral bone density and hip axis length from single and fan beam DXA scans. Calcif Tissue Int 1995;56:26–31.
[48] Bonnick S, Nichols D, Sanborn C, Payne S, Moen S, Heiss C. Right and left proximal femur analyses: is there a need to do both? Calcif Tissue Int 1996;58: 307–10.
[49] Fordham J, Chinn D, Kumar N. Identification of women with reduced bone density at the lumbar spine and femoral neck using BMD at the os calcis. Osteoporos Int 2000;11:797–802.
[50] Sweeney A, Malabanan A, Blake M, et al. Bone mineral density assessment: comparison of dual-energy X-ray absorptiometry measurements at the calcaneus, spine, and hip. J Clin Densitom 2002;5: 57–62.
[51] Kalender W, Brestowsky H, Felsenberg D. Bone mineral measurements: automated determination of the mitvertebral CT section. Radiology 1988;168: 219–21.
[52] Felsenberg D, Gowin W. Knochendichtemessung mit Zwei-Spektren-Methoden. Radiologe 1999;39: 186–93.
[53] Glüer C, Genant H. Impact of marrow fat in accuracy of quantitative CT. J Comput Assist Tomogr 1989;13: 1023–35.
[54] Genant HK, Boyd DP. Quantitative bone mineral

analysis using dual energy computed tomography. Invest Radiol 1977;12:545–51.
[55] Genant HK, Cann CE, Pozzi-Mucelli RS, Kanter AS. Vertebral mineral determination by quantitative computed tomography: clinical feasibility and normative data. J Comput Assist Tomogr 1983;7:554.
[56] Cann C, Genant H. Precise measurement of vertebral mineral content using computed tomography. J Comput Assist Tomogr 1980;4:493–500.
[57] Arnold B. Solid phantom for QCT bone mineral analysis. In: Proceedings of the 7th International Workshop on Bone Densitometry. Palm Springs, California, September 17–21, 1989.
[58] Kalender WA, Klotz E, Süss C. Vertebral bone mineral analysis: an integrated approach. Radiology 1987; 164:419–23.
[59] Kalender WA, Süss C. A new calibration phantom for quantitative computed tomography. Med Phys 1987; 9:816–9.
[60] Steiger P, Block J, Steiger S. Spinal bone mineral density measured with quantitative CT: effect of region of interest, vertebral level and techniques. Radiology 1990;175:537–43.
[61] Sandor T, Kalender WA, Hanlon WB, Weissman BN, Rumbaugh C. Spinal bone mineral determination using automated contour detection: application to single and dual-energy CT. SPIE Med Imaging Instrum 1985;555:188–94.
[62] Kalender W, Felsenberg D, Louis O, et al. Reference values for trabecular and cortical vertebral bone density in single and dual-energy quantitative computed tomography. Eur J Radiol 1989;9:75–80.
[63] Block J, Smith R, Glüer CC, Steiger P, Ettinger B, Genant HK. Models of spinal trabecular bone loss as determined by quantitative computed tomography. J Bone Miner Res 1989;4:249–57.
[64] Kalender W, Schmidt B, Zankl M, Schmidt M. A PC program for estimating organ dose and effective dose values in computed tomography. Eur Radiol 1999;9: 555–62.
[65] Lang T, Li J, Harris S, Genant H. Assessment of vertebral bone mineral density using volumetric quantitative CT. J Comput Assist Tomogr 1999;23: 130–7.
[66] Lang T, Keyak J, Heitz M, et al. Volumetric quantitative computed tomography of the proximal femur: precision and relation to bone strength. Bone 1997; 21:101–8.
[67] Butz S, Wüster C, Scheidt-Nave C, Götz M, Ziegler R. Forearm BMD as measured by peripheral quantitative computed tomography (pQCT) in a German reference population. Osteoporos Int 1994;4:179–84.
[68] Augat P, Fan B, Lane N, et al. Assessment of bone mineral at appendicular sites in females with fractures of the proximal femur. Bone 1998;22:395–402.
[69] Augat P, Fuerst T, Genant H. Quantitative bone mineral assessment at the forearm: a review. Osteoporos Int 1998;8:299–310.
[70] Grampp S, Genant H, Mathur A, et al. Comparisons of noninvasive bone mineral measurements in assessing age-related loss, fracture discrimination, and diagnostic classification. J Bone Miner Res 1997;12:697–711.
[71] Njeh CF, Boivin CM, Langton CM. The role of ultrasound in the assessment of osteoporosis: a review. Osteoporos Int 1997;7:7–22.
[72] Njeh CF, Richards A, Boivin CM, Hans D, Fuerst T, Genant HK. Factors influencing the speed of sound through the proximal phalanges. J Clin Densitom 1999;2:241–9.
[73] Njeh CF, Chen MB, Fan B, et al. Evaluation of a gel-coupled quantitative ultrasound device for bone status assessment. J Ultrasound Med 2001;20:1219–28.
[74] Njeh CF, Saeed I, Grigorian M, et al. Assessment of bone status using speed of sound at multiple anatomical sites. Ultrasound Med Biol 2001;27:1337–45.
[75] Fogelman I, Blake G. Different approaches to bone densitometry. J Nucl Med 2000;41:2015–25.
[76] Baran DT, Kelly AM, Karellas A, et al. Ultrasound attenuation of the os calcis in women with osteoporosis and hip fractures. Calcif Tissue Int 1988;43: 138–42.
[77] Bauer DC, Gluer CC, Genant HK, Stone K. Quantitative ultrasound and vertebral fracture in postmenopausal women: Fracture Intervention Trial Research Group. J Bone Miner Res 1995;10:353–8.
[78] Nicholson P, Bouxsein ML. Influence of temperature on ultrasonic properties of the calcaneus *in situ*. J Bone Miner Res 1999;14(Suppl 1):S498.
[79] Allgayer B, Flierdt E, Gumppenberg S, et al. NMR tomography compared to skeletal scintigraphy after traumatic vertebral body fractures. ROFO Fortschr Geb Rontgenstr Nuklearmed 1990;152:677–81.
[80] Wiener SN, Neumann DR, Rzeszotarski MS. Comparison of magnetic resonance imaging and radionuclide bone imaging of vertebral fractures. Clin Nucl Med 1989;14:666–70.
[81] Stabler A, Krimmel K, Seiderer M, Gartner C, Fritsch S, Raum W. [The nuclear magnetic resonance tomographic differentiation of osteoporotic and tumor-related vertebral fractures: the value of subtractive TR gradient-echo sequences, STIR sequences and Gd-DTPA.]. ROFO Fortschr Geb Rontgenstr Neuen Bildgeb Verfahr 1992;157:215–21.
[82] Davis CA, Genant HK, Dunham JS. The effects of bone on proton NMR relaxation times of surrounding liquids. Invest Radiol 1986;21:472–7.
[83] Rosenthal H, Thulborn KR, Rosenthal DI, Kim SH, Rosen BR. Magnetic susceptibility effects of trabecular bone on magnetic resonance imaging of bone marrow. Invest Radiol 1990;25:173–8.
[84] Majumdar S, Thomasson D, Shimakawa A, Genant HK. Quantitation of the susceptibility difference between trabecular bone and bone marrow: experimental studies. Magn Reson Med 1991;22:111–27.
[85] Ford JC, Wehrli FW, Chung HW. Magnetic field distribution in models of trabecular bone. Magn Res Med 1993;30:373–9.
[86] Brismar TB, Hindmarsh T, Ringertz H. Experimen-

tal correlation between T2* and ultimate compressive strength in lumbar porcine vertebrae. Acad Radiol 1997;4:426–30.

[87] Brismar TB, Karlsson M, Li T, Ringertz H. The correlation between R2' and bone mineral measurements in human vertebrae: an *in vitro* study. Eur Radiol 1999;9:141–4.

[88] Kang C, Paley M, Ordidge R, Speller R. R'2 measured in trabecular bone *in vitro*: relationship to trabecular separation. Magn Res Imaging 1999;17: 989–95.

[89] Takahashi M, Wehrli FW, Hwang SN, Wehrli SL. Relationship between cancellous bone induced magnetic field and ultrastructure in a rat ovariectomy model. Magn Res Imaging 2000;18:33–9.

[90] Majumdar S, Genant HK. *In vivo* relationship between marrow T2* and trabecular bone density determined with a chemical shift-selective asymmetric spin-echo sequence. J Magn Reson Imaging 1992;2: 209–19.

[91] Wehrli FW, Ford JC, Attie M, Kressel HY, Kaplan FS. Trabecular structure: preliminary application of MR interferometry. Radiology 1991;179:615–21.

[92] Ford JC, Wehrli FW. *In vivo* quantitative characterization of trabecular bone by NMR interferometry and localized proton spectroscopy. Magn Reson Med 1991;17:543–51.

[93] Sugimoto H, Kimura T, Ohsawa T. Susceptibility effects of bone trabeculae: quantification *in vivo* using an asymmetric spin-echo technique. Invest Radiol 1993;28:208–13.

[94] Fransson A, Grampp S, Imhof H. Effects of trabecular bone on marrow relaxation in the tibia. Magn Reson Imaging 1999;17:69–82.

[95] Majumdar S. Quantitative study of the susceptibility difference between trabecular bone and bone marrow: computer simulations. Magn Reson Med 1991;22: 101–10.

[96] Engelke K, Majumdar S, Genant HK. Phantom studies simulating the impact of trabecular structure on marrow relaxation time, T2'. Magn Reson Med 1994;31: 384–7.

[97] Selby K, Majumdar S, Newitt DC, Genant HK. Investigation of MR decay rates in microphantom models of trabecular bone. J Magn Reson Imaging 1996;6:549–59.

[98] Yablonskiy DA, Reinus WR, Stark H, Haacke EM. Quantitation of T2' anisotropic effects on magnetic resonance bone mineral density measurement. Magn Reson Med 1997;37:214–21.

[99] Jergas MD, Majumdar S, Keyak JH, et al. Relationships between young modulus of elasticity, ash density, and MRI derived effective transverse relaxation T2* in tibial specimens. J Comput Assist Tomogr 1995;19:472–9.

[100] Chung H, Wehrli FW, Williams JL, Kugelmass SD. Relationship between NMR transverse relaxation, trabecular bone architecture, and strength. Proc Natl Acad Sci USA 1993;90:10250–4.

[101] Beuf O, Newitt DC, Mosekilde L, Majumdar S. Trabecular structure assessment in lumbar vertebrae specimens using quantitative magnetic resonance imaging and relationship with mechanical competence. J Bone Miner Res 2001;16:1511–9.

[102] Sebag GH, Moore SG. Effect of trabecular bone on the appearance of marrow in gradient echo imaging of the appendicular skeleton. Radiology 1990; 174(3 Pt 1):855–9.

[103] Majumdar S, Thomasson D, Shimakawa A, Genant HK. Quantitation of the susceptibility difference between trabecular bone and bone marrow: experimental studies. Magn Reson Med 1991;22:111–27.

[104] Guglielmi G, Selby K, Blunt BA, et al. Magnetic resonance imaging of the calcaneus: preliminary assessment of trabecular bone-dependent regional variations in marrow relaxation time compared with dual X-ray absorptiometry. Acad Radiol 1996;3:336–43.

[105] Link TM, Majumdar S, Augat P, et al. Proximal femur: assessment for osteoporosis with T2* decay characteristics at MR imaging. Radiology 1998;209: 531–6.

[106] Wehrli FW, Hopkins JA, Hwang SN, Song HK, Snyder PJ, Haddad JG. Cross-sectional study of osteopenia with quantitative MR imaging and bone densitometry. Radiology 2000;217:527–38.

[107] Majumdar S, Link T, Ouyang J, et al. Fractal analysis of radiographs: comparison of techniques and correlation with BMD and biomechanics. J Bone Miner Res 1997;12(Suppl):S264.

[108] Ouyang X, Majumdar S, Link TM, et al. Morphometric texture analysis of spinal trabecular bone structure assessed using orthogonal radiographic projections. Med Phys 1998;25:2037–45.

[109] Majumdar S, Lin J, Link T, et al. Fractal analysis of radiographs: Assessment of trabecular bone structure and prediction of elastic modulus and strength. Med Phys 1999;26:1330–40.

[110] Lin JC, Grampp S, Link T, et al. Fractal analysis of proximal femur radiographs: correlation with biomechanical properties and bone mineral density. Osteoporos Int 1999;9:516–24.

[111] Millard J, Augat P, Link TM, et al. Power spectral analysis of trabecular bone structure from radiographs: correlation with bone mineral density and biomechanics. Calcif Tissue Int 1998;63:482–9.

[112] Majumdar S, Link TM, Millard J, et al. *In vivo* assessment of trabecular bone structure using fractal analysis of distal radius radiographs. Med Phys 2000;27: 2594–9.

[113] Caligiuri P, Giger ML, Favus M. Multifractal radiographic analysis of osteoporosis. Med Phys 1994;21: 503–8.

[114] Caligiuri PC, Giger ML, Favus M, Jia H, Doi K, Dixon L. Computerized texture analysis of bone radiographs for the evaluation of osteoporosis. Presented at the 9th International Workshop of Bone Density. Traverse City, MI, September 26–30, 1992.

[115] Caligiuri P, Giger M, Favus M, Jia H, Doi K, Dixon L.

Computerized radiographic analysis of osteoporosis: preliminary evaluation. Radiology 1993;186: 471–4.

[116] Buckland-Wright JC, Lynch JA, Rymer J, Fogelman I. Fractal signature analysis of macroradiographs measures trabecular organization in lumbar vertebrae of postmenopausal women. Calcif Tissue Int 1994;54: 106–12.

[117] Link TM, Majumdar S, Konermann W, Meier N, Lin JC, Newitt D, et al. Texture analysis of direct magnification radiographs: correlation with bone mineral density and biomechanical properties. Academic Radiology 1997;4:167–76.

[118] Veenland J, Link T, Konermann W, Meier N, Grashuis J, Gelsema E. Unraveling the role of structure and density in determining vertebral bone strength. Calcified Tissue Int 1997;61:474–9.

[119] Lespessailes E, Benhamou CL, Touliere D, et al. Fractal evaluation of trabecular bone microarchitecture of calcaneus: study of reproducibility. J Bone Miner Res 1993;8(Suppl 1):264.

[120] Lespessailles E, Jacquet G, Harba R, et al. Anisotropy measurements obtained by fractal analysis of trabecular bone at the calcaneus and radius. Rev Rhum 1996;63:337–43.

[121] Lespessailles E, Eynard E, Royant V, et al. Fractal evaluation of trabecular bone texture from calcaneus radiographs in corticosteroid induced bone changes. Seattle: American Society for Bone and Mineral Research; 1996.

[122] Pothuaud L, Lespessailles E, Harba R, et al. Fractal analysis of trabecular bone texture on radiographs: discriminant value in post menopausal osteoporosis. Osteoporos Int 1998;8:618–25.

[123] Gluer CC, Wu CY, Genant HK. Broadband ultrasound attenuation signals depend on trabecular orientation: an in-vitro study. Osteoporos Int 1993;3:185–91.

[124] Hans D, Wu C, Njeh CF, et al. Ultrasound velocity of trabecular cubes reflects mainly bone density and elasticity. Calcif Tissue Int 1999;64:18–23.

[125] Muller R, Hahn M, Vogel M, Delling G, Ruegsegger P. Morphometric analysis of non-invasively assessed biopsies: comparisons of high resolution QCT and histologic sections. Presented at the 24th International Sun Valley Workshop on Hard Tissue Biology. Sun Valley, Idaho, August 2–6, 1993.

[126] Muller R, Hildebrand T, Ruegsegger P. Non-invasive bone biopsy: a new method to analyze and display three dimensional structure of trabecular bone. Phys Med Biol 1994;39:145–64.

[127] Muller R, Hahn M, Vogel M, Delling G, Ruegsegger P. Morphometric analysis of non-invasively assessed bone biopsies: comparison of high resolution computed tomography and histologic sections. Bone 1996;8:215–20.

[128] Muller R, Hildebrand T, Hauselmann HJ, Ruesegger P. *In vivo* reproducibility of three-dimensional structural properties of noninvasive bone biopsies using 3D-pQCT. J Bone Miner Res 1996;11:1745–50.

[129] Hipp JA, Jansujwicz A, Simmons CA, Snyder B. Trabecular bone morphology using micro-magnetic resonance imaging. J Bone Miner Res 1996;11:286–97.

[130] Majumdar S, Newitt D, Mathur A, et al. Magnetic resonance imaging of trabecular bone structure in the distal radius: relationship with X-ray tomographic microscopy and biomechanics. Osteoporos Int 1996; 6:376–85.

[131] Kothari M, Chen T, Lin J, Newitt D, Majumdar S, Genant H. Three dimensional bone architecture assessment: impact of image resolution. Osteoporos Int 1997;7:289.

[132] Majumdar S, Kothari M, Augat P, et al. High-resolution magnetic resonance imaging: three-dimensional trabecular bone architecture and biomechanical properties. Bone 1998;22:445–54.

[133] Vieth V, Link TM, Lotter A, et al. Does the trabecular bone structure depicted by high-resolution MRI of the calcaneus reflect the true bone structure? Invest Radiol 2001;36:210–7.

[134] Lin JC, Amling M, Newitt DC, et al. Heterogeneity of trabecular bone structure in the calcaneus using magnetic resonance imaging. Osteoporos Int 1998; 8:16–24.

[135] Laib A, Beuf O, Issever A, Newitt DC, Majumdar S. Direct measures of trabecular bone architecture from MR images. Adv Exp Med Biol 2001;496:37–46.

[136] Link TM, Majumdar S, Lin JC, et al. A comparative study of trabecular bone properties in the spine and femur using high resolution MRI and CT. J Bone Miner Res 1998;13:122–32.

[137] Majumdar S, Genant HK, Grampp S, Jergas MD, Newitt DC, Gies AA. Analysis of trabecular bone structure in the distal radius using high resolution MRI. Eur Radiol 1994;4:517–24.

[138] Majumdar S, Genant HK, Grampp S, et al. Correlation of trabecular bone structure with age, bone mineral density, and osteoporotic status: *in vivo* studies in the distal radius using high resolution magnetic resonance imaging. J Bone Miner Res 1997;12:111–8.

[139] Majumdar S, Link TM, Augat P, et al. Trabecular bone architecture in the distal radius using magnetic resonance imaging in subjects with fractures of the proximal femur. Osteoporos Int 1999;10:231–9.

[140] Newitt DC, Van Rietbergen B, Majumdar S. Processing and analysis of *in vivo* high resolution MR images of trabecular bone for longitudinal studies: reproducibility of structural measures and micro-finite element analysis derived mechanical properties. Osteoporos Int 2002;13:278–87.

[141] Newitt DC, Majumdar S, Van Rietbergen B, et al. *In vivo* assessment of architecture and micro-finite element analysis derived indices of mechanical properties of trabecular bone in the radius. Osteoporos Int 2002;13:6–13.

[142] Saha PK, Gomberg BR, Wehrli FW. Three-dimensional digital topological characterization of cancellous bone architecture. Int J Imag Syst Tech 2000;11: 81–90.

[143] Newitt DC, Lin JC, Wald LL, Majumdar S, Vigneron DB. High resolution MRI of the human calcaneus *in vivo* using phased array surface coils. In: Proceedings of the 4th Annual Meeting of the ISMRM. New York, April 27–May 3, 1996.

[144] Engelke K, Hahn M, Takada M, et al. Structural analysis of high resolution MR images of the calcaneus compared to histomorphometry. Seattle: American Society of Bone Mineral Research; 1996.

[145] Link T, Majumdar S, Augat P, Lin J, Newitt D, Genant H. Can texture analysis of high resolution MR-images of the calcaneus be used to differentiate post-menopausal patients with and without osteoporotic fractures? Osteoporos Int 1997;7:271.

[146] Link TM, Majumdar S, Augat P, et al. *In vivo* high resolution MRI of the calcaneus: differences in trabecular structure in osteoporosis patients. J Bone Miner Res 1998;13:1175–82.

[147] Kuehn B, Stampa B, Heller M, Glueer C. *In vivo* assessment of trabecular bone structure of the human phalanges using high resolution magnetic resonance imaging. Osteoporos Int 1997;7:291.

[148] Jara H, Wehrli FW, Chung H, Ford JC. High-resolution variable flip angle 3D MR imaging of trabecular microstructure *in vivo*. Magn Reson Med 1993;29: 528–39.

[149] Majumdar S, Newitt D, Jergas M, et al. Evaluation of technical factors affecting the quantification of trabecular bone structure using magnetic resonance imaging. Bone 1995;17:417–30.

[150] Link TM, Lotter A, Beyer F, et al. Changes in calcaneal trabecular bone structure after heart transplantation: an MR imaging study. Radiology 2000;217: 855–62.

[151] van Rietbergen B, Majumdar S, Pistoia W, et al. Assessment of cancellous bone mechanical properties from micro-FE models based on micro-CT, pQCT and MR images. Technol Health Care 1998;6(5–6): 413–20.

[152] Pothuaud L, Newitt DC, Majumdar S. Trabecular bone microarchitecture derived from high-resolution MRI of the ultradistal radius: relationship to osteoporotic status. Presented at the 23rd Annual Meeting of the ASBMR. Phoenix, October 12–16, 2001.

[153] van Rietbergen B, Majumdar S, Newitt DC, MacDonald B. High-resolution MRI and micro-FE for the evaluation of changes in calcaneal bone mechanical properties in postmenopausal women after one year of idoxifene treatment. Presented at the 47th Annual Meeting of ORS. San Francisco, February 25–28, 2001.

[154] Pothuaud L, Newitt DC, Chesnut C, Genant HK, MacDonald B, Majumdar S. New descriptors of trabecular bone microarchitecture: an *in vivo* longitudinal study using magnetic resonance imaging. Presented at the 23rd Annual Meeting of the ASBMR. Phoenix, October 12–16, 2001.

[155] Hwang SN, Wehrli FW. Estimating voxel volume fractions of trabecular bone on the basis of magnetic resonance images acquired *in vivo*. Int J Imaging Syst Technol 1999;10:186–98.

[156] Antoniadis T, Scarpelli JP, Ruaud JP, Gonord P, Guillot G. Bone labelling on micro-magnetic resonance images. Med Image Anal 1999;3:119–28.

[157] Pothuaud L, Porion P, Levitz P, Benhamou CL. 3D thresholding of trabecular bone images obtained by magnetic resonance imaging: effect of the threshold value on the 3D microarchitecture. Presented at the 20th Annual Meeting of the ASBMR. Toronto, September 22–26, 2000.

[158] Wu Z, Chung HW, Wehrli FW. A Bayesian approach to subvoxel tissue classification in NMR microscopic images of trabecular bone. Magn Reson Med 1994; 31:302–8.

[159] Hwang SN, Wehrli FW, Williams JL. Probability-based structural parameters from three-dimensional nuclear magnetic resonance images as predictors of trabecular bone strength. Med Phys 1997;24: 1255–61.

[160] Wehrli FW, Hwang SN, Ma J, Song HK, Ford JC, Haddad JG. Cancellous bone volume and structure in the forearm: noninvasive assessment with MR microimaging and image processing. Radiology 1998; 206:347–57 [Erratum appears in Radiology 1998; 207:833].

[161] Laib A, Newitt DC, Lu Y, Majumdar S. New model-independent measures of trabecular bone structure applied to *in vivo* high-resolution MR images. Osteoporos Int 2002;13:130–6.

[162] Ballon D, Jakubowski A, Gabrilove J, et al. *In vivo* measurements of bone marrow cellularity using volume-localized proton NMR spectroscopy. Magn Reson Med 1991;19:85–95.

[163] Derby K, Kramer DM, Kaufman L. A technique for assessment of bone marrow composition using magnetic resonance phase interference at low field. Magn Reson Med 1993;29:465–9.

[164] Hermann G, Shapiro RS, Abdelwahab IF, Grabowski G. MR imaging in adults with Gaucher disease type I: evaluation of marrow involvement and disease activity. Skeletal Radiol 1993;22:247–51.

[165] Ishizaka H, Tomiyoshi K, Matsumoto M. MR quantification of bone marrow cellularity: use of chemical-shift misregistration artifact. AJR Am J Radiol 1993; 160:572–4.

RADIOLOGIC
CLINICS OF
NORTH AMERICA

Radiol Clin N Am 41 (2003) 841–856

Current uses of ultrasound in the evaluation of the breast

Tejas S. Mehta, MD, MPH

Department of Radiology, Beth Israel Deaconess Medical Center, 330 Brookline Avenue, Boston, MA 02215, USA

Breast ultrasound is used routinely as an adjunct to mammography to help differentiate benign from malignant lesions. In patients younger than 30 years of age or patients who are pregnant, ultrasound may be the first or sole imaging modality to evaluate for breast pathology. Other less common uses of breast ultrasound include potential staging of breast cancer and evaluating breast implants. Ultrasound is useful in guiding interventional breast procedures. Although still controversial, some studies have advocated using ultrasound for screening for breast carcinoma in asymptomatic women [1–3]. This article reviews the multiple current uses of ultrasound in the evaluation of the breast.

Technique

Breast ultrasound should be performed using a high-frequency transducer of 7.5 MHz or higher. A linear array transducer is preferred. A standoff pad may be used to evaluate superficial lesions. The patient should be placed in a supine or oblique position, with ipsilateral arm above the head. The breast is scanned in either the transverse and sagittal planes or the radial and antiradial planes. The retroareolar area is evaluated by angling the transducer in multiple planes to avoid shadowing artifact produced by the nipple. Focal zone placement should be optimized and gain settings adjusted so that the fat in the breast appears gray. If a lesion is present, it should be imaged in two planes, and the location should be noted by clock face position on the breast and distance from the nipple.

Improper technique of breast imaging can result in improper interpretation of breast lesions. The Mammography Quality Standards Act passed by congress in 1992 oversees aspects of screening mammography [4]. Although there are no such laws for breast ultrasound, the American College of Radiology has guidelines for imaging the breast with sonography [5]. One study [6] reviewed 152 breast ultrasounds performed at 86 sites and found that 60.5% did not comply with at least one of the American College of Radiology guidelines. Some of these errors in compliance resulted in misinterpretation of normal breast tissue as a mass, classic benign lesions as indeterminate, and cancers as benign lesions [6].

Several recent studies have used relatively new sonographic techniques of spatial compound imaging [7], tissue harmonics imaging [8], and three-dimensional imaging [9–11] in the evaluation of breast disease. Compound imaging of the breast has been shown to increase lesion conspicuity by enhancing soft tissue contrast, improving the definition of tumor margins, and improving evaluation of the internal architecture and surrounding distortion. A potential disadvantage of compound imaging is that it decreases acoustic shadowing [7]. No study has evaluated if these improvements affect sensitivity and specificity of breast ultrasound. In the author's department, conventional and compound imaging techniques are used in scanning the breast, because it is easy to switch from one technique to the other.

A study that evaluated 73 breast lesions (25 cysts, 36 solid lesions, and 12 indeterminate lesions) with tissue harmonics imaging found that it was significantly preferred for lesion conspicuity and overall image quality [8]. The study did not address whether this improved the accuracy of ultrasound in diagnosing breast lesions, however.

E-mail address: tmehta@bidmc.harvard.edu

0033-8389/03/$ – see front matter © 2003 Elsevier Inc. All rights reserved.
doi:10.1016/S0033-8389(03)00040-X

Another study that compared two-dimensional to three-dimensional ultrasound found that three-dimensional ultrasound had a higher specificity (64.1% by two-dimensional imaging compared with 86.9% by three-dimensional imaging) for diagnosing malignancy [11]. The researchers evaluated 186 solid nodules and used three-dimensional ultrasound to examine the peripheral tissues of the lesion. Depending on the pattern of peripheral tissue, all lesions were placed into two groups. When hyperechoic bands of surrounding fibrous tissue appeared to be pushed smoothly aside from the central image, it was defined as a "compressive pattern." When thick hyperechoic bands converged according to a stellar pattern, toward a hyperechoic, irregular rim that surrounded a hypoechoic central core of a mass, it was defined as a "converging pattern." The researchers concluded that a compressive pattern on three-dimensional ultrasound provided an additional argument to alleviate biopsy for a lesion with a low index of suspicion on two-dimensional ultrasound; however, if a lesion had suspicious features on two-dimensional imaging, regardless of the three-dimensional results, intervention was warranted. Three-dimensional imaging is cumbersome and time consuming. In the author's department, where all patients are scanned real-time by the radiologist, three-dimensional imaging has been found to be of little diagnostic value.

Normal breast anatomy

The skin is seen as an echogenic layer that measures up to 3 mm in thickness. Deep to the skin is breast tissue, which has different appearances depending on the overall density of the breast and the distribution of fatty and fibroglandular tissue. Unlike other areas of the body, fat within the breast is hypoechoic. The dense breast tissue is echogenic on ultrasound (Fig. 1). Solid masses are usually hypoechoic, and caution should be made not to mistake an island of fat surrounded by dense breast tissue for a solid mass. Shadowing from Coopers ligaments can be seen; however, this does not persist with compression or change in scanning plane and should not be mistaken for pathology.

Gray-scale sonographic evaluation of the breast

Cystic lesions

Ultrasound is 96% to 100% accurate in the diagnosis of cysts [12–15]. In the 1970s, ultrasound decreased the number of biopsies for benign masses 25% to 35% by reliably identifying simple cysts [15,16]. A simple cyst is defined as a thin-walled anechoic lesion with sharp anterior and posterior borders and posterior acoustic enhancement (Fig. 2). Reverberation artifact can result in linear internal echoes at the anterior part of a cyst [15]. A proposed breast ultrasound lexicon [17] suggests that if a cyst does not meet all of these criteria, it should be classified as either "complicated" or "complex." A "complicated" cyst has multiple low-level internal echoes but other features of a simple cyst (Fig. 3). One study that evaluated 308 such lesions with ultrasound found a malignancy rate of 0.3%, which is lower that the 2% for a Breast Imaging Reporting and Data System (BI-RADS) 3, probably benign [18] lesion, which suggests that such lesions can be managed with follow-up imaging studies instead of intervention [19]. In contrast, a "complex" cystic mass has suspicious features, such as a mural nodule, thick septations, or a

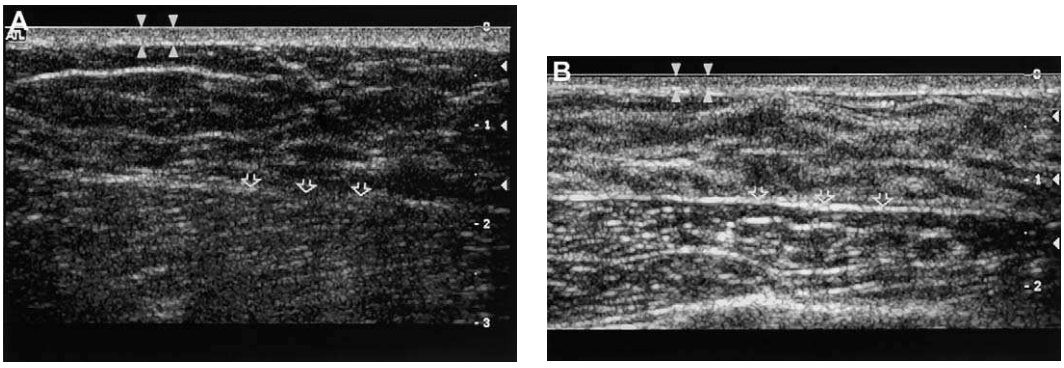

Fig. 1. Normal breast ultrasound. Arrowheads denote normal skin, and open arrows denote the interface between the breast tissue and pectoralis muscles in a diffusely fatty (*A*) and diffusely dense (*B*) breast.

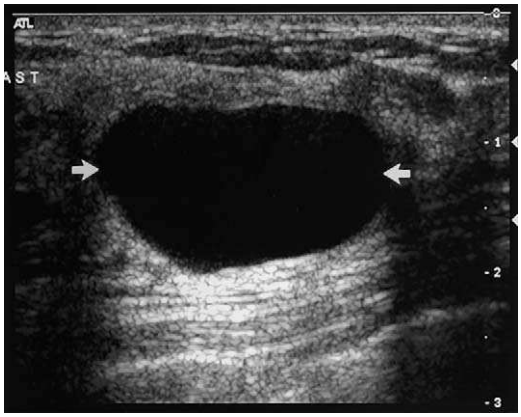

Fig. 2. Simple cyst. Arrows mark a breast lesion that meets all the criteria for a simple cyst. It is anechoic with a thin wall and enhanced through transmission.

thick or irregular wall (Fig. 4). ''Complex'' cystic lesions should be classified as BI-RADS 4, suspicious, and require aspiration or biopsy [17].

When aspiration is performed, if a lesion does not resolve to completion, biopsy of the remaining component should be considered to exclude malignancy. When an aspirate is bloody, fluid also should be sent to cytology, and subsequent biopsy may be necessary to exclude malignancy. Intracystic carcinomas are rare and account for less than 1% of breast cancers [20]. They are usually papillary carcinomas. The differential diagnosis includes intracystic papillomas, necrotic solid tumor, and cysts with adherent blood clot/debris. Other cystic lesions that can have a ''complicated'' or ''complex'' appearance include abscesses and hematomas. Often the clinical history is pertinent in making such diagnoses and guiding management of these lesions (Fig. 5).

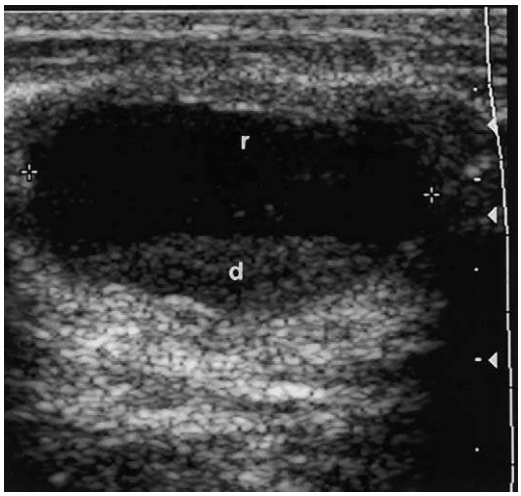

Fig. 3. Complicated cyst. Calipers mark a ''complicated'' cyst with debris (d) at its dependent portion and reverberation artifact (r) anteriorly. This cyst was aspirated with ultrasound guidance for symptomatic relief to complete resolution.

Solid lesions

In addition to distinguishing cysts from solid masses, a major advance in gray-scale ultrasound has been the ability to help differentiate benign from malignant solid lesions. Several studies have shown that the addition of ultrasound to mammography can reduce the number of biopsies for benign solid lesions [21–24].

A landmark study by Stavros et al [22] classified 750 solid lesions as benign, indeterminate, or malignant based on sonographic appearances. Malignant features included spiculations, angular margins, marked hypoechogenicity, shadowing, presence of calcifications, duct extension, microlobulation, and a branching pattern. If a lesion had any of these features, it was classified as malignant. A lesion was classified as benign if it lacked all malignant features and was intensely or uniformly hyperechoic, or ellipsoid in shape with a thin, echogenic capsule, or had two to three gentle lobulations and a thin, echogenic capsule. Indeterminate lesions were ones that did not meet criteria for malignancy or benignity. Based on this classification scheme, the authors reported a sensitiv-

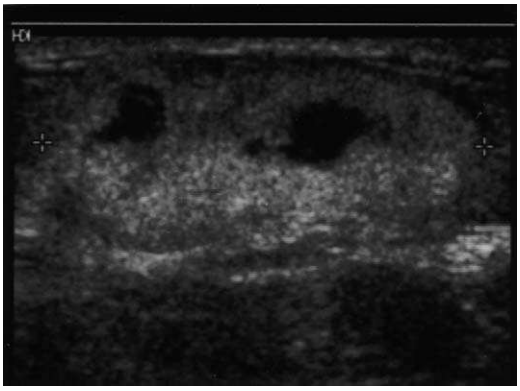

Fig. 5. Breast hematoma. Calipers mark a heterogeneous, predominantly echogenic mass with multiple internal hypoechoic and anechoic cystic spaces. This patient presented a few days after a severe motor vehicle accident with a palpable lump and area of ecchymosis on the breast. Sonographic and clinical findings suggested presence of hematoma. Follow-up showed this area to resolve completely in 2 months.

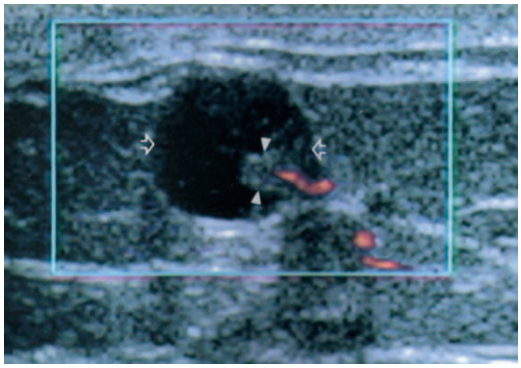

Fig. 4. Complex cyst. Ultrasound demonstrates a "complex" cyst (*open arrows*) with soft tissue mass (*arrowheads*) with internal power Doppler flow. Pathology revealed an intraductal papilloma.

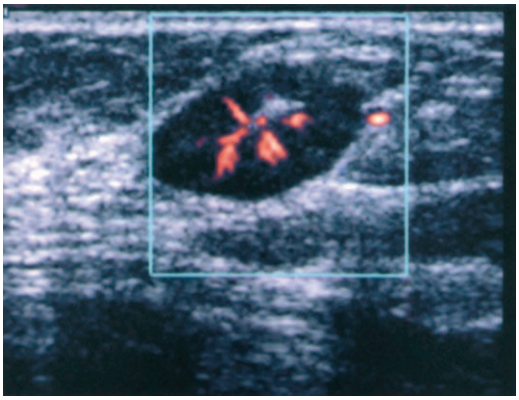

Fig. 14. Inflammatory lymph node. Ultrasound of the axillary tail of the breast, performed for a newly palpable and mammographically enlarging nodule, shows a hypoechoic lymph node with small amount of fatty hilum and typical branching vessels on power Doppler. Histology from excisional biopsy revealed an inflammatory lymph node.

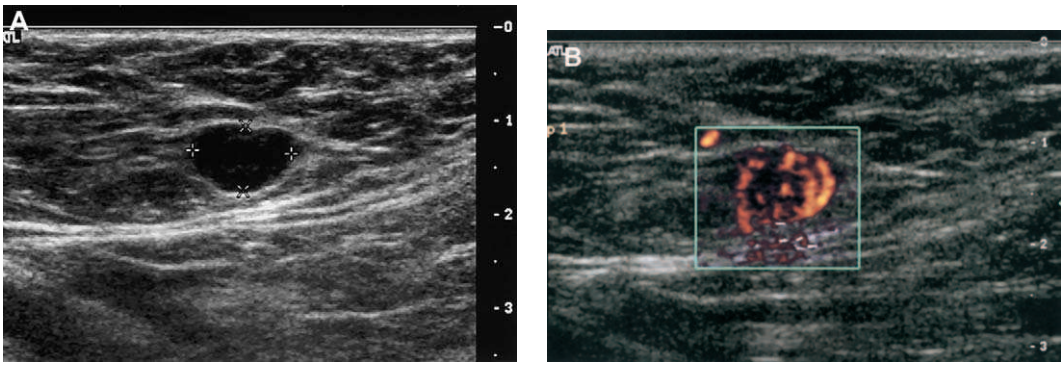

Fig. 12. Use of power Doppler to increase specificity for malignancy. (*A*) Gray-scale ultrasound of a palpable abnormality in a 28-year-old woman shows a relatively benign appearing nodule (calipers). (*B*) Power Doppler ultrasound shows hypervascularity with multiple penetrating vessels. Histology from ultrasound-guided core biopsy revealed infiltrating ductal carcinoma.

ity rate of 98.4% and negative predictive value (NPV) of 99.5% [22].

Stavros et al have been criticized for including in their study masses that by standard mammographic criteria should not have been biopsied [25]. Zonderland et al [24] used criteria similar to Stavros et al and classified lesions into five categories (benign, probably benign, equivocal, probably malignant, and malignant) based on mammography and combination of mammography and ultrasound. In their study, for patients who underwent mammography and ultrasound, the addition of ultrasound increased sensitivity from 86% to 95% and specificity from 89% to 92%. Ultrasound increased diagnostic accuracy by diagnosing 25 additional cancers out of the 338 total cancers in their study population (7.4%) [24].

Skaane et al [21] examined 142 fibroadenomas and 194 invasive ductal carcinomas with respect to shape, contour, echotexture, echogenicity, sound transmission, and surrounding tissues and found NPV of 100% for palpable tumors and NPV of 96% for nonpalpable tumors, if strict criteria were applied. They found that a thin echogenic pseudocapsule was a feature most predictive of benignity. Irregular shape and contour, extensive hypoechogenicity, shadowing, echogenic halo, and distortion of the surrounding tissue were highly predictive of malignancy [21].

In a study by Rahbar et al, three radiologists each reviewed 162 solid masses [26]. Characteristics evaluated included shape, margins, width-anteroposterior dimension ratio, echotexture, echogenicity, posterior echo intensity, presence/absence of pseudocapsule, edge refraction, and calcifications. They found that if the three most reliable criteria were strictly applied, the overall cancer biopsy yield would have increased from 23% to 39%. They also found false-negative interpretations in 4 of 38 (10.5%) cancers by at least one of the three reviewers, however. A high interobserver variability for evaluating sonographic features of tumors also has been reported by other researchers [27].

Common features of some benign and malignant solid lesions

Infiltrating ductal carcinoma not otherwise specified is the most common breast cancer [28]. This cancer classically appears as an irregularly shaped hypoechoic mass with shadowing and distortion of the surrounding tissues (Fig. 6). Infiltrating lobular carcinoma, which comprises 7% to 10% of all breast cancers [29,30], invades the breast tissue in a single-file pattern without a desmoplastic reaction, which potentially makes it harder to detect on imaging. Up to 12% of cancers may not be seen on ultrasound, and up to 15% of those seen may present with only vague shadowing without a mass (Fig. 7) [2,31]. Medullary carcinoma, although uncommon, can appear as a well-defined solid mass with posterior acoustic enhancement and be mistaken for a benign lesion on ultrasound [26,32]. Although ductal carcinoma in situ typically is seen as isolated microcalcifications on mammography, 6% to 10% can be seen as a solid mass on ultrasound [33,34].

Inflammatory breast cancer typically produces nonspecific skin thickening on ultrasound. This thickening unfortunately is indistinguishable from other causes of skin thickening, including infectious causes, such as mastitis. The presence of an abscess favors an infectious etiology.

Metastases to the breast are rare and can occur via lymphatic or hematogenous spread [35]. Metastases that occur via lymphatic spread can be indistinguish-

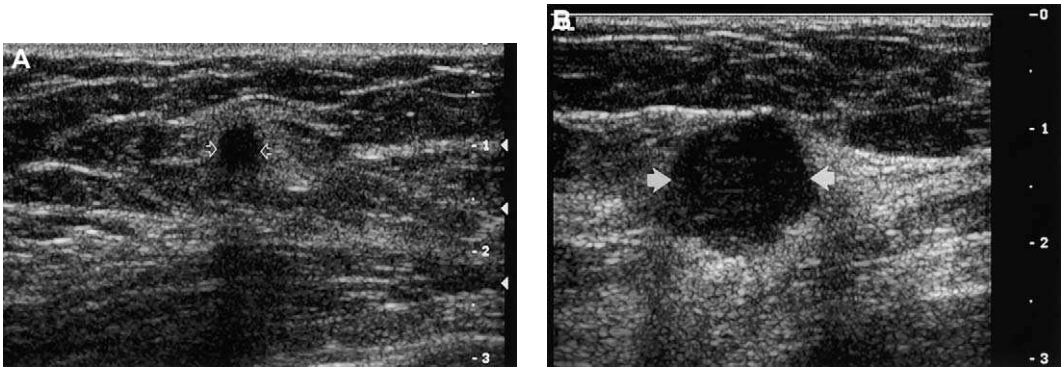

Fig. 6. Infiltrating ductal carcinoma. (*A*) Open arrows mark a 4-mm irregular, hypoechoic mass with shadowing. (*B*) In another patient, arrows mark a 1-cm microlobulated hypoechoic mass with mild posterior acoustic enhancement. Both lesions had histology of infiltrating ductal carcinoma.

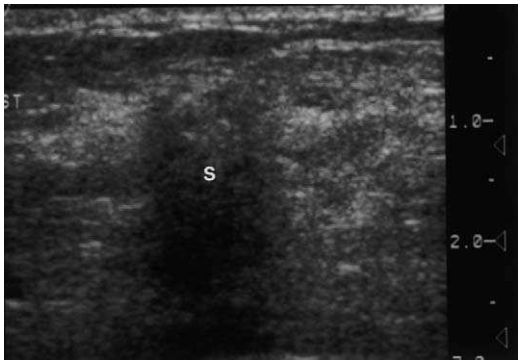

Fig. 7. Infiltrating lobular carcinoma. Ultrasound shows a 1-cm area of shadowing (s) with distortion of the surrounding tissues but no discrete mass. Histology revealed infiltrating lobular carcinoma.

able from inflammatory breast carcinoma [36]. Causes of hematogenous metastases to the breast include lymphoma, leukemia, melanoma, and lung cancer. Many cases of metastatic disease to the breast present as multiple breast masses that involve one or both breasts [36,37].

Sometimes it can be difficult to distinguish between architectural distortion that is caused by malignancy from architectural distortion that is caused by scar in an area of prior surgery [38]. When the architectural distortion can be tracked through the breast to the skin scar, postoperative scar tissue is the more likely diagnosis (Fig. 8).

Fibroadenomas are some of the more common benign solid lesions seen on breast ultrasound. They typically are ovoid in shape, with their long axis

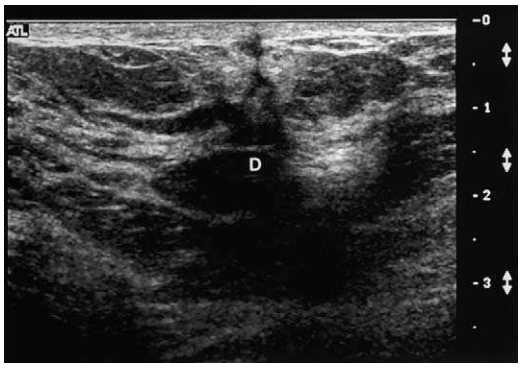

Fig. 8. Scar tissue. Ultrasound of an area prior to surgery was performed because of change on clinical examination. There is a large area of hypoechoic architectural distortion (D) with spiculations extending to the skin surface (*arrows*). Patient underwent excisional biopsy based on clinical grounds. Histology revealed no evidence of malignancy.

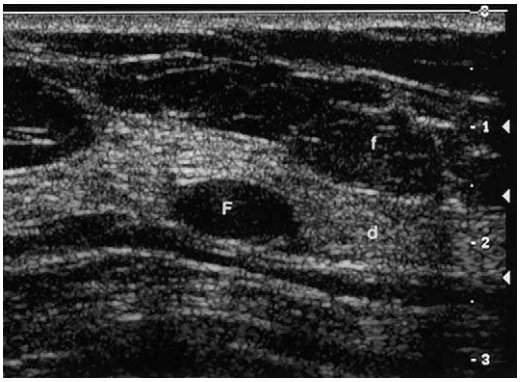

Fig. 9. Fibroadenoma. Ultrasound shows an ovoid, well-circumscribed nodule (F) isoechoic to the fatty breast tissue (f) surrounded by dense breast tissue (d). Ultrasound-guided core biopsy was performed, and histology revealed fibroadenoma.

parallel to the chest wall, and they have a thin, echogenic capsule (Fig. 9). They can have a few macrolobulations and demonstrate posterior acoustic enhancement. They are similar in echogenicity to the fatty parenchyma and may be difficult to see sonographically in a fatty breast. When they calcify, the macrocalcifications can obscure borders and cause shadowing that results in a ''suspicious'' appearance on ultrasound. Correlation with mammographic findings, which are typical, should prevent further evaluation or intervention of such lesions.

Hyperechogenicity is a reliable predictor for benignity but is seen in only 2% of masses [26]. Fat necrosis can have a variable appearance on ultrasound, including a focal hyperechoic nodule (Fig. 10), echogenic nodule with central lucency, possible associated

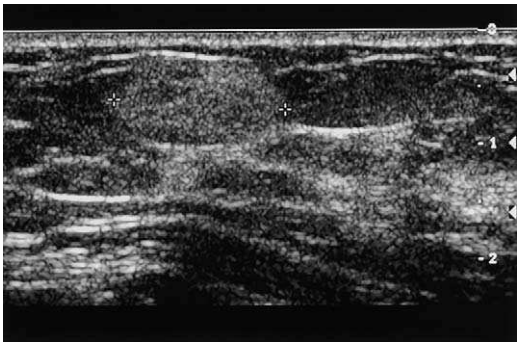

Fig. 10. Fat necrosis. Calipers mark a hyperechoic, palpable nodule excised for clinical reasons, with pathology showing fat necrosis.

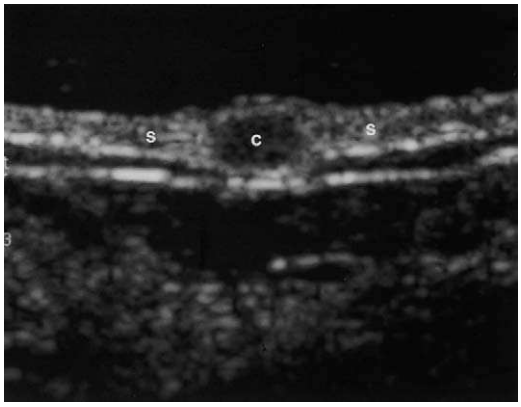

Fig. 11. Sebaceous cyst. Ultrasound with standoff pad shows a hypoechoic lesion (c) with the skin layer (s) consistent with a sebaceous cyst.

calcifications, and it can progress to have cystic spaces within it.

Ultrasound also can be used to determine whether a palpable or mammographically detected lesion is within the skin as opposed to within the underlying superficial breast tissue. A sebaceous cyst (Fig. 11) is a common skin lesion seen while evaluating the breast. Once intradermal location is documented, no further imaging or intervention is necessary (unless required for symptoms of infection).

Doppler imaging of benign and malignant lesions

Non–contrast-enhanced Doppler ultrasound

Although gray-scale sonographic features are useful in distinguishing benign from malignant solid breast lesions, a significant number of breast masses do not present with the typical expected sonographic appearance [39–41]. Angiogenesis is defined as the formation of new blood vessels through the sprouting of capillaries from preexisting microvessels [42]. The formation of these new, abnormal vessels is associated with an increased risk of malignancy [43]. These concepts of angiogenesis have led researchers to assess the use of Doppler ultrasound in distinguishing benign from malignant solid masses.

In 1988, Schoenberger et al [44] studied 38 patients with pulsed duplex Doppler and reported 100% sensitivity and specificity rates for predicting malignancy. Since then, advances in technology and equipment have led to detection of Doppler flow in many solid lesions, including 14% to 60% of benign lesions and 65% to 98% of malignant lesions [45–53]. Studies that evaluated the number of detectable vessels showed a significantly higher number of vessels in cancers than in benign lesions [54–57]. Raza et al [46] characterized patterns of vascularity by Power Doppler ultrasound in 86 solid breast masses as none, peripheral, central, and penetrating. They found that the addition of Power Doppler to gray-scale evaluation increased the sensitivity rate from 92% to 100% and NPV from 95% to 100% (Fig. 12). In their study, as in others [45,52,58], penetrating vessels were more likely to be present in malignant tumors. Although Doppler findings cannot be used to determine histology, pure invasive lobular carcinomas are less likely to have Doppler detectable vessels compared with invasive carcinomas with ductal features [33,46,59].

Contrast-enhanced Doppler ultrasound

A few studies have assessed the role of contrast-enhanced Doppler in helping distinguish benign from malignant breast lesions [54,60–62] and evaluating breast cancer patients suspected of having recurrent disease [63]. Currently, however, the use of contrast-enhancement breast ultrasound is experimental.

Kedar et al [54] studied 34 patients (18 with cancer and 16 with various benign lesions) before and after contrast enhancement. They found that the appearance on contrast-enhanced ultrasound changed the diagnosis in 4 patients, which increased the sensitivity rate from 88.9%, specificity rate from 87.5%, and accuracy rate from 88.2%, all to 100%. They found differences in enhancement, number of new detectable vessels, and duration of enhancement between cancers and benign lesions.

Huber et al [61] performed contrast-enhanced ultrasound in 47 patients (31 with cancer and 16 with benign lesions) and found that cancers typically had early and marked enhancement followed by marked decline of color pixel density, whereas benign lesions had later enhancement. Given complexity of some time-color pixel density curves, however, contrast-enhanced Doppler assessment was of ‘‘limited value for prospective diagnosis’’ [61]. Two other studies [60,62] showed no role for contrast-enhanced Doppler to improve accuracy in distinguishing benign from malignant lesions.

Winehouse et al [63] evaluated contrast-enhanced color Doppler imaging in 58 patients suspected of having breast cancer recurrence. They reported a sensitivity rate of 94% and specificity rate of 67% with contrast enhancement. In their study, contrast enhancement increased diagnostic accuracy from 80% to 90%.

Staging

Tumor size and grade

Ultrasound cannot assess the size of a tumor accurately and usually underestimates the true size [64]. Ultrasound also cannot assess tumor grade accurately [33,47,59,65]. One study found that high-grade invasive ductal carcinomas were significantly larger at time of diagnosis, however, and were more likely to have better-defined margins and acoustic enhancement compared with low- and intermediate-grade tumors [66]. Some researchers believe that the enhancement is caused by increased tumor cellularity [67,68], whereas others believe that the organization of the tissue in the tumor—and not the absolute amount of fibrous tissue within the tumor—determines the enhancement characteristics [69].

Nodal involvement: assessment of the axilla

Lymph node status is an important prognostic indicator of survival in patients with breast cancer [70,71]. Axillary node dissection is responsible for much of the morbidity associated with breast surgery [72–74]. Sentinel node biopsy can predict the presence or absence of nodal metastases; however, success rates have varied depending on patient age, location of the primary cancer, and surgical technique [75]. A patient with a T1 lesion who undergoes nodal dissection has an 80% chance of having no nodal involvement, and a patient with a T2 lesion has a 65% chance of no nodal involvement [76,77].

Clinical examination is not a reliable method for assessing nodal status and shows false-negative rates as high as 50% [78,79]. Various studies have examined the role of axillary sonography in assessing nodal status [78,80,81]. On ultrasound, lymph nodes that have a prominent echogenic fatty hilum with thin, uniform, homogeneous hypoechoic cortex are believed to be "benign" (Fig. 13A). Lymph nodes that have little to no fatty hilum and are predominantly hypoechoic, inhomogeneous, or enlarged are believed to be "suspicious" (Fig. 13B) [81].

Verbanck et al [78] performed axillary ultrasound on 144 breast cancer patients. In their population, in which the prevalence of lymph node involvement was 55.3%, they found ultrasound to have a sensitivity rate of 92%, specificity rate of 95%, positive predictive value of 96%, and NPV of 91% in detecting malignant nodes. Vaidya et al [80] performed axillary ultrasound on 200 breast cancer patients. They found that ultrasound had a specificity rate and positive predictive value of 90%. When combined with clinical examination, the sensitivity rate and NPV were 82% and 76%, respectively. In the subset of younger women, the sensitivity rate and NPV were even higher, at 91% and 89%, respectively. They concluded that "Using clinical exam and ultrasound to avoid axillary dissection in some patients is feasible."

Yang et al [82] performed color Doppler axillary ultrasound on 81 women with breast cancer and 106 asymptomatic women. They found color Doppler flow in 84% of normal nodes and 88% of metastatic nodes in patients with breast cancer and 87% of normal nodes in asymptomatic women. The presence of color Doppler flow is highly nonspecific as a criterion for malignancy. There is no method to distinguish Doppler flow in malignant nodes from inflammatory nodes (Fig. 14) [83,84].

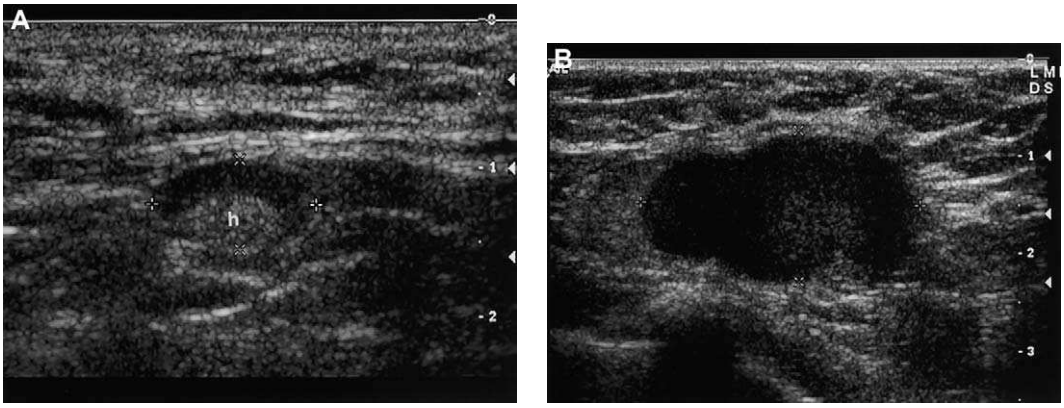

Fig. 13. Lymph nodes. (*A*) Calipers mark a benign axillary lymph node with echogenic, fatty hilum (h). (*B*) Calipers mark highly suspicious, enlarged lymph node with no fatty hilum in a patient with breast cancer.

Nodal involvement: assessment of the primary cancer

Several studies have evaluated the role of Doppler flow in the primary breast carcinoma in assessing nodal status [33,47,48,85–87]. One study that used Power Doppler found that although many breast cancers demonstrated flow with Power Doppler, patients with cancers in whom vessels were not detectable were unlikely to have lymph node involvement (NPV, 90%) [33]. Lee et al [48] used color Doppler to study 32 breast cancers and found a significant association between higher tumor flow and nodal metastases for T1 lesions (≤ 2 cm) but not for larger lesions. Holcombe et al [86] studied color Doppler flow in 28 breast cancers and found that when three or more vessels were seen on color Doppler, the patients were more likely to have lymph node involvement.

Screening ultrasound in patients with known breast cancer

Evaluation of mastectomy specimens has shown additional malignant foci in 30% to 63% of patients believed to have unifocal breast cancer by clinical and mammography evaluation [88,89]. Three studies [90–92] evaluated a cumulative total of 391 patients with known breast cancer or high suspicion of breast cancer. Using whole breast(s) ultrasound, they found one or more additional cancers in 55 of 391 (14%) patients. Management was altered in 47 of these 55 women (12% of total of 391 women). Based on these studies, some researchers advocate routinely scanning the ipsilateral or both breasts when an index lesion is seen. Others continue to scan only the region of interest. Some patients who have multifocal cancer and have only been scanned in the region of interest may escape detection because they are treated with post-lumpectomy irradiation. Other patients may present later with "recurrent" or "new" breast cancer lesions that actually were present but undiagnosed previously.

Ultrasound-guided procedures

Fine needle aspiration biopsy and core needle biopsy

Assuming a lesion can be seen, there are certain advantages to performing aspiration, biopsy, or localization with ultrasound guidance. The lesion can be visualized at all times during sampling, which ensures accurate needle placement. The procedure is easier for the patient, who can be supine to slightly oblique versus upright or prone for mammographic or stereotactic procedures. There is no radiation, which is particularly important to pregnant patients.

Fine needle aspiration biopsy in breast tumors was first reported by Fornage et al [93] in 1987. The success rate is variable, however, and it requires adequate sampling using proper technique and proper handling of the specimen. It also depends on the experience of the cytopathologist [94–96]. In the proper setting, fine needle aspiration biopsy can have a high sensitivity rate of 95% and NPV of 98% [97]. In the study by Fornage et al, in which one radiologist obtained all 1136 specimens, there were 27 (2%) inadequate samples. Of these, 14 occurred in the first 150 samples and 13 in the subsequent 986 samples. These results highlight the point that there is a "learning curve" to the technique of performing fine needle aspiration biopsy [97].

In 1993, Parker et al [98] reported the use of core-needle biopsy of the breast using real-time ultrasound. They used a 14-gauge needle and reported 100% accuracy after sampling 132 lesions, with no complications. The following year, Parker et al [99] performed a larger, multi-institutional study that evaluated the results of core-needle biopsy in 6152 lesions, performed with sonographic or stereotactic guidance. They reported a cancer miss rate of 1.2% to 1.5% (depending on the inclusion or exclusion of mammary intraepithelial neoplasia, respectively) but also pointed out that "surgical excisional biopsy is not perfect" either. In this larger study, there was a 0.2% rate of clinically significant complications.

The results of these studies and others [100,101] have led to the routine use of ultrasound in guiding for core-needle biopsy (Fig. 15A) and preoperative needle location (Fig. 15B) of breast lesions.

Intraoperative ultrasound guidance

Intraoperative ultrasound, when performed by trained individuals, is another method of localizing breast lesions. Harlow et al [102] used intraoperative ultrasound to excise 65 breast cancers and reported achieving negative excision margins at first operation in 97%. They point out certain advantages of intraoperative ultrasound compared with preoperative needle location. The advantages include improved patient comfort, more optimal choice of location of incision, and ability to evaluate the specimen and surgical bed such that if the lesion is found close to margin, reexcision could be performed immediately at time of initial operation.

Moore et al [103] evaluated 51 patients who underwent lumpectomy for palpable breast cancer, 27 of whom had intraoperative ultrasound and 24 of

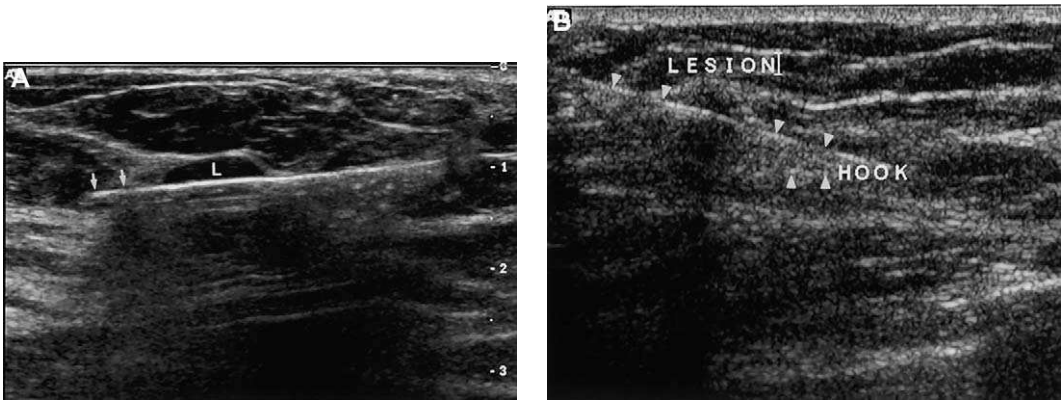

Fig. 15. Ultrasound-guided procedures. (*A*) Core needle biopsy shows the biopsy needle (tip marked by *arrows*) through the lesion (L) being sampled. (*B*) Preoperative wire localization shows the hook wire (*arrowheads*) to be through the lesion to be excised.

whom did not. They found surgical accuracy and margin status to be improved with intraoperative ultrasound. They also reported no significant change in operating room cost or length of total surgery time. Smith et al [104] used intraoperative ultrasound to assist in the excision of 81 lesions, including 25 cancers and 56 benign lesions. They reported 100% accuracy of intraoperative ultrasound to localize the lesions and 96% accuracy in predicting margins of the carcinomas.

Microcalcifications on ultrasound

Thirty-five percent to 45% of nonpalpable breast cancers detected at screening present as clusters of microcalcifications on mammography [105]. With higher frequency transducers, we are more able to detect mammographically isolated microcalcifications with ultrasound (Figs. 16A, B). One study examined 76 patients with 7.5 MHz and 10 MHz transducers and found increased visibility of microcalcifications from 45% to 74% in benign breast lesions and 91% to 97% in malignant lesions [106]. The ability of ultrasound to identify microcalcifications more often when associated with a mass also has been reported by other authors [22,107,108]. The hypoechogenicity of the underlying mass provides more contrast for detection of the echogenic nonshadowing foci that are the microcalcifications (Fig. 16C). Although ultrasound cannot be used to distinguish benign from malignant microcalcifications definitively, when the microcalcifications are seen associated with a mass on ultrasound (even if isolated on mammography), there is a higher incidence of invasive cancer [22,108].

Yang et al [109] examined 89 breast cancers with high-resolution ultrasound and found it to be 95% sensitive and 91% accurate for detection of microcalcifications. Gufler et al [107] examined 49 clusters of microcalcifications seen on mammography and found ultrasound to have an overall sensitivity rate of 75%, with 66.6% sensitivity rate for detection of benign lesions and 100% detection of malignant in situ and invasive cancers. Teh et al [110] used high-frequency ultrasound and Power Doppler to visualize and biopsy microcalcifications in 37 patients. They found the presence of Power Doppler flow helpful in directing successful biopsy in eight cases (including benign and malignant lesions).

Screening for breast cancer

Mammography is the only widely accepted imaging modality used to screen for early, otherwise occult breast cancers. Many lesions are indistinguishable by mammography. Three older studies reported a cumulative total of 236 incidental sonographically detected lesions and found none to be malignant based on either biopsy or long-term follow-up [13,111,112]. More recent studies have shown that incidental cancers are detected with sonography performed in asymptomatic patients and in patients being scanned for benign and malignant disease [1,3,22,97,113].

Buchberger et al [1] performed ultrasounds on 6113 asymptomatic patients with dense breasts on mammography and found 23 malignancies in 21 patients seen on ultrasound only. Of another 687 patients scanned because of palpable or mammographic abnormalities, ultrasound found 5 additional cancers, 3 in

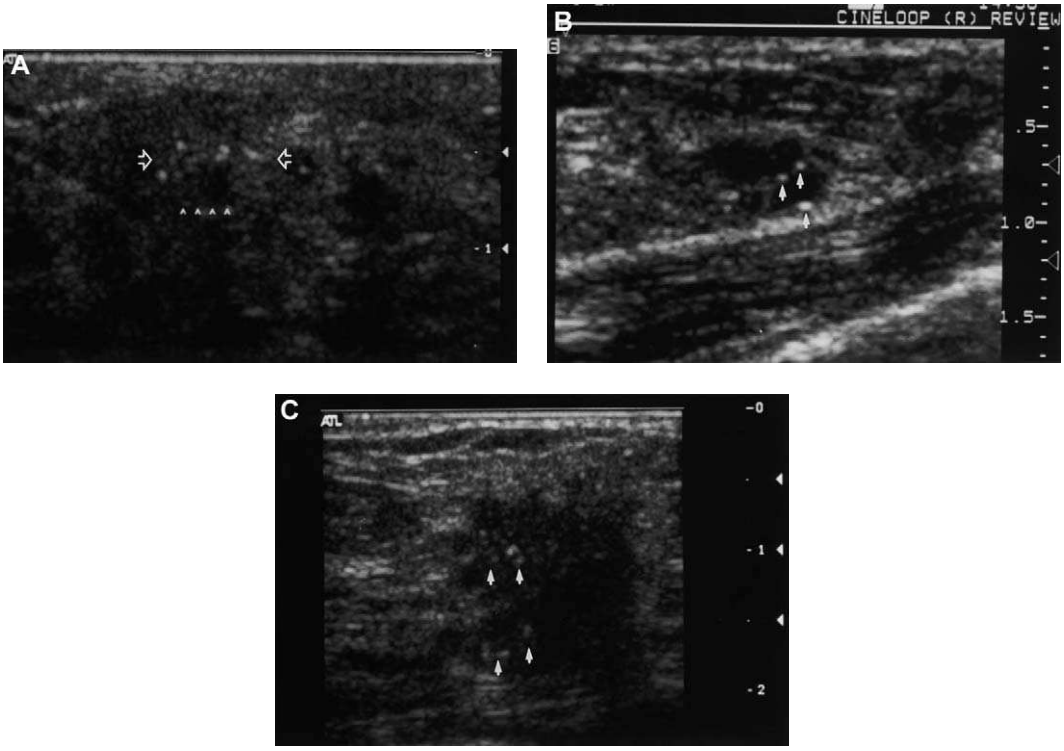

Fig. 16. Microcalcifications. (*A*) Screening mammogram (not shown) revealed an area of pleomorphic microcalcifications without associated mass. Ultrasound of this region shows multiple tiny echogenic foci (*open arrows*) that correspond to the microcalcifications seen mammographically. Ultrasound-guided core biopsy was performed, with specimen radiograph demonstrating microcalcifications. Histology revealed high-grade ductal carcinoma in situ. (*B*) Another patient had multiple more diffuse microcalcifications on mammography (not shown). Ultrasound that was performed for a lump was negative for the area of clinical concern. Sonographic evaluation of the area of mammographic microcalcifications was performed. It showed tiny echogenic foci (*arrows*) adjacent to small anechoic cysts consistent with microcalcifications within microcysts. Although no histologic diagnosis is available, these have been stable mammographically for more than 2 years. (*C*) Ultrasound in another patient shows a suspicious hypoechoic mass with tiny echogenic foci (*arrows*) within it. Histology revealed infiltrating ductal carcinoma.

women with malignant index lesions and 2 in women with benign index lesions. Gordon et al [113] scanned 12,706 women with palpable or mammographic abnormalities and found 44 additional cancers detected with ultrasound only. These cancers were in 30 women, 15 with malignant index lesions and 15 with benign index lesions. Kolb et al [3] performed 3626 ultrasounds in asymptomatic women with dense breasts on mammography and found an additional 11 cancers seen only on ultrasound.

There is no current dispute that if ultrasound is performed, incidental cancers will be found. The controversies lie in weighing the benefits against the cost and assessing whether detection of these otherwise occult cancers will result in increased patient survival. In addition to the incidentally found cancers, in three studies [1,3,113] ultrasound detected an additional 2088 benign lesions, some of which were followed and others that were biopsied. The added ''cost'' (of performing the test, potentially increasing patient anxiety and discomfort, and potentially increasing morbidity from increased number of biopsies) must be weighed against the benefits of finding these sonographically detected cancers. The only way to determine the true independent contribution of ultrasound to breast cancer screening is to perform a randomized, blinded, controlled trial with death as an endpoint [114].

Breast implants

MR imaging currently is more sensitive and accurate than ultrasound at evaluating silicone implants for rupture [115]. When MR imaging is not readily available or if it cannot be performed (because of claustro-

phobia, internal metallic clips, or other causes), ultrasound is an alternative. An intact implant, without rupture, appears anechoic with echogenic wall anteriorly on ultrasound [116]. Implant ruptures can be classified as ''intracapsular'' or ''extracapsular,'' the former having an intact fibrous capsule and the latter having a ruptured fibrous capsule. Both of these types of ruptures must be distinguished from a ''gel bleed,'' which results from leakage of silicone through the prosthetic shell without a tear in the shell.

DeBruhl et al [117] described the ''stepladder sign,'' in which multiple horizontal echogenic lines are seen within the lumen of the implant (Fig. 17). This is the term commonly used to describe intracapsular rupture. On ultrasound, this sign also can be seen in patients with heavy silicone gel bleed and in patients with severe capsular contractures, in which the fibrous capsule compresses an intact implant and produces infolding of the implant shell. In these cases, ultrasound results in a false-positive diagnosis of intracapsular rupture [117–119].

Harris et al [120] described the ''snowstorm sign'' in cases of extracapsular rupture. There is increased reverberation from leakage of silicone coming into contact with the surrounding tissues. Their study found that 100% of patients who had this sign had extracapsular rupture; however, it was only seen in 23% of patients with rupture and thus had a low sensitivity rate. More subtle signs of extracapsular rupture include focal extracapsular echogenic masses.

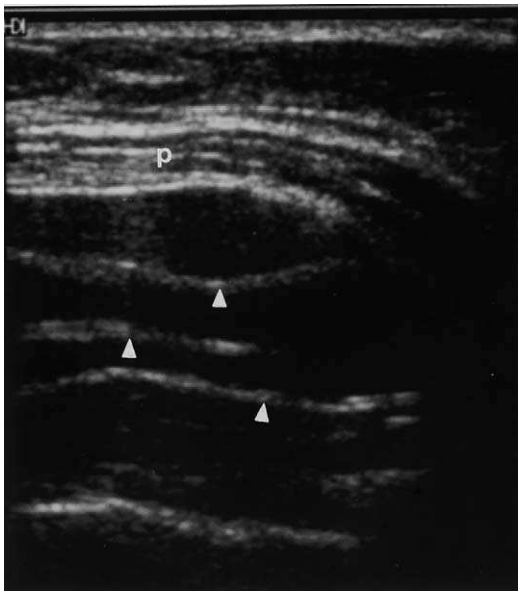

Fig. 17. Implant. Ultrasound shows a subpectoral implant (P, pectoralis muscle) with ''stepladder sign'' (*arrowheads*). Surgery revealed an intracapsular rupture.

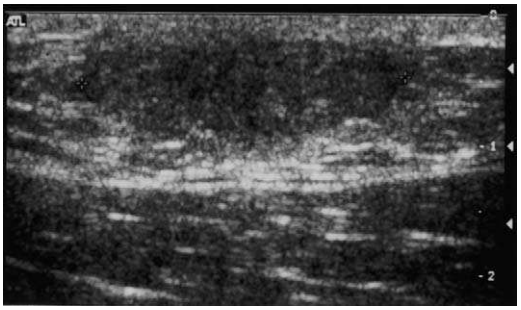

Fig. 18. Gynecomastia. Calipers mark an area of asymmetric breast tissue in a man who presented with a lump and breast pain. Sonographic findings, interpreted in conjunction with mammographic findings (not shown), led to the diagnosis of gynecomastia.

Venta et al [119] evaluated 236 implants with sonography. They found that abnormal sonographic findings were present in intact implants, many of these caused by ultrasound's inability to distinguish prominent folds from rupture. They also reported that a normal ultrasound was highly predictive of an intact implant, however, with NPV of 91%.

The male breast

Breast cancer in men is rare. It represents 1% of all breast cancers and only 1% of all malignancies in men [121]. Ultrasound has been used to evaluate the male breast [122,123]. There is an overlap in appearance of benign and malignant diseases using mammography and ultrasound individually; however, the combination of these modalities is believed to improve accuracy. A common benign breast condition in men is gynecomastia. Men with this condition usually present with symptoms of a lump or pain. On ultrasound, this can appear as subareolar hypoechogenic or hyperechoic fibroglandular tissue (Fig. 18).

Summary

Ultrasound is an important imaging modality in evaluating the breast. One of the most common uses of ultrasound is to help distinguish benign from malignant breast disease, primarily with gray-scale ultrasound but also with Doppler ultrasound. Another common use is to provide guidance for interventional procedures. Less common uses include assisting in

staging of breast cancer and evaluating patients with implants. Recently there has been an interest in using ultrasound to screen asymptomatic women for breast cancer, as is done with mammography. Further studies must be performed to assess if this reduces mortality from breast cancer. Although primarily used to image the female breast, ultrasound also can be used to evaluate breast-related concerns in men. Uses of contrast-enhanced ultrasound are still experimental and would add an invasive component to an otherwise noninvasive study.

References

[1] Buchberger W, DeKoekkoek-Doll P, Springer P, Obrist P, Dunser M. Incidental findings on sonography of the breast: clinical significance and diagnostic workup. AJR Am J Roentgenol 1999;173:921–7.

[2] Butler RS, Venta LA, Wiley EL, Gliss RL, Dempsey PJ, Rubin E. Sonographic evaluation of infiltrating lobular carcinoma. AJR Am J Roentgenol 1999;172: 325–30.

[3] Kolb TM, Lichy J, Newhouse JH. Occult cancer in women with dense breasts: detection with screening US-diagnostic yield and tumor characteristics. Radiology 1998;207:191–9.

[4] Mammography Quality Standards Act of 1992. Pub L No. 102–539. 1992.

[5] American College of Radiology. American College of Radiology standards. Reston (VA): American College of Radiology; 2002.

[6] Baker JA, Soo MS. Breast US: assessment of technical quality and image interpretation. Radiology 2002; 223:229–38.

[7] Entrekin RR, Porter BA, Sillesen HH, Wong AD, Cooperberg PL, Fix CH. Real-time spatial compound imaging: application to breast, vascular, and musculoskeletal ultrasound. Semin Ultrasound CT MR 2001; 22:50–64.

[8] Rosen EL, Soo MS. Tissue harmonic imaging sonography of breast lesions: improved margin analysis, conspicuity, and image quality compared to conventional ultrasound. Clin Imaging 2001;25:379–84.

[9] Downey DD, Fenster A, Williams JC. Clinical utility of three-dimensional US. Radiographics 2000;20: 559–71.

[10] Huber S, Wagner M, Medl M, Czembirek H. Real-time spatial compound imaging in breast ultrasound. Ultrasound Med Biol 2002;28:155–63.

[11] Rotten D, Levaillant JM, Zerat L. Analysis of normal breast tissue and of solid breast masses using three-dimensional ultrasound mammography. Ultrasound Obstet Gynecol 1999;14:114–24.

[12] Jellins J, Kossoff G, Reeve TS. Detection and classification of liquid-filled masses in the breast by gray scale echography. Radiology 1977;125:205–12.

[13] Sickles EA, Filly RA, Callen PW. Benign breast lesions: ultrasound detection and diagnosis. Radiology 1984;151:467–70.

[14] Egan RL, Egan KL. Automated water-path full-breast sonography: correlation with histology in 176 solid lesions. AJR Am J Roentgenol 1984;143:499–507.

[15] Hilton SW, Leopold GR, Olson LK, Willson SA. Real-time breast sonography: application in 300 consecutive patients. AJR Am J Roentgenol 1986;147:479–86.

[16] Rubin E, Miller VE, Berland LL, Han SY, Koehler RE, Stanley RJ. Hand-held real-time breast sonography. AJR Am J Roentgenol 1985;144:623–7.

[17] Mendelson EB, Berg WA, Merritt CRB. Toward a standardized Breast Ultrasound Lexicon BI-RADS: ultrasound. Semin Roentgenol 2001;36:217–25.

[18] BIRADS–American College of Radiology. Breast imaging reporting and data system (BI-RADS). 3rd edition. Reston (VA): American College of Radiology; 1998.

[19] Venta LA, Kim JP, Pelloski CE, Morrow M. Management of complex breast cysts. AJR Am J Roentgenol 1999;173:1331–6.

[20] Czernobilsky B. Intracystic carcinoma of the female breast. Surg Gynecol Obstet 1967;124:93–8.

[21] Skaane P, Engedal K. Analysis of sonographic features in the differentiation of fibroadenoma and invasive ductal carcinoma. AJR Am J Roentgenol 1998;170: 109–14.

[22] Stavros AT, Thickman D, Rapp CL, Dennis MA, Parker SH, Sisney GA. Solid breast nodules: use of sonography to distinguish between benign and malignant lesions. Radiology 1995;196:123–34.

[23] Taylor KJW, Merritt C, Piccoli C, Schmidt R, Rouse G, Fornage B, et al. Ultrasound as a complement to mammography and breast examination to characterize breast masses. Ultrasound Med Biol 2002;28: 19–26.

[24] Zonderland HM, Coerkamp EG, van de Vijver MJ, van Voorthuisen AE. Diagnosis of breast cancer: contribution of US as an adjunct to mammography. Radiology 1999;213:413–22.

[25] Jackson VP. Management of solid breast nodules: what is the role of sonography? Radiology 1995;196:14–5.

[26] Rahbar G, Sie AC, Hansen GC, Prince JS, Melany ML, Reynolds HE, et al. Benign versus malignant solid breast masses: US differentiation. Radiology 1999; 213:889–94.

[27] Skaane P, Engedal K, Skjennald A. Interobserver variation in the interpretation of breast imaging: comparison of mammography, ultrasonography, and both combined in the interpretation of palpable noncalcified breast masses. Acta Radiol 1997;38:497–502.

[28] Stalsberg H, Thomas DB. Age distribution of histologic types of breast cancer. Int J Cancer 1993;54:1–7.

[29] Le Gal M, Ollivier L, Asselain B, Meunier M, Laurent M, Vielh P, et al. Mammographic features of 455 invasive lobular carcinomas. Radiology 1992;185: 705–8.

[30] Hilleren DJ, Andersson IT, Lindholm K, Linnell FS.

Invasive lobular carcinoma: mammographic findings in a 10-year experience. Radiology 1991;178:149–54.
[31] Chapellier C, Balu-Maestro C, Bleuse A, Ettore F, Bruneton JN. Ultrasonography of invasive lobular carcinoma of the breast: sonographic patterns and diagnostic value. Report of 102 cases. Clin Imaging 2000; 24:333–6.
[32] Meyer JE, Amin E, Lindfors KK, Lipman JC, Stomper PC, Genest D, et al. Medullary carcinoma of the breast: mammographic and US appearance. Radiology 1989; 170:79–82.
[33] Mehta TS, Raza S. Power Doppler sonography of breast cancer: does vascularity correlate with node status or lymphatic vascular invasion? AJR Am J Roentgenol 1999;173:303–7.
[34] Stomper PC, Connolly JL, Meyer JE, Harris JR. Clinically occult ductal carcinoma in situ detected with mammography: analysis of 100 cases with radiologic-pathologic correlation. Radiology 1989;172:235–41.
[35] Paulus DD, Libshitz HI. Metastasis to the breast. Radiol Clin North Am 1982;20:561–8.
[36] Lee SH, Park JM, Kook SH, Han BK, Moon WK. Metastatic tumors to the breast: mammographic and ultrasonographic findings. J Ultrasound Med 2000; 19:257–62.
[37] Chung SY, Oh KK. Imaging findings of metastatic disease to the breast. Yonsei Med J 2001;42:497–502.
[38] Balu-Maestro C, Bruneton JN, Geoffray A, Chauvel C, Rogopoulos A, Bittman O. Ultrasonographic post treatment follow-up of breast cancer patients. J Ultrasound Med 1991;10:1–7.
[39] Cole-Beuglet C, Soriano RZ, Kurtz AB, Goldberg BB. Fibroadenoma of the breast: sonomammography correlated with pathology in 122 patients. AJR Am J Roentgenol 1983;140:369–73.
[40] Heywang SH, Lipsit ER, Glassman LM, Thomas MA. Specificity of ultrasonography in the diagnosis of benign breast masses. J Ultrasound Med 1984;3: 453–61.
[41] Jackson VP, Rothschild PA, Kreipke DL, Mail JT, Holden RW. The spectrum of sonographic findings of fibroadenoma of the breast. Invest Radiol 1986; 21:34–40.
[42] Battegay E. Angiogenesis: mechanistic insights, neovascular diseases, and therapeutic prospects. J Mol Med 1995;73:333–46.
[43] Folkman J. How is blood vessel growth regulated in normal and neoplastic tissue? GHA Clowes Memorial Award lecture. Cancer Res 1986;46:467–73.
[44] Schoenberger SG, Sutherland CM, Robinson AE. Breast neoplasms: duplex sonographic imaging as an adjunct in diagnosis. Radiology 1988;168:665–8.
[45] Kook S, Park H, Lee Y, et al. Evaluation of solid breast lesions with power Doppler sonography. J Clin Ultrasound 1999;27:231–7.
[46] Raza S, Baum JK. Solid breast lesions: evaluation with power Doppler US. Radiology 1997;203:164–8.
[47] Cosgrove DO, Kedar RP, Bamber JC, al-Murrani B, Davey JB, Fisher C, et al. Breast diseases: color Doppler US in differential diagnosis. Radiology 1993;189: 99–104.
[48] Lee WJ, Chu JS, Huang CS, Chang MF, Chang KJ, Chen KM, et al. Breast cancer vascularity: color Doppler sonography and histopathology study. Breast Cancer Res Treat 1996;37:291–8.
[49] Lee WJ, Chu JS, Chang KJ, Chen KM. Occult breast carcinoma: use of color Doppler in localization. Breast Cancer Res Treat 1996;37:299–302.
[50] Britton PD, Coulden RA. The use of duplex Doppler ultrasound in the diagnosis of breast cancer. Clin Radiol 1990;42:399–401.
[51] Lee SK, Lee T, Lee KR, Su YG, Liu TJ. Evaluation of breast tumors with color Doppler imaging: a comparison with image-directed Doppler ultrasound. J Clin Ultrasound 1995;23:367–73.
[52] Rizzatto G, Chersevani R, Abbona M, Lombardo VL, Macorig D. High-resolution sonography of breast carcinoma. Eur J Radiol 1997;24:11–9.
[53] Peters-Engl CH, Fran W, Leodolter S, Medl M. Tumor flow in malignant breast tumors measured by Doppler ultrasound: an independent predictor of survival. Breast Cancer Res Treat 1999;54:65–71.
[54] Kedar RP, Cosgrove D, McCready VR, Bamber JC, Carter ER. Microbubble contrast agent for color Doppler US: effect on breast masses. Work in progress. Radiology 1996;198:679–86.
[55] Adler DD, Carson PL, Rubin JM, Quinn-Reid D. Doppler ultrasound color flow imaging in the study of breast cancer: preliminary findings. Ultrasound Med Biol 1990;16:553–9.
[56] McNicholas MMJ, Mercer PM, Miller JC, McDermott EW, O'Higgins NJ, MacErlean DP, et al. Color Doppler sonography in the evaluation of palpable breast masses. AJR Am J Roentgenol 1993;161:765–71.
[57] Madjar H, Sauerbrei W, Prompeler HJ, Wolfarth R, Gufler H. Color Doppler and duplex flow analysis for classification of breast lesions. Gynecol Oncol 1997;64:392–403.
[58] Blohmer JU, Oellinger H, Schmidt C, Hufnagl P, Felix R, Lichtenegger W, et al. Comparison of various imaging methods with particular evaluation of color Doppler sonography for planning surgery for breast tumors. Arch Gynecol Obstet 1999;262:159–71.
[59] Dixon JM, Walsh J, Paterson D, Chetty U. Colour Doppler ultrasonography studies of benign and malignant breast lesions. Br J Surg 1992;79:259–60.
[60] Alamo L, Fischer U. Contrast-enhanced color Doppler ultrasound characteristics in hypervascular breast tumors: comparison with MRI. Eur Radiol 2001;11: 970–7.
[61] Huber S, Helbich T, Kettenbach J, Dock W, Zuna I, Delome S. Effects of a microbubble contrast agent on breast tumors: computer-assisted quantitative assessment with color Doppler US. Early experience. Radiology 1998;208:485–9.
[62] Reinikainen H, Rissanen T, Paivansalo M, Paakko E, Jauhiainen J, Suramo I. B-Mode, power Doppler and contrast-enhanced power Doppler ultrasonography in

the diagnosis of breast tumors. Acta Radiol 2001;42: 106–13.
[63] Winehouse J, Douek M, Holz K, Madjar H, Gillams A, Lees W, et al. Contrast-enhanced colour Doppler ultrasonography in suspected breast cancer recurrence. Br J Surg 1999;86:1198–201.
[64] Finlayson CA, MacDermott TA. Ultrasound can estimate the pathologic size of infiltrating ductal carcinoma. Arch Surg 2000;135:158–9.
[65] Sterns EE, Sen Gupta S, Saunders F, Zee B. Vascularity demonstrated by Doppler ultrasound and immunohistochemistry in invasive ductal carcinoma of the breast. Breast Cancer Res Treat 1996;40:197–203.
[66] Lamb PM, Perry NM, Vinnicombe SJ, Wells CA. Correlation between ultrasound characteristics, mammographic findings and histological grade in patients with invasive ductal carcinoma of the breast. Clin Radiol 2000;55:40–4.
[67] Kobayashi T. Diagnostic ultrasound in breast cancer: analysis of retrotumerous echo patterns correlated with sonic attenuation by cancerous connective tissue. J Clin Ultrasound 1979;7:471–9.
[68] Kossoff G. Causes of shadowing in breast sonography. Ultrasound Med Biol 1988;14:211–5.
[69] Gozzi G, Cressa C, Bazzocchi M, Stanta G, Vidali C. Causes of attenuation of the sound waves in neoplasm of the breast: histologic and echographic correlation study. Radiol Med (Torino) 1986;72:195–8.
[70] Carter CL, Allen C, Henson DE. Relation of tumor size, lymph node status, and survival in 27,740 breast cancer cases. Cancer 1989;63:181–7.
[71] Fisher B, Bauer M, Wickerham DL, Redmond CK, Fisher ER, Cruz AB, et al. Relation of number of positive axillary nodes to the prognosis of patients with primary breast cancer: an NSABP update. Cancer 1983;52:1551–7.
[72] Larson D, Weinstein M, Goldberg I, Silver B, Recht A, Cady B, et al. Edema of the arm as a function of the extent of axillary surgery in patients with stage I–II carcinoma of the breast treated with primary radiotherapy. Int J Radiat Oncol Biol Phys 1986;12:1575–82.
[73] Maunsell E, Brisson J, Deschenes L. Arm problems and psychological distress after surgery for breast cancer. Can J Surg 1993;36:315–20.
[74] Hladiuk M, Huchcroft S, Temple W, Schnurr BE. Arm function after axillary dissection for breast cancer: a pilot study to provide parameter estimates. J Surg Oncol 1992;50:47–52.
[75] Krag D, Weaver D, Ashikaga T, Moffat F, Klimberg VS, Shriver C, et al. The sentinel node in breast cancer: a multicenter validation study. N Engl J Med 1998;339:941–6.
[76] Silverstein MJ, Eugene DG, Waisman JR, Senofsky GM, Colburn WJ, Gamagami P, et al. Axillary node dissection in T1a breast carcinoma. Cancer 1994;73: 664–7.
[77] Cady B. The need to re-examine axillary lymph node dissection in invasive breast carcinoma. Cancer 1994; 73:505–8.
[78] Verbanck J, Vandeweile I, De Winter H, Tytgat J, Van Aelst FV, Tanghe W. Value of axillary ultrasound and sonographically guided puncture of axillary nodes: a prospective study in 144 consecutive patients. J Clin Ultrasound 1997;25:53–6.
[79] Sacre RA. Clinical evaluation of axillary lymph nodes compared to surgical and pathological findings. Eur J Surg Oncol 1986;12:169–73.
[80] Vaidya JS, Vyas JJ, Thakur MH, Khandelwal KC, Mittra I. Role of ultrasonography to detect axillary node involvement in operable breast cancer. Eur J Surg Oncol 1996;22:140–3.
[81] Bonnema J, van Geel AN, van Ooijen B, Mali SPM, Tijam SL, Henzen-Logmans SC, et al. Ultrasound-guided aspiration biopsy for detection of nonpalpable axillary node metastases in breast cancer patients: new diagnostic method. World J Surg 1997;21:270–4.
[82] Yang WT, Betreweli C. Colour Doppler flow in normal axillary lymph nodes. Br J Radiol 1998;71:381–2.
[83] Swischuk LE, Desai PB, John SD. Exuberant blood flow in enlarged lymph nodes: findings on colour flow Doppler. Pediatr Radiol 1992;22:419–21.
[84] Mountford RA, Atkinson P. Doppler ultrasound examination of pathologically enlarged lymph nodes. Br J Radiol 1979;52:464–7.
[85] Kuijpers TJA, Obdeijn AIM, Kruyt RH, Oudkerk M. Solid breast neoplasms: differential diagnosis with pulsed Doppler ultrasound. Ultrasound Med Biol 1994;20:517–20.
[86] Holcombe C, Pugh N, Lyons K, Douglas-Jones A, Mansel RE, Horgan K. Blood flow in breast cancer and fibroadenoma estimated by colour Doppler ultrasonography. Br J Surg 1995;82:787–8.
[87] Kubek KA, Chan L, Frazier TG. Color Doppler flow as an indicator of nodal metastasis in solid breast masses. J Ultrasound Med 1996;15:835–41.
[88] Lagios MD, Westdahl PR, Rose MR. The concept and implications of multicentricity in breast carcinoma. In: Sommers S, Rosen P, editors. Pathology annual, Volume 16. New York: Appleton-Century-Crofts; 1981. p. 83–102.
[89] Holland R, Veling SHJ, Mravunac M, Hendriks JH. Histologic multifocality of Tis, T1–2 breast carcinomas: implications for clinical trials of breast-conserving surgery. Cancer 1985;56:979–90.
[90] Berg WA, Gilbreath PL. Multicentric and multifocal cancer: whole-breast US in preoperative evaluation. Radiology 2000;214:59–66.
[91] Kolb TM, Lichy J, Newhouse JH. The impact of bilateral whole breast ultrasound in women with dense breasts and recently diagnosed breast cancer [abstract]. Radiology 2000;217(P):318.
[92] Moon WK, Im J, Noh D. Multifocal, multicentric, and contralateral breast cancer: bilateral whole breast ultrasound in preoperative assessment [abstract]. Radiology 2000;217(P):318–9.
[93] Fornage BD, Faroux MJ, Simatos A. Breast masses: US-guided fine-needle aspiration biopsy. Radiology 1987;162:409–14.

[94] Fornage BD. Guided fine-needle aspiration biopsy of nonpalpable breast lesions: calculation of accuracy values [letter]. Radiology 1990;177:884–5.
[95] Fornage BD. Percutaneous biopsy of the breast: state of the art. Cardiovasc Intervent Radiol 1991; 14:29–39.
[96] Kopans DB. Fine-needle aspiration of clinically occult breast lesions. Radiology 1989;170:313–4.
[97] Gordon PB, Goldenberg SL, Chan NHL. Solid breast lesions: diagnosis with US-guided fine-needle aspiration biopsy. Radiology 1993;189:573–80.
[98] Parker SH, Jobe WE, Dennis MA, Stavros TA, Johnson KK, Yakes WF, et al. US-guided automated large-core breast biopsy. Radiology 1993;187:507–11.
[99] Parker SH, Burbank F, Jackman RJ, Aucreman CJ, Cardenosa G, Cink TM, et al. Percutaneous large-core breast biopsy: a multi-institutional study. Radiology 1994;193:359–64.
[100] Hatada T, Ishii H, Ichii S, Okada K, Fujiwara Y, Yamamura T. Diagnostic value of ultrasound-guided fine-needle aspiration biopsy, core-needle biopsy, and evaluation combined use in the diagnosis of breast lesions. J Am Coll Surg 2000;190:299–303.
[101] Logan-Young W, Dawson AE, Wilbur DC, Avila EE, Tomkiewicz ZM, Sheils LA, et al. The cost-effectiveness of fine-needle aspiration cystology and 14-gauge core needle biopsy compared with open surgical biopsy in the diagnosis of breast carcinoma. Cancer 1998;82:1867–73.
[102] Harlow SP, Krag DN, Ames SE, Weaver DL. Intraoperative ultrasound localization to guide surgical excision of nonpalpable breast carcinoma. J Am Coll Surg 1999;189:241–6.
[103] Moore MM, Whitney LA, Cerilli L, Imbrie JZ, Bunch M, Simpson VB, et al. Intraoperative ultrasound is associated with clear lumpectomy margins for palpable infiltrating ductal breast cancer. Ann Surg 2001; 233:761–8.
[104] Smith LF, Rubio IT, Henry-Tillman R, Korourian S, Klimberg VS. Intraoperative ultrasound-guided breast biopsy. Am J Surg 2000;180:419–23.
[105] Sickles EA. Mammographic detectability of breast microcalcifications. AJR AM J Roentgenol 1982; 139:913–8.
[106] Rizzatto G, Chersevani R, Solbiati L. High-resolution ultrasound assists in breast diagnosis. Diagnostic Imaging International 1993;9:42–5.
[107] Gufler H, Buitrago-Tellez CH, Madjar H, Allmann KH, Uhl M, Rohr-Reyes A. Ultrasound demonstration of mammographically detected microcalcifications. Acta Radiol 2000;41:217–21.
[108] Ranieri E, D'Andrea MR, D'Alessio A, Bergomi S, Caprio G, Calabrese GB, et al. Ultrasound in the detection of breast cancer associated with isolated clustered microcalcifications, mammographically identified. Anticancer Res 1997;17:2831–6.
[109] Yang WT, Suen M, Ahuja A, Metreweli C. In vivo demonstration of microcalcification in breast cancer using high resolution ultrasound. Br J Radiol 1997; 70:685–90.
[110] Teh WL, Wilson ARM, Evans AJ, Burrell H, Pinder SE, Ellis IO. Ultrasound guided core biopsy of suspicious mammographic calcifications using high frequency and power Doppler ultrasound. Clin Radiol 2000;55:390–4.
[111] Fung HM, Jackson FI. Clinically and mammographically occult breast lesions demonstrated by ultrasound. J R Soc Med 1990;83:396–8.
[112] Kopans DB, Meyer JE, Lindfors KK. Whole-breast US imaging: four-year follow-up. Radiology 1985;157: 505–7.
[113] Gordon PB, Goldenberg SL. Malignant breast masses detected only by ultrasound. Cancer 1995;76:626–30.
[114] Kopans D. Breast-cancer screening with ultrasonography. Lancet 1999;354:2096–7.
[115] Beekman WH, Hage JJ, Taets van Amerongen AHM, Mulder JW. Accuracy of ultrasonography and magnetic resonance imaging in detecting failure of breast implants filled with silicone gel. Scand J Plast Reconstr Hand Surg 1999;33:415–8.
[116] Park AJ, Walsh J, Reddy PSV, Chetty U, Watson ACH. The detection of breast implant rupture using ultrasound. Br J Plast Surg 1990;49:299–301.
[117] DeBruhl ND, Gorczyca DP, Ahn CY, Shaw WW, Bassett LW. Silicone breast implants: US evaluation. Radiology 1993;189:95–8.
[118] Chung KC, Wilkins EG, Beil RJ, Helvie MA, Ikeda DM, O'Neal RM, et al. Diagnosis of silicone gel breast implant rupture by ultrasonography. Plast Reconstr Surg 1996;97:104–9.
[119] Venta LA, Salomon CG, Flisak ME, Venta ER, Izquierdo R, Angelats J. Sonographic signs of breast implant rupture. AJR Am J Roentgenol 1996;166:1413–9.
[120] Harris KM, Ganott MA, Shestak KC, Losken HW, Tobon H. Silicone implant rupture: detection with US. Radiology 1993;187:761–8.
[121] Treves N, Holleb AI. Cancer of the male breast: a report of 146 cases. Cancer 1955;8:1239–50.
[122] Cole-Beuglet C, Schwartz GF, Kurtz AB, Patchefsky AS, Goldberg BB. Ultrasound mammography for male breast enlargement. J Ultrasound Med 1982;1:301–5.
[123] Jellins J, Kossoff G, Reeve TS. The ultrasonic appearance of pathology in the male breast. Ultrasound Med Biol 1975;2:43–4.

RADIOLOGIC CLINICS OF NORTH AMERICA

Radiol Clin N Am 41 (2003) 857–862

Index

Note: Page numbers of article titles are in **boldface** type.

A

Abdominal wall, ultrasonography of, in first trimester, 683–684

Abscesses, tubo-ovarian, MR imaging of, 808–809

Acardiac parabiotic twin, radiofrequency ablation of, 721–722
ultrasonography of, 7190722

Actinomycosis, ovarian, MR imaging of, 808–809

Adnexal masses, benign, MR imaging of, 809, 811
in ectopic pregnancy, ultrasonography of, 672–673

Aliasing, on fetal MR imaging, 736

Amniocentesis, to diagnose aneuploidy, 695–696

Amnioreduction, for twin-twin transfusion syndrome, 717–718

Anencephaly, ultrasonography of, in first trimester, 676, 681

Aneuploidy, prenatal diagnosis of, **695–708**
amniocentesis in, 695–696
chorionic villus sampling in, 696
cordocentesis in, 696
maternal serum screening in, 696–697, 704–705
ultrasonography in, 676–677, 697–699, 704
Down syndrome, 699–702
triploidy syndrome, 698–699
trisomy 13, 698
trisomy 18, 697–698, 702, 704
trisomy 21, 697
Turner syndrome, 698

Arterio-arterial anastomoses, in placenta, 712–713

Arteriovenous anastomoses, in placenta, 713

Axillary involvement, by breast cancer, ultrasonography of, 847–848

B

Biopsy, fine-needle aspiration, of breast cancer, ultrasonography in, 849

Bleeding, ovarian, MR imaging of, 802
postmenopausal. *See* Postmenopausal bleeding.

Bone mineral density, definition of, 813
dual x-ray absorptiometry of, 818

Bowel herniation, ultrasonography of, in first trimester, 683–684

Breast cancer, screening for, ultrasonography in, 851

Breasts, ultrasonography of, **841–856**
contrast-enhanced Doppler, 846–847
for cystic lesions, 842–843
for implants, 851–852
for microcalcifications, 850–851
for solid lesions, 843–846
in males, 852
intraoperative, 849–850
non-contrast-enhanced Doppler, 846
normal anatomy in, 842
screening, for cancer, 851
for known cancer, 848–849
technique for, 841–842
to guide fine-needle aspiration biopsy, 849
to stage cancer, 847–849
nodal involvement in, 847–848
tumor size and grade in, 847

Brenner tumors, MR imaging of, 805

Bulk motion, on fetal MR imaging, 734

C

Central nervous system, ultrasonography of, in first trimester, 681–682

Cervix, in female infertility, 758

Chorionic villus sampling, to diagnose aneuploidy, 696

0033-8389/03/$ – see front matter © 2003 Elsevier Inc. All rights reserved.
doi:10.1016/S0033-8389(03)00090-3

Color duplex Doppler imaging, of postmenopausal bleeding, 775

Computed tomography, quantitative, of osteoporosis, 820–824

Congenital heart disease, ultrasonography of, in first trimester, 684

Conjoined twins, ultrasonography of, 723–724
in first trimester, 691–692

Cordocentesis, to diagnose aneuploidy, 696

Cystourethrography, voiding, of pelvic floor relaxation, 749

Cysts, breasts, ultrasonography of, 842–843
ovarian, MR imaging of, 800, 802–803

D

Defecography, of pelvic floor relaxation, 749–750

Dermoid cysts, ovarian, MR imaging of, 808

Digital x-ray radiogrammetry, of osteoporosis, 817

Discordant anomalies, in monochorionic twins, 722

Doppler imaging, of breasts, 846–847
of postmenopausal bleeding, 775

Double decidual reaction sign, in ultrasonography, of gestational sac, 664–665

Down syndrome, maternal serum screening for, in first trimester, 704
ultrasonography of, in second trimester, 699–702

Dual x-ray absorptiometry, of osteoporosis, 818–820

E

Ectopic pregnancy, hematosalpinx and hematocele due to, MR imaging of, 809
ultrasonography of. *See* Ultrasonography, in first trimester.

Edema, ovarian, MR imaging of, 809, 811

Edward syndrome, ultrasonography of, in second trimester, 696–698

Embryonic heartbeat, ultrasonography of, 666–667

Embryonic pole, ultrasonography of, 666

Encephaloceles, ultrasonography of, in first trimester, 681

Endometriomas, MR imaging of, 803

Endometriosis, and female infertility, 766
solid, MR imaging of, 811

Endometrium, in ectopic pregnancy, ultrasonography of, 673
in postmenopausal bleeding, ultrasonography of. *See* Postmenopausal bleeding.
sonohysterography of. *See* Sonohysterography.

F

Fallopian tube, in female infertility, 760–764

Fat saturation, on fetal MR imaging, 742

Female infertility, **757–767**
cervix in, 758
congenital uterine anomalies and, 759–760
endometriosis and, 766
fallopian tube in, 760–764
peritoneal cavity in, 764
polycystic ovary syndrome and, 764–766
uterine cavity filling defects and, 758–759
uterus in, 758
versus normal ovaries, 764
versus normal reproduction, 757

Fetal abnormalities, ultrasonography of, in first trimester, 674–676, 682

Fetal magnetic resonance imaging, **729–745**
artifacts on, 734–738
aliasing, 736
bulk motion, 734
fluid motion, 734–735
Gibbs ringing artifact, 738
motion artifact, 734
partial volume artifact, 738
radiofrequency interference, 737
repeat visualization or nonvisualization, 735–736
susceptibility artifact, 737
consent for, 729
image quality on, 738, 740–742
fat saturation, 742
patient body habitus and use of surface coil, 740–741
signal inhomogeneity, 741–742
signal-to-noise ration, 738, 740
indications for, 729
interpretation of, 730–731
monitoring during, 730
patient positioning for, 729–730
pitfalls in, 742
protocol for, 730

versus ultrasonography, 729
viewing during, 730

Fetal structural abnormalities, ultrasonography of, in first trimester, 676–677

Fibroadenomas, of breasts, ultrasonography of, 845

Fibromas, ovarian, MR imaging of, 805

Fine-needle aspiration biopsy, of breast cancer, ultrasonography in, 849

Fluid motion, on fetal MR imaging, 734–735

Fractures, osteoporosis and, 814–817

G

Genitourinary tract, ultrasonography of, in first trimester, 684

Germ cell tumors, ovarian, MR imaging of, 808

Gestational sac, ultrasonography of, in first trimester, 663–665

Gibbs ringing artifact, on fetal MR imaging, 738

H

Heartbeat, embryonic, ultrasonography of, 666–667

Hematoceles, MR imaging of, 809

Hematosalpinx, MR imaging of, 809

Herniation, of bowel, ultrasonography of, in first trimester, 683–684

Hormone replacement therapy, and assessment of postmenopausal bleeding, 777

Human chorionic gonadotropin levels, in ectopic pregnancy, 673–674

Hydrocephalus, ultrasonography of, in first trimester, 682

Hyperreactio luteinalis, MR imaging of, 802

Hysterography, saline infusion.
See Sonohysterography.

Hysteroscopy, of postmenopausal bleeding, 775
versus sonohysterography, 793–794

I

Implants, breasts, ultrasonography of, 851–852

Infertility, female. *See* Female infertility.

Inflammatory breast cancer, ultrasonography of, 845

Inflammatory masses, ovarian, MR imaging of, 808–809

Intradecidual sign, in ultrasonography, of gestational sac, 664

Intrauterine adhesions, sonohysterography of, 789

K

Krukenberg tumors, MR imaging of, 805

L

Laser photocoagulation, for twin-twin transfusion syndrome, 718

Leiomyomas, submucosal, sonohysterography of, 787
uterine, and postmenopausal bleeding, ultrasonography of, 773

M

Magnetic resonance imaging, fetal. *See* Fetal magnetic resonance imaging.
of osteoporosis, 825–827
of ovaries. *See* Ovaries.
of pelvic floor relaxation. *See* Pelvic floor relaxation.
of trabecular bone structure, in osteoporosis, 830–834

Maternal serum screening, to diagnose aneuploidy, 696–697, 704

Metastatic disease, to breasts, ultrasonography of, 845

Micro-computed tomography, of trabecular bone structure, in osteoporosis, 830–831

Microcalcifications, in breasts, ultrasonography of, 850–851

Monoamniotic twins, ultrasonography of, 724–725

Monochorionic twins, embryology of, 709–710
ultrasonography of, **709–727**
chorionicity and amnionicity in, 710–712
for acardiac parabiotic twin, 719–722
radiofrequency ablation of, 721–722
for conjoined twins, 723–724
for discordant anomalies, 722
for monoamniotic twins, 724–725
for twin embolization syndrome, 719

for twin-twin transfusion syndrome, 714–719
amnioreduction for, 717–718
laser photocoagulation for, 718
for unequal placental sharing, 714
placental vascular anatomy in, 712–713

Motion artifacts, on fetal MR imaging, 734

N

Nodal involvement, by breast cancer, ultrasonography of, 847–848

Nuchal translucency, ultrasonography of, in first trimester, 674–676, 682, 704

O

Osteodensitometry, of osteoporosis, 817–818

Osteoporosis, **813–839**
and vertebral fractures, 814–817
definition of, 813–814
dual x-ray absorptiometry of, 818–820
MR imaging of, 825–827
osteodensitometry of, 817–818
plain films of, 816–817
quantitative CT of, 820–824
quantitative ultrasonography of, 824–825
trabecular bone structure in, 827, 829–834
micro-CT of, 830–831
MR imaging of, 830–834
plain films of, 829–830
quantitative ultrasonography of, 830

Ovarian hyperstimulation syndrome, MR imaging of, 802

Ovaries, MR imaging of, **799–812**
for benign neoplasia, 803–805, 808
germ cell tumors, 808
sex-cord stromal tumors, 805, 808
surface epithelial tumors, 804–805
for bleeding, 802
for endometriomas, 803
for functional cysts, 800, 802–803
for hematosalpinx and hematocele, 809
for inflammatory masses, 808–809
for massive edema, 809, 811
for peritoneal inclusion cysts, 803
for solid endometriosis, 811
for torsion, 809
normal ovaries, 799–800
technique for, 799
normal, versus female infertility, 764

P

Partial volume artifact, on fetal MR imaging, 738

Patau syndrome, ultrasonography of, in second trimester, 698

Pelvic floor relaxation, **747–756**
anatomy of, 747, 749
defecography of, 749–750
MR imaging of, 750–755
anatomy in, 751–752
for anterior compartment pathology, 752–753
for middle compartment pathology, 753
for posterior compartment pathology, 753–754
seated imaging in, 754–755
severe cases of, 754
technique for, 751
three-dimensional volumetric analysis in, 755
ultrasonography of, 749
voiding cystourethrography of, 749

Pelvic fluid, in ectopic pregnancy, ultrasonography of, 672

Percutaneous umbilical cord sampling, to diagnose aneuploidy, 696

Peritoneal cavity, in female infertility, 764

Peritoneal inclusion cysts, MR imaging of, 803

Photocoagulation, laser, for twin-twin transfusion syndrome, 718

Placenta, vascular anatomy of, 712–713

Plain films, of fracture and deformity, due to osteoporosis, 816–817
of trabecular bone structure, in osteoporosis, 829–830

Polycystic ovary syndrome, and female infertility, 764–766
MR imaging of, 803

Polyps, endometrial, and postmenopausal bleeding, ultrasonography of, 771–772
sonohysterography of, 785–786

Postmenopausal bleeding, color duplex Doppler imaging of, 775
Doppler imaging of, 775
hysteroscopy of, 775
sonohysterography of, 771–772, 775, 783–784, 791–793
three-dimensional ultrasonography of, 775–776
ultrasonography of, **769–780**
atrophic endometrium in, 770–771
endometrial carcinoma in, 773–775

endometrial hyperplasia in, 772–773
endometrial polyps in, 771–772
in women on hormone replacement therapy, 777
in women on tamoxifen, 776–777
uterine leiomyomas in, 773

Pregnancy, ectopic, hematosalpinx and hematocele due to, MR imaging of, 809
ultrasonography of. *See* Ultrasonography, in first trimester.
normal, ultrasonography of. *See* Ultrasonography, in first trimester.

Q

Quantitative computed tomography, of osteoporosis, 820–824

Quantitative ultrasonography, of osteoporosis, 824–825
of trabecular bone structure, in osteoporosis, 830

R

Radiofrequency ablation, of acardiac parabiotic twin, 721–722

Radiofrequency interference, on fetal MR imaging, 737

Retained products of conception, sonohysterography of, 789–790

S

Saline infusion hysterography. *See* Sonohysterography.

Salpingitis isthmica nodosa, and female infertility, 762–763

Sclerosing stromal tumors, MR imaging of, 805, 808

Serum human chorionic gonadotropin levels, in ectopic pregnancy, 673–674

Sex-cord stromal tumors, MR imaging of, 805, 808

Signal-to-noise ratio, on fetal MR imaging, 738, 740

Single-photon absorptiometry, of osteoporosis, 817–818

Snowstorm sign, in ultrasonography, of breast implants, 852

Sonohysterography, **781–797**
catheter insertion for, 782–783
of dysfunctional uterine bleeding, 784–785
of endometrial carcinoma, 788–790
of endometrial hyperplasia, 787–788, 790
of endometrial polyps, 785–786
of intrauterine adhesions, 789
of normal endometrium, 783
of postmenopausal bleeding, 771–772, 775, 783–784, 791–793
of retained products of conception, 789–790
of subendometrial changes, due to tamoxifen, 790–791
of submucosal leiomyomas, 787
patient preparation for, 781–782
versus hysteroscopy, 793–794

Stepladder sign, in ultrasonography, of breast implants, 852

Struma ovarii, MR imaging of, 808

Surface epithelial tumors, ovarian, MR imaging of, 804–805

Susceptibility artifact, on fetal MR imaging, 737

T

Tamoxifen, and assessment of postmenopausal bleeding, 776–777
subendometrial changes due to, sonohysterography of, 790–791

Teratomas, ovarian, MR imaging of, 808

Thecomas, MR imaging of, 805

Three-dimensional ultrasonography, of postmenopausal bleeding, 775–776

Three-dimensional volumetric analysis, in ultrasonography, of pelvic floor relaxation, 755

Torsion, ovarian, MR imaging of, 809

Trabecular bone structure, in osteoporosis. *See* Osteoporosis.

Transvaginal ultrasonography, of tamoxifen-induced subendometrial changes, 792

Triploidy, ultrasonography of, in first trimester, 684, 686, 691

Triploidy syndrome, ultrasonography of, in second trimester, 698–699

Trisomy 13, ultrasonography of, in second trimester, 698

Trisomy 18, ultrasonography of, in second trimester, 696–698, 702, 704

Trisomy 21, ultrasonography of, in second trimester, 696

Tuberculosis, ovarian, MR imaging of, 808–809

Tubo-ovarian abscesses, MR imaging of, 808–809

Turner syndrome, ultrasonography of, in second trimester, 698

Twin embolization syndrome, ultrasonography of, 719

Twins, monochorionic. *See* Monochorionic twins.

Twin-twin transfusion syndrome. *See* Monochorionic twins.

U

Ultrasonography, fetal, versus fetal MR imaging, 729
in first trimester, **663–679, 681–693,** 704–705
of anterior abdominal wall, 683–684
of central nervous system, 681–682
of congenital heart disease, 684
of conjoined twins, 691–692
of early pregnancy failure, 668, 670
of ectopic pregnancy, 670–674
adnexal mass in, 672–673
endometrium in, 673
free fluid in, 672
management of, 674
serum hCG levels in, 673–674
of fetal abnormalities, 674–676
nuchal translucency, 674–676, 682, 704
of fetal structural abnormalities, 676–677
of genitourinary tract, 684
of normal pregnancy, 663–667
age assessment in, 667
embryonic pole in, 666
gestational sac in, 663–665
heartbeat in, 666–667
yolk sac in, 665–666
of triploidy, 684, 686, 691
of umbilical cord, 682–683
transducer technology in, 663
of breasts. *See* Breasts.
of monochorionic twins. *See* Monochorionic twins.
of pelvic floor relaxation, 749
of postmenopausal bleeding. *See* Postmenopausal bleeding.
quantitative, of osteoporosis, 824–825
of trabecular bone structure, in osteoporosis, 830
to diagnose aneuploidy. *See* Aneuploidy.
transvaginal, of tamoxifen-induced subendometrial changes, 792

Umbilical cord, ultrasonography of, in first trimester, 682–683

Umbilical cord sampling, to diagnose aneuploidy, 696

Uterine anomalies, congenital, and female infertility, 759–760

Uterine bleeding, dysfunctional, sonohysterography of, 784–785

Uterine cavity filling defects, and female infertility, 758–759

Uterine leiomyomas, and postmenopausal bleeding, ultrasonography of, 773

Uterus, in female infertility, 758

V

Voiding cystourethrography, of pelvic floor relaxation, 749

Y

Yolk sac, ultrasonography of, 665–666